PROTECTION OF SERIES COMPENSATED TRANSMISSION LINES

A THESIS

Submitted in partial fulfilment of the requirements for the award of the degree of

DOCTOR OF PHILOSOPHY
in
ELECTRICAL ENGINEERING

by

VYAS BHARGAV YASHVANTRAI

DEPARTMENT OF ELECTRICAL ENGINEERING
INDIAN INSTITUTE OF TECHNOLOGY ROORKEE
ROORKEE – 247 667 (INDIA)

OCTOBER, 2014

INDIAN INSTITUTE OF TECHNOLOGY ROORKEE
ROORKEE

CANDIDATE'S DECLARATION

I hereby certify that the work which is being presented in this thesis entitled **"PROTECTION OF SERIES COMPENSATED TRANSMISSION LINE"** in partial fulfilment of the requirements for the award of *the Degree of Doctor of Philosophy* and submitted in the Department of Electrical Engineering of Indian Institute of Technology Roorkee, Roorkee is an authentic record of my own work carried out during a period from July, 2010 to April, 2014 under the supervision of Dr. R. P. Maheshwari, Professor and Dr. Biswarup Das, Professor, Department of Electrical Engineering, Indian Institute of Technology Roorkee, Roorkee.

The matter presented in this thesis has not been submitted by me for the award of any other degree of this or any other Institution.

(VYAS BHARGAV YASHVANTRAI)

This is to certify that the above statement made by the candidate is correct to the best of our knowledge.

(R. P. Maheshwari)
Supervisor

(Biswarup Das)
Supervisor

Date:

The Ph.D. Viva-Voce Examination of ***Mr. Vyas Bhargav Yashvantrai***, Research Scholar, has been held on …………….

Signature of Supervisors   Chairman, SRC   Signature of External Examiner

Head of the Deptt./Chairman, ODC

ABSTRACT

Series compensation is an attractive option for maximizing power transfer through existing power transmission networks. Series compensation offers considerable technical and economic advantages in long Extra-High Voltage (EHV) transmission systems. In view of the benefits offered by the series compensators, they find increasing applications. It is therefore, imperative that relevant existing transmission line protection approaches are investigated and modified in series compensated environment along with the primary system developments.

Although series compensation is effective in increasing the transient stability and optimizing the power flow in the system, the protection of series compensated line is more complex than that of the uncompensated transmission lines. Series compensation can significantly modify the apparent impedance presented to the impedance based relays. In this respect, the transmission line protection in series compensated environment needs a significant modification for reliability of the power supply.

The work presented in this thesis addresses the problems encountered by distance relaying scheme, when employed in series compensated transmission line. Besides fault detection, fault classification, fault zone identification and fault location estimation are main relaying tasks. An attempt has been made in this thesis to improve the performance of distance relaying scheme through improvement in all these aspects separately.

A detailed analysis of the impact of series compensation on the transmission line protection has been carried out in the initial part of the thesis with up to date bibliographical survey. Based on this survey, a requirement of accurate, reliable and fast protection algorithms for the series-compensated transmission lines has thus been identified.

The work presented in this thesis mainly deals with problems and their solutions for the protection of the transmission lines with mid-line series compensation. Both variants of series compensation, fixed and controllable (thyristor controlled series compensator, TCSC) are considered for this study. On the basis of the requirements identified from available literature, various techniques for fault detection, classification, fault zone identification and estimation of the fault location on the series compensated transmission line are reported in this work. All the methods developed in this thesis are single-end algorithms (based on the measurements taken at the relaying end only) without the need for data communication between two line ends.

Further, in this work, a versatile and new protection algorithm is developed that can provide effective protection to uncompensated and series compensated transmission line without any modification in the methodology.

All these algorithms were tested on a mid-line series compensated transmission line connecting a two-area system. The system model is developed using Power System Computer Aided Design (PSCAD) and measured fault data from these simulations are imported into the MATLAB platform to implement the algorithms. Upon testing, the obtained results show improvement in performance of all fault classification, fault zone identification and fault location algorithms as compared to those reported in the literature.

In addition, fault classification and fault zone identification algorithms are further modified and improved for application to a TCSC compensated transmission line.

ACKNOWLEDGEMENTS

Action is Thy Duty; Reward is Not Thy Concern – **Bhagwad Gita**

It is a pleasant task to express my sincere thanks to all those who digested the above proverb and contributed in many ways to the success of this study and made it an unforgettable experience for me.

First and foremost, I would like to express my sincere gratitude to my supervisors, Dr. R. P. Maheshwari and Dr. B. Das for supporting me over my entire candidature in every possible way. They have been critical when needed for my own very best, pulled me out of difficulties and motivated me when I felt low. They have guided me through the very basics of conducting research to documenting and writing research papers and presenting them in public. I have learned a lot from their insightful and professional stands and it would not be exaggerating to consider them my professional mentor. This thesis would not have been possible without their help and support and my sincere regards and appreciation towards them.

Special thanks to my research committee members, Dr. Manoj Tripathy, Dr. Vinay Pant and Dr. R. Balasubramanian, for their support and helpful suggestions. Their guidance has served me well and I owe them my heartfelt appreciation.

I take this opportunity to sincerely acknowledge the Head of the Depatment, Department of Electrical Engineering, Indian Institute of Technology, Roorkee, I thank all Professors in the department for their help during my study and for providing necessary infrastructure and resources to accomplish my research work.

I gratefully acknowledge Dr. S. R. Upadhyay for his encouragement and attention which have provided good and smooth basis for my Ph.D. tenure. My thanks are due to Jatinbhai Patel for his untried support, help and encouragement during my research tenure at IIT, Roorkee.

It is my pleasure to acknowledge all of current and previous research scholars in the department. Specially, Amit Kumar Singh, Dr. Jignesh Makwana, Bhavik Patel, Dr. Subramaniam Murala, Dr. A. B. Gonde, Dr. G. R. Biswal, Pratul Arvind, Dr. Megha Agarwal, Haresh Sabhadiya for their enormous support and providing an encouraging atmosphere for research in departmental laboratory. I would also like to thank some people who accompanied me for entire tenure, right from course work. A detail discussion with Ajay Khunteta, Nagendra Narona, Yatindra Kumar, Subramanya Bhakar, Guruswamy K. P. and many others helped me to develop scientific approach and attitude.

I am indebted to thank friends and research scholars in the department, few of them are Ambrish Mishra, N. Biradar, Ashok Manori, Shailendra Bhasker, Anubhav Agarwal, Nagendra Gautam, Sachin Singh, Arvind Kumar Yadav and many others for their continues encouragement and moral support.

I would like to thank my friends at IIT, Roorkee campus, whose motivation and support helped me to work in all type of situations. Dr. Haresh Patoliya, Dr. J. J. Patel, Vishwas Raval, Viredra Rao, Tapan Trivedi, Mitesh Panchal, Bhavin Shah, Mehulkumar Gor, Dilip Jani, A. B. Dohare, R. P. Singh, Srinivasa Kishore T. and many more are always supportive and helping in every aspect of research and social life.

I would like to extend my gratitude towards Commissioner of Technical Education, Gujarat State and Prof. M. V. Garach (Principal, GECR) for granting me deputation for this research. Active help from Prof. C. H. Vithalani, Prof. Amee Chhaya, Prof. A. M. Joshi, Prof. P. C. Sheth, Prof. D. R. Jolapura, Prof. M. K. Kathiriya and Prof. P. D. Rawal for carrying my teaching load at the institute as per CTE requirement made this deputation possible.

The sense of achievement and appreciation can never be complete without acknowledging my family. This journey would have never been successful without the blessings of my parents, Chandrikaben and Yashvantrai Vyas. My sister Kajal has been supported throughout with faith and encouragement. I would like to thank my wife, Riddhi, whose love and encouragement allowed me to finish this journey. She has always been there through the smooth and rough patches, through joys and sorrows. I am indebted to her for her immeasurable love, kindness and support. I also want to thank to my in-laws, Hinaben and Ashok Kumar Trivedi for their unconditional support. We lost Hinaben Trivedi in very initial part of this journey, but felt she is always with us with all kind of blessings and support.

Lastly but not the least, I would like to extend my gratitude to all those, whose names I may have missed out but they have been an integral part of my research journey

CONTENTS

LIST OF FIGURES

LIST OF TABLES

LIST OF ACRONYMS

AC	Alternating Current
AG	Air Gap
AI	Artificial Intelligence
ANN	Artificial Neural Network
ASC	Advance Series Compensator
BP	Back-propagation
CB	Circuit Breaker
ChNN	Chebyshev Neural Network
CT	Current Transformer
CVT	Capacitive Voltage Transformer
CWT	Continuous Wavelet Transform
Db	Daubechies mother wavelet
DBD	Delta-Bar-Delta
DC	Direct Current
DDA	Deterministic Differential Approach
DFT	Discrete Fourier Transform
DSP	Digital Signal Processing
DWPT	Discrete Wavelet Packet Transform
DWPTE	Discrete Wavelet Packet Transform Entropy
DWT	Discrete Wavelet Transform
EFR	Energy Feature Ratio
EHV	Extra High Voltage
ELM	Extreme Learning Machine
EMTDC	Electro Magnetic Transits for DC
FACTS	Flexible AC Transmission Systems
FCR	Fault Classification Ratio
FDR	Fault Detection Ratio
FFT	Fast Fourier Transform
FIA	Fault Inception Angle
FL	Fuzzy Logic

FLNN	Functional Link Neural Networks
FT	Fourier Transform
GA	Genetic Algorithm
GBI	Generator Base Impedance
GDR	Gear Differentiation Rule
GT	Gabor Transform
HOS	Higher-Order Statistic
Lib-SVM	Library of Support Vector Machine
LM	Linear Model
LSE	Least Square Estimation
LSLM	Least Square Levenberg-Marquardt
ML	Machine Learning
MLP	Multilayer Perceptron
MLPNN	Muli-Layer Perceptron Neural Network
MOV	Metal Oxide Varistor
MW	Mega Watt
PLL	Phase Lock Loop
PNN	Probabilistic Neural Network
PSCAD	Power System Computer Aided Design
PT	Potential Transformer
R	Resistance
RBF	Radial Base Function
RBF	Radial Basis Function
RBFNN	Radial Base Function Neural Network
RLSFF	Recursive Least Square Algorithm with Forgetting Factor
SC	Series Compensation
STFT	Short Time Fourier Transform
SVC	Support Vector Classifier
SVM	Support Vector Machine
SVR	Support Vector Regression
TCR	Thyristor Controlled Reactor
TCSC	Thyristor Controlled Series Compensator

TLS-ESPRIT	Total Least Square Estimation of Signal Parameters via Rotational Invariance Technique
UDWT	Undecimatted Wavelet Transform
WPD	Wavelet Packet Decomposition
WPT	Wavelet Packet Transform
WT	Wavelet Transform

LIST OF SYMBOLS

X_L	Total inductive reactance of the transmission line
X_C	Effective capacitive reactance of the compensator
Z_{SG1}	Generator impedance for source generator G_1
Z_{SG2}	Generator impedance for source generator G_2
δ	Transmission line loading angles
Rf	Fault Resistance
L	Fault distance
fs	Sampling Frequency
$()^*$	Complex Conjugate
P	Active Power
Q	Reactive power
I_{MOV}	Current passing through the MOV
I_0	Maximum permissible reference current for MOV
V_{REF}	Knee-point voltage for the MOV
f	System Frequency
f_n	Natural frequency of oscillation
ψ	Mother Wavelet
Y	Output vector of the classifier
b	Bias used for the classifier
$\uparrow 2$	Up sampling by two
$\downarrow 2$	Down sampling by two
$T_n(x)$	Chebyshev expansion component
X	Input pattern vector for a classifier
L-g	Line to ground fault
L-L-g	Double line to ground fault
L-L	Double line fault
L-L-L-g	Triple line to ground fault
A-g	A-phase to ground fault
B-g	B-phase to ground fault
C-g	C-phase to ground fault

A-B-g	A and B phase fault with ground
B-C-g	B and C phase fault with ground
C-A-g	C and A phase fault with ground
A-B-C-g	A, B and C phase fault with ground
A-B	A and B phase fault
B-C	B and C phase fault
C-A	C and A phase fault

CHAPTER 1: INTRODUCTION

This chapter gives an introduction to the research work. It starts with a brief background on transmission line protection and requirement of changes in the protection schemes with installation of the series compensation in a transmission line. Moreover, this chapter concisely introduces the scope and methodology of the work along with the contribution made in this thesis.

1.1 GENERAL BACKGROUND

Development of any society is measured in terms of per capita electric power consumption. As the society is continuously developing, power consumption is also continuing to increase rapidly. Due to this fact, power networks are getting more and more complex and stressed. Because of this stressed operation, abnormal conditions in the system occur frequently which may cause very heavy damage to the system. As large capital investment is made for development of a power system right from generation to transmission and distribution, this heavy damage involves a huge cost to the successful operation of the system and thus, proper protection system is a must for every power apparatus [1, 2].

Continuously growing demand has resulted in increasing load on the transmission system. This increase has resulted into the requirement of enhancing the power transfer in any line up to the corresponding thermal limit of the line. To realise this goal, installation of series compensation on long extra-high voltage (EHV) transmission lines is a preferred option. Series compensation reduces the effective reactance of the transmission line by cancelling a part of the inductive reactance. This results in an increase of power transfer capability. Besides increasing the power transfer capacity, series compensation also improves system transient stability, voltage control and power flow control. Further, series compensation helps to control distribution of power flow in an inter-connected network such that, overall transmission line losses are reduced for the network. Series compensation can be provided either by fixed or controllable capacitor, each with their own advantages [3]. The detailed analysis of overall impact of series compensation on transmission line is summarized in the next chapter.

To take full advantage of the series compensation in an utility network, it is necessary to understand the impact of series compensation on the transmission line protection system. The work presented in this thesis investigates the important issues in transmission line protection system due to the presence of series compensation and their effective solutions.

1.2 OUTLINE OF TRANSMISSION LINE PROTECTION

It is expected that the demanded electrical energy be made available to the consumers with appropriate quality. These requirements could be met through proper planning, design and operation of the large scale interconnected power system. Owing to the large capital investment involved, it is important to operate it at peak efficiency and protect it from faults. Despite best efforts made, power system components do suffer from faults, which are unpredictable and random in nature.

Faults are basically the phenomena of insulation breakdown due to electrical or mechanical reasons. Major causes of these faults are lightning surges, natural calamities, power swings or exposure of external bodies in the transmission system, switching overvoltage, insulation failure due to aging or contamination, faulty design, lower quality components or lack of maintenance, etc. Transmission line faults can be broadly classified based on their physical nature as:

- ***Symmetrical Faults***

A fault that involves all the three phases equally and effectively is called a symmetrical fault. A triple line fault (L-L-L) or a triple line to ground (L-L-L-g) fault is of symmetrical nature. However, possibilities of this type of fault are least in the power system [4].

- ***Unsymmetrical Faults***

An unsymmetrical fault does not affect each of the three phases equally. Single line to ground (L-g), double line (L-L), double line to ground (L-L-g) are these types of faults.

Therefore, for a three-phase transmission system (with phases A, B, and C), ten possible types of faults can occur. These are: A-g, B-g, C-g, A-B, A-C, B-C, A-B-g, A-C-g, B-C-g, A-B-C-g/A-B-C. Fault currents are generally of very high amplitude and liable to be very harmful for the power system devices because of the involvement of the tremendous amount of energy. Therefore, as mentioned earlier, these faults have very adverse effects on power system stability, security, reliability, continuity and economics.

To avoid such losses, instruments are integrated into the system to identify the faulty condition and to isolate the faulty part of the system to protect the entire system against fault. Such instruments are known as relays, Current Transformers (CT), Voltage Transformer (VT) and Circuit Breakers (CB), which together perform as the protection system.

Among the above components, circuit breaker interrupts the high fault currents in compliance to the fault detection signal provided by the relay. Thus, relay is the most important element of the protection system. The relay, after processing its inputs, produces an output signal depending on its preset threshold values. Relays are usually designed to respond to abnormal conditions such as faults, while they remain unresponsive in normal operating conditions. For successful operation, the relays continuously monitor various quantities of the system. These quantities are voltage, current, phase-angle and frequency. Upon occurrence of a fault, these quantities change abruptly from their corresponding steady state values and based on these abrupt changes, the relays take appropriate decision.

Transmission line protection

Transmission lines are used to transmit bulk power from generating sources to load areas or to adjacent power systems. Factors such as de-regulated market environment, economics, right of way clearance and environmental concerns have pushed utilities to operate transmission lines close to their operating limits [5].

Most faults experienced in a power system occur on the transmission lines. Since transmission circuits vary widely in their characteristics, configurations, length, and relative importance, their protection techniques also vary accordingly. The protective relays commonly employed for transmission line protection are:

- Overcurrent relay
- Differential relay
- Pilot wire relays
- Impedance based relay

Impedance based distance protection scheme is most widely used transmission line protection scheme. Thus, the work presented in this thesis is focused to identify problems due to introduction of series compensation in a transmission line on impedance based protection schemes. Solutions to these problems are also proposed.

The impedance of a transmission line measured from one end of the line is proportional to its length. Therefore, for measuring the fault distance, a relay is used which is capable of measuring the impedance of the line. Owing to this fact the relay is known as an impedance relay and since the impedance of the line is proportional to its length, it is also called a distance relay.

1.3 RESEARCH MOTIVATION AND OBJECTIVE OF RESEARCH

As mentioned earlier, series compensation is normally introduced in high-power EHV transmission lines, which usually employ impedance based protection schemes. With the incorporation of series compensation, the impedance based protection system fails to provide appropriate protection due to variations in system parameters introduced by inclusion of series compensation in the fault circuit. An overall summary of impact of series compensation on transmission line protection system is presented in the following chapter.

As the inclusion of series compensation in the transmission line alters the impedance of the line, the transmission line impedance relay experiences problems. Moreover, to minimize damage to the system, fast operation of the protection system is required. Therefore, design of an accurate and fast relaying system for series compensated transmission line is a prime requirement for successful integration of series compensation in the transmission line.

Several protection algorithms for series compensated transmission lines are reported in the literature. Detailed reviews of these techniques with their relative merits and demerits are presented in the following chapters. Most of these methods suffer from limited accuracy and/or slower operating time. On the other hand, many algorithms for estimating the fault locations are reported in the literature which uses measurements from both the ends of the transmission line. These algorithms require dedicated communication channel and/or synchronization of measurements at both the ends. The requirement of communication channel makes the overall protection system more complex as well as prone to error and delay in the communication link. On the other hand, single end algorithms lack in overall accuracies. This necessitates the requirement of a single-ended fault location estimation algorithm having higher accuracy. Further, the operating time of the single-ended algorithm should also be as low as possible. Moreover, as all the transmission lines are not provided with series compensation, any protection algorithm which can work with same accuracy for both compensated and uncompensated transmission line will be quite useful.

From the discussion it is clear that there is need of a distance protection scheme for transmission lines with the following characteristics:

- The protection scheme should be robust, accurate, fast acting and able to provide effective protection under different operating conditions of the series compensated transmission lines.
- The protection scheme should be able to detect topological changes as a result of over-voltage protection of the series compensator.
- The protection scheme should be capable of taking into account the effect of resonance, voltage inversion and current inversion occurring in a series compensated transmission line.
- The protection scheme should be able to estimate the location of the fault in series compensated transmission line with single-ended measurements.
- In order to reduce processing requirements and thereby reducing the operating time, the scheme should require minimum number of measurements.
- The scheme should remain unaffected with application of series compensation.

1.4 RESEARCH CONTRIBUTION

A distance protection scheme for series compensated transmission line is expected to deliver the following characteristics:

- It should be able to discriminate between fault and no-fault condition.
- In fault condition, it should be able to identify the type of fault.
- It should be able to detect the fault zone

- It should be able to estimate the location of the fault accurately.

On the basis of protection needs identified in the previous section, each of this impedance based relay algorithms is developed in this work. For this purpose, an advanced signal processing tool, namely, discrete wavelet transform (DWT) and an improved artificial intelligence (AI) classifier, namely Chebyshev neural network (ChNN) have been utilized to develop fault detection, classification, zone identification and fault location algorithms. With these developed algorithms, improvements in terms of accuracy and speed have been achieved vis-a-vis the methods reported in the literature.

To enhance the speed of the protection scheme, direct pattern recognition method for fault classification and fault zone identification has been employed. This approach not only reduces the time of operation but also has been proved to be accurate as well. Applications of modified and advanced signal processing tools, namely, undecimated discrete wavelet transform (UDWT) and discrete wavelet packet entropy measure (DWPEM) are found to enhance classification capabilities resulting in improved accuracy. Moreover, to establish the superiority of ChNN, the results obtained by the ChNN based scheme have been compared with those obtained by two different schemes in which ChNN has been replaced by support vector machine (SVM) and multi layer perceptron neural network (MLPNN) respectively.

To meet the need of the time, a versatile fault detection and fault classification algorithm has been developed which provides comparable accuracy for uncompensated and series compensated transmission line, that too for various levels of compensation. The algorithm does not require any modification in the basic technique to take care of series compensation. Therefore, it can be applied universally to any transmission line (either uncompensated or series compensated).

Lastly, fault classification and fault zone identification algorithms developed in this work have been further modified to accommodate the changes that occur in a thyristor compensated series capacitor (TCSC) compensated transmission line. This has been achieved by increasing the levels of decomposition, making improvement in the classifiers or by introduction of wavelet packet entropy.

1.5 THESIS ORGANIZATION

Based on the identified research objectives, the thesis consists of the following chapters.

Chapter 2 provides the necessary background on application of series compensation on transmission line. Influence of series compensation on impedance based transmission line protection system is discussed in detail. A state of the art of historical developments in series compensated transmission line protection is presented with discussion of relative merits and demerits.

Ready references about Digital Signal Processing (DSP) and Artificial Intelligence (AI) techniques used in this work are provided in the third chapter of this thesis. Advanced time-frequency extraction tools such as DWT, Discrete Wavelet Packet Transform (DWPT) and UDWT are represented in detail. DWT energy and DWPT entropy measures are introduced as information enhancing mechanism for protection application. Moreover, AI classifier such as MLPNN is described along with SVM and ChNN.

Chapter 4 focuses on development of fault type identification algorithms for series compensated transmission line. A new digital fault classification scheme employing both DWT and ChNN is presented. Further, an improved scheme is presented in which a pattern recognition based approach using ChNN is used. Moreover, the performances of two learning algorithms of ChNN, namely, Least Square Levenberg-Marquardt (LSLM) and Recursive Least Square algorithm with Forgetting Factor (RLSFF) have been compared for protection application. Lastly relay performance under CT saturation and the effects of the untransposed transmission line are also investigated.

New fault zone identification schemes for series compensated transmission line are developed and described in Chapter 5. A new high speed scheme is presented with application of ChNN along with DWT for fault zone identification. Moreover, a comparative study of SVM, MLPNN and ChNN schemes (along with DWT feature extraction) for fault zone identification in series compensated transmission line. To avoid the problem of aliasing and loss of information due to downsampling operation in DWT, a new and more accurate fault zone identification scheme has been proposed using UDWT and ChNN.

The issue of estimation of fault location in series compensated transmission line is addressed in Chapter 6. Performances of phasor estimation based approaches have been investigated for one-end fault location estimation. These are: Discrete Fourier Transform (DFT), DWT and Least Square Estimation (LSE). However, each of these methods has notable problems in estimating the fault location due to errors in phasor estimation. To overcome these problems, a fault location approach based on DWT and ChNN is proposed. The scheme proved to be highly accurate and fast for estimating the fault location in series compensated transmission line.

A versatile fault detection and classification algorithm for a transmission line is developed in Chapter 7 utilising DWT energy and ChNN. This algorithm has been found to be highly accurate for both uncompensated and series compensated transmission line (even at different levels of compensation).

Chapter 8 addresses some of the issues of a distance protection scheme for a TCSC compensated transmission line. In this chapter, fault classification and fault zone identification schemes developed in the previous chapters are modified and enhanced to take care of the presence of TCSC in a transmission line. Application of ChNN for fault classification and fault zone identification approaches with and without the help of DWT are developed. The DWT based scheme has further been improved for fault classification with application of DWPT entropy.

The last chapter presents comprehensive summary and conclusions of the work carried out in this thesis. Some suggestions for carrying out further work in the area of series compensated transmission line protection scheme have also been given.

CHAPTER 2: LITERATURE SURVEY ON PROTECTION OF SERIES-COMPENSATED TRANSMISSION LINES

This chapter describes the need and application of series compensation in long EHV transmission lines. The effect of series compensation on transmission line protection is discussed and a bibliographical survey for protection solutions of fixed series compensated transmission line is presented to identify the research gaps in this area.

2.1 INTRODUCTION

Due to environmental concerns and economic constraints, option of building new transmission corridor is limited. Therefore, the power engineers are required to utilize the existing transmission system in a better way to cater to ever increasing demand of electricity. To achieve this goal, the series capacitive compensation technique is increasingly being used with the existing transmission lines. The series capacitive compensator (henceforth written in short as “Series Compensator (SC)”) compensates the inductive reactance of the long transmission lines to increase their power transfer capacity. It also improves the transient stability, reduces losses and improves the voltage profile of the system [3]. It can also increase the utilization index of the transmission system by optimizing the sharing of real power between alternate paths originating from the same bus-bars [4]. More and more series compensators are nowadays being inducted into the power system with sustainable growth of the power market. With increased applications, the series compensators also make advancements because of the improvement in capacitor technology and compensator protection system that improves the reliability of the overall system.

The series compensators are of two types, fixed series capacitor compensator and controllable capacitor compensator (Advance Series Compensator (ASC)), with their own advantages and limitations [3]. The average compensation provided by the series compensator normally ranges from 20% to 70% of the total inductive reactance of the transmission line. Further, there are two possible types of arrangements according to the position of the compensator on the transmission lines. Usually, the compensator is placed at the middle of the line (mid-line compensation). This arrangement is the most effective for reactive power control [5]. Compensating devices provide stabilized voltage support when placed at the center of the line [5, 6]. In another arrangement, the series compensators are placed on either ends of the transmission line (end-line compensation). In this arrangement, half of the total compensation is provided at either side of the line. However, the mid-line arrangement has been found to be more advantageous [4].

2.2 TRANSMISSION LINE WITH SERIES COMPENSATION

As discussed earlier, the series compensation in a transmission line increases the system stability, power transfer capability and can also optimize the sharing of real power between parallel lines. The series capacitors compensate the inductive reactance of the line so as to maximize the power transfer capability of a long transmission line.

Arrangements for uncompensated and compensated Extra High Voltage (EHV) long transmission line are shown in Figure 2.1. In this figure, X_L represents the total inductive reactance of the transmission line while X_S and X_R denote the source inductance of the sending end and the receiving end respectively. With mid-line series compensator with a capacitive reactance of X_C, the transmission line reactance splits into two equal parts of X_{L1} and X_{L2}.

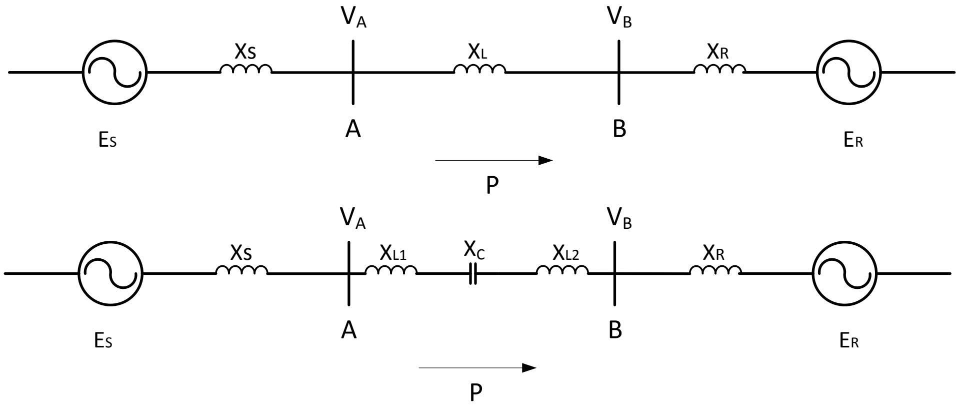

Figure 2.1: EHV transmission line without and with series compensation

The real power flowing towards bus bar B in the uncompensated line AB is:

$$P_{Real} = \frac{(V_A * V_B)}{X_L} \times \sin\delta \tag{2.1}$$

Here, V_A and V_B are voltage magnitudes at bus A and B respectively while δ is the phase angle difference (loading angle) between the voltages of bus A and bus B. With series compensation (X_C) added to the transmission line, the real power flow from bus A to bus B becomes,

$$P_{Real} = \frac{(V_A * V_B)}{(X_L - X_C)} \times \sin\delta \tag{2.2}$$

It is evident from equations (2.1) and (2.2) that, the added series capacitance in the transmission line increases the real power transfer capability through the line. On the other hand, the difference in phase angle between the voltages V_A and V_B can be reduced by keeping the real power transferred fixed which, in turn, will increase the transient stability of the system.

Moreover, in a condition when a transmission line with lowest power transfer capacity reaches its limit, this bottleneck may be reached for other unsaturated lines as well. The power transfer capacity of the complete system can be increased by rearranging the distribution of line impedances with series compensation. Furthermore, the overall system losses can be minimized by appropriately sharing the power flow between parallel paths with the help of series capacitance.

2.3 OVERVOLTAGE PROTECTION OF SERIES CAPACITOR AND ITS OPERATING PRINCIPLE

With application of series compensation, as described by equation (2.2), the power and hence the current carrying capacity of the line increases without expensive up gradation of the line. A problem with this scheme of operation is that a fault on the transmission system can cause the capacitors to be overloaded. In order to protect the capacitor against damage, suitable protection scheme for the capacitor bank is needed. The capacitor bank protection scheme requires that the series capacitor is bypassed during fault. However, after the fault is cleared, the compensating capacitor is needed to be reinserted into the circuit as it was before the fault. Normally, single-gap, double-gap and Metal Oxide Varistor (MOV) are used for overvoltage protection of the series compensator.

Figure 2.2 [6] shows a single-gap capacitor overvoltage protection arrangement. An air-gap and a bypass breaker are connected in parallel with the series capacitor bank. The protection level (spark-gap flash overvoltage level) is usually chosen to be two to three times the rated voltage of the capacitor bank [7, 8]. The rated voltage of the capacitor bank is normally defined as the voltage drop across the capacitor bank at maximum load current. In fault condition, the ignition of the air-gap takes place when the capacitor voltage exceeds the air-gap design voltage limit. The air-gap itself cannot usually carry the fault current for a long time. This will close the contacts of bypass circuit breaker, which operates more slowly than the air-gap thereby extinguishing the spark in the air-gap consequently. After the fault is cleared, the bypass breaker opens and the voltage of the compensator reaches its pre-fault level. The scheme operates little slowly during reinsertion of the capacitor as the air-gap requires cooling. Therefore, the air-gap & breaker based overvoltage protection scheme is used as a back-up protection in recent installations.

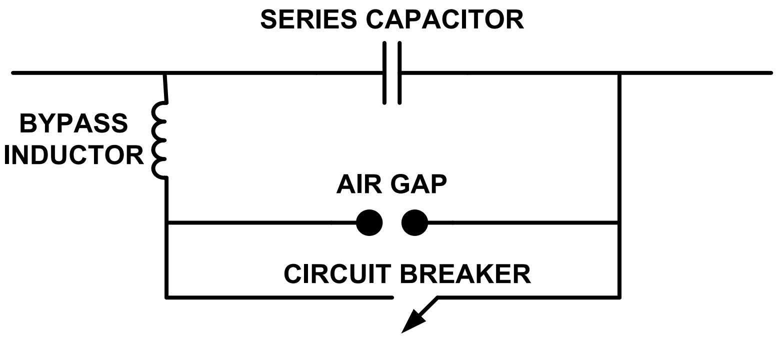

Figure 2.2: Single-gap capacitor overvoltage protection

A dual-gap capacitor overvoltage protection scheme is shown in Figure 2.3 [6]. As compared to the scheme shown in Figure 2.2, this scheme has an additional air-gap (air-gap 2) with a lower setting (as compared to the other air-gap). This air-gap can be isolated from the circuit by the accompanying circuit breaker (CB2). The other air-gap (with a higher setting) acts as a backup protection during reinsertion of the capacitor.

In the event of a fault, air-gap 2 ignites first and bypasses the current with CB2 is in close position. With appropriate settings, CB2 will open only after the bypass circuit breaker is closed. After the fault is cleared, the circuit breaker will open giving air-gap 2 sufficient time to cool down. As the overall operation does not require cooling down time for air-gap 2, the overall reinsertion time of the scheme is lower than that obtained by the single air-gap scheme. However, with the present day availability of MOV based over-voltage protection schemes, the applications of double-gap schemes are nowadays limited.

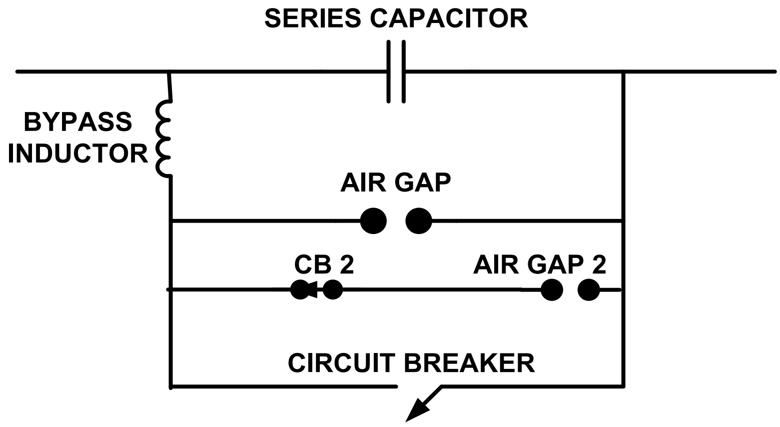

Figure 2.3: Double-gap capacitor overvoltage protection scheme

Figure 2.4 [6] shows a typical series compensator arrangement for any one of the phases with MOV for overvoltage protection of the series capacitance. The MOV is a non-linear variable resistor. Under normal operating conditions, the MOV presents a very high resistance til the voltage across the capacitor is below the threshold level. When the voltage across the capacitor becomes more than the threshold level, the MOV conducts and offers a very low resistance thereby diverting a part of the fault current away from the capacitor.

Since there is an upper limit for energy dissipation in the MOV, a backup arrangement is always provided with the help of an air-gap and a circuit breaker as shown in Figure 2.4. If the MOV remains in conduction long enough to let its temperature (energy) rise to a dangerous level, the air-gap is triggered to bypass both the MOV and the capacitor thereby changing the fault loop impedance.

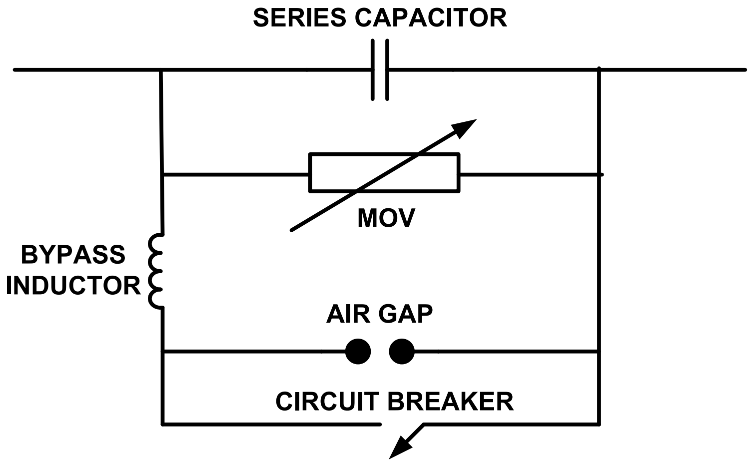

Figure 2.4: MOV for overvoltage protection for series compensation

The voltage-current characteristic of a MOV can be given by [9]:

$$I_{MOV} = I_0 \times [V / V_{REF}]^q \qquad (2.3)$$

Where, I_{MOV} = Current passing through the MOV

V = Voltage across the MOV

I_0 = Maximum permissible reference current

V_{REF} = Knee-point voltage for the MOV

q = Exponent of the characteristic (normally $1 < q < 1.1$)

During an event of fault that triggers the MOV conduction, the line current splits into two parts. The first part flows through the series compensator and other flows through the MOV. As the fault current is also of alternating nature, the MOV conduction takes place in the form of short pulses (as the conduction of MOV depends on dV/dt) [10] during both positive and negative half cycle of the fault current. Normally, the MOV operates in the first-half cycle after fault inception and continues conduction depending on the severity of the fault and operation of the air-gap.

The MOV keeps the capacitor continuously in the circuit. Therefore, the reinsertion time is nearly zero at the end of fault instance. In other words, the MOV improves the system stability.

2.4 EFFECT OF SERIES COMPENSATION ON IMPEDANCE BASED PROTECTION SCHEME FOR TRANSMISSION LINE

Inclusion of the series compensator in the transmission line makes the protection procedure complex due to the abrupt changes in line parameters at the point of series compensation. As a result, the protection and control of a transmission line need to be adapted to the variations introduced by the series compensator.

To take full advantage of the series capacitor installation in a utility network, it is necessary to understand the impact of series compensation on protection system and implement appropriate remedial measures. Various impacts of series compensation on distance protection of transmission line are discussed below.

2.4.1 Change in Line Impedance Seen by Relay

The distance relay computes the line impedance from instantaneous measurements of the voltages and currents obtained at the relaying point. The apparent impedance seen by the distance relay (at the relaying end) for an uncompensated line is shown by a dashed line in Figure 2.5 (a) and on a R-X plane in Figure 2.5 (b). With inclusion of series compensation at the middle of the line, the impedance characteristic is modified at the point of compensation, as shown by solid lines in Figure 2.5 (a) and Figure 2.5 (b) [11]. It is evident from Figure 2.5 (b) that, the distance relay overreaches if the SC is included within the fault circuit [12, 13]. Moreover, if the SC is located near bus A, a fault just after the series compensator will lead the line impedance vector to the third quadrant so as to perceive the fault in the reverse direction as shown in Figure 2.6 [11].

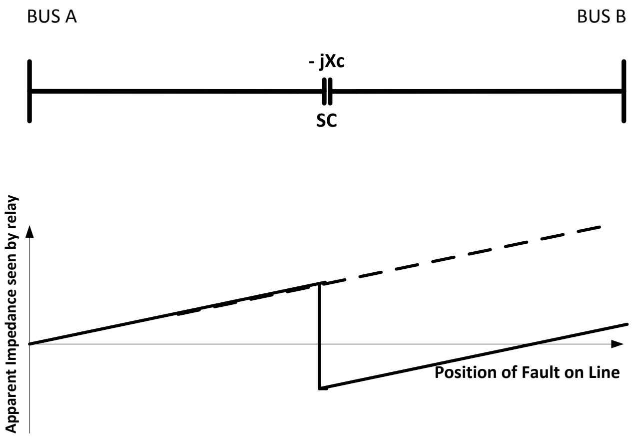

Figure 2.5 (a)

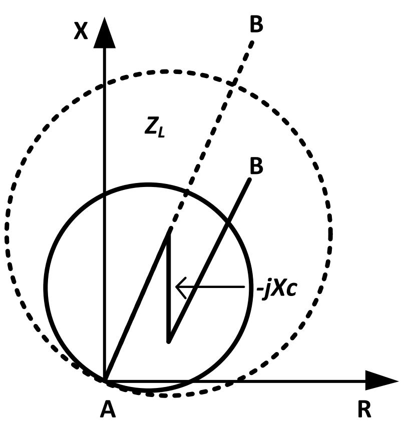

Figure 2.5 (b)
Figure 2.5: Change in impedance as seen from relay

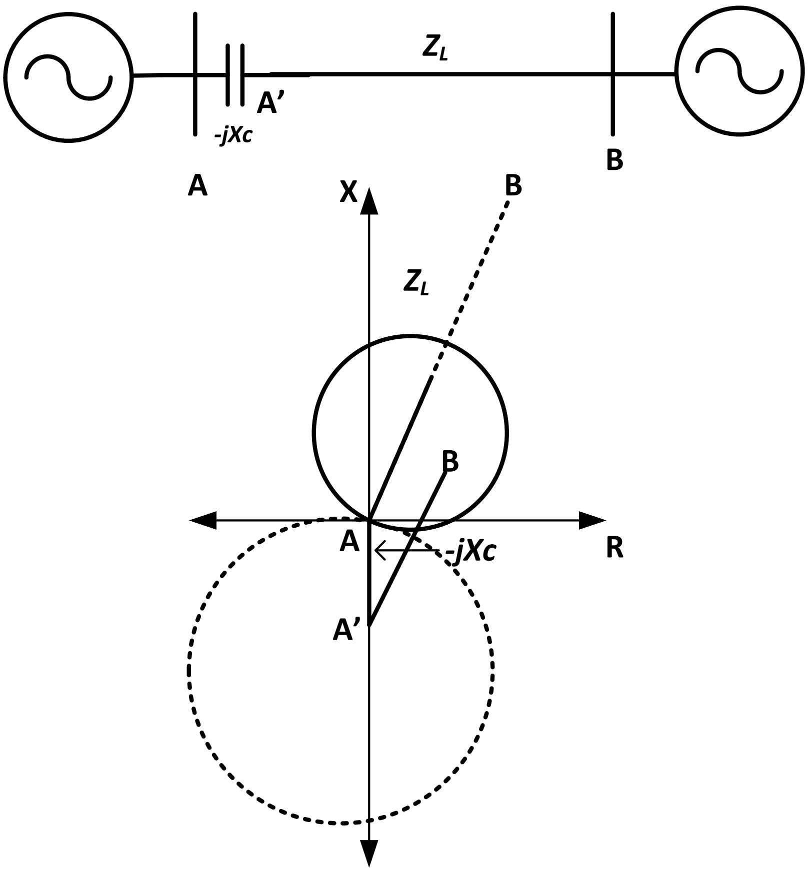

Figure 2.6: Loss of directional integrity in case of end line compensation

2.4.2 Voltage Inversion

Voltage inversion is the change of voltage phase angle by more than 90˚. This type of condition occurs for a fault after compensator in the case where the source impedance (Z_S) is much higher than X_C. One such typical condition is shown in Figure 2.7 [14]. In this case, the current supplied by the source at the left hand side would be predominantly inductive and as a result, the fault voltage at bus C would be reversed with respect to the source voltage at the left hand side.

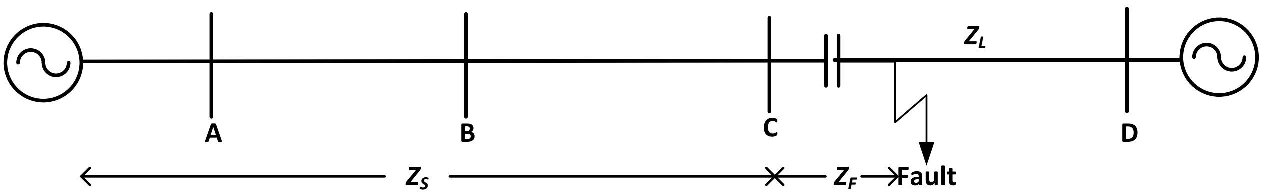

Figure 2.7: Case of voltage inversion

For a transmission line protected with self-polarized mho relay, the mho circle crosses the origin. The relay utilizes local voltage measurement as the polarizing quantity. For close-in faults, measured voltages are of very small amplitude that create problem for detecting the falt with mho characteristic. Because of voltage inversion, the measured conductance shifts to the third quadrant on R-X plane. This makes the relay to under-reach which may result in loss of directional integrity.

2.4.3 Current Inversion

Current inversion is a phenomenon in which the phase angle of current gets shifted by more than 90˚. This happens for a series compensated transmission line in which the source impedance is much less than X_C. For example, in Fig. 2.8, if X_C is much greater than the inductive line impedance from the left hand source to the fault point ($m*X_L$), then the current supplied from the left hand side would lead the left hand source while the current supplied from the right hand side would lag the right hand source. Clearly, these two currents are out of phase with each other. It is worth noticing here that, the current inversion and the voltage inversion occur at opposite system conditions. Therefore, the voltage and current inversion cannot occur simultaneously. Either of this inversion makes the protective relay to see the fault in the reverse direction [7-10].

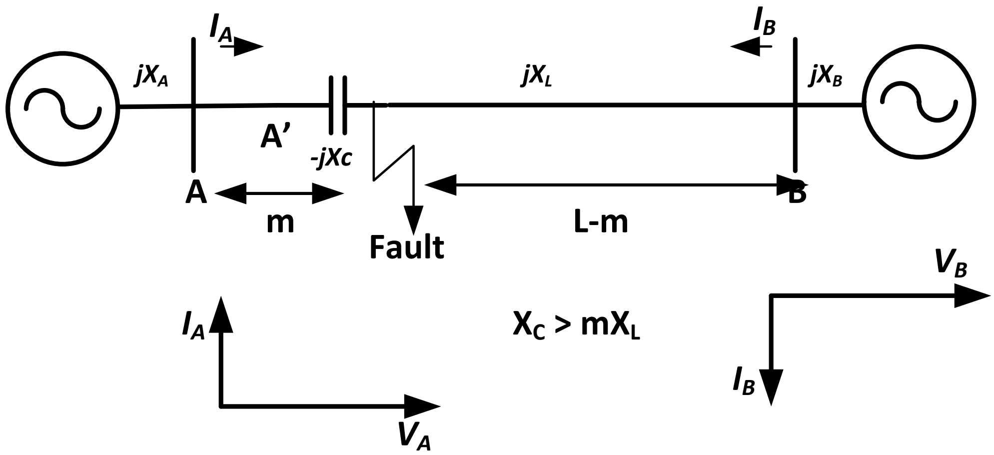

Figure 2.8: The case of current inversion [10]

2.4.4 Effect of Capacitor Over-voltage Protection on Impedance Based Protection Scheme

As mentioned in Section 2.3, a MOV based overvoltage protection not only provides necessary protection to the series capacitor, but also improves reinsertion time and hence improves the system stability. However, inclusion of the MOV in the power circuit creates difficulties for the impedance based transmission line protection schemes. This is due to the fact that, the conduction of the MOV depends upon the severity of the fault current. This leads to two different impedance conditions during fault:

1) In a fault with a higher value of fault currents, the MOV conducts to reduce the potential stress on the series compensator. As mentioned earlier, the fault current splits between the SC and the MOV. The equivalent impedance is dependent upon in the sharing of current between these parallel paths. Moreover, the MOV conducts for a portion of the half-cycle only in every half cycle. This makes prediction of the equivalent impedance of the SC-MOV combination difficult during fault conditions. This necessitates the requirement of an algorithm for estimating the voltage across the SC-MOV combination.
2) In a fault with low value of fault currents, the voltage drop across the series capacitor may not increase up to the critical level for the MOV. In this condition, the MOV sustains its high impedance state. The series capacitance will be part of the circuit for the entire period of the fault. The equivalent impedance of the SC-MOV combination is reactance of the series capacitor only.

The above two facts compound the difficulty of relay setting more. A setting of the relay made without consideration of MOV conduction can make the relay to overreach and loose its directional integrity. If the settings are made with assumptions of continuous presence of MOV, the relay may under-reach for fault with low value of fault currents.

2.4.5 Transient Issues

A transient associated with the fault on an uncompensated transmission line normally carries a decaying Direct Current (DC) component (along with the other harmonic components). However, the transients generated for faults on a series compensated line carry an Alternating Current (AC) decaying component the frequency of which is defined by a combination of the system inductive reactance and the capacitive reactance of the compensator. Addition of these AC components adversely affects the estimation of current and voltage phasor and overall impedance based protection algorithm.

2.4.5.1 Subsynchronous Frequencies

The series capacitance of the compensated transmission line introduces a sub-synchronous frequency in the system. The frequency depends on the parameters of the series capacitor and the line. The natural frequency is proportional to the degree of compensation and is inversely proportional to the impedance from source to the fault location.

The series combination of the capacitor and the inductance of the system sets up a series resonant circuit, the natural frequency of which (neglecting resistance) can be calculated by:

$$f_n = \frac{1}{2\pi\sqrt{LC}} = f\sqrt{\frac{X_c}{X_L}} \tag{2.4}$$

In the above equation X_C is the reactance of the compensator, X_L is the line reactance up to the fault point and *f* represents the nominal power frequency. For faults just after the series compensator, the natural frequency is normally of a higher-frequency range. These frequencies are not much critical as the MOV will typically short the capacitor in these cases. However, for far end line faults, the natural frequency will be of lower orders. If this transient frequency is less than the fundamental frequency, the voltage drop in the line inductance dominant system would be much lower than that in the normal operating condition. Conversely, the transient voltage drop across the capacitor will be much larger due to the lower frequency of the transient current. Thus, for the low frequency transient component, the line would appear to have a much higher percent compensation.

If the voltage drops across the series compensation due to the load current are small compared to the voltage drop due to the fault current, then in the first half cycle of voltage after the fault inception, the voltage drop across the inductor is essentially of the same polarity as the voltage drop in the capacitor [14] as shown in Figure 2.9. Therefore, the capacitor initially tends to reduce the fault current. Now when the capacitor voltage shifts out of phase with the inductor voltage, the current would be larger than the current that would occur if the capacitor is bypassed. This results in inappropriate impedance measurements for the distance based protection algorithms.

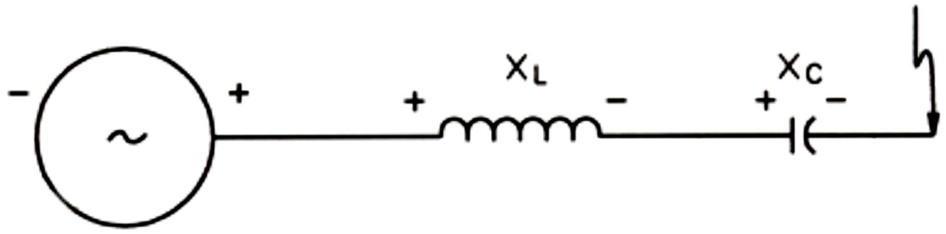

Figure 2.9: Effect of capacitor on fault current frequency

With decay in transient, the impedance will approach its actual steady-state value for the corresponding fault condition. This forces the protection engineers to reduce the impedance settings to prevent zone 1 operation during the period in which sub harmonic-frequency transients are present in the system.

2.4.6 Other Factors

2.4.6.1 Unbalanced Line Impedance

A non-transposed or partially transposed transmission line offers unbalanced impedance. This unbalance is significantly magnified with inclusion of series compensation.

This amplification is largely measured in terms of percentage of the total impedance of the line under fault. This in turn, increases the zero and negative sequence components of the currents thereby necessitating change in protection algorithms, especially for earth sensing relays.

2.4.6.2 Parallel Lines

Problems with protection of the series compensated lines amplify with the parallel line configuration. The series compensator cancels the self-impedance of the transmission line partially. However, it makes no effect on the mutual impedance between the parallel lines. Moreover, the outage of any line and grounding on either end change the impedance seen by the relay. Therefore, all these conditions should also be considered during the design of parallel transmission line protection scheme with series compensation.

2.4.6.3 Faults in Capacitor Bank

The series compensators are normally installed as a bank on a platform. As discussed earlier, an internal overvoltage protection is provided for this bank of capacitors. The compensator protection system bypasses the whole capacitor bank in case of overvoltage (for example, group overvoltage because of fuse blowing). For a single-phase fault, capacitor bank protection system needs to bypass other two-phase capacitor bank also to nullify any possibility of unbalance and consequent instability. A delay in bypassing the other two capacitor banks in the other two phases provides a window of opportunity for a high speed sensitive ground directional comparison schemes to operate, as this capacitor unbalances appears as an internal fault to the protection system [15].

2.5 SERIES COMPENSATED TRANSMISSION LINE PROTECTION APPROACHES

Addition of series compensation forces changes into the design of the transmission line protection system. These changes are made according to the changes in system parameters according to the size, location and overvoltage protection of the compensator as discussed earlier. Besides the detection of faulty condition, fault type classification is an essential protective relaying aspect for transmission line protection. Now, in any transmission line, the fault currents for faults occurring at the end of the line may be of the same order as that of the load currents. However, for a series compensated line, because of the modified impedance locus owing to the presence of the compensator, the reach of the relay needs to be evaluated properly. Moreover, identical impedance conditions may exist on either side of the series compensator (Figure 2.5 (a)). This necessitates the information about location of fault with respect to the compensator (fault zone). Therefore, the final impedance calculations of the distance relay always use the information of fault type and fault zone.

Reviews for fault analysis (fault zone and type identification) methods with fault location methods are presented in this section.

In recent times, considerable efforts have been made for development of protective relaying schemes for series compensated transmission lines. The available approaches can broadly be classified in following categories:

1) Application of multiple/ dynamic impedance characteristics according to the presence of the series compensator in the fault circuit [16], or use of memory polarization to eliminate the effect of change in voltage (both in magnitude and phase) due to the presence of compensator [17, 18].
2) Development of a mathematical model of the compensator to estimate its impedance during a fault. The voltage across the compensator is estimated to correct the measured voltage [9, 19, 20].
3) Protection of the series compensated line with a digital protection system that employs an advanced digital signal processing tool and/or AI technique [21-23]. Normally, these schemes operate in two stages as shown in Figure 2.10 [11]:

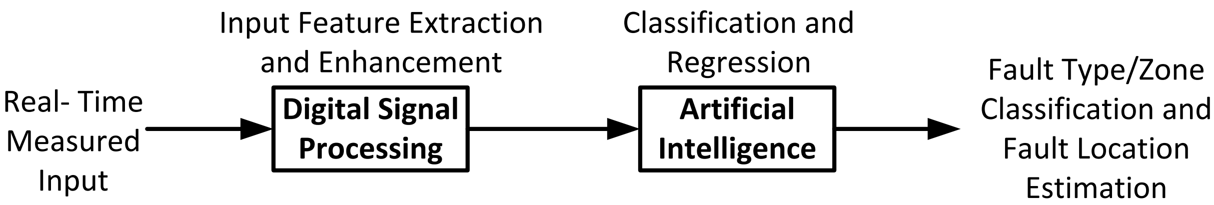

Figure 2.10: Basic structure of DSP and AI based protection schemes

i) Signal Pre-processing and Feature extraction

   In this stage, features of the measured electrical quantities are extracted and enhanced for further analysis. Signal processing tools such as Fourier Transform (FT), Discrete Fourier Transform (DFT), Fast Fourier Transform (FFT), Wavelet Transform (WT), and Discrete Wavelet Transform (DWT) are normally used for this purpose.

ii) Artificial Intelligence

   In the second stage, the extracted features are used by AI techniques for decision making. Normally used classifiers are Artificial Neural Network (ANN), Fuzzy Set Theory, Support Vector Machine (SVM), Extreme Learning Machine (ELM), etc.

In recent times, researchers made efforts for direct implementation of the AI techniques as pattern recognition tools for fault analysis also [22, 24, 25].

In elementary implementation of the distance relay for series compensated transmission line protection, the settings of the reach of the relay have been reduced to accommodate effects of series compensation. The first zone used to be set far below its factual reach; around 30% of the line length instead of 80% to 90% [10]. This cautious approach takes care of the disproportionality between actual and measured fault impedances. However, during a high-current fault, conduction of MOV bypasses the capacitor that makes the relay to under-reach during MOV operation. One more solution to avoid over reaching of the relay is to use line side voltage measurement with respect to the compensator (Figure 2.11(b)) instead of normally used bus side voltage (Figure 2.11(a)) [11]. With line side measurement of voltage, the effect of compensator on this voltage can be eliminated. However, this solution can be applied easily in case of end line compensation, where the compensator is available inside the sub-station only [18, 26]. This solution is impractical for a mid-line compensation scheme.

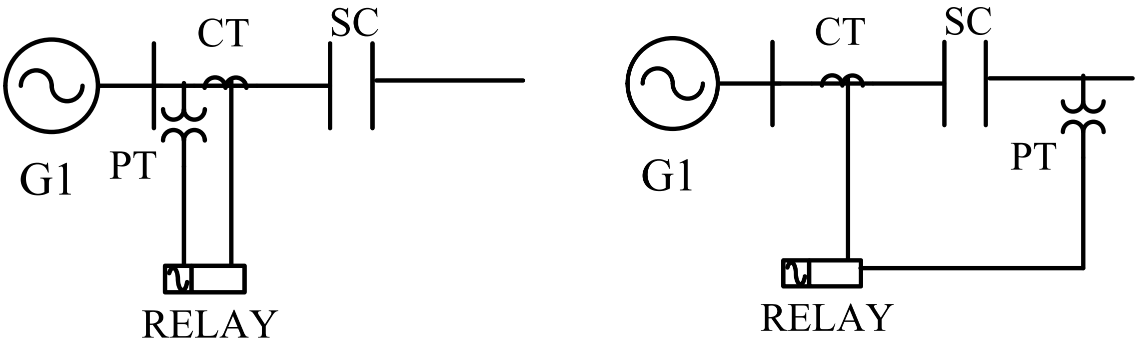

Figure 2.11 (a)

Figure 2.11 (b)

Figure 2.11 :(a) Bus side measurement
Figure 2.11 :(b) Line side measurement

2.5.1 Multiple Relay Characteristics

An algorithm for detection fault zone is a prime requirement in this type of relaying, which determines the presence of series compensation in the fault circuit. The relay alters the impedance characteristic according to the size, shape and reactance of the compensator. In an initial approach for adapting the distance relay characteristic to series compensation, utilizeed the existence of sub-harmonic components in the fault current to determine the participation of the compensator in the fault circuit [27]. Based on the determined fault zone, appropriate impedance characteristic is chosen for the relay. However, the compensator model employed in this work utilizes spark-gap for capacitor overvoltage protection. In another work, presented an algorithm for generation of multiple characteristics of the relay (according to the level of fixed compensation) is presented in [16]. This charectaristic is shown in Figure 2.12. The dynamic characteristic has been developed using offline network details. However, requirement of more than one cycle of post fault data proved this approach to be slow as compared to recent requirements. A protective algorithm proposed in [28] divides the transmission line into two sub-systems of linear and nonlinear components to modify the characteristics according to the compensation level.

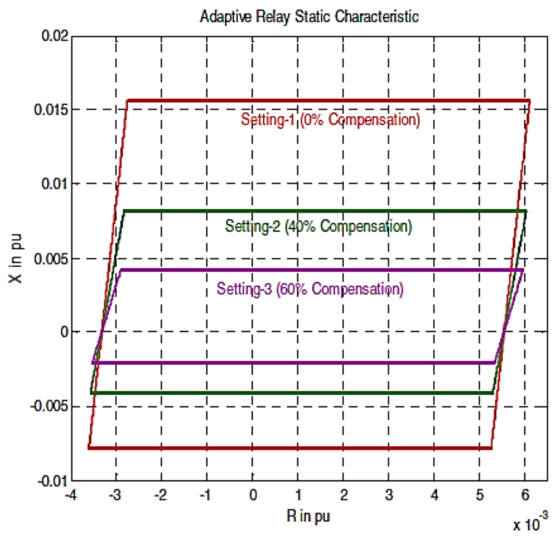

Figure 2.12: Relay multiple characteristics

The prime advantage gained through this type of schemes is that the relay characteristics gets modified /selected adaptively according to the level of the compensation. However, these algorithms usually proved to be slower as modification / adoption necessitates the knowledge of the fault zone before proceeding to the final characteristics.

2.5.2 Compensator Modeling

As already mentioned, the distance protection scheme for transmission line protection might calculate the fault impedance fallaciously due to the voltage drop across the compensator. This problem can be eliminated by calculating this voltage drop with real-time measured quantities. One of the methods is to develop an equivalent impedance model of the compensator for calculations. A linearized equivalent impedance model of the SC-MOV combination, as shown in Figure 2.13, has been presented in [19]. This model provides only an approximate behavior of the SC-MOV combination. However, this model has been preferred by many researchers as it is fairly simple in application. Based on the model presented in [19], a quasi-linear model of the SC-MOV combination has been reported in [9] which can be used in simulation studies. These models have been used by several researchers for protection studies of series compensated lines. These models are found to be fairly useful for calculating the impedance of the SC-MOV combination and hence for estimating voltage across the compensator [10, 16, 20, 28-34].

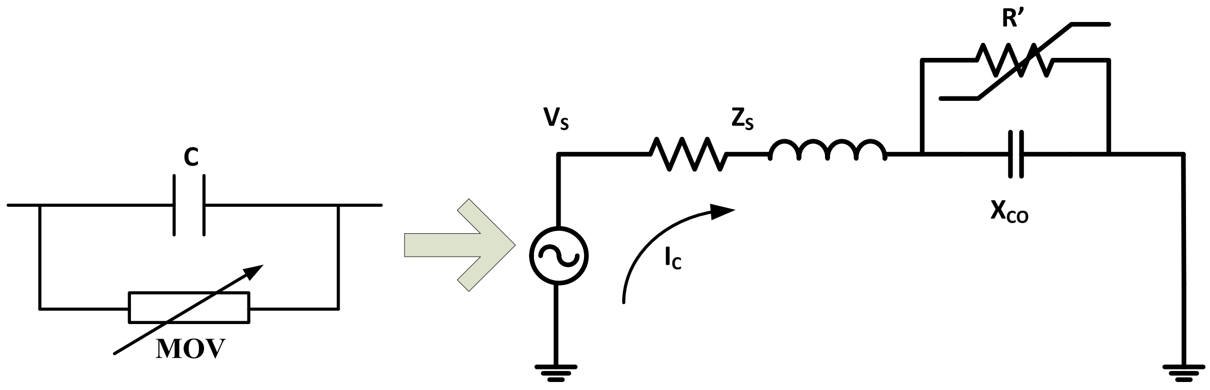

Figure 2.13: Equivalent impedance model of the SC-MOV combination [24]

A more recent non-linear model of parallel combination of SC and MOV has been developed in [20]. The model utilizes measured value of compensator current as an input parameter. This necessitates a dedicated communication channel with real-time measurements in case of mid-line compensation. Use of interpolation technique for the calculation of the parameters of this model reduces the prediction accuracy. Moreover, increased computational complexity of this model encourages the researchers to use the linear models proposed earlier. An algorithm for predicting the impedance of the SC-MOV combination by calculating two different impedances across the compensator has been presented in [31]. The first impedance is realized with measured voltage and current and the other one is realized with measured current and calculated compensation voltage with the help of 2nd order Gear Differentiation rule. In this method, the final impedance is estimated by checking the position of these two calculated impedances on three specially shaped regions on the impedance plane.

The compensator modeling approach provides a great advantage for the protection of compensated lines, as the voltage across the compensator can be estimated. However, it is difficult to replicate the exact non-linearity of the compensator in mathematical modeling and as a result, the values predicted by these models differ from the actual measured values. This indicates the requirement of more sustained efforts in the development of equivalent model.

2.5.3 Travelling Wave Based Approaches

A travelling wave is a multi-frequency transient wave generated from the fault point due to sudden change in system parameters with the inception of fault. These travelling waves propagate on either side of the line and are reflected back continuously until they die down. This is shown in Figure 2.14. Travelling wave equations are sufficient for development of a transmission line protection system. However, with inclusion of the non-linear component of the series compensator in the system, these equations need modification to incorporate these non-linearities. A modified travelling wave equation, which includes the non-linearity of the compensator has been developed in [35]. This equation was further improved in [33]. The algorithm estimates the voltage on either side of the compensator instead of modeling the compensator device. This makes the algorithm independent of compensator type, mode of operation and its parameters. However, this two-ended scheme requires a dedicated communication channel and a high amount of calculations to compute the final result which make it slow.

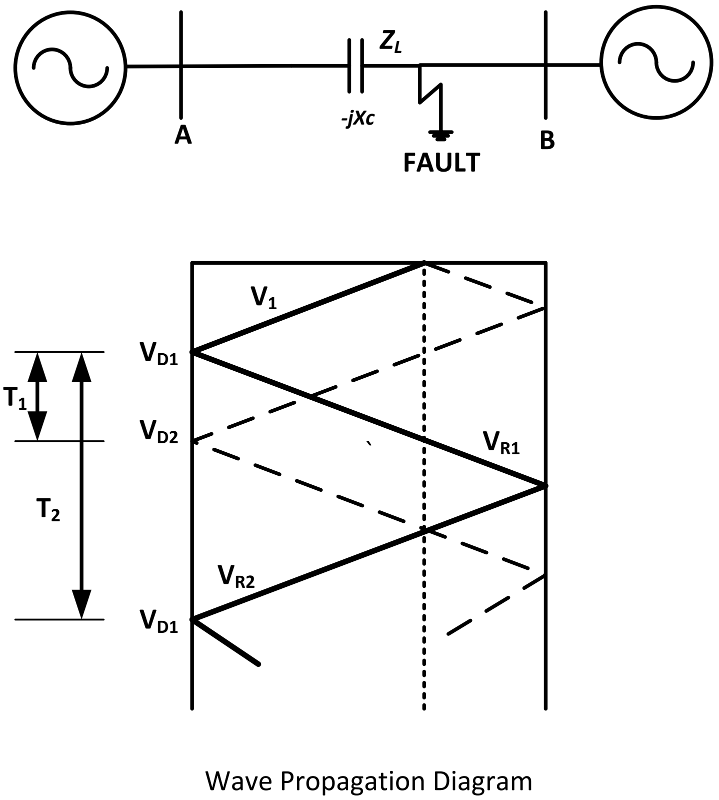

Figure 2.14: Travelling wave (Bewley-Lattice diagram) [35]

It is worth to note that, travelling wave is almost absent when the fault inception angle is near to zero. Moreover, involvement of the series compensator can produce frequencies in a very high range. These frequencies can be too high for a Capacitive Voltage Transformer (CVT) for a close-in fault after compensating device, as it can be out of its measureable bandwidth [13].

2.5.4 Signal Processing Tool and Artificial Intelligence

DSP is the method to describe a signal into another form that makes certain features of the original signal more amenable for study. DSP is able to describe the electrical signal more completely for power system stability and protection analysis.

2.5.5 Advancement in Filtering

The basic signal processing tool, namely DFT, decomposes a periodic continuous time signal into an infinite sum of sinusoids of different frequencies. The FT, in other words, is based on the principle of resolving the original waveform into reference sinusoidal waves. Therefore, DFT separates out all spectral details of the original time domain signal in the frequency domain. In [36] and [37], DFT based algorithms have been proposed for non-compensated transmission line which completely remove the decaying DC component of fault currents. Based on these works, a Fourier filter based protection scheme for series compensated transmission line is presented in [38] for simultaneous removal of the subsynchronous frequency components along with the decaying dc to compute the fundamental frequency component quickly. With series compensation, this process can take a long time to extract the features due to the presence of sub-harmonic components having large time constants.

The DFT is one of the most preferred tools for protection system. The computational cost of the recursive DFT filter is lower than many other signal processing tools. Moreover, a very good harmonic immunity can be achieved by DFT filtering process, which improves the calculation of fault parameters. However, during approximation of a discontinuous function (fault inducd current / voltage), the function is defined in the whole interval of interest by a global basis set. Therefore, Gibb's phenomenon will restrict the final resolution [39, 40]. With the availability of recent signal processing tools such as Gabor Transform (GT) and Wavelet transforms (WT), the interest in DFT has reduced drastically, as GT and WT can provide more meaningful information for protection requirements.

2.5.6 Higher Order Statistic

Spectral analysis produces a good measure for judgment concerning the predictability of the signal. Second order measures produced by tools like DFT generate non-zero values in its output due to the presence of Gaussian noise in the signal. Higher-Order Statistic (HOS) eliminates this Gaussian noise and can produce more accurate spectrum of higher frequency, which is advantageous for fault analysis with series compensation. The use of HOS with fuzzy classifier was investigated in [41] for fault classification. However, this method involves a heavy computation burden that makes the implementation sluggish.

2.5.7 Wavelet Transform

Both time and frequency resolution of a given signal is achieved by time localization of different frequency components using WT [42]. In WT, the inputs are manipulated through a process of translation (i.e. movements along the time axis) and dilation (i.e. spreading out of the wavelet) to transform the signal into another form which 'unfolds' the given signal in time and scale. WT measures the correlation between the input signal and scaled and translated version of the 'Mother Wavelet' which is of limited duration and has zero average value. Two application of WT for series compensated lines have been proposed in [35]; i) for fault-zone identification using 'db4' mother wavelet and ii) for fault classification with 'Haar' mother wavelet. In this work, the use of sampling frequency of 240 kHz is quite high for practical implementation and requires a large amount of calculations. An algorithm for fault type identification and zone classification using WT analysis for a controllable compensated transmission line is presented in [43]. The same authors again proposed fault type identification and zone identification scheme with Wavelet Packet Transform (WPT) in [37]. In another work, wavelet entropy based fault classification, zone identification and location schemes have been proposed in [44]. An approach based on s-transform and probabilistic neural network for phase selection and fault section identification has been presented in [45]. The s-transform is an extension of Gabor transform and wavelet transform, and is based on moving and scalable localizing Gaussian window. However, application of the Probabilistic Neural Network (PNN) in this work requires an extensive training and memory as PNN stores all the training information within its network. Another application of s-transform in unit type Thyristor Controlled Series Compensator (TCSC) compensated transmission line protection is described in [46]. The scheme in this work utilizes the differential energy which has been defined as the difference of spectral energy content (calculated by s-transform) of the current signals at the sending and receiving ends. The scheme requires synchronization of the measurements at the relay end with the data from the remote end. Therefore, it requires dedicated communication channel between the line ends. Moreover, necessity of two-cycle post fault data makes this technique to be slower in comparison with the recently available techniques. An advancement in s-transform, known as hyperbolic s-transform, has been applied for fault classification, zone identification and fault location estimation with Support Vector Machine (SVM), Support Vector Classifiers (SVCs), and Support Vector Regressions (SVRs) respectively in [47]. However, choice of the support vector parameters is a major concern for the scheme. Moreover, requirement and selection of a large input vector make it slow in implementation.

In recent developments the ability of WT has been widely appreciated for transmission line protection. As the fault generated signals are non-stationary, the information about particular spectral components occurring at the time of fault is very important for protection schemes. As WT expands a signal in terms of a wavelet, generated using translation and dilation of a fixed wavelet function, it extracts time and frequency features simultaneously. With the help of WT, the changes introduced by the compensating device can be identified clearly. However, most of the wavelet based techniques use multi-level decomposition that requires multi-level filtering and a higher amount of calculations. Therefore, it would be beneficial if reduction in filtering requirement and calculations can be achieved by improving the methodology.

2.5.8 Artificial Intelligence Techniques with/without Digital Signal Processing Tools

(A) ***Artificial Neural Network***

An ANN is a computational model based on the structure and functions of biological neurons. The ANN helps to estimate the underlying function in a set of input-output data in the most efficient way. Thus, ANN is a very good function approximation tool. Many contributions have been reported in the literature for fault analysis with ANN in a series compensated line with or without help of a signal-processing tool. The ANN is considered as one of the better methods for voltage and current pattern classification as compared to other artificial intelligence techniques [48, 49]. By comparing its performance with that obtained by Deterministic Differential Approach (DDA) and Linear Model (LM) methods for on-line calculation of the voltage across a non-linear SC-MOV model [9, 19], it is found that the performance of ANN is superior to than obtained with DDA and LM.

In [50], ANN has been applied for pattern recognition based adaptive relaying for a series compensated transmission line. The delta-bar-delta (DBD) training algorithm used in this work improves the training of the ANN by accelerating the convergence. However, the performance of this method has been investigated only for first zone protection and that is also with fixed series compensation with end-line configuration (compensator on both ends of the line) only. An approach for protection of a controllable compensated transmission line has been developed with use of Radial Base Function based Neural Network (RBFNN) in [51]. A RBFNN is a three-layer NN with the middle layer carrying radial basis as activation functions. However, to fit in today's protection requirement, the protection scheme should not only be accurate, but fast also. RBFNN requires comparatively large processing time as its activation function is non-monotonic as compared to back-propagation multi-layer ANN.

However, there are few bottlenecks for AI techniques. They require extensive training for pattern recognition that requires generation of large numbers of fault cases. Moreover, AI techniques are sensitive to classification parameters and may require change in classification parameters with variations in system parameters. These limitations can be overcome by inclusion of a pre-processing signal analysis tool. Different protection schemes with two stages, i.e i) signal processing and ii) pattern recognition are available in the literature. A combination of DFT as and ANN has been proposed in [21], with special emphasis on the zone-1 protection scheme. However, a two-cycle window after fault inception required in this scheme is not very acceptable in today's requirement of fast protection scheme. Moreover, this scheme claims to achieve improvement in fault classification accuracies produced with data obtained from four-cycle window. In the first stage of a two-stage algorithm presented in [52], the modal information from the measured signal has been extracted by the Total Least Square Estimation of Signal Parameters via Rotational Invariance Technique (TLS-ESPRIT) with non-fundamental portion of the measured transient signal (extracted by a suitable filtering process). This modal information is used for high-resolution signal parameter estimation. In the second stage, an ANN is designed to estimate the faulted phase based upon the features extracted from the first stage. The TLS-ESPRIT requires a very high amount of calculations. The performance of this method has been validated with fault studies under variation of system parameters. In another approach, the use of a modal transform techniques along with ANN for fault detection and for fault classification on a series compensated transmission line has been proposed [53]. In this work, the authors have used 'Wedepohl' transformation for fault detection and 'Karrenbauer' transformation for fault classification. Extreme Learning Machine (ELM) is a learning algorithm for ANN proposed in [54]. The ELM provides faster training speed by eliminating issues like local minima, improper learning rate and over-fitting. The ELM trained ANN has been used with DWT in [55] for fault classification and fault zone identification in a series compensated transmission line.

The ANN has been proved to be a simple, robust and efficient classifier for protection applications. Significant efforts have also been made towards making the ANN scheme more practicable by increasing its training speed and accuracy with various training methods. Following advantages of ANN can be separated out over other classifiers:

- It is able to acquire complex, non-linear relationships.
- Its generalization capabilities are good and as a result, it can be used for different applications.
- It is quick in response.
- It is very easy to implement in a digital system.

However, it requires an extensive training stage that necessitates a large training data set and time. This leads to generation of a large number of example simulations. Further, the ANN needs to be trained afresh for every line where the relay is to be used. Further, the ANN is also sensitive to variation in system parameters such as frequency.

(B) ***Support Vector Machine***

Support Vector Machine is a computational learning method based on statistical learning theory. In recent years, SVM has emerged as a powerful tool for classification and regression problems. In SVM, the input features are mapped into a higher dimensional space for better classification. This high-dimensional space is created by the dot product of the inputs and is called the feature space. In this feature space, the SVM finds out separating hyperplane according to the training data that contains 'target value' (class type) and 'attributes' (features). The training is carried out to find out the 'support vectors' on and around this hyper plane in a way such that the separation between the classes is maximum. This optimal hyper plane is found by applying a suitable optimization technique along with application of the statistical learning theory.

An algorithm developed in [56] utilizes RBF kernel based SVM for fault zone identification in a series compensated transmission line. The DWT has been implemented as a pre-processing tool in this method. After successful development of fault zone detection algorithm, SVMs have been used in [22] for fault type classification using non-linear SVMs. An application of the SVM as a classifier to classify fault type and fault section for controllable series compensation was shown in [25]. In a fault classification scheme proposed in [57], 'db1' has been implemented as mother wavelet for first level of decomposition to generate a feature vector to be further classified by SVMs.

In all these applications, SVMs have been used as a potential tool for classification tasks in protection application. The SVM has a capability to handle very large feature spaces, so it is very efficient to handle classification problems with large data set. Moreover, by defining the support vectors, it is possible to separate classes which are very close to each other. However, SVMs are very sensitive to their classification parameters. In the absence of this parameter selection mechanism, the SVM parameters such as cost (C), gamma (γ) and kernel function have been chosen by trial-and-error methods in all these schemes.

To address the above limitation, application of Genetic Algorithm (GA) for deciding the parameters of the SVM for TCSC compensated transmission line protection is proposed in [58]. However, the choice of the Kernel function is still an issue and 5-fold cross-validation based parameter estimation by GA exhibits higher computation burden. Moreover, requirement of determining a new set of classification parameters for SVM for each new protection application is a major concern for practical implementatio. A comprehensive methodology for parameter identification of SVM methodology for protection applications is still needed.

(C) ***Fuzzy Logic Based Schemes***

A fuzzy logic system represents a nonlinear data mapping of input quantity into a scalar value between zero and unity. A fuzzy logic based system aided with pre-processing of the signal by DWT for fault classification and fault zone identification has been presented in [23]. The scheme applies fourteen rule based 'min-max' type fuzzy system for fault classification. The fault zone identification scheme is presented by a nine rule based fuzzy system in which two separate ratios generated from DWT are given as inputs. The fuzzy output is highly sensitive to input parameters and fuzzy rules adopted in the scheme. The spectral pattern of inputs varies significantly with variation in fault system parameters such as fault inception angle, fault resistance, etc. Therefore, fuzzy rules are required to be modified to accommodate these changes. Thus, this approach cannot guarantee same level of accuracy always as input to the fuzzy system varies with variation in system and fault parameters.

The application of fuzzy logic for series compensated line protection is limited due to large variation in system parameters. The formation of fuzzy rules under such variation makes it difficult and slow in nature. However, other classifier along with the help of a fuzzy system can make the protection system more accurate and simple.

2.6 SUMMARY

Table 2.1 gives a summary of the problems faced by the distance protection scheme, when subjected to protect a transmission line with series compensation.

Table 2.1: Summary of series compensation effects on distance relay

Effect of Series Compensation	Consequences	Problem with Distance Relay
Abrupt change in line impedance at the point of series compensation		• Relay overreach • In a close in fault after compensation, relay can see fault in reverse direction.
Capacitor bypassed by gap for overvoltage protection	• Produces low frequency transients. • Capacitor will be bypassed before its voltage limit	• Relay overreach
Capacitor is bypassed by series reactor for overvoltage protection of capacitor	• Will produce high frequency transients	• Relay underreach
MOV is used for overvoltage protection of capacitor	• Low fault current: impedance = capacitive reactance • High fault current: impedance = combination of SC reactance and MOV resistance	• Change of impedance with MOV conduction. • Overreach of relay.
Voltage inversion	• Voltage phase angle shifts more than 90˚	• Overreach if fault include capacitor • A potential underreach if fault occurs just after capacitor (reverse direction).
Current inversion	• Current phase angle shifts more than 90˚.	• Relay fails to operate for some portion of line.
Sub harmonic frequency	• Produced due to combination of SC and line inductive reactance	• Can conduct MOV at low fault currents. • Relay overreach.
Unbalanced line impedance	• Increase in imbalance due to unblanaced loading or lack of transposition	• Affect the ground relay.
Faults in capacitor bank	• Will produce imbalance in the system	• Affect the ground relay.

Based on the literature review presented above, following gaps in the protection of series compensated transmission lines have been identified which have been addressed in this thesis:

1. The AI techniques, such as ANN are fast but lack in accuracy and take more efforts for training. On the other side, the fuzzy systems are difficult to design to accommodate variations. Moreover, their size increases exponentially with an increase in the dimension of input feature space. Their ability to separate two classes which are very close to each other is limited. Although SVMs can overcome these problems, they are sensitive to their classification parameters. Therefore, these require experimental investigation for determining proper values in the absence of proper parameter adjustment mechanism. This indicates a need to identify a faster and accurate artificial intelligence technique that can handle more nonlinearity and a large feature space with reduced computational burden.
2. In the literature, usually one or two aspects of the protection scheme (i.e. fault classification and/or fault zone identification) of a series compensated transmission line have been addressed. However, for an effective distance protection scheme, all the aspects, i.e. fault detection, fault classification, fault zone identification and impedance calculation need to be properly studied.
3. For modern applications, the speed of operation of a protective scheme becomes an important aspect. This indicates the requirement to explore the newly developed data processing tools to develop fast and accurate protection algorithms.
4. A comprehensive protection algorithm is desirable, which can work with uncompensated and series compensated transmission line without any functional modification.
5. Many compensator equivalent impedance models have been proposed in the literature. The equivalent impedance leads to estimation of the voltage drop across the series compensator. However, the equivalent impedance does not replicate the non-linearity of the compensator in mathematical modeling. An accurate compensator model that takes care of entire non-linearity of the compensator is still required. Alternately, a method to remove/compensate the effect of voltage drop across the compensator needs to be developed.

CHAPTER 3: TIME-FREQUENCY ANALYSIS AND ARTIFICIAL INTELLIGENCE TECHNIQUES

This chapter presents a ready reference to Digital Signal Processing (DSP) and Artificial Intelligence (AI) methods used in this research work. The requirement, application and advantage of the DWT are presented in initial sections of this chapter. The usefulness of the DWPT with entropy measures for protection application is described in the next section. A more efficient signal information extraction tool, namely, Discrete Undecimatted Wavelet Transform (UDWT) is introduced thereafter for power system protection applications. Classifiers based on ANN and SVM are discussed and subsequently Chebyshev Neural Network (ChNN) technique is presented.

3.1 INTRODUCTION

Digital Signal Processing describes a signal in some other form that makes certain features of the original signal more amenable for study. DSP tools can describe the electrical signal more completely for power system stability and protection analysis.

The basic signal processing tool, namely, Fourier Transform, decomposes the continuous time signal into a sum of infinite number of sinusoids having different amplitudes and frequencies. The FT, in other words, is based on the principle of dilation of reference sinusoidal waves. The FT separates out all spectral details of the processed time domain signal in the frequency domain. However, the main disadvantage of the FT is that, during approximation of a discontinuous function that is defined in the whole interval of interest by a global basis set, Gibb’s phenomenon will restrict the final resolution. According to Gibb’s phenomenon, when approximation of a function is performed with discontinuity (as the case of FT), an anomaly appears near discontinuity. The values of the partial sums near the discontinuity overshoot or undershoot the function value [59, 60]. Therefore, when the Fourier Transform is applied, information in the time domain, while not lost, cannot be observed in case of the non-stationary phenomenon. The spectral information obtained from FT may not be sufficient for protection applications. This is due to the fact that the fault signal is dynamic in nature and FT provides the magnitude and phase angle content of the signal without any information regarding the time instant at which the signal occurs.

In order to compensate these shortcomings of the FT, several efforts have been made. One such initial method is Short Time Fourier Transform (STFT) which utilizes sliding time windows to incorporate the time information with the frequency. In this method, the size of the window plays a significant role in final frequency resolution. Choice of very small window provides better high-frequency information; however, this leads towards reduction of lower frequency resolution. Moreover, longer window makes the higher frequency resolution poor. This leads towards variable width window analysis: small windows to capture the high-frequency information and large windows to capture the low-frequency information. As wavelet transform is based on this philosophy, it is well suited for such applications. In WT, the inputs are manipulated through a process of translation (i.e. movements along the time axis) and dilation (i.e. spreading out of the wavelet) to transform the signal into another form which 'unfolds' it in time and scale.

3.2 THE WAVELET TRANSFORM AND ITS IMPLEMENTATION

The WT is an efficient signal processing tool for power system protection applications. As any fault is a non-stationary phenomenon, during fault analysis, the information about particular spectral components occurring at the time of fault is very important. Using WT, both time and frequency resolution of a given signal is achieved by time localization of different frequency components [42].

The wavelet transform measures the correlation between the input signal and scaled and translated version of the 'Mother Wavelet' which is of limited duration and has zero average value as shown in equation (3.1) [61].

$$\int_{-\infty}^{+\infty} \psi(t)dt = 0 \tag{3.1}$$

and can be defined as:

$$\psi_{a,b}(t) = \frac{1}{\sqrt{a}}\psi\left(\frac{t-b}{a}\right) \tag{3.2}$$

Where, '*a*' represents the scale, '*b*' represents a position along the time axis (translation). A large library of mother wavelet exists with variable shapes. Figure 3.1 (generated with Wavelet Toolbox of MATLAB [62]) shows few of the basic wavelet functions for the analysis.

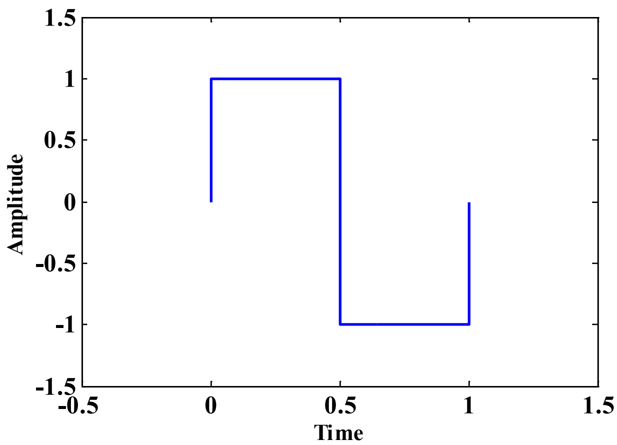

Figure 3.1 (a) : 'haar'

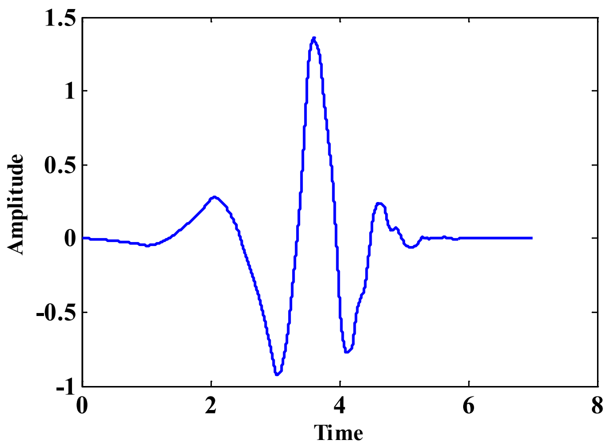

Figure 3.1 (b) : 'db4'

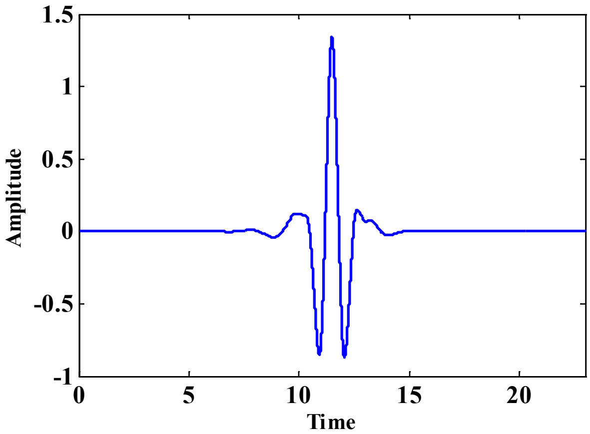

Figure 3.1 (c) : ‘Coeiflet 1.3’

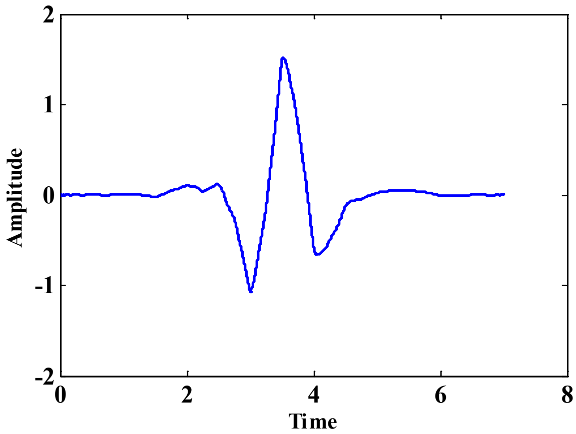

Figure 3.1 (d) : ‘sym13’

Figure 3.1: Mother wavelets: (a) Haar, (b) db4, (c) Coiflet 1.3, (d) sym13

The shape of the mother wavelet for any particular analysis has to be chosen upon the similarity of the input signal and the mother wavelet. A rapidly changing signal is best analyzed using a mother wavelet having sharp crests and troughs similar to the input signal. A slow changing signal is best analyzed with a wavelet with slow transients.

3.2.1 Discrete Wavelet Transform

The discrete wavelet transform is best explained by initially considering continuous wavelet transform (CWT). The continuous wavelet transform is defined as the sum over all time of the signal multiplied by scaled and shifted versions of the wavelet function *Ψ* as [5]:

$$C(a,b) = \frac{1}{\sqrt{|a|}} \int_{-\infty}^{+\infty} x(t)\psi\left(\frac{t-b}{a}\right)dt \tag{3.3}$$

where, ‘*x(t)’* is the signal function, and ‘*C(a,b)’* is a vector of wavelet coefficients. The coefficients are functions of scale and time. Each coefficient denotes the amplitude ‘*C*’ of the scale ‘*a’* at time *‘b’.* Therefore, if the x-axis represents the time *‘b*t’*, y-axis represents the scale ‘*a*’, then the z-axis represents the amplitude ‘*C*’ of the specified coefficient. CWT is continuous in the sense that ‘*a’* and ‘*b’* can be varied continuously in their respective domains. The scaling factor controls the width of the wavelet. A high value of scale corresponds to a longer wavelet and low frequency content and vice versa.

Since each of the scaled wavelets corresponds to a bandpass filter, a peak in the continuous wavelet transform coefficients, for a particular input, would indicate the presence of a specific frequency content (corresponding to scale ‘a’) in a specific time interval. Thus, a wavelet transform provides time-frequency localization of a signal.

Figure 3.2 (a) and (b) show fault current signals for an identical fault with same system and fault parameters, but at different times of inception. The FT of these current waveforms shows a negligible change in the amplitude only as shown in Figure 3.2 (c) and (d). However, no information about the time of fault inception could be derived from it. The WT of these signals in Figure 3.2 (e) and (f) reveals an advantage of WT compare to FT as WT is also able to include time base for frequency analysis.

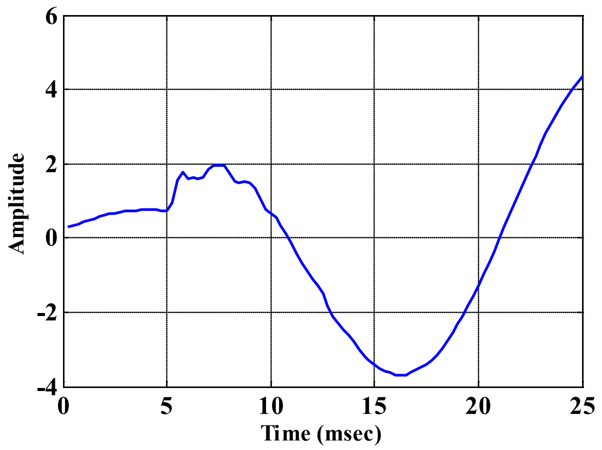

Figure 3.2 (a)

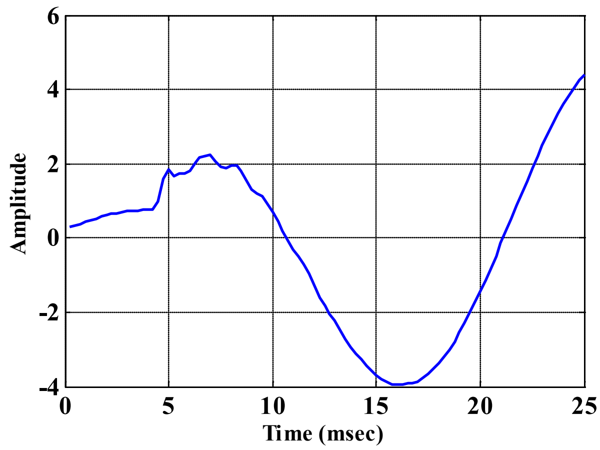

Figure 3.2 (b)

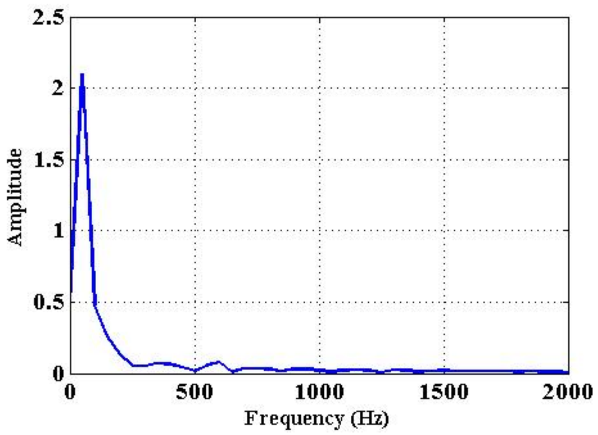

Figure 3.2 (c)

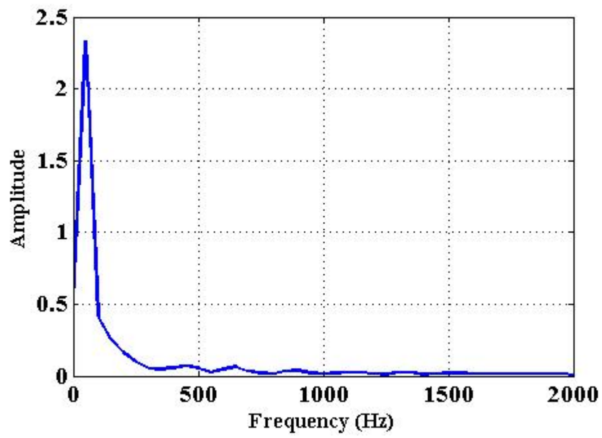

Figure 3.2 (d)

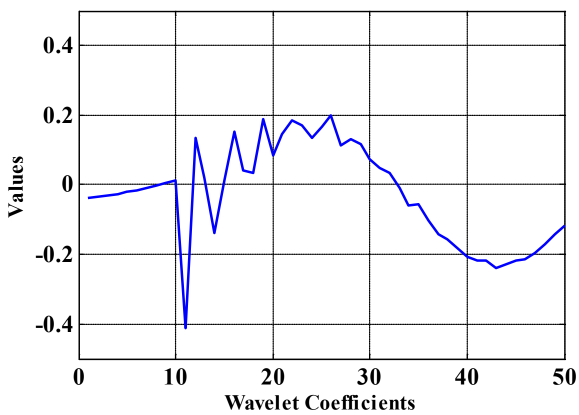

Figure 3.2 (e)

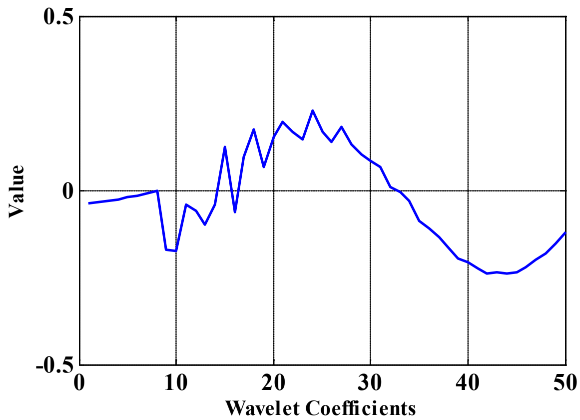

Figure 3.2 (f)

Figure 3.2: Comparison of WT and FT

With DWT, the mother wavelet is dilated and translated discretely by selecting $a = a_0^m$ and $b = nb_0 a_0^m$ where a_0 and b_0 are fixed constants with $a_0 > 1, b_0 > 1$, $m \text{ and } n \in Z$, and Z the set of positive integers. The discretized mother wavelet can be given as [5],

$$\psi_{m,n}(t) = |a_0|^{-m/2} \psi\left(\frac{t - nb_0 a_0^m}{a_0^m}\right) \tag{3.4}$$

and the corresponding discrete wavelet transform for a discrete sequence *x(t)* becomes [5];

$$DWT[m,n] = \frac{1}{\sqrt{a_0^m}} \sum_{k=-\infty}^{\infty} x[k] \psi\left(k - \frac{a_0^m nb_0}{a_0^m}\right) \tag{3.5}$$

As the purpose of the discretization is to eliminate the redundancy of the continuous form, proper choice of a_0 and b_0 must be made so that mother wavelets form an orthonormal basis. For a value of $a_0 = 2$ and $b_0 = 1$ this condition is satisfied. Consequently, DWT can be expressed as:

$$DWT(m,n) = C(i,j) = \sum_{n=0}^{N-1} x(n) 2^{-j/2} \psi(2^i n - j) \tag{3.6}$$

3.2.2 DWT Implementation

DWT can be easily implemented by filter bank techniques if the coefficients are thought of as a filter as suggested in [63]. The method is based on the classical two-channel sub-band coder and yields a fast wavelet transform. In this method, the DWT is obtained by using a multistage filter with the mother wavelet as the low-pass filter *g(n)* and its dual as the high-pass filter *h(n)*.This enables the technique to decompose the original signal into the approximation (low frequency-A) and detail (high frequency-D) components using low-pass and high-pass filters. At the next stage, the low-pass output is again decomposed using a low-pass and a high-pass filter. So, the overall technique can be represented by a multi-stage filter bank implementation as shown in Figure 3.3 [63], where x(n) is the original signal, *h(n)* and *g(n)* are high-pass and low-pass filters, respectively. Further, (2↓) represents down sampling of the input signal.

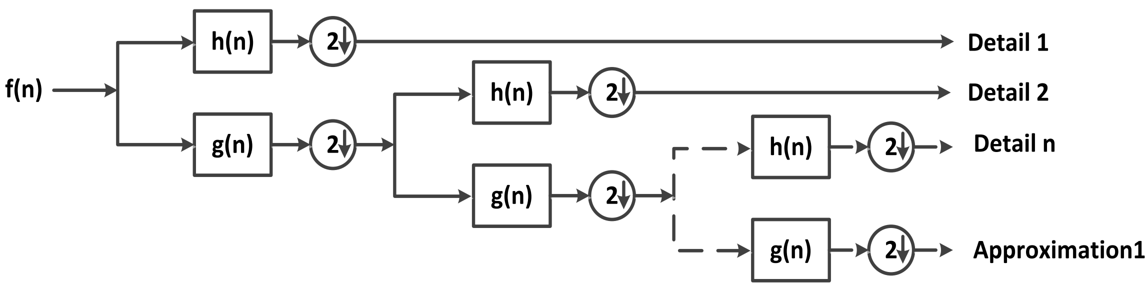

Figure 3.3: Wavelet tree representation

3.3 WAVELET ENERGY

In case when wavelets form an orthogonal basis, according to Parseval's theorem, the energy of each expansion component is related to its wavelet coefficients. In other words, the energy of the signal *f(t)* can be separated in terms of the expansion coefficients as,

$$\int |f(t)|^2 dt = \sum_{k=\infty} |s(k)|^2 + \sum_{j=0}^{\infty} \sum_{k=-\infty}^{\infty} |w_j(k)|^2 \tag{3.7}$$

Here, *s* and *w* are expansion coefficients of the transform. The energy contained within the transform vector at all stages of the multi-resolution decomposition remains constant. Therefore, in general the energy can be expressed as:

$$E = \sum_{i=0}^{N-1} (W_i^m)^2 \tag{3.8}$$

In equation (3.8), W_i^m are the individual components of the wavelet transform vector, where, m is level of decomposition.

3.4 WAVELET PACKET TRANSFORM AND ITS IMPLEMENTATION

Wavelet analysis provides improved signal processing for transient signal analysis. It results in better time localization in higher frequencies in return of poorer frequency resolution. In many protection applications, simultaneous exploration of higher frequency components and lower frequency components are required. To improve the frequency resolution at higher frequencies, wavelet packet transform was introduced in [64]. In wavelet packet transform, a new and more informative link is generated between each level of multiresolution approximation. Wavelet packet analysis offers a more efficient decomposition for a signal containing both transient and stationary components.

3.4.1 Discrete Wavelet Packet Transform – Decomposition of All Frequencies

DWPT is an extension of Discrete DWT whereby all nodes in the tree structure are allowed to split further at each level of decomposition. With DWPT, both the approximation and detail coefficients are decomposed into approximation and detail components, in comparison to DWT that decomposes only the approximation coefficients of the signal. Therefore, it provides more information on different decomposition levels. The DWPT of a signal *f(t)* can be defined as [61]:

$$W_b^{n,a} = 2^{a/2} \int f(t) \psi_n (2^{-a} t - b) dt \tag{3.9}$$

Where, *a* is the wavelet scale and *b* is the wavelet position parameter while ψ_n represents the mother wavelet. After decomposing signal *f(t)* by WPT, sequences can be produced up to the D^{th} level. The recursive relations between the *n* level and the *n+1* level are [66];

$$W_k^{2n+1,a+1} = \sum h(b-2k) W_b^{n,a} \quad (3.10)$$

$$W_k^{2n+1,a+1} = \sum g(b-2k) W_b^{n,a} \quad (3.11)$$

Where, $h(n)$ and $g(n)$ are wavelet quadrature mirror filter coefficients (Figure 3.4 [61]). In this manner, each signal can be represented by a selected set of wavelet packet components for required level of resolution. Figure 3.4 shows 2nd level of WPT decomposition that produces four decomposed components namely H_{DD}, H_{DA}, H_{AD} and H_{AA}..

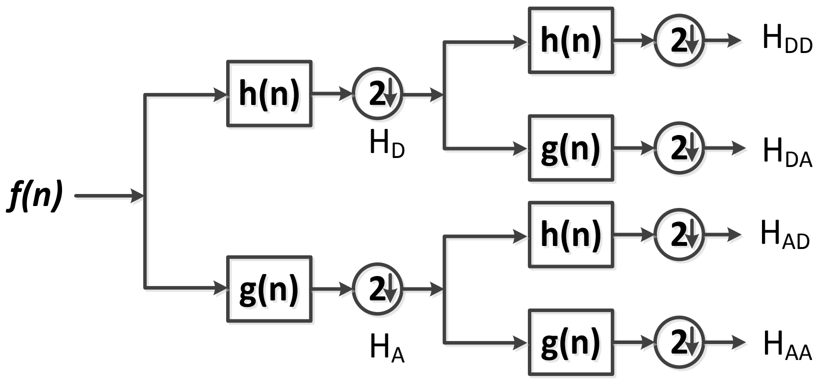

Figure 3.4: Discrete Wavelet Packet Transform

3.4.2 Advantages of Using WPT with Respect to DWT

The resolution of the wavelet transform is not uniform in time-frequency plane. Figure 3.5 shows graphically the frequency allocation of a signal being decomposed up to second wavelet level [65]. With expansion of the scale of decomposition, the frequency expansion takes place with contraction in time.

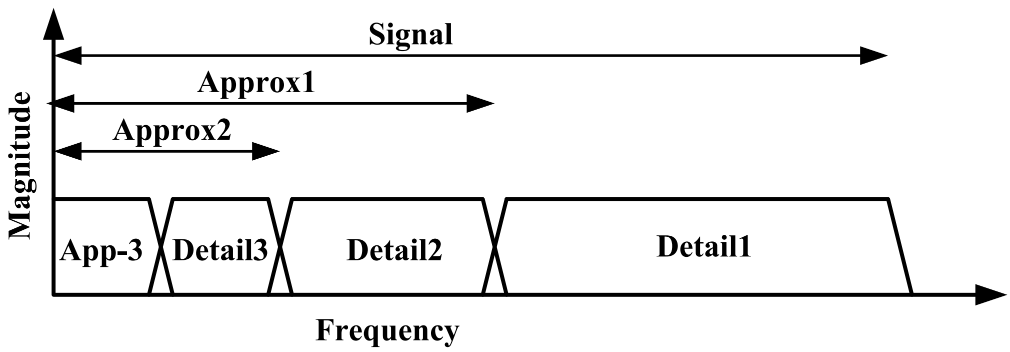

Figure 3.5: Frequency allocation for second level of decomposition

The WPT is performed in a similar manner as the multiresolution DWT explained earlier. As mentioned in the previous sub-section, the WPT decomposes both the approximate and detail resolutions further into approximate and detail resolutions. This leads towards a decomposition structure shown in Figure 3.4. In comparison to DWT decomposition shown in Figure 3.3, the WPT splits the time-frequency plane into constant aspect ratios. The decomposition becomes wider (in time) and narrower (in frequency) as the decomposition proceeds as shown in Figure 3.6 [65].

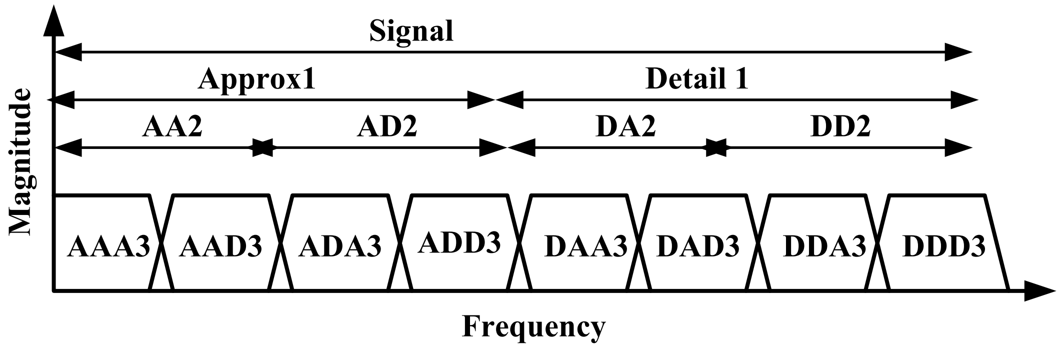

Figure 3.6: Frequency allocation at various resolutions for DWPT

The DWPT produces same numbers of decomposition coefficients irrespective of type and level of resolutions. This gives an edge to DWPT to utilize specific frequency range for further processing.

The wavelet transform are normally computed by fast filter algorithms. However, this results in separation of the subjected waveform into various frequency bands. These frequency bands are further sub-divided into uni-directional frequency spaces due to successive application of filters. This results in less information on time-based features which generally exhibit aliasing artefacts, and could disappear in some cases after thresholding. With equal time-frequency localization throughout the spectrum directional selectivity can be improved with WPT [66].

3.5 WAVELET PACKET ENTROPY MEASURES

There are many useful cost functions associated with wavelet analysis that gives quantitative measures for wavelet decomposition. One of them is Shannon entropy. Entropy was, firstly, introduced by Clausius in 1872 for thermodynamic applications. In 1948, Shannon introduces the entropy in information theory [67] as an extension of the uncertainty measures in the information.

The wavelet entropy combines the wavelet analysis with information entropy. For dynamic/non-stationary signals, wavelet entropy enhances the time-frequency resolution of the signal. Consequently, more amount of information can be retrieved from the signal by wavelet entropy. As in contrast to the WT, the WPT analysis decomposes the signal evenly in the entire spectral range, the time-frequency resolution is improved. Therefore, the WPT based entropy provides more information than the WT entropy for same level of decomposition.

Because of its ability to analyse a non-stationary signal, the WPT entropy measure is a potential tool for fault analysis [68]. Different types of entropy such as log, norm, Shannon, sure, and threshold can be used to characterize the current signals. However, in this thesis, the Shannon entropy has been utilized.

The wavelet packet Shannon entropy [69] can be defined as:

$$S_{wp} = -\sum p_l \ln[p_l] \tag{3.12}$$

Where, $p_{l,}$ represents relative wavelet packet energy [9] at frequency band l. The total numbers of frequency bands are defined by the maximum order of wavelet decomposition.

Entropy is a description of uncertainty in the entire duration of a signal. The signal is divided into K non-overlapping windows each having a time length of M each (total length of signal $N = K*M$). Wavelet packet entropy computation is performed in each time window. As the entropy is a function of the discrete wavelet packet energy, let the mean discrete wavelet packet energy at frequency band l for the time window k be defined as [68]:

$$E_l^k = \frac{1}{N_l} \sum_{t=(k-1)M+1}^{kM} f_j^i(t)^2 \tag{3.13}$$

where, N_l is the number of points at the frequency band l for the time window k. The relative mean wavelet packet energy in the window k can be given as [10]:

$$P_l^{(k)} = \frac{E_l^{(k)}}{\sum_{l=0}^{l} E_l^{(k)}} \tag{3.14}$$

Following equation (3.12), the average wavelet packet entropy which can reflect the complexity of whole signal is given as:

$$S_{wp}^{(k)} = -\sum P_l^{(k)} \ln[P_l^{(k)}] \tag{3.15}$$

3.6 UNDECIMATED DISCRETE WAVELET TRANSFORM

The DWT and DWPT already discussed within this chapter down-sample the coefficients after each level of filtering process. This down-sampling of the coefficients allows usage of the same pair of filter at different levels of decompositions. Due to down-sampling at each level of decomposition, these transforms suffer from the lack of shift invariance. This means that a small shift in the input signal can cause major variation on the distribution of the energy between the coefficients at different levels. That can create errors in the information for further processing. The solution to this problem is carried out by eliminating the down sampling step at each level in UDWT [70]. By eliminating down sampling, the number of coefficients at each level remains the same.

3.6.1 UDWT Implementation

The UDWT can be implemented through a filter bank series as described with DWT with a variation. After each level of filtering process, the output is not down-sampled by two as in case of DWT, but filters are altered to accommodate the outputs of the previous level. The UDWT technique up-samples the filter coefficients of the low-pass and high-pass filters at each level of decomposition (Figure 3.7) [71, 72]. This property is known as redundancy of the UDWT. The up-sampling operation is equivalent to dilation of the wavelets. Therefore, the approximation and detail coefficients are of same length at each level of resolutions.

The UDWT of a signal using the filter bank (*h – high pass, g – low pass*) of a signal *x(t)* leads to a set W=[w_1, ……, w_j,c_j], where w_j are the wavelet coefficients at the scale j and c_j are the coefficients at the coarsest resolution. The traversal from one resolution to the next one is obtained using the "à trous" algorithm [73],

$$C_{j+1}[l] = (h^{(j)} * c_j)[l] = \sum_k h[k] c_j [l + 2^j k] \tag{3.16}$$

$$w_{j+1}[l] = (g^{(j)} * c_j)[l] = \sum_k g[k] c_j [l + 2^j k] \tag{3.17}$$

where, $h^{(j)}[l] = h(l)$ if $l / 2^j$ is an integer and otherwise '0'.

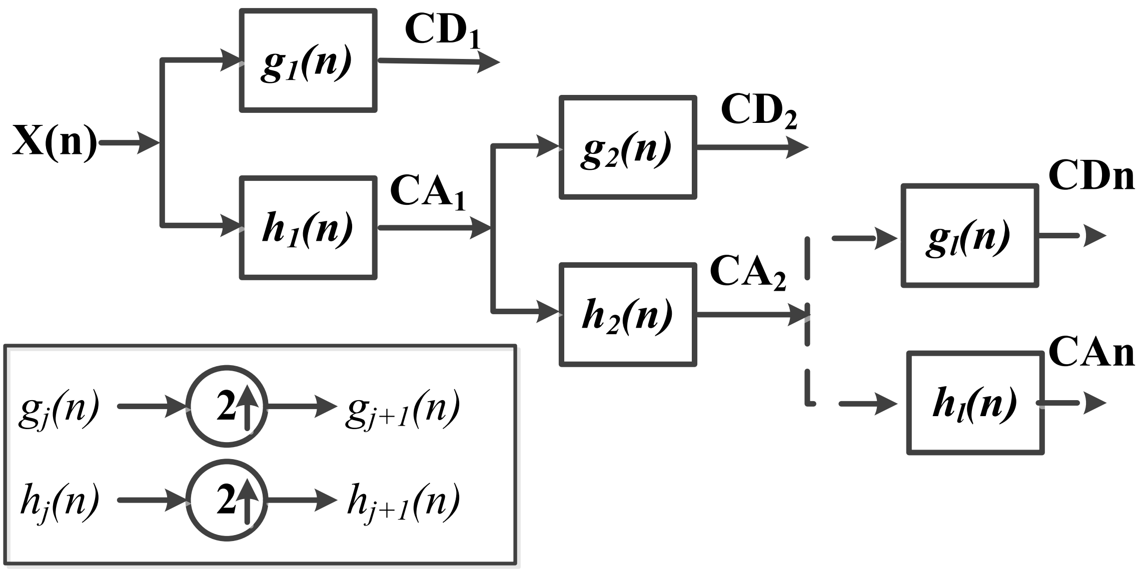

Figure 3.7: Undecimated wavelet transform

Therefore, the UDWT carries a similar wavelet tree structure as shown for DWT in Figure 3.3 without any decimation/down-sampling step (Figure 3.7). However, a level dependent zero-padding interpolation [73] to the low-pass and high-pass filters is performed. This preserves the time-frequency relationship at each level of decomposition. DWT of such a kind is based on the 'à trous' algorithm, which modifies the filters through insertion of holes.

However, in absence of down-sampling and time-invariance property, the memory requirement of the UDWT is more as compared to that required by DWT.

3.6.2 Comparison Between DWT and UDWT

The UWT does not decimate/down-sample the input vector by two at each level of decomposition as in the DWT. Therefore, UDWT and DWT do not generate the same results in output. UDWT gives the same number of detail coefficients at the output as the number of the input coefficients at each level, while in the DWT, 50% of the coefficients at each successive level are "lost" from output. Both involve convolving the input with low-pass and high-pass filters, but the decimated version down-samples the filter outputs while the other doesn't. Thus, UDWT provides a larger amount of information about the transformed signal as compared to DWT. The amount of information is important when statistical approaches are used for analyzing the wavelet coefficients. Therefore, the shift-invariant property is important in feature extraction applications for power system protection and analysis.

The wavelet coefficients, generated at each level of the DWT, are mainly signal components with frequencies located in the band-pass of the equivalent filter sequence. Since downsampling contracts time, it is natural that frequency expands accordingly. This leads towards a perceptually disturbing effect known as aliasing. In aliasing, the frequencies will appear across the frequency spectrum of the wavelet coefficients as aliases where a significant band of the spectrum has been lost. The complexity of UDWT is increased by an increase of level of decomposition with respect to that of DWT.

3.6.3 Advantages of UDWT Compared to DWT

There are some advantages and disadvantages of the undecimated version of the WT. The summary of advantages gained by UDWT over DWT is as follows:

- With expansion of natural frequency in DWT, an overlapping of frequency (aliasing) occurs in the output. With implementation of UDWT this problem is eliminated.
- With better time-frequency resolution, UDWT provides a larger amount of information about input signal.
- UDWT is shift-invariance and therefore, can be implemented in the real time system more accurately such as for power system protection application.

However, the absence of inverse transform capability of UDWT, increased mathematical complexity and requirement of the higher storage space for same level of decomposition must be considered before implementation [74].

3.7 NEURAL NETWORK

Artificial Neural Networks (ANNs) have evolved considerably from a linear single perceptron to higher-order networks. Complex input and output mapping capability of ANN to produce arbitrary nonlinear decision boundaries, a higher amount of parallelism and inherent approximation capability make it popular among protection engineers.

The concept of ANN is inspired by the biological nervous system. It was first introduced in early 1940's as a simple computational model [75]. This neural model was exposed to training with introduction of Hebbian learning rule and rapidly gained linear learning capabilities with back-propagation learning method. A multi-layer structure of the ANN can efficiently represent non-linear relations between inputs and outputs. Presently the feedforward network with a back propagation learning algorithm [76] is widely used in static information processing, pattern recognition, and function approximation problems with finite inputs under the universal approximation capabilities. Another neural network structure, namely, the recurrent neural networks is much more suitable when the length of data is infinite, and hence not considered in this work. Figure 3.8 shows a simplified model of a neuron characterized by a input vector $X=[x_1, x_2, \ldots x_n]$, connection weights of $[w_1, w_2, \ldots w_n]$ and a bias '*b*' with activation function $F(\bullet)$. The inputs are multiplied by synaptic weights and then added up to form the input to the activation function. The activation function transforms its input into an output expressed by the equation:

$$y = F\left[\sum_{k=1}^{n} w_k x_k - b\right] \tag{3.18}$$

The use of synaptic weights is to adjust the relative importance of connections to input vector elements. Activation function is a vital parameter in the perceptron. It represents the output from the neuron in terms of the activity level at its input. Mainly used activation functions are threshold function, piecewise-linear function and widely used sigmoidal function.

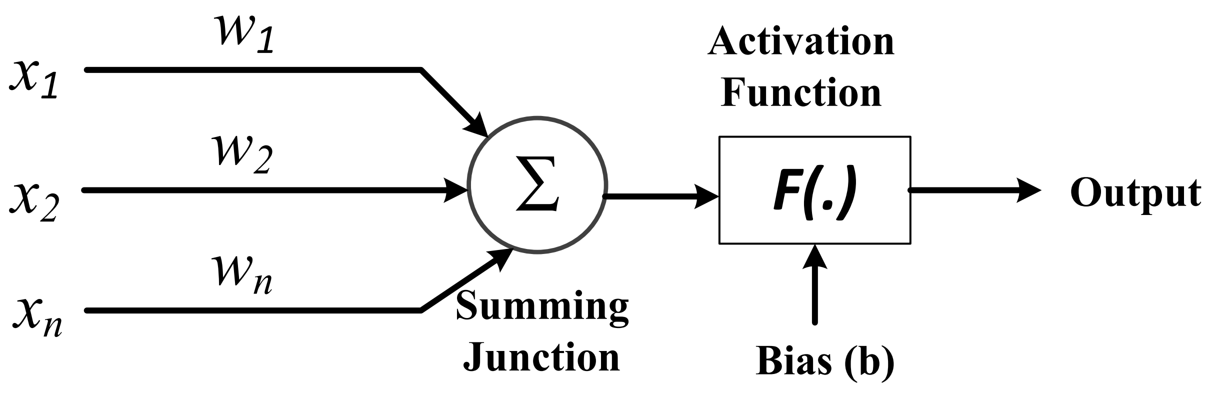

Figure 3.8: Perceptron model

3.7.1 Multi-Layer Perceptron

Basic single layer perceptron resolves the linearization problem with minimization of a mean square error by adjusting the neuron weights. However, their classification and regressing capability is limited to linearly separable problems only. The classification performance for linearly separable data also reduces drastically with the increase in input dimension [77]. This necessitates a more complex structure of Multi-Layer Perceptron (MLP) that can handle large feature space and able to produce non-linear classification.

Addition of a hidden layer between the input and output layer improves the boundary mapping dramatically. With sufficient number of hidden units, ANN is capable of approximating any measurable function from one finite dimensional space to another space upto any desired degree of accuracy [78]. An ANN with one or more hidden layer is known as MLP and has been successfully applied in this work for fault analysis with series compensated transmission lines.

Figure 3.9 shows a simplified MLP model with a single hidden layer. The network is made for n number of input units with input vector $X=[x_1, x_2,\ldots x_n]$, a set of m output units with output vector $Y=[y_1, y_2,\ldots y_m]$ and a set of p number of hidden units. Let, the hidden layer unit H_i receives a net input and produces the output:

$$h_i = F^{(1)}\left[\sum_{j=1}^{n} w_{ij}^{1} I_i + b_i^{1}\right] \tag{3.19}$$

The output from the jth neuron of the output layer will be given as:

$$o_j = F^{(2)}\left[\sum_{p=1}^{n} w_{pi}^{2} h_p + b_p^{2}\right] \tag{3.20}$$

Where, $F^1(\bullet)$ and $F^2(\bullet)$ are activation functions of hidden layer and output layer respectively.

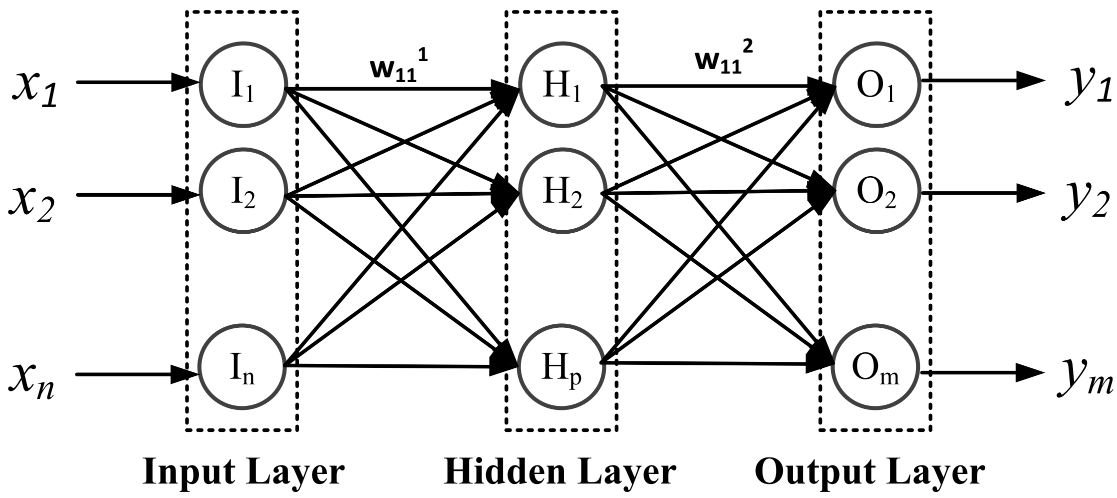

Figure 3.9: Multi-layer perceptron model

The MLP has found many applications due to its learning ability. The Back-Propagation (BP) learning technique is the most successfully utilized learning method for the MLP [75] with a supervised trend. The BP technique adjusts the connection weights to minimize the objective function that is the sum of the squared errors between the desired and the actual outputs. The BP algorithm works in two separate phases: the forward pass and the backward pass. In the forward pass, the inputs are presented to the network, and an output pattern is retrieved. During this phase, the weights and biases are fixed at their initial values. In the backward phase, the weights and biases are updated according to the error between the actual and target outputs. The use of bias is optional. This updating of the weights continues until the prescribed goal of reduction in error is achieved. A cross-validation during training can also be opted to increase the speed of the training. The cross-validation not only helps to reduce the size of the network but significantly improves the generalization performance of the network.

However, it is very difficult to design correct architecture of the MLP with a proper number of hidden layers and the number of neurons in each hidden layer. This is because when the size of the MLP becomes large, it faces a problem of reduction in generalization ability and over-fitting thereby requiring more computational time. On the other hand, a smaller network is inadequate to achieve the targeted precision. Due to this, the design of the MLP is performed in following steps as described in Figure 3.10.

1) Data Preparation: In the first stage for deciding the architecture of the MLP, the entire set of the training data has been selected for the procession.
2) Design of basic ANN topology and activation and learning function: In this stage, a basic MLP topology with estimated hidden layers and number of neurons are assumed with suitable activation function and learning algorithm.
3) Training: The chosen structure of the MLP is subjected to learning using the training data to adjust weights and biases (if used) to achieve the least squared error.
4) Performance Evaluation: In this final phase of MLP structure design, a set of data is presented to the network for checking the performance. This testing data should be different than that used for the training. The performance, if acceptable, will finalize the network architecture or the network structure is customized to evaluate again until acceptable performance is obtained.

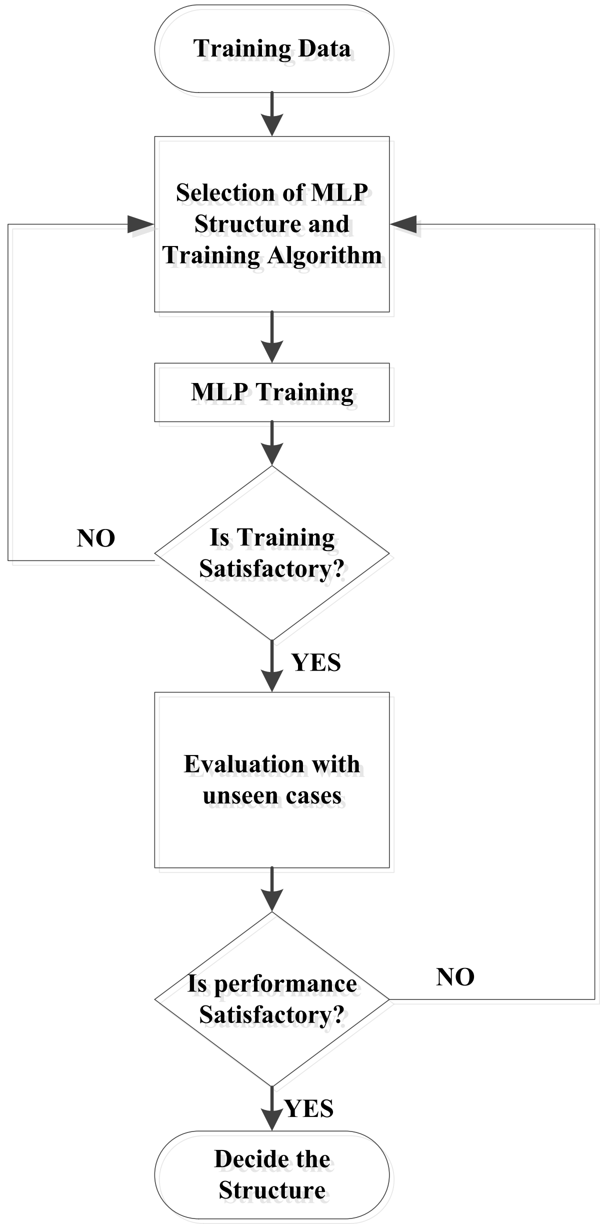

Figure 3.10: MLP architecture selection process

3.7.2 Functional Link Neural Network

Besides the problem of designing the architecture as discusses in previous section, the MLPs are much slower in training than the single-layer structures. This is due to the propagation of the error back in different levels of neural layers from output to input. Moreover, the MLP training procedure suffers from the problems such as local minima trapping, saturation, dependence on initial weight and over fitting to the training data.

An introduction of additional higher-order units in the inputs can avoid these problems [79]. This higher-order network can perform non-linear mapping with a single layer of units without giving up nonlinearity. This can be proved by Hornik's theorems [80]. These higher-order inputs can be supplied by the functional expansion of the input and as a result, the type of ANN which uses these higher order inputs is known as Functional Link Neural Networks (FLNN) [81]. For an example, a feature of input x, say x_i, can be enhanced as [$x_i x_j$, $x_i x_j x_k$, ….], where $i<j<k$. These expansions can be made with different functions.

This technique has shown its capability to improve the learning rate of the ANN dramatically for same applications. There are two different methods for creating additional input nodes. In the first method, the cross-product of the input terms is added into the input model (also known as combine convolution) [81]. In this method, each of the inputs multiplies with the entire input vector. For example, for a ANN with three inputs of (P, Q and R), their cross products PP, QQ, RR, PQ, PR and RQ can be used as an enhanced input pattern. In this case, second-order terms are added to the ANN input structure. In the same way, as per requirement, higher-order terms could also be added.

Another method for providing higher dimensions to the input is to use functional expansion of the original inputs. Normally used functional expansions are sine, cosine, logarithmic functions, max function, etc. For the same ANN given above with inputs P, Q and R, the higher-order inputs might be (P, Q ,R, max(P, Q, R), sin(P), sin(PQ), log(Q)…..). In this model, input variables are individually acted upon by appropriate functions. Applications of polynomial function for input enhancement are also suggested in the literature. Widely used polynomial expansions in FLNN are Chebyshev, Legendre and power series expansions. It is important to choose suitable expansion function for an FLNN according to the application requirements. Principally, the simple expansion will be adopted if the accuracy is enough for the application in hand [79]. The following section discusses the chebyshev polynomial expanded FLNN for the protection applications which has been used in this thesis.

3.7.3 Chebyshev Neural Network

Chebyshev Neural Network (ChNN) is a type of FLNN. It has a single-layer flat structure where the hidden layers of MLP are eliminated by transforming the input pattern to a higher-dimensional space. It uses Chebyshev polynomials as functional expansion. The Chebyshev polynomials are sets of orthogonal polynomials defined as the solution to the Chebyshev differential equation [82]. Due to the absence of hidden layer, ChNN provides computational advantages over the MLP [83]. It is well known that non-linear approximation capacity of the Chebyshev orthogonal polynomial is very powerful by the best approximation theory [82].

3.7.3.1 Chebyshev Polynomials

Chebyshev polynomials arise as the solution to the Chebyshev differential equation:

$$(1-x^2)\frac{d^2y}{dx^2} - x\frac{dy}{dx} + n^2 y = 0 \tag{3.21}$$

Solution of this equation can be given by [84],

$$\begin{aligned} &y = A\cos(nt) + B\sin(nt) \qquad |x| \le 1 \\ &y = A\cos(n\arccos\ x) + B\sin(n\arccos\ x) \qquad |x| \le 1 \\ &y = AT_n(x) + BU_n(x) \end{aligned} \tag{3.22}$$

Where, $T_n(x)$ and $U_n(x)$ are defined as Chebyshev polynomials of the first and second kind respectively with degree n. Both Chebyshev polynomials are in the domain $[-1; 1]$ and have their degree $n \in Z$. The first type of the Chebyshev expansion is more important for approximation and hence explored with ANN in this work.

The Chebyshev polynomial can be generated by the following recurrence relation [84]:

$$\begin{aligned} &T_0(x) = 1 \\ &T_1(x) = x \\ &T_{n+1}(x) = 2xT_n(x) - T_{n-1}(x) \end{aligned} \tag{3.23}$$

A plot for first four Chebyshev polynomials is given in Figure 3.11 [84]

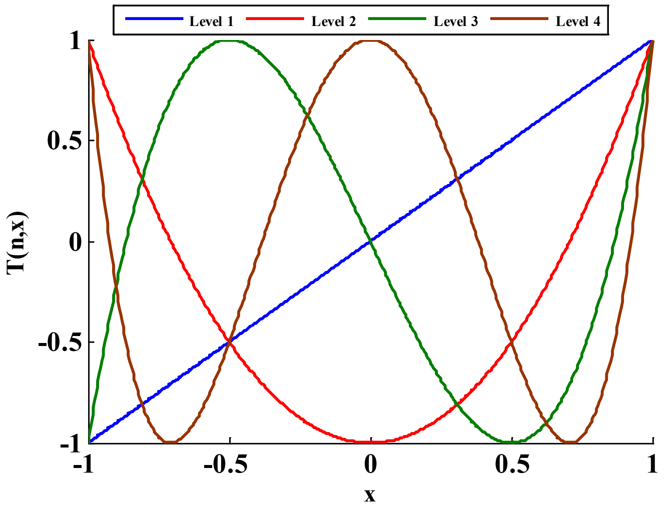

Figure 3.11: Chebyshev polynomial plots for level 1-4

These Chebyshev polynomials can be given as:

$$\begin{aligned} &T_0(x) = 1, \\ &T_1(x) = x, \\ &T_2(x) = 2x^2 - 1, \\ &T_3(x) = 4x^3 - 3x, \\ &T_4(x) = 8x^4 - 8x^2 - 1, \end{aligned} \tag{3.24}$$

By using the Chebyshev functional expansion, an n-dimensional input pattern of $X=[x_1, x_2, \ldots x_n]$, will be expanded to a $[(m\ X\ n) + 1]$- dimensional pattern, that can be applied to a neural structure with [(m X n) + 1] inputs as shown in Figure 3.12. The weighted sum of the components of the expanded inputs is then passed through an activation function to produce an output. The ChNN is normally trained with the BP training algorithm for adjustment of the weights to obtained the desired output.

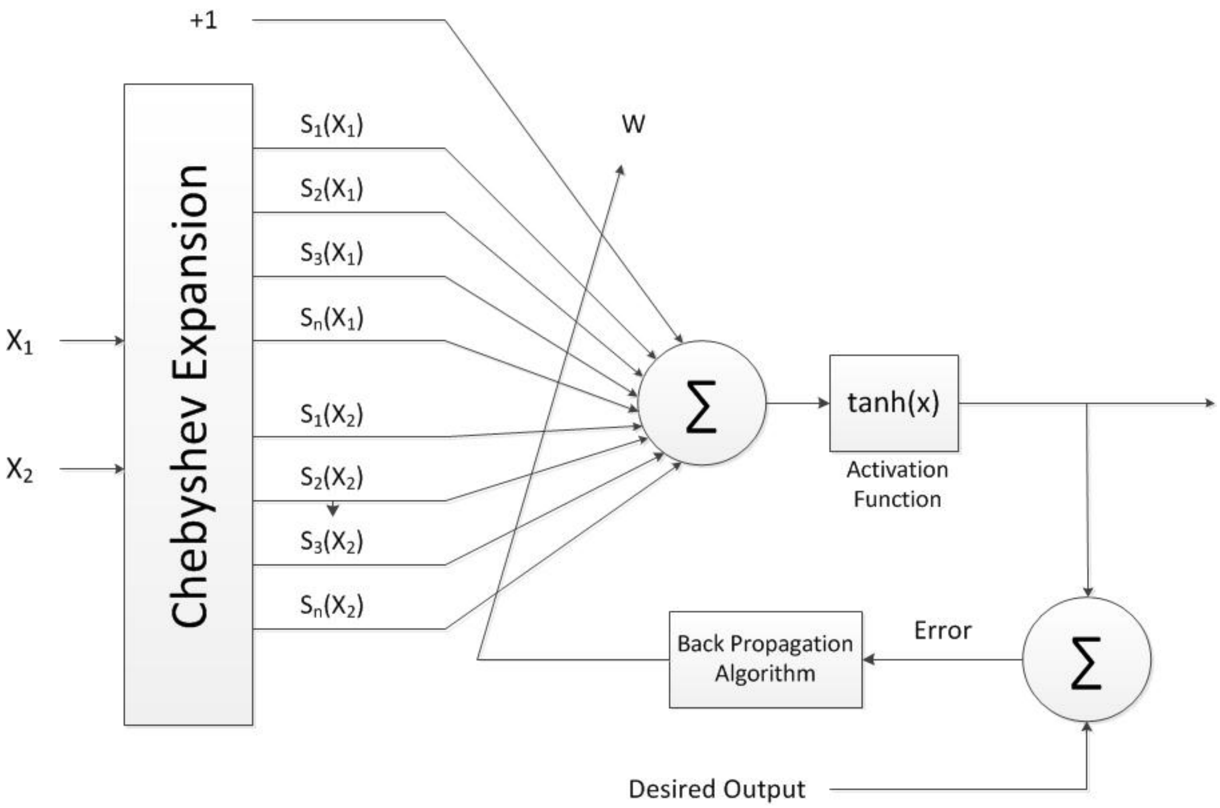

Figure 3.12: Flow diagram of Chebyshev Neural Network

With an increase in the order of Chebyshev expansion, the nonlinear processing capability of the ChNN will be stronger. However, this would result in the increase in the computational burden. Therefore, for digital applications, due to finite processing time of computers, it is important that the inputs are not expanded more than the required for obtaining the solution with sufficient accuracy.

The overall computational complexity for training the ChNN is quite less as compared to that required for the MLP [83].

3.8 SUPPORT VECTOR MACHINE

Support Vector Machine is a computational learning method based on statistical learning theory. In recent years, SVM has emerged as a powerful tool for classification and regression problems. In SVM, the input features are mapped into higher dimensional dot product space for better classification. This high-dimensional space is called the feature space. In this feature space, the SVM finds separating hyperplane according to the training data that contains 'target value' (class type) and 'attributes' (features). The training is made to find out the 'support vectors' on and around this hyper plane in a way that the separation between the classes is maximum. This optimal hyper plane is found by utilizing the optimization theory with application of the statistical learning theory.

3.8.1 Linear Classification with SVM

Consider a two-class training data set $\{x_{i,} y_i\}_{i=1}^{N}$ consisting of N data points. x_i is ith real valued input vector, and y_i is the corresponding class of x_i with value of either +1 or -1. A hyper-plane, separating these points according to their classes, can be given by equation: $w^T x_i + b = 0$ as shown in Figure 3.13 [85]. '***w***' and '*b*' represents the weight vector and bias term (vector) respectively and determines the position of the separating hyperplane. The training is performed to find out the value of '***w***' and '*b*' such that the separation between the classes is maximum. It can be shown that the separation margin (m) is given by [75]:

$$m = \frac{2}{\|\boldsymbol{w}\|} \tag{3.25}$$

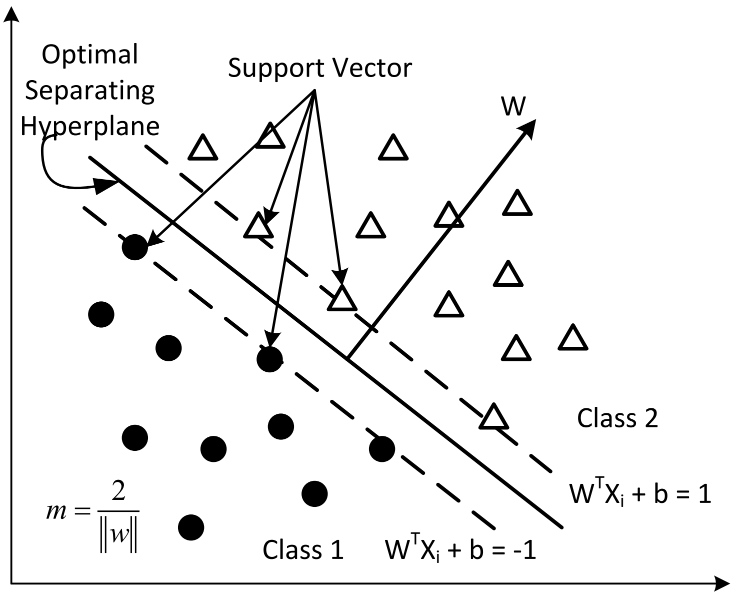

Figure 3.13: Support vector machine hyper plane

For better separation, the value of 'm' should be increased with training with reducing the value of $\|\mathbf{w}\|^2$ to its minimum value. Hence, for linearly separable data, the SVM can be constructed by minimization of $\mathbf{v(\ \ w)}$where

$$\mathbf{V(w)} = \frac{1}{2}\boldsymbol{w}^T\boldsymbol{w} \tag{3.26}$$

Subject to,

$$y_i(\boldsymbol{w}^T x_i + b) \geq 1 \tag{3.27}$$

3.8.2 Non-linear Classification with SVM

The non-linear classification problem can also be dealt with SVMs. This can be done by mapping the classified data onto a high-dimensional feature space where the linear classification is possible using nonlinear vector function,

$$\mathbf{\Phi(x)} = \{\Phi_1(x), \Phi_2(x)..........\Phi_m(x) \tag{3.28}$$

Expansion of the non-linear function, the non-linear function can make it seperable. In practice, the nonlinear data transformation is accomplished indirectly by using the so called kernel functions [56], which is defined by

$$K(x_i, x_j) = \mathbf{\Phi(x_i)^T \Phi(x_j)} \tag{3.29}$$

This expansion generates a higher dimensional space; the SVM can be trained to find out the maximum margin between the classes by equation (3.26). However, there is a possibility that, the expanded data is still not linearly separable. In that case it will be impossible to separate out the data and satisfy condition of equation (3.25). Hence, instead of the function $v(w)$, a new function $\mathbf{v(w,\varepsilon)}$ can be used, and given by [85]:

$$\mathrm{v(w,\varepsilon)} = \frac{1}{2}\boldsymbol{w^T w} + C\sum_{i=1}^{N} \varepsilon_i \tag{3.30}$$

Subject to,

$$y_i\{w^T \mathbf{\Phi(x_i)} + b\} \geq 1 - \varepsilon_i \ \text{; where, } \varepsilon_i > 0 \tag{3.31}$$

Where, ε_i = 1, 2, …..N are slack variables and N represents the total data points for classification. C > 0 and known as regularization parameter. The vectors $\mathbf{v(w,\varepsilon)}$ are known as support vectors and are used to determine the decision surface of the classifier. The classification accuracy largely depends on selection of Kernel function and value of C for classification.

3.9 SUMMARY

WT gains advantage over FT as signal processing tool due to its time-frequency localization capability. The most common form of WT, namely DWT, has been preferred in many protection applications, due to its flexibility of the application with filter-bank implementation and wide variety of mother wavelets. However, in spite of all the advantages of WT, it has limitations such as shift-sensitivity and directional selectivity.

Directional selectivity of the DWT can be improved by application of DWPT. The UDWT has been introduced as a better variant of the DWT. UDWT is linear [86, 87], shift-invariant, redundant and undecimated. The drawbacks are lack of orthogonality, increased computational complexity and increased size of output.

Moreover, this chapter discusses different AI techniques used in this thesis with their basic operation and implementation. Specifically, the FLNN (ChNN) and SVM have been presented. The applications and detail analysis of these signal processing and AI tools are presented in the following chapters in details.

This chapter presents the development of two schemes for classifying faults on a series compensated transmission line. The term fault classification is often used synonymously to identification of faulty phase. The first scheme proposed in this chapter makes use of ChNN along with DWT to accomplish the objectives. The second scheme applies ChNN for direct fault classification (based on the patterns of the fault currents in all three phases) without any help of signal processing tool. The scheme also examines performance of two ChNN learning algorithms for fault classification in a series compensated transmission line. These training approaches are Least Square Levenberg-Marquardt (LSLM) and Recursive Least Square Algorithm with Forgetting Factor (RLSFF). The performances of these algorithms have been evaluated based on their generalization capability in relating the fault current parameters with a fault in any particular phase. After being trained for only a small set of generated fault data, the developed paradigms have been tested over a large number of fault cases with wide variation of system and fault parameters. Lastly, the performances of the algorithms under current transformer (CT) saturation and for untransposed transmission lines are also investigated.

4.1 INTRODUCTION

An important objective of the power system is to maintain the quality and continuity of the supply in the most economical way through the transmission networks. However, it is practically impossible to avoid natural calamities, physical accidents, component failure or human errors that can result in faults on the transmission system. Most of the faults due to natural events or equipment failure are single-phase to ground in nature. Normally, the faults that occur in the transmission lines can be categorized as given in Table 4.1, with their probability of occurrence in percentage of the total observed faults [88].

Table 4.1: Type of transmission line faults with their probable occurrence values

Type of Fault	Fault	Percentage of Occurrence
Single Line-to-Ground Fault	A-g, B-g, C-g	70-80%
Double Line-to-Ground Faults	A-B-g, A-C-g, B-C-g	10-17%
Double Line Faults	A-B, A-C, B-C	8-10%
Three Phase Faults	A-B-C/ A-B-C-g	2-3%

The series compensation is usually employed on EHV long transmission lines which are normally protected by impedance based distance relaying schemes. The purpose of distance protection scheme is to ensure tripping of the line for faults within its protected zone only. To achieve this goal, the distance protection system involves fault detection, fault classification and estimation of fault distance as measured from the relay [89]. With inclusion of the series compensation, the protection system also requires dentification of the fault location with respect to the compensator as well (fault zone identification). The post-fault analysis is important for the protection engineers for system restoration and to get specific information for operation of the protection system.

Fault classification plays an important role for an impedance based relaying system. The knowledge of the fault type is required to improve the accuracy of estimation of fault distance as measured from the relay. As a result, the risk of unwanted over-reach/under-reach is reduced. The fault classification algorithm should be capable of classifying all possible types of faults of Table 4.1 to enable single-pole tripping and auto-reclosing.

Fault classification algorithms for series compensated transmission line are presented in this chapter. These algorithms utilize the changes in current waveforms (due to occurrence of a fault) for identifying the fault type. The initial approach employs WT to identify the spectral changes in the fault current and subsequently, these spectral changes are used by a ChNN to identify the type of the fault. Subsequently, application of a ChNN for direct pattern recognition based fault classification was found to be superior to the combined WT-ChNN scheme. Moreover, performances of two ChNN training algorithms have been compared for direct pattern recognition based fault classification scheme.

4.2 SYSTEM SIMULATION AND ANALYSIS

A single-line diagram of the transmission system used for evaluation of the developed fault classification algorithms is shown in Figure 4.1. The system shown in Figure 4.1 is a 400 kV, 300 km line connected between two sides with mid line fixed series compensation and the two external systems at the two sides have been represented by corresponding Thevenin equivalent sources in series with the corresponding Thevenin's equivalent impedance. The series compensator is provided with a MOV for overvoltage protection. The MOV characteristic is given as [56]:

$$i = Kv^{\alpha} \tag{4.1}$$

In eqn. (4.1), 'i' and 'v' represent the instantaneous MOV current and voltage respectively. Constant 'K' can be given by [19, 48, 90]

$$K = \frac{I_{\max}}{(V_{\max})^{\alpha}} \tag{4.2}$$

Where, 'I_{max}' and 'V_{max}' are maximum permissible MOV current and peak capacitor voltage respectively. The typical value of α is chosen between 30 to 50 [48, 90, 91] such that the MOV conducts only after the current exceeds 2.5 times the rated value. The MOV is protected against its dissipation capacity by a circuit breaker (CB) as shown in Figure 4.1.

The parameters of the transmission line and the generator equivalent sources (henceforth termed as 'generator' in this thesis) are given in appendix-A.

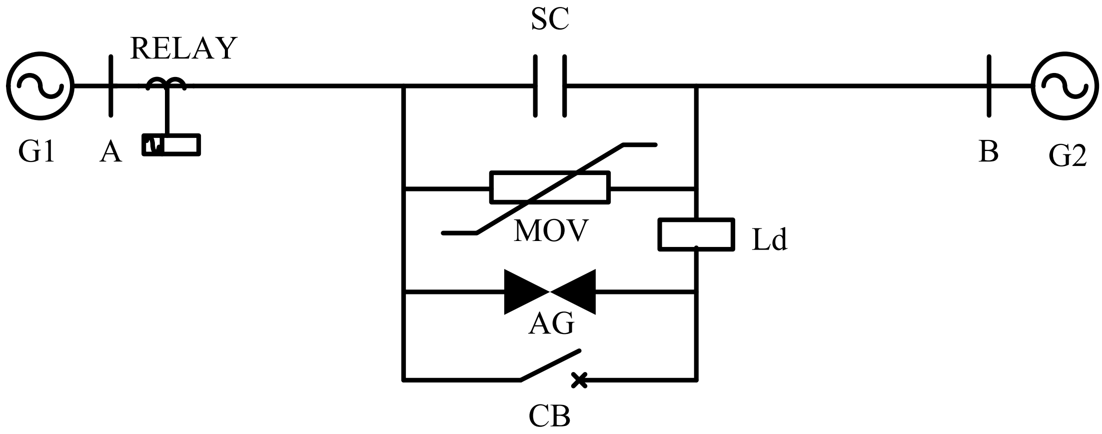

Figure 4.1: Test system for study

To evaluate the effectiveness of the developed algorithm it needs to be tested on large number of data sets encompassing different variety of fault case and conditions. Towards this goal, a model for the study system of Figure 4.1 has been developed in PSCAD/EMTDC [92] and a large number of fault cases have been generated by varying the system and the fault parameters. The details of these variations are presented in the next sub-section. The transmission line has been simulated using the distributed parameter line model in PSCAD.

4.3 APPLICATION OF DWT AND ChNN FOR FAULT CLASSIFICATION

Response of the protection system to the fault condition primarily depends on identifiable changes in fault current and voltage signals. Therefore, the development of an accurate fault classification system can be treated as a problem of identification of these variations (manifested in magnitude, phase and frequency of the signals). The proposed algorithm in this section utilizes DWT of the measured current signal as a feature extraction tool along with a ChNN as a classifier. For this purpose, the samples of the post fault currents (measured at the relaying end) obtained during half-cycle period (after the occurrence of the fault) have been utilized. It is to be noted that, a sampling frequency of 4 kHz. has been chosen in this work. It is further to be noted that instead of ChNN, other classifiers such as SVM or MLPNN could also have been chosen. However, as already discussed in Chapter 3, it is a non-trivial task to determine the appropriate configuration of MLPNN while for SVM, determination of appropriate kernel function and proper value of regularization parameter is not at all straightforward. To avoid these limitations of SVM and MLPNN, in this work ChNN has been chosen as a classifier and subsequently as a pattern recognition tool.

4.3.1 DWT Feature Extraction

The feature extraction is a procedure for determining the relevant shape information contained in an input pattern. The goal of feature extraction is to find as the least number of features as possible that adequately differentiate any pattern from other patterns.

Every fault pattern is characterized by a set of features such as frequency, phase and magnitude. DWT is capable of providing the time and frequency information simultaneously for any given signal thereby giving a time-frequency representation of the signal. Detail descriptions about WT and DWT can be found in Chapter 3, Section 3.2. The DWT has been applied to all the three phase currents after the occurrence of a fault to extract the pertinent features. In this scheme, wavelet decomposition up to 4^{th} level has been found to be necessary and sufficient for fault classification. Figure 4.2 shows the wavelet decomposition of all the three phase half cycle current waveforms for an A-g fault. The fault has been assumed to be occurred at a distance of 60 km from the relaying end with 0 Ω fault resistance, 45˚ fault inception angle and line loading angle of 10˚. The line loading angle is the angle between the sending and receiving end voltages of the transmission line [92, 93]. The differences in the coefficients at various levels of decomposition for the faulted and unfaulted phase currents are clearly evident in this figure.

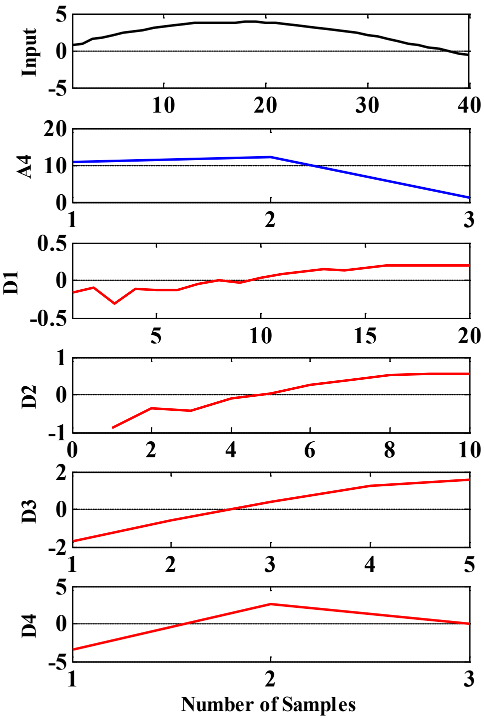

Figure 4.2 (a) : A-Phase

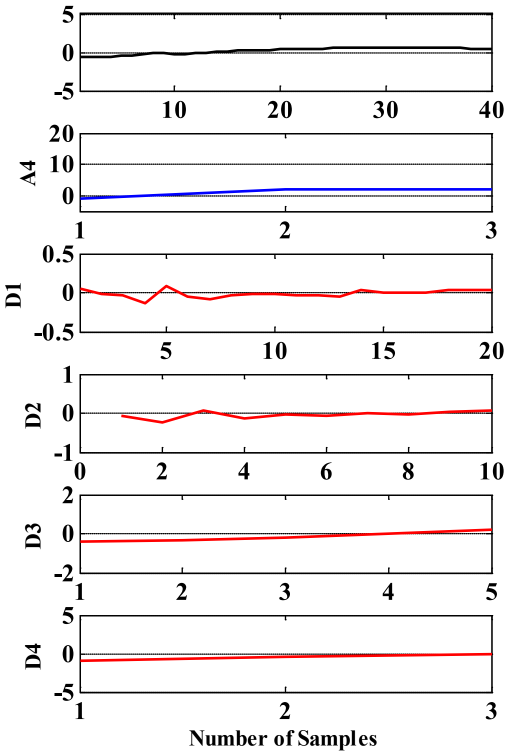

Figure 4.2 (b): B-Phase

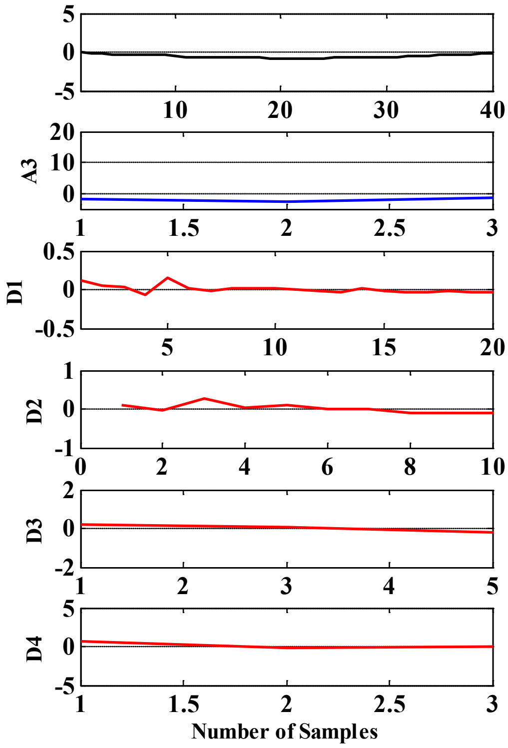

Figure 4.2 (c): C-Phase

Figure 4.2: Extracted features by DWT for an A-g fault up to 4th level of decomposition

4.3.2 Fault Classification Scheme

The response of the digital protection system to the fault condition primarily depends on the distinctive changes in fault current and voltage signals. Therefore, the development of an accurate protection system can be treated as the problem of identifying these changes. As discussed in the previous chapter, the ChNN has exceptional capability of classifying these changes in the patterns into required output classes through learning from training examples.

The schematic flow diagram of Figure 4.3 shows the fault classification scheme based on DWT and ChNN for series compensated transmission line. A ChNN is used for each phase to identify the involvement of that phase in the fault. A separate ChNN is further used which takes at its input the outputs of DWT of zero sequence current for determining the involvement of the ground in the fault. The ChNN is expected to generate '1' if the corresponding phase/ ground is involved in the fault, otherwise it should give an output of '0'. Therefore, a cluster of four ChNNs, generates four outputs, each to identify the involvement of phase or ground associated with it, in the event of a fault. The basic flowchart for training of the DWT-ChNN scheme used in this work for fault classification is shown in Figure 4.4.

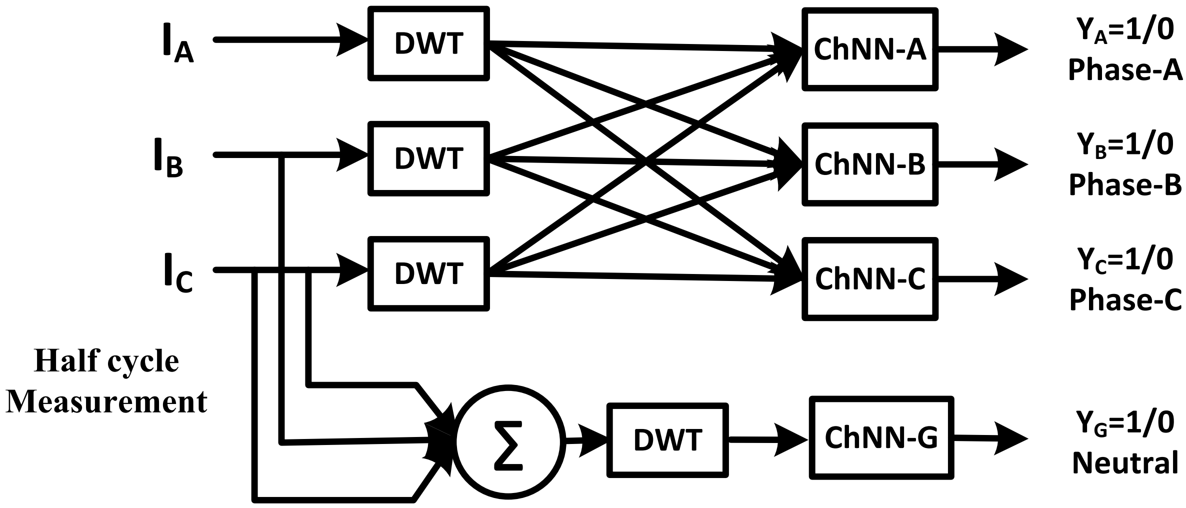

Figure 4.3: DWT and ChNN based fault classification scheme block-diagram

To facilitate fault classification using DWT, the mother wavelet is first to be selected. This step is very important in the fault classification process, as the mother wavelet presents an important role on the performance of the algorithm. Therefore, the mother wavelet that provides significant difference in various coefficients for faulted and non-faulted phase should be selected [94]. The mother wavelet for this scheme was selected based on repeated simulation studies. Several studies were conducted with different mother wavelets under different fault conditions. It was found that the difference between the faulted and the healthy phase was substantial when ‘db1’ (Daubechies) was selected as the mother wavelet and as a result, ‘db1’ has been selected as the mother wavelet in this work.

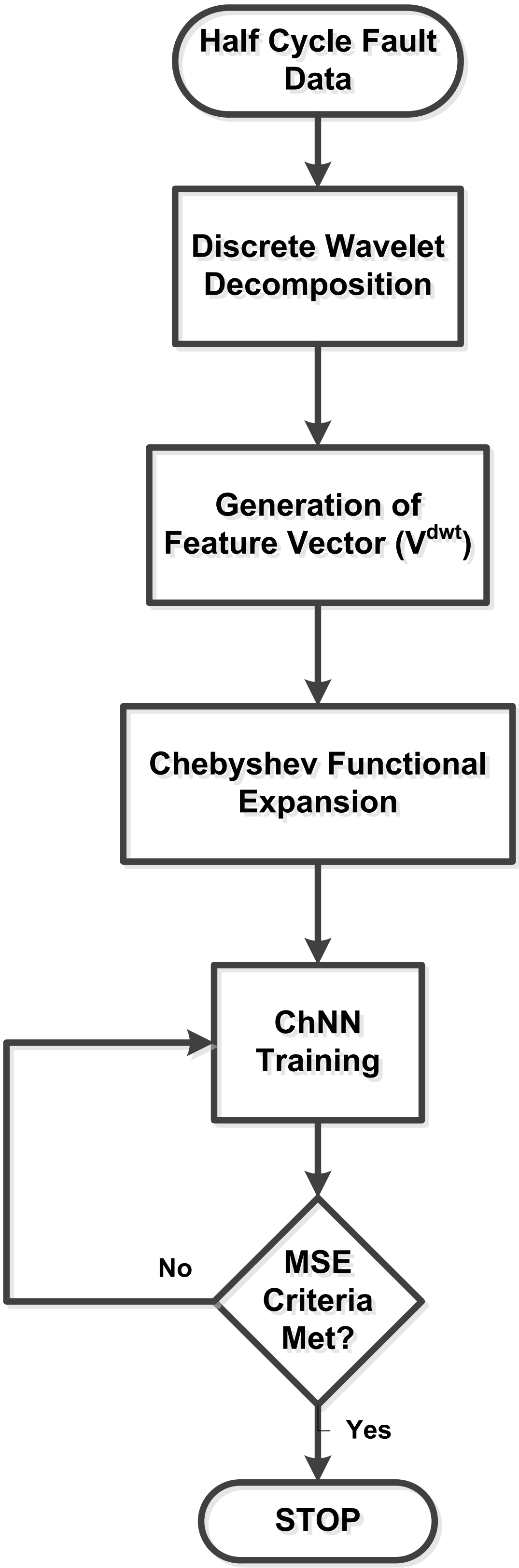

Figure 4.4 : Fault classification with DWT and ChNN

In the scheme of Figure 4.3, DWT up to 4th level of resolution is performed on the half cycle post fault current signal for each phase up to 4th level of *resolution* is performed (as shown in Figure 4.5).

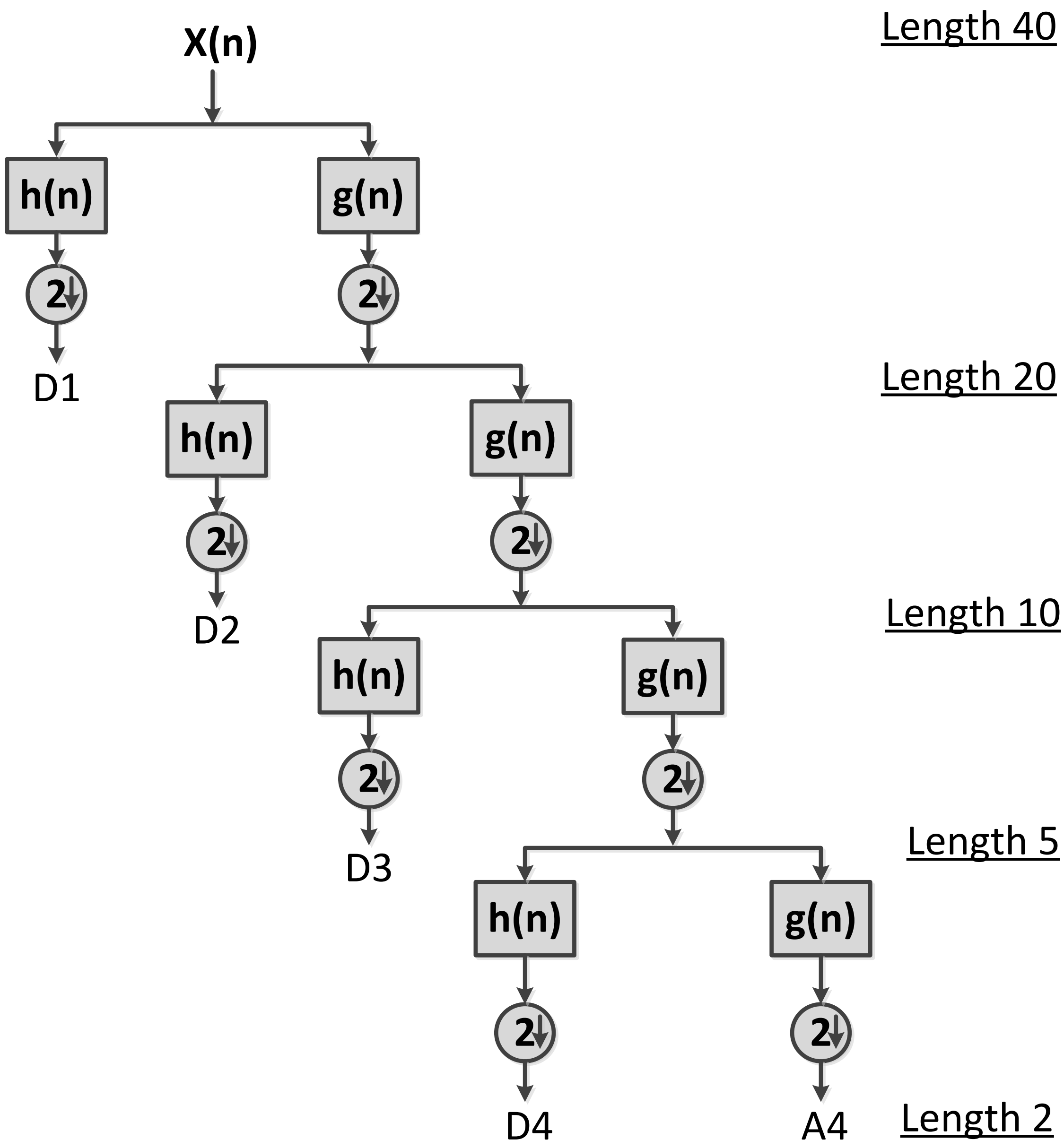

Figure 4.5 : Discrete wavelet decomposition of the half cycle waveform up to 4th level of decomposition

Out of total 5 sub bands (4 wavelet sub-band (D1 to D4) and one approximation sub-band (A4)) shown in Figure 4.5, 4 detail sub-bands have been used for further pattern recognition analysis for fault classification. The ith element of the feature pattern vector can be expressed as:

$$\boldsymbol{v}_{\boldsymbol{i}}^{\boldsymbol{dwt}} = \frac{1}{n_i}\sum_{j=1}^{n_i} b_{i,j}^2 \qquad (4.3)$$

where, $i = 1,2,3,4$, n_i is the number of samples in an individual sub band and $b_{i,j}$ is the j^{th} coefficient of the i^{th} sub band.

Thereafter, the DWT feature vector for any phase *p* is formed and is given by:

$$\mathbf{V}_p^{dwt} = \left[\mathbf{v}_1^{dwt}, \mathbf{v}_2^{dwt}, \mathbf{v}_3^{dwt}, \mathbf{v}_4^{dwt}\right] \tag{4.4}$$

With half cycle input per phase, a total of 40 samples per phase are subjected to the DWT. Therefore, as shown in Figure 4.5, a total of 37 DWT resolutions per phase are generated for further processing with ChNN for fault classification. The total feature vector can be given as:

$$\mathbf{V}^{dwt} = \left[\mathbf{V}_A^{dwt}, \mathbf{V}_B^{dwt}, \mathbf{V}_C^{dwt}\right] \tag{4.5}$$

4.3.3 ChNN for Classification Application

ANN is considered to be a powerful pattern recognition tool for classification. Therefore, many applications of ANN can be found in the literature for development of relaying algorithms for power system protection. However, the size of the ANN increases with an increase of number and complexity of inputs. As mentioned previously in Section 3.7, the ChNN provides computational, learning and designing advantages over MLPNN. Inclusion of the functional expansion increases the generalization ability of the network for any given problem. With addition of the higher dimensions in the input space, basically no information is added, but the input representation is enhanced for the purpose of classification. The higher-order representation of the input data can make the network easier to get trained. Figure 4.6 to Figure 4.9 demonstrate these capabilities of the Chebyshev expansion for ANN.

Figure 4.6 and Figure 4.7 show the wavelet coefficients generated for an A-B-g fault and A-B fault respectively for the system of Figure 4.1. Figure 4.6 shows the DWT feature vector $\mathbf{V}^{dwt}$ (as given in Equation (4.5)) for an A-B-g fault occurring at a distance of 51% of the total line length (measured from the location of the relay), with 5 Ω fault resistance and fault inception angle (FIA) of 45° for a line loading angle (δ) is of to 10°. Figure 4.7 shows the feature vector $\mathbf{V}^{dwt}$ for an A-B fault with the same fault conditions of Figure 4.6. It is clear from these figures that, a very small difference exists in terms of patterns between the feature vectors of A-B-g fault and A-B fault. With similarity in the inputs, size, design and learning for the classifier become difficult and tedious.

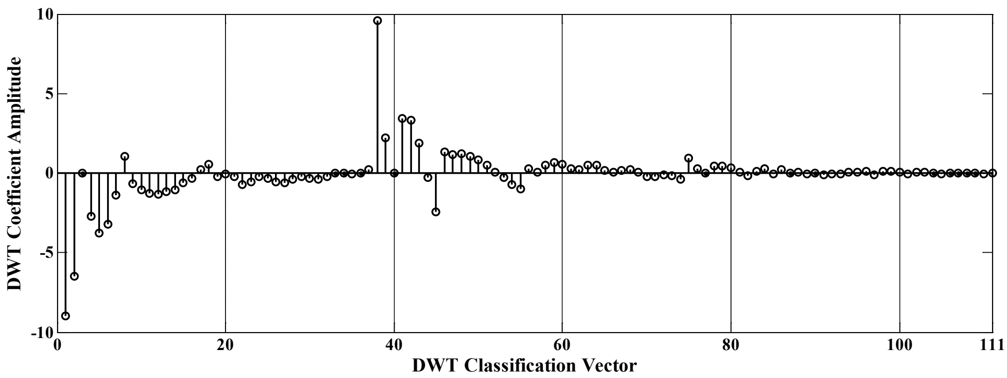

Figure 4.6: DWT feature vector for an A-B-g fault

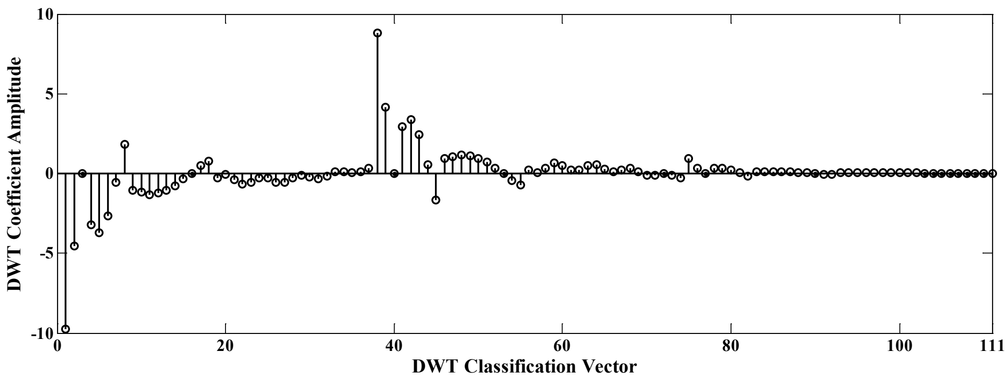

Figure 4.7: DWT feature vector for an A-B fault

However, application of Chebyshev functional expansion generates higher dimensional feature vector patterns. These generated higher dimensional feature vector patterns are more clearly classifiable as shown in Figure 4.8 and Figure 4.9. Figure 4.8 shows the Chebyshev functional expansion of the ChNN input patterns of Figure 4.6 in the three-dimensional higher-order classification plane. The fourth order Chebyshev expansion of the DWT feature vector of Figure 4.7 is shown in Figure 4.9. It is evident from Figure 4.8 and Figure 4.9 that, a considerable difference exists for classification in this higher-dimensional plane. Therefore, design and learning of the classifier become simplified, which enhances the overall classification performance of the classifier.

4.3.4 System and Fault Parameter Variations in PSCAD Simulation

In order to test the performance of the proposed scheme for different fault conditions, a large fault data set has been generated with variations in the fault parameters such as fault resistance (R_f), fault inception angle (FIA), location of the fault (expressed as the distance of the fault from the relay end) and type of fault. These fault parameters have been varied under different system conditions. These different system conditions have been created with variation in compensation level, generator impedances and line loading angle. Considering

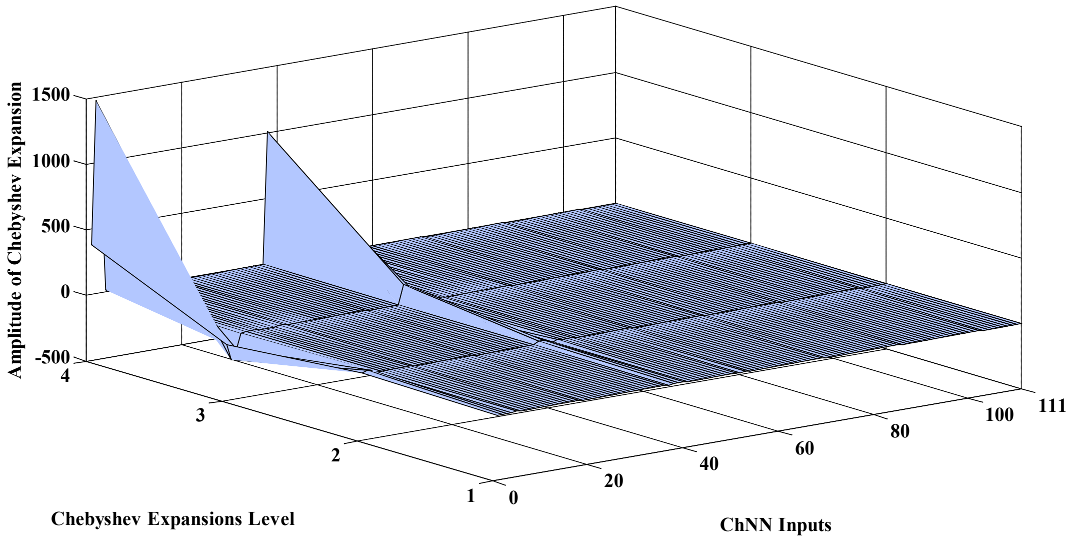

Figure 4.8: Chebyshev functional expansion of the DWT vector in Figure 4.6

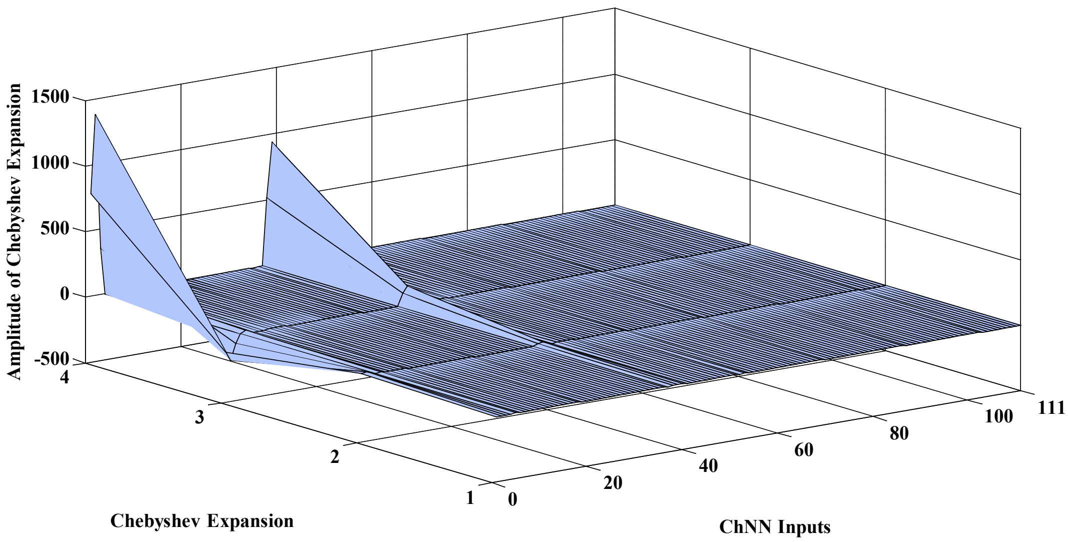

Figure 4.9: Chebyshev functional expansion of the DWT vector in Figure 4.7

the generator impedance values (given in Appendix-A) as the base value (Generator Base Impedance (GBI)), the variations considered in the system parameters are:

i) Compensation level (X_C) : 25%, 50%, 75% of the total line reactance

ii) Source impedances : Five combinations of generator impedances Z_{SG1} and Z_{SG2} (75%-100%, 125%-100%, 100%-100%, 100%-125% and 100%-75% of GBI) (Z_{SG1} is impedance of generator G1 and Z_{SG2} is of generator G2 of Figure 4.1)

iii) Line loading angles (δ) : 10˚, 20˚, 30˚.

A total of 45 distinct system conditions are thus considered for this study as given in Table 4.2.

Table 4.2: System conditions for testing of the developed algorithm

Compensation level (Xc) In % of Total Line Reactance	**Load Angle (δ)**	**Z_{SG1} In % of GBI**	**Z_{SG2} In % of GBI**	**System Conditions**
25, 50, 75	10, 20, 30	100	100	1-9
25, 50, 75	10, 20, 30	100	125, 75	10-27
25, 50, 75	10, 20, 30	125, 75	100	28-45

For all of these 45 different system conditions, various fault cases have been simulated by varying the fault parameters. The fault parameters considered for this study are:

i) Fault resistance (R_f) : 0 Ω, 5 Ω, 25 Ω, 50 Ω;

ii) Fault inception angle (FIA) : 0˚, 45˚, 80˚, 115˚

iii) Fault distance (L) : 60 km, 120 km, 138 km, 147 km, 153 km, 162 km, 180 km and 240 km on the 300 km line

iv) Fault type : All ten types (L-g, L-L-g, L-L, L-L-L-g)

Thus, a total of 1280 fault combination have been generated for a specific system condition [(4(R_f) * 4(FIA) * 8(L) * 10(fault type) = 1280]. With 45 system conditions, a total of 57600 fault cases thus have been generated for this study.

4.3.5 Chebyshev Neural Network Training

The ChNN training is similar to the MLPNN learning and can be divided into two classes, supervised learning and unsupervised learning. In supervised training the network is provided with the desired output along with the inputs while in unsupervised learning, the network has to discover the inherent patterns in the inputs without any outside help. Normally the unsupervised self-learning is impractical for protection applications. Therefore, the supervised back-propagation learning with Least Square Levenberg-Marquardt (LSLM) algorithm is used for ChNN training in present work.

Let, **X** is the input pattern with n components; $\mathbf{X}=[x_1,x_2,\ldots\ldots, x_n]$;

Therefore, **Ø** represents its Chebyshev expansion vector (Section 3.7.3) as

$$\mathbf{Ø}=[1,T_1(x_1), T_2(x_1),\ldots\ldots\ldots T_m(x_1), T_1(x_2), T_2(x_2),\ldots\ldots, T_m(x_2),\ldots\ldots\ldots\ldots T_m(x_n)] \quad (4.6)$$

Where, '*m*' represents order of Chebyshev expansion and **Ø** carries (m*n)+1 (=z) components (Section 3.7.3). Therefore,

$$\mathbf{Ø}=[t_1, t_2,\ldots\ldots\ldots\ldots t_z]; \quad (4.7)$$

Let, the output ($\hat{Y}$) of the single layer neural network for input vector ($\boldsymbol{\Phi}$) is given by:

$$\hat{Y} = \hat{W}^T \phi \tag{4.8}$$

Where, $\hat{\boldsymbol{W}}$ is the weight vector of the single layer neural network given as:

$$\hat{\boldsymbol{W}} = [w_1, w_2, \ldots\ldots w_z]^T \tag{4.9}$$

In equation 4.7, and 'w_1', 'w_2',....w_z' represent the weights (multiplication factor) of the individual interconnection between the input and output layer neurons and 'z' represents the total number of interconnections.

Therefore, the error (e) in the network at the output node can be defined as the difference between the desired output (Y) and generated output ($\hat{Y}$):

$$e = Y - \hat{Y} \tag{4.10}$$

The aim of the learning procedure is to find an appropriate set of values for the weight vectors to minimize the error between the actual and the desired output. With this objective the global sum of the squared errors between the actual output, and the desired output is minimized over the entire training set and all the output nodes. The weights have been found out by following the LSLM learning algorithm [75].

4.3.5.1 ChNN Training with Back Propagation Least Square Levenberg-Marquardt algorithm

Let,

- p is the index of input patterns, from 1 to P, where P is the number of patterns used for training.
- z is the index of weights, from 1 to Z, where Z is the number of weights.
- k is the index of iterations.

Considering the ChNN of Section 3.7.3, Figure 3.12, the task considered with the network training is to learn the associations between a specified set of input-output pairs $[(X_1, Y_1), (X_2, Y_2), \ldots\ldots\ldots, (X_P, Y_P)]$.

For any iteration 'k', with the input as Chebyshev vector $\boldsymbol{\phi_n}$ for single layer neural structure of Figure 3.12, output is given by,

$$\hat{Y}_{k,p} = f\left(\left(\sum_{z=1}^{Z} (w_{k,z} t_{p,z}\right) + b_k \right) \tag{4.11}$$

Where, '$w_{k,z}$' represent the z^{th} weight of the single layer neural structure, and '$t_{p,z}$' is the corresponding component of expanded Chebyshev vector of p^{th} pattern as input to the ANN; 'b_k' is the value of bias at k^{th} iteration. The goal of the learning algorithm is to minimize error (e_k), the cost function (performance index) at k^{th} instant, which can be given by

$$\hat{V}_k = \frac{1}{2}\sum_{p=1}^{P} e_{k,p}{}^2 \tag{4.12}$$

Where, $e_{k,p} = \hat{Y}_{k,p} - Y_{k,p}$ and

$Y_{k,p}$ = Desired output for p^{th} input

$\hat{Y}_{k,p}$ = Generated output of the network for p^{th} instance

By applying approximate steepest (gradient) descent algorithm [75], one can get,

$$\mathbf{\Delta W_k = -\alpha \frac{\partial \hat{V}_k}{\partial W_k}} \tag{4.13}$$

Where, $\boldsymbol{W_k} = [w_{k,1}, w_{k,2}, ..., w_{k,z}]^T$ represents weight vector of the neural network for k^{th} iteration, and

$$\Delta b_k = -\alpha \frac{\partial \hat{V}_k}{\partial b_k}, \tag{4.14}$$

where 'α' is the fixed learning rate.

Levenberg-Marquardt is a modification of Newton's method for function optimization with respect to a variable. With this method, the change in weight vector can be given as

$$\mathbf{\Delta w_k = [J_k^T J_k + \mu I]^{-1} J_k^T e_k} \tag{4.15}$$

Where, '***W***' is a weight vector, '***I***' is the identity matrix and '$\boldsymbol{J_k}$' is Jacobean matrix and can be given as,

$$\boldsymbol{J_k} = \begin{bmatrix} \frac{\partial e_{k,1}}{\partial w_{k,1}} & \frac{\partial e_{k,1}}{\partial w_{k,2}} & \cdots\cdots\cdots & \frac{\partial e_{k,1}}{\partial w_{k,z}} \\ \frac{\partial e_{k,2}}{\partial w_{k,1}} & \frac{\partial e_{k,2}}{\partial w_{k,2}} & \cdots\cdots\cdots & \frac{\partial e_{k,2}}{\partial w_{k,z}} \\ : & & & \\ : & & & \\ \frac{\partial e_{k,p}}{\partial w_{k,1}} & \frac{\partial e_{k,p}}{\partial w_{k,2}} & \cdots\cdots\cdots & \frac{\partial e_{k,p}}{\partial w_{k,z}} \end{bmatrix} \tag{4.16}$$

'$\mathbf{e_k}$' is error vector for the network for the 'k^{th}' iteration and given as:

$$\boldsymbol{e_k} = \begin{bmatrix} e_{k,1} \\ e_{k,2} \\ . \\ . \\ e_{k,P} \end{bmatrix} \tag{4.17}$$

The parameter μ is multiplied by some factor *(β)* whenever a step would result in an increased $\hat{V}_k$ [95]. When a step reduces $\hat{V}_k$, μ is divided by *β (0.001 in this work)*. When μ is large the algorithm becomes steepest descent (with step up), while for small μ the algorithm becomes Gauss-Newton. For this updation, the input pattern vector is subjected to inputs of the network to generate corresponding output. The weights and bias are updated as:

$$W_{k+1} = W_k + \Delta W_k \text{ and } b_{k+1} = b_k + \Delta b_k \quad (4.18)$$

to minimize the cost function, that can be calculated with updated weights and bias.

Out of total 57600 fault cases generated with PSCAD, a set of 3600 fault patterns (6.27% of total fault patterns) had been considered for ChNN training. Remaining 54000 fault patterns have been used for evaluation of the DWT and ChNN based fault classification scheme. All 3600 training fault patterns have been generated at 50% compensation level and other relevant system and fault parameters for these 3600 fault cases are given in Table 4.3.

Table 4.3: Fault data for ChNN training

Parameters							**Number of Fault Cases**
Xc	**Z_{SG1} In % of GBI**	**Z_{SG2} In % of GBI**	**δ**	**R_f (Ω)**	**FIA**	**L (km)**	
50%	100	100	10° & 30°	0, 5 & 50	0, 45 & 115	60, 138, 162, 240	720
50%	100	75					720
50%	100	125					720
50%	125	100					720
50%	75	100					720
Total Fault Cases							**3600**

4.3.6 Results and Discussion

Once the ChNN was trained, it was subjected to testing and evaluation. All 54000 fault cases were subjected to the DWT to generate the feature vector using equation (4.3). The resultant feature vector is then applied to the ChNN for classifying the fault and generated outputs are compared with the desired outputs for computing the classification accuracy.

The performance of the DWT-ChNN based fault classification scheme has been investigated for different orders of Chebyshev expansions to determine the preferred level of expansion. The accuracy obtained for various levels of expansions is given in Table 4.4. From this table it is observed that the performance of the DWT-ChNN based scheme is best for fourth order of Chebyshev expansion and as a result, the fourth order Chebyshev expansion has been selected in this work.

Table 4.4: Performance of the DWT-ChNN based scheme with different levels of Chebyshev expansions

Sr. No.	Order of ChNN	Overall Accuracy Obtained
1	Third Order	97.07 %
2	Fourth Order	99.33 %
3	Fifth Order	99.14 %

Table 4.5 and Table 4.6 provide the summary of the fault classification performance for the system shown in Figure 4.1. Table 4.5 gives the fault classification accuracy for 25%, 50% and 75% compensation level. From this table it is observed that, out of total 54000 test cases, a misclassification rate of just 0.67% was detected. Table 4.6 tabulates the performance of the developed fault classification method for faults at various locations of the line.

Table 4.5: Performance of the developed algorithm for different compensation levels

Compensation Level	Numbers of Test Cases	Fault Type Detection Errors	Accuracy
25%	19200	128	99.33 %
50%	15600	60	99.62 %
75%	19200	174	99.09 %
Total	**54000**	**362**	**99.33 %**

Table 4.6: Performance of the DWT and ChNN based algorithm at various fault locations

Fault distance in % of Total Line Length	Number of Test Fault Patterns	Number of Misclassification	Accuracy
20%	6300	64	98.98 %
40%	7200	38	99.47 %
46%	7200	34	99.46 %
49%	6300	35	99.51 %
51%	6300	57	99.20 %
54%	7200	41	99.43 %
60%	7200	41	99.43 %
80%	6300	52	99.17 %
Total	**54000**	**362**	**99.33 %**

A close scrutiny of Table 4.5 reveals that the level of accuracy reduces slightly corresponding to a compensation level of 75%. This is due to the fact that, the ChNN has been trained at 50% compensation level only. At 75% compensation level, capacitive reactance included in the circuit is higher. Higher value of capacitance in series with the line inductance produces higher frequency components and more severe ac transients. Therefore, higher spectral deviations in the signals (from the non-faulty, sinusoidal signals) are observed at 75% compensation level than at 50% compensation level. Moreover, from Table 4.6 it is observed that the performance of the scheme is slightly poorer for close in faults and for the faults at the end of the line. Changes in current magnitude and frequency spectrum for a close in fault are very severe and are less for faults at the end of the line. However, the performances at these levels are also comparable or better than those reported in the literature i.e. 97.45% in [96] and 97.95% in [97]. It is further to be noted that in [12] and [13], samples of post fault currents corresponding to full cycle period have been used in contrast to the samples corresponding to the half cycle period used in this work.

Figure 4.10 shows the fault classification accuracy for the developed algorithm corresponding to all possible type of faults with 5400 fault patterns for each type of fault. As can be seen from this figure, the performance of the DWT-ChNN based scheme is slightly poor for ABC fault. However, possibility of such fault is least in actual practice.

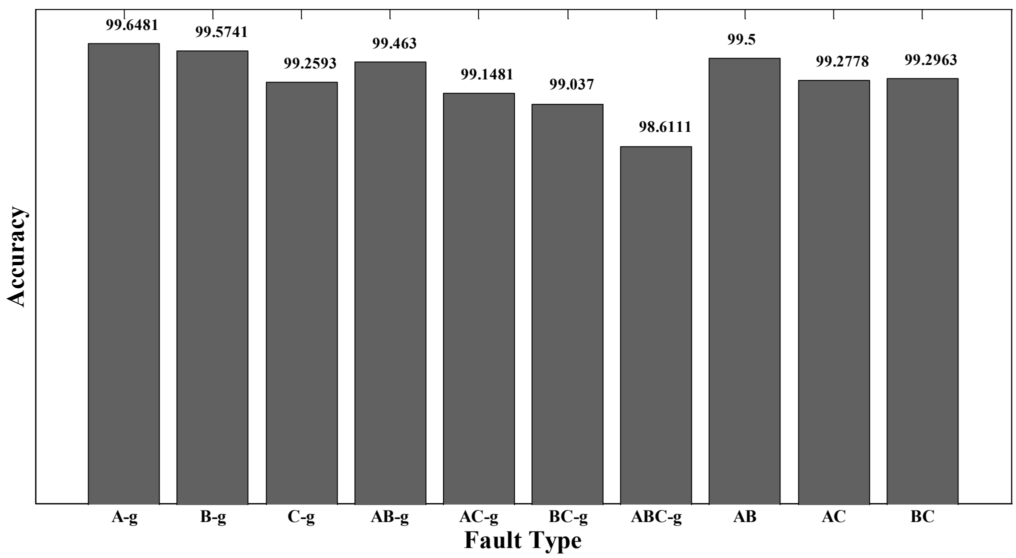

Figure 4.10: Fault classification accuracy for different types of faults

4.4 PATTERN RECOGNITION APPLICATION OF CHNN FOR FAULT CLASSIFICATION WITH SERIES COMPENSATED TRANSMISSION LINE

4.4.1 Motivation to Adopt Pattern Recognition

The signal processing tools applied at the first-stage of the two-stage algorithms as described in previous section enhances the fault features which in turn is expected to improve the fault classification capability. However, it also increases the overall detection time due to enhanced computational complexity.

The longer any algorithm takes to identify and clear the fault, more will be the damage to the grid. This can have serious effects on the continuity and economic operation of the power networks. A timely and accurate fault analysis reduces the system down time and timely restoration of the supply. This leads towards single-stage application of AI techniques for fault classification.

Towards this goal, in this work a single-stage fault classification scheme is proposed in which a ChNN is used as a classifier. Since ChNN is a computational model comprising a number of neurons interconnected to solve a designated task, the computational effort mainly depends on the size of the ChNN and the learning algorithm used for its training. The size of the ChNN has been chosen on the basis of the degree of Chebyshev expansion. However, a detailed study on the learning algorithm for ChNN in fault classification problem is quite limited. Therefore, in this work, a detailed study has been conducted to investigate the performance of two different ChNN learning algorithms for fault classification in a series compensated transmission line. These algorithms are compared on the basis of their generalization capability, prediction performances and noise immunity during training and testing.

4.4.2 Fault Classification Scheme

A change in the magnitude and frequency of the three phase currents can be observed during fault. The fault classification algorithm proposed in this section captures this change in the post-fault currents immediately after the occurrence of the fault. In this scheme, half cycle three-phase current samples after fault inception are utilized with a group of four ChNNs and the outputs identify the fault type. The proposed scheme is shown in Figure 4.11.

In this scheme, three of the four ChNNs determine the involvement of the corresponding phase in the fault. The fourth one is used to detect the involvement of the ground in the fault. Three ChNNs designed to identify the involvement of the phases in fault use 40 samples (number of samples corresponding to half cycle duration at 4 kHz sampling frequency) of fault current from each phase measured at the location of the relay. Each ChNN therefore is supplied with a total of 40 samples of fault currents. From Section 3.7.3, for 40 input samples (m=40), the ChNN input patterns for any phase can be given as:

$$\boldsymbol{P}_n = [x_1, x_2, ..., x_{40}]^T \tag{4.19}$$

In equation (4.19), n = [phase-A, phase-B, Phase-C]. These inputs are expanded by Chebyshev expansion up to ‘R’th order. The expanded pattern consists of (R*40+1) components and can be given as:

$$T_n = \left\{\left[1; S_1(x_1); S_2(x_1); S_3(x_1); ....S_R(x_1); S_1(x_2) ....S_R(x_{40})\right]\right\} \tag{4.20}$$

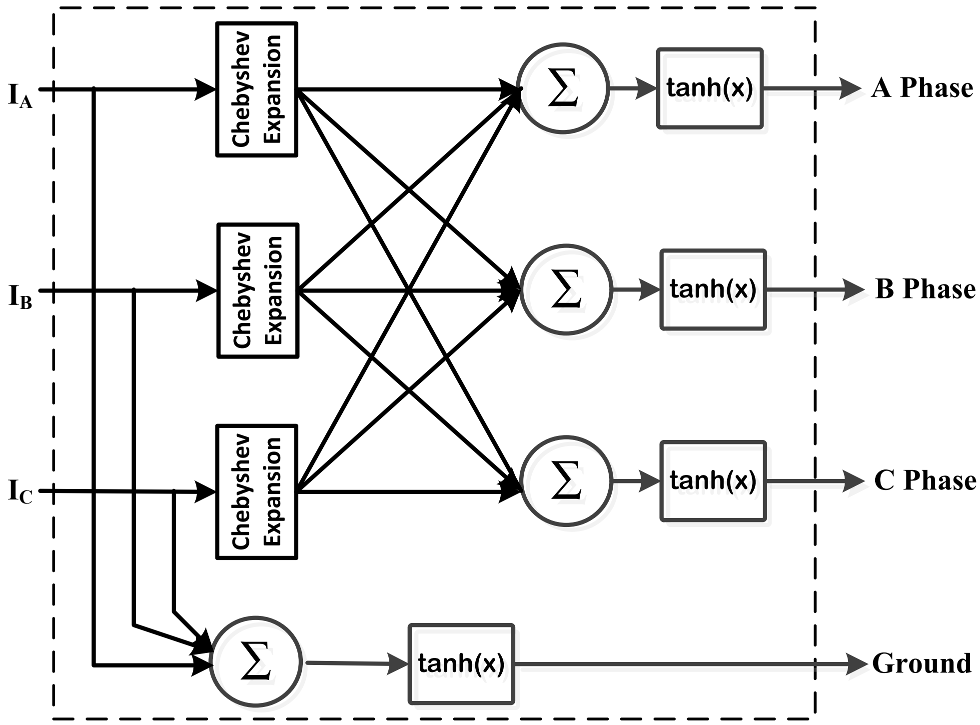

Figure 4.11: Pattern recognition based fault classification with ChNN

Chebyshev expanded patterns for each phase are added together to increase the classification performance. Therefore, the total pattern subjected to the single layer neural network is given as:

$$T = \{T_A, T_B, T_C\} \tag{4.21}$$

The pattern T for each neuron consists of 3*(R*40+1) components (Chapter 3, section 3.7.3). This expanded higher order pattern is capable to map the output more efficiently. A detailed investigation to identify the appropriate order of the Chebyshev expansion is given in Section 4.4.3. A sum of all the three phase currents (40 samples) is supplied to the ChNN designated to identify the involvement of ground. After training, the ChNN produces '1(0)' to indicate the involvement (non-involvement) of the corresponding phase or ground in the fault. For the task of fault classification with ChNN only, the performance of two training algorithms, namely, LSLM and RLSFF have been investigated. As the details of the LM algorithm have already been described earlier in Subsection 4.3.5, in the next subsection the RLSFF algorithm is discussed in detail.

As already discussed for DWT based feature vector in Section 4.3.2, for direct current pattern recognition also, Chebyshev expansion increases the generalization capability of the neural network. With addition of the higher dimensions in the input space, basically no information is added. However, due to the addition of higher dimensions, the information contained in the input gets more prominent. The higher order representation of the input data can make the network easier to train as well. Figure 4.12 and Figure 4.13 show ChNN input patterns for A-B-g (P1) and A-B (P2) fault at a distance of 0.6L (L being the length of the transmission line) that is compensated with a capacitor providing 75% of compensation at the middle of the line length and with R_f = 5 Ω, FIA = 45° and δ = 20°. The input patterns are of identical nature and require a complex interconnected neural structure for an ANN for classification. However, a certain classifiable pattern can be seen for fourth order Chebyshev functional expansion (T1 and T2) with the same ChNN input patterns P1 and P2 respectively as shown in Figure 4.14 and Figure 4.15.

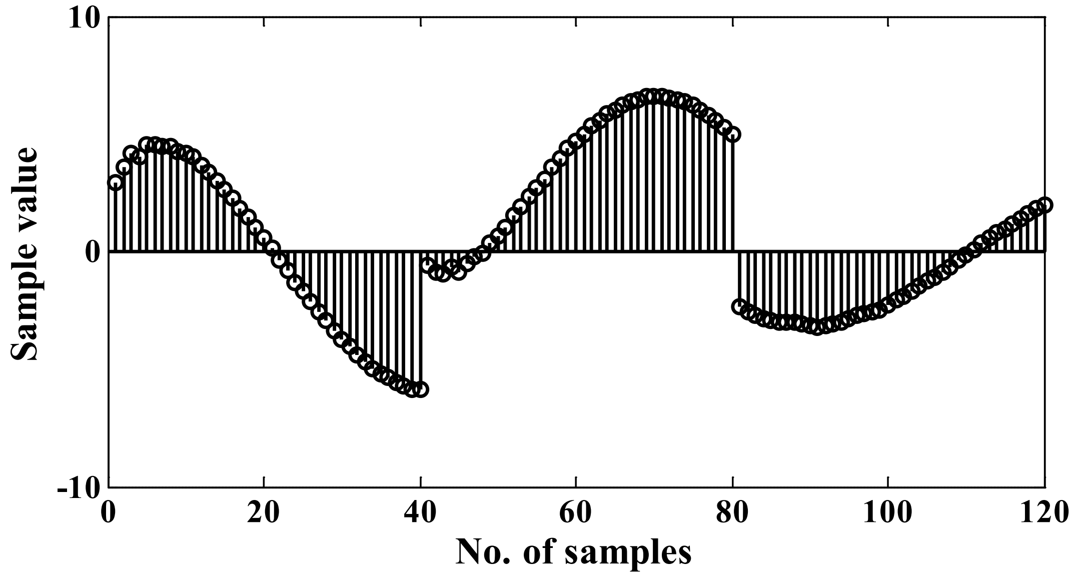

Figure 4.12: ChNN input vector for an A-B-g fault

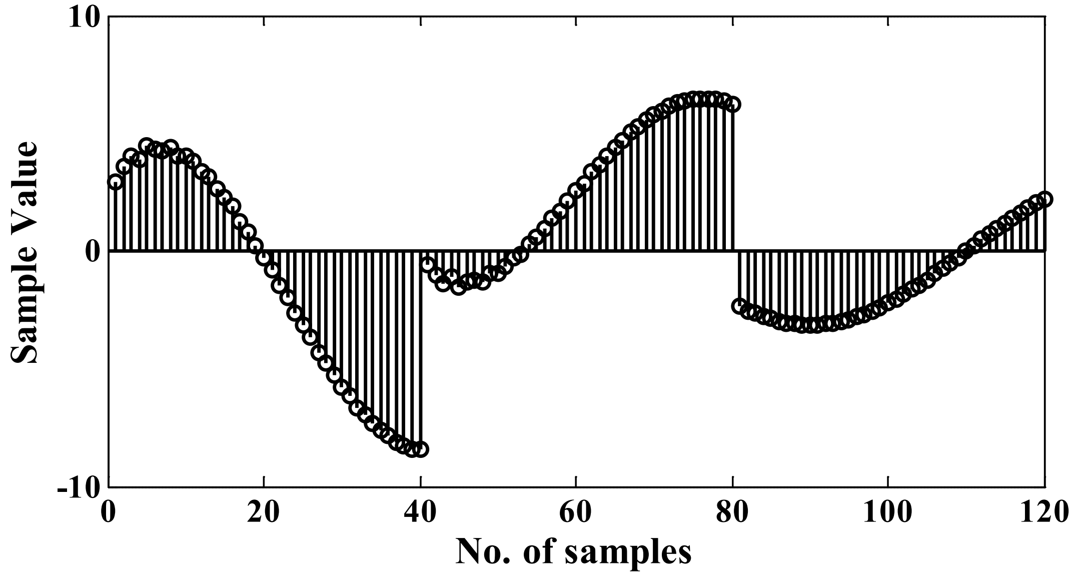

Figure 4.13: ChNN input vector for an A-B fault

Due to the absence of hidden layer, ChNN provides computational advantage over the MLP [83]. It is well known that non-linear approximation capability of Chebyshev orthogonal polynomial is very powerful as per the 'Best Approximation Theory' [82]. This makes the proposed algorithm more accurate and fast as well. Because of these advantages of ChNN, the proposed method is easy to implement in practical large power systems.

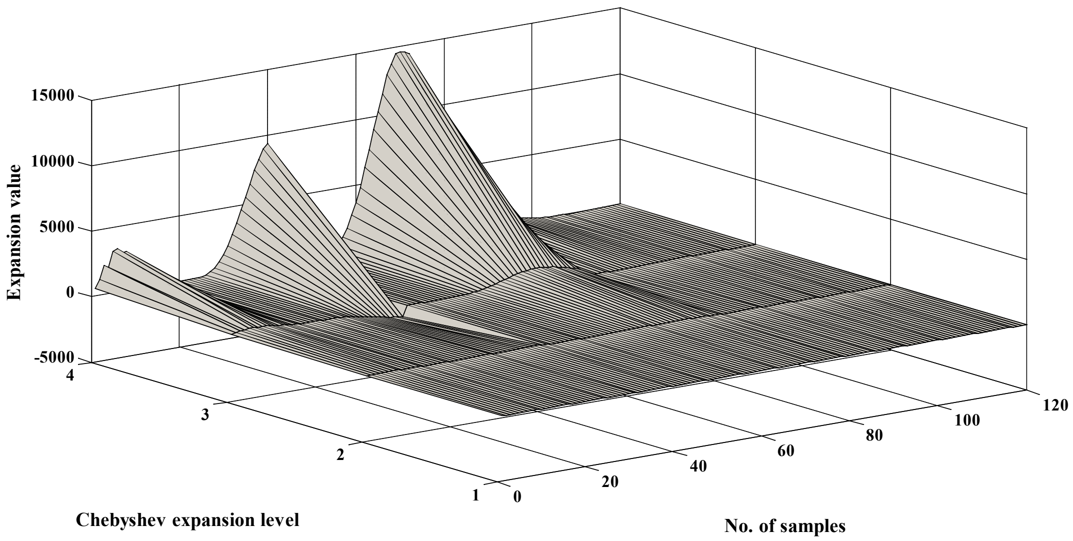

Figure 4.14: Chebyshev expanded feature space for fault A-B-g (of pattern P1 from Figure 4.12)

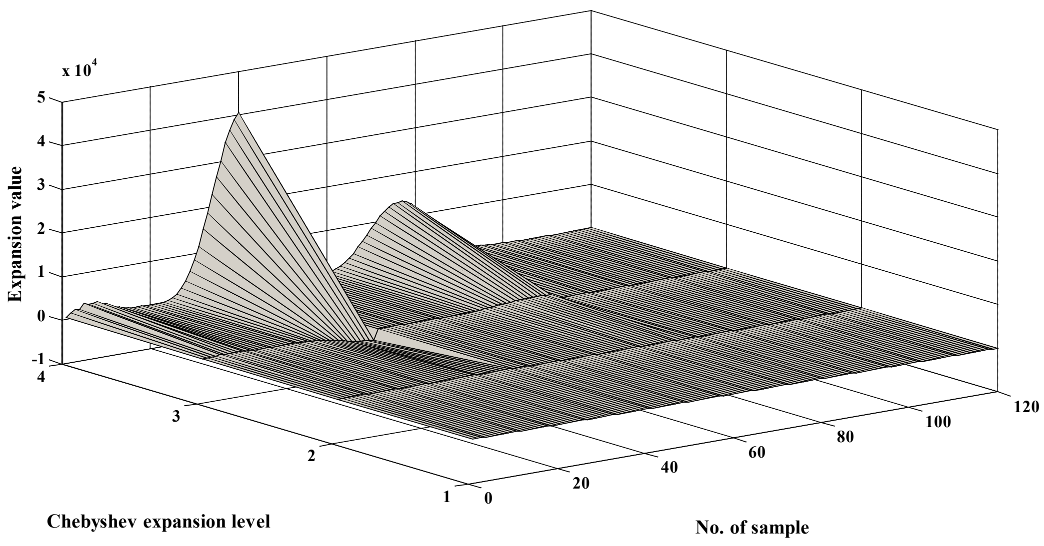

Figure 4.15: Chebyshev expanded feature space for fault A-B (of pattern P2 from Figure 4.13)

4.4.3 Recursive Least Squares Learning Method with Forgetting Factor

In this method, the forgetting factor is included to give the present input data higher weightage than the past ones. Therefore, the classification characteristic of the ANN gets modified for each training pattern independently. This makes the algorithm capable of identifying the fault current variation more efficiently in fault condition. Thus, this method has faster training and stronger time-vary tracking capacity [98]. In this method, the performance function to be minimized is given by:

$$E = \sum_{p=1}^{P} \lambda^{p-i} \left| e_p \right|^2 \tag{4.22}$$

In equation (4.22), 'λ' represents the forgetting factor of the algorithm. The algorithm for the discrete time model is given by:

$$\mathbf{\hat{W}_p = \hat{W}_{p\text{-}1} + K_p e_p} \tag{4.23}$$

Where,

$$\mathbf{K_p = \frac{\lambda^{-1} R_{p\text{-}1} f_p}{1 + \lambda^{-1} f^T R_{p\text{-}1} f_p}} \tag{4.24}$$

$$\mathbf{e_p = Y_p - \hat{Y}_p} \tag{4.25}$$

$$\mathbf{R_p = \lambda^{-1} R_{p\text{-}1} - \lambda^{-1} K_p f_p^T R_{p\text{-}1}} \tag{4.26}$$

In the above equations, $\hat{Y}(n)$ is the desired output and $Y(n)$ gives the generated output. '*Φ'* is the basis function formed by the functional expansion of the input and $R_0 = C^*I$, C is a positive constant, $||R_0|| < Q_0$, *where* Q_0 is a constant that serves as an upper bound for $||R_0||$. All matrix and vectors are of compatible dimension for the purpose of computation.

The choice of the forgetting factor often affects the convergence rate and the classification capability of the algorithm. Studies show that the classifier has better performance with value of $\lambda \approx 1$ $(0 > \lambda < 1)$ [99-101].

The algorithm, which does not require the storage of all the data and matrix inversion operation, is suitable for online applications.

4.4.4 Performance Evaluation of Two Learning Methods for Fault Classification

For performance evaluation, the ChNN has been trained with the same training set given in Table 4.3. The same set of 3600 fault cases (given in Table 4.3) had been considered to train the ChNN for both the training methods.

(A) ***Performance of ChNN trained with LSLM***

The first step of the application of the ChNN after obtaining the training samples is to determine the optimal order of the input Chebyshev expansion. An application based performance evaluation has been carried out to identify the appropriate level of expansion.

All four ChNNs have been trained with 3600 fault patterns of Table 4.3 with various orders of Chebyshev expansions. Subsequently, all the 54000 test patterns described earlier have been used to test the performance of the ChNNs with various orders of Chebyshev expansions. The overall accuracy obtained for various order of ChNNs is shown in Table 4.7.

Table 4.7: Fault classification accuracies for various order ChNN trained with LSLM

Sr. No.	Order of ChNN	Overall Accuracy Obtained (LSLM)
1	Third Order	93.91%
2	Fourth Order	99.44%
3	Fifth Order	99.46%
4	Sixth Order	98.69%

It is evident from Table 4.7 that the performances of the third and fourth order of Chebyshev expansions are on higher side than those obtained by other orders of expansion. If higher order of Chebyshev expansion is taken, the non-linear processing capability of ChNN would be stronger. However, this would result in heavier computational burden [82] and problem of over fitting. Overfitting reduces the classification capability and results in poorer accuracy. This fact is evident in Table 4.7 corresponding to sixth order ChNN.

Moreover, the fourth and fifth order ChNN gives almost identical level of accuracies for fault classification in series compensated transmission lines. However, higher order expansion requires more input nodes to be processed for transformation of the original inputs. For power system protection applications, because of the limited processing time, it is important that the inputs are not expanded unnecessarily to get an accurate solution. Thus, the fourth order ChNN, being the best choice, has been chosen as classifier for this method.

Table 4.8 shows the accuracy of the LSLM algorithm at different levels of compensations with fourth order of ChNN. The results indicate the ability of ChNN to acquire quite a necessary shape of the classification boundary for fault current pattern recognition to generate a higher level of accuracy for various levels of compensation (more than 99% for all three levels), while it is trained for 50% compensation level only.

Table 4.8: Fault classification accuracy at different compensation levels for ChNN trained with LSLM

Compensation Level	Numbers of Test Cases	ChNN Trained with LSLM algorithm	
		Fault Type Detection Errors	Accuracy
25%	19200	103	99.46 %
50%	15600	22	99.86 %
75%	19200	175	99.08 %
Total	**54000**	**300**	**99.44 %**

The breakup of the accuracy according to the type of faults is given in Table 4.9. The ChNN trained with LSLM algorithm produces adequate level of accuracies for all possible types of the faults. An inferior performance can be observed for L-L-L-g fault. However, the L-L-L-g fault is the least possible type of fault in the power system [88].

Table 4.9: Accuracy for different fault types with ChNN trained with LSLM training algorithm

Type of Fault	Numbers of Test Cases	ChNN Trained with LSLM algorithm	
		Fault Classification Errors	Accuracy
L-g	16200	21	99.87 %
L-L-g	16200	69	99.57 %
L-L	16200	88	99.46 %
L-L-L-g	5400	122	97.74 %
Total	**54000**	**300**	**99.44 %**

A detail breakup of the fault classification performance of LSLM learning based ChNN for faults at different line lengths corresponding to 25%, 50% and 75% compensation levels are given in Table 4.10. Classification accuracies for various fault distances are quite close to each other. The developed scheme in this work yields a slightly lower accuracy at a fault distance of 60 km (20% of the total line length). The change in fault pattern is comparatively prominent for close in faults (i.e. for 20% fault distance), that makes them different than fault patterns at other fault distances. Therefore, the pattern recognition based ChNN gives a poorer fault classification accuracy at this fault length.

Table 4.10: Detailed break-up of fault classification accuracy for ChNN trained with LSLM algorithm

Fault Distance In Km	25% Series Compensation			50% Series Compensation			75% Series Compensation		
	Test cases	Errors	Accuracy	Test cases	Errors	Accuracy	Test cases	Errors	Accuracy
Before Compensator									
60	2400	15	99.37%	1500	10	99.33%	2400	64	97.33%
120	2400	00	100.0%	2400	00	100.0%	2400	00	100.0%
138	2400	19	99.20%	1500	11	99.26%	2400	17	99.29%
147	2400	24	99.00%	2400	00	100.0%	2400	14	99.41%
After Compensator									
153	2400	15	99.37%	2400	01	99.95%	2400	22	99.08%
162	2400	15	99.37%	1500	00	100.0%	2400	23	99.04%
180	2400	10	99.58%	2400	00	100.0%	2400	35	98.54%
240	2400	5	99.79%	1500	00	100.0%	2400	00	100.0%
TOTAL	**19200**	**103**	**99.46%**	**15600**	**22**	**99.86%**	**19200**	**175**	**99.08%**

(B) ***Performance of the ChNN trained with RLSFF method***

The results for this case are shown in Table 4.11 to Table 4.14. The ChNN has been trained and tested with identical fault cases as in the previous section.

It is apparent from Table 4.11 that the ChNN with RLSFF learning generates the highest level of accuracy with third order of Chebyshev expansion. Therefore, the third order of Chebyshev functional expansion has been considered in this work for ChNN with RLSFF training. The following parameters have been used for the RLSFF training algorithm: forgetting factor $\lambda = 0.80$ and P = diag(0.1) (Equation (4.22), (4.24) and (4.26)). The values for P and λ have been chosen using trial-and-error method.

Table 4.11: Fault classification accuracies for various order ChNN trained with RLSFF

Sr. No.	Order of ChNN	Overall Accuracy Obtained (RLSFF)
1	Third Order	98.81%
2	Fourth Order	96.83%
3	Fifth Order	96.37%
4	Sixth Order	95.64%

The learning algorithm with RLSFF produces the necessary changes in weight vector of the ChNN in proportional to the error between the generated and the desired output with the Chebyshev polynomial expanded input pattern (Equation (4.22)). As these changes are proportional to the input patterns, the required modification in neural weights will be achieved rapidly. Therefore, the training with RLSFF method converges with fewer numbers of epochs. However, it is achieved with increased computational burden during training as weight modification calculation involves (n x n) matrix for P. Therefore, the ChNN learning with RLSFF is sluggish as compared to LSLM algorithm. But, due to preferred changes in training, the level of accuracy achieved with 3rd order expansion only compares well to that obtained with 4th order expansion in LSLM method.

It can be seen from Table 4.12 and Table 4.14 that, the ChNN has been trained very efficiently for the fault cases corresponding to 50% compensation levels. The weight vector takes a necessary shape in third-order ChNN with RLSFF method as compared to fourth order ChNN with LSLM method. However, the performance deteriorates with change in input space. This can be explained as over fitting of the ChNN to the data with 50% compensation. The same can be noticed in Table 4.13 that shows the performance of the ChNN with RLSFF learning algorithm for different types of faults. A considerable variation in the accuracy is noticed as compared to LSLM trained ChNN with change in fault types, compensation level and fault distances. Therefore, a reduction in fault classification accuracy can be noticed in RLSFF trained ChNN.

Table 4.12: Fault classification accuracy at different compensation levels for ChNN trained with RLSFF

Compensation Level	Numbers of Test Cases	ChNN Trained with RLSFF algorithm	
		Fault Type Detection Errors	Accuracy
25%	19200	187	99.02%
50%	15600	15	99.90%
75%	19200	431	97.75%
Total	**54000**	**633**	**98.82%**

Table 4.13: Accuracy for different fault types with ChNN trained with RLSFF training algorithm

Type of Fault	Numbers of Test Cases	ChNN Trained with RLSFF algorithm	
		Fault Classification Errors	Accuracy
L-g	16200	136	99.16%
L-L-g	16200	223	98.62%
L-L	16200	226	98.60%
L-L-L-g	5400	48	99.11%
Total	**54000**	**633**	**98.82%**

Table 4.14: Detailed break-up of fault classification accuracy for ChNN trained with RLSFF algorithm

Fault Distance In Km	25% Series Compensation			50% Series Compensation			75% Series Compensation		
	Test cases	Errors	Accuracy	Test cases	Errors	Accuracy	Test cases	Errors	Accuracy
Before Compensator									
60	2400	28	98.83%	1500	04	99.73%	2400	47	98.04%
120	2400	15	99.37%	2400	00	100.0%	2400	33	98.62%
138	2400	17	99.29%	1500	07	99.53%	2400	31	98.70%
147	2400	19	99.20%	2400	00	100.0%	2400	24	99.00%
After Compensator									
153	2400	37	98.45%	2400	02	99.91%	2400	96	96.00%
162	2400	22	99.08%	1500	00	100.0%	2400	74	96.91%
180	2400	12	99.50%	2400	00	100.0%	2400	37	98.45%
240	2400	37	98.45%	1500	02	99.86%	2400	89	96.29%
TOTAL	**19200**	**187**	**99.02%**	**15600**	**15**	**99.90%**	**19200**	**431**	**97.75%**

4.4.5 Comparative Analysis of LSLM and RLSFF Learning Methods for ChNN Training

4.4.5.1 Learning Speed

Due to involvement of higher order matrix multiplication, the RLSFF training algorithm is much more computationally intensive. For a single update of the network weights, the RLSFF algorithm requires exactly the same calculations of response and back propagated errors as normal gradient descent. In addition, the RLSFF algorithm requires the calculation and storage of a P-matrix for each neuron in the network. The LSLM learning technique requires equivalent subroutine of the normal gradient descent. Therefore, the RLSFF learning is slower compared to LSLM training for the ChNN. Although these calculations are computationally intensive, an important point to note is that they can be done independently. Table 4.15 compares these two ChNN learning algorithms in terms of the training parameters. Either of the learning method can be utilized for on-line applications and can be trained off-line or on-line as per requirement.

Table 4.15: Learning performance comparison for LSLM and RLSFF

Parameter	LSLM	RLSFF
Number of Epoch for Training	About 120-140	About 30-40
Learning Computation	Less	Higher
Comparative Accuracy Reached with Chebyshev Expansion Order	4	3

4.4.5.2 Performance

The performance of pattern recognition based fault classification scheme using ChNN for series compensated transmission line can be compared from Table 4.8 and Table 4.12 for different compensation levels. The training for the ChNN has been carried out with few of the fault cases generated at 50% compensation level. Therefore, highest order of accuracy can be observed at this compensation level for either learning method. The RLSFF exhibits superior performance at this level due to preferred changes made during the training process. However, at other unseen compensation levels, the performance of the RLSFF method varies more as compared to LSLM method. Variation in performance hints over-fitting of the ChNN weight matrix during training to the learning cases. The LSLM exhibits a consistent performance for various levels of the compensation levels. However, it is worth to note here that the performance of the ChNN with either learning method is better than most of the cited methods in the literature.

A clear variation in performance accuracy can also be seen for different types of faults from Table 4.9 and Table 4.13. Performance of the LSLM trained ChNN is superior for all types of faults except L-L-L-g fault. However, the possibility of the three phase fault is least in the power transmission system and therefore, the LSLM method found to be better over RLSFF in this analysis.

4.5 APPLICATION OF MLPNN FOR PATTERN RECOGNITION BASED FAULT CLASSIFICATION

MLPNN is one of the preferred AI tool for classification tasks in recent years. It is well known that, MLPNN are capable of extract features from the line current and voltage waveforms, that helps in fault classification [102]. Therefore, the MLPNN has been applied for fault classification in this work to evaluate its performance with respect to the ChNN.

A three-layer structure (one hidden layer) of the MLPNN has been chosen for this non-linear task. Involvement of the phase in fault is identified by a MLPNN for each phase (Figure 4.16). A separate MLPNN is employed to investigate the involvement of the ground with zero sequence current as input as shown in Figure 4.16. Identical training and testing cases have been applied for MLPNN based classification as was used with ChNN.

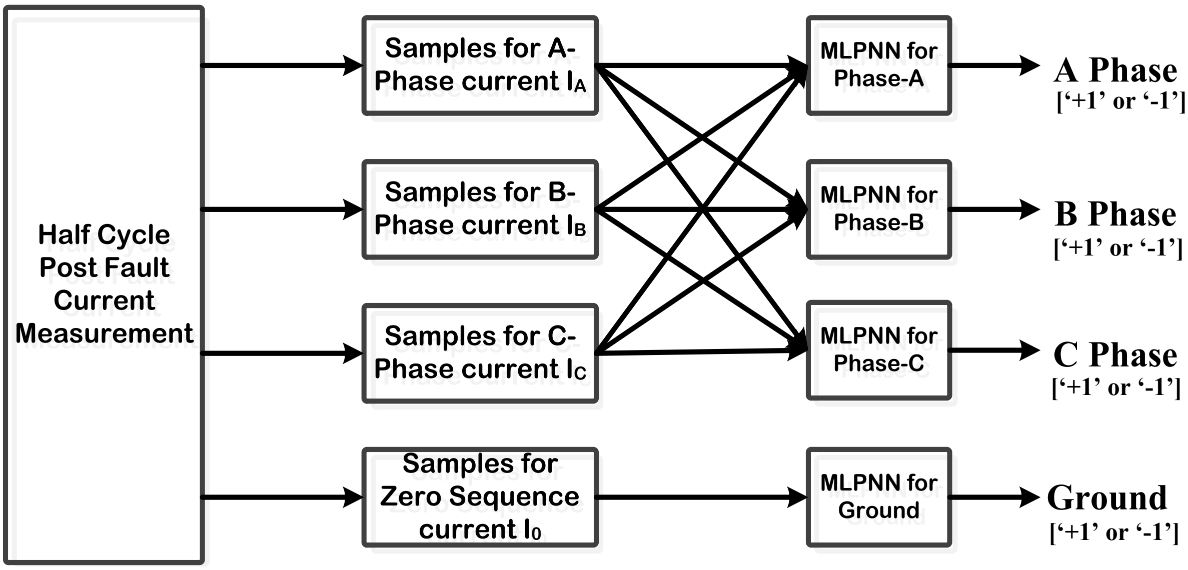

Figure 4.16: Pattern recognition based fault classification scheme by application of MLPNN

The number of neurons in the hidden layer largely affects the non-linear mapping and classification capability of the MLPNN. Therefore, investigations have been made to find out the most suitable architecture of MLPNN to be used in this work. Table 4.16 describes the performance of the scheme with various numbers of neurons in the hidden layer. With 40 input and single output node (for each MLPNN), the investigation has been made by varying the number of neurons in the hidden layer from 8 to 24. Overall accuracy is found to be superior with 17 hidden layer neurons as shown in Table 4.16.

Table 4.16 : Performance of MLPNN with different architecture

No. of Neurons in hidden layer	Accuracy
8	95.34885 %
12	94.1588 %
16	96.95184 %
17	97.34185 %
18	97.05783 %
19	96.66667 %
20	96.18245 %
24	95.67566 %

Overall performance of the MLPNN based scheme at different compensation level is shown in Table 4.17. It can be seen from this table that, the performance of the MLPNN for fault classification is lower than that of ChNN for all levels of compensations. However, MLPNN exerts good performance for 50% compensation at which it is trained. Performance at lower compensation of 25% is also comparable with 50%. A large reduction in the performance can be observed for higher compensation level of 75%. This is due to the fact that a large variation in wave shape is observed at this compensation level due to inclusion of high-frequency oscillations.

Table 4.17: Fault classification accuracy with MLPNN for direct pattern recognition scheme

Compensation Level	Numbers of Test Cases	Fault Type Detection Errors	Accuracy
25%	19200	352	98.17%
50%	15600	214	98.63%
75%	19200	868	95.48%
Total	**54000**	**1434**	**97.34%**

Table 4.18 gives the performance accuracy for different types of faults. Performance of the scheme can be considered to be relatively poor for single line to ground fault and triple line to ground fault. Moreover, the performance is inferior for all types of faults compared to that obtained with ChNN based scheme. Table 4.19 gives the performance of the scheme for different fault distanes at different compensation levels.

Table 4.18: Performance of the MLPNN based fault classification scheme for different types of faults

Type of Fault	Numbers of Test Cases	Fault Classification Errors	Accuracy
L-g	16200	428	96.17%
L-L-g	16200	400	97.53%
L-L	16200	457	97.18%
L-L-L-g	5400	149	94.48%
Total	**54000**	**1434**	**97.34%**

Table 4.19: Performance of the MLPNN based fault classification scheme at various fault location

Fault Distance In Km	25% Series Compensation			50% Series Compensation			75% Series Compensation		
	Test cases	Errors	Accuracy	Test cases	Errors	Accuracy	Test cases	Errors	Accuracy
Before Compensator									
60	2400	54	97.75	1500	17	98.87	2400	75	96.88
120	2400	75	96.88	2400	34	97.73	2400	25	98.96
138	2400	33	98.63	1500	17	99.29	2400	26	98.92
147	2400	32	98.67	2400	14	99.42	2400	21	99.13
After Compensator									
153	2400	11	99.54	2400	22	99.08	2400	155	93.54
162	2400	12	99.50	1500	24	99.00	2400	177	92.63
180	2400	50	97.92	2400	40	97.33	2400	210	91.25
240	2400	85	96.46	1500	46	96.93	2400	179	92.54
TOTAL	**19200**	**352**	**98.17%**	**15600**	**214**	**98.63%**	**19200**	**868**	**95.48%**

4.6 APPLICATION OF SVM FOR PATTERN RECOGNITION BASED FAULT CLASSIFICATION

SVMs are binary classifier based on statistical learning theory resulting from the development of ANN and its combination with the optimization, kernel theory and generalization theories [85]. The SVM maps its input space into a high-dimensional dot product space called the feature space for classification. An optimal hyper plane is determined by using a suitable optimization theory in the feature space to maximize the generalization ability of the classifier. The basic SVM operation can be found as ready reference in Section 3.8 of the thesis.

In this work, the classification task is highly non-linear in nature due to the presence of series compensation and the kernel based SVM has been applied for the classification task. The classified data is mapped onto a high-dimensional feature space with the help of 'kernel function' [103] where the linear classification is possible. Specifically, in this work RBF kernel has been used. The RBF has is comparatively less sensitive to classification parameters which influence the complexity of the SVM model. Furthermore, reduction in numerical computation makes RBF a better choice than the other kernel functions [99].

The fault classification scheme shown in Figure 4.17 uses a cluster of four SVMs (one each for phase and ground) as described in the MLPNN based fault classification scheme in the previous section. The SVMs used for this method has been trained with the identical fault data set as given in Table 4.3. The identical test set of 54000 fault cases have also been applied for performance investigation of this scheme.

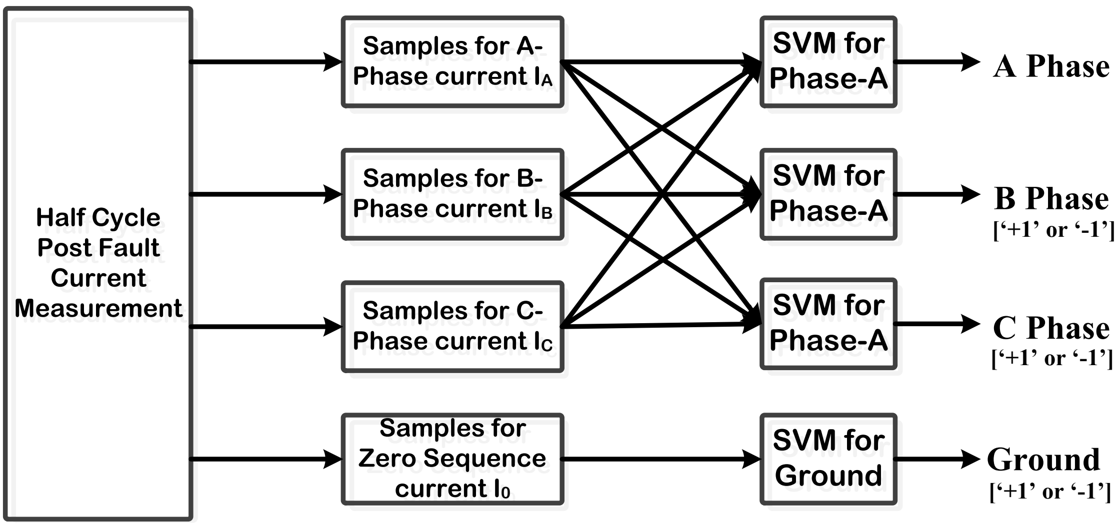

Figure 4.17: SVM pattern recognition based fault classification scheme

When a RBF is selected as kernel function, two parameters (the error penalization constant C and the kernel parameter (γ) have to be set to tune the classification algorithm. The classification accuracy largely depends on selection of the value of C and γ for classification. It is not known beforehand, which values for them are the best choices for the problem at hand. So some 'parameter search' must be required to identify the optimal values for these parameters. Those are the optimal values of these parameters for which the classifier can accurately predict the output for unknown data after training, i.e. testing data. A common way to ensure acceptable performance is to separate the training data into two parts of which one part is considered to be unknown in training the classifier. Then the prediction accuracy on this set can more precisely reflect the performance of classifying the unknown data. By this method, higher level of accuracies can be achieved without sacrificing the generalization ability. This method is called ‘cross-validation’.

The SVM in this method has been implemented with Lib-SVM [104] in windows environment. The cross validation performance for a data set of 1000 fault cases is shown in Table 4.20. These 1000 fault cases have been arbitrarily chosen from 3720 fault cases for 50% compensation level with 5 Ω fault resistances. Identical values of these parameters have been used for all four SVMs used in this method. From Table 4.20 it is seen that by using ‘C=100’ and ‘γ=0.00045’, the best performance is obtained and these parameters have been used in this work.

Table 4.20: ‘Cross validation’ performance investigation for different values of 'C' and "γ"

C	γ	Accuracy
10	0.1	94.37%
50	0.01	95.23%
100	0.001	96.63%
500	0.001	95.08%
100	0.1	96.02%
100	0.001	96.93%
100	0.00045	98.13%

A half cycle post fault data (40 samples at sampling frequency of 4 kHz) of three phase currents have been taken for the analysis. A SVM input vector has been derived from these samples as in equation (4.5). This feature vector is then subjected to the cluster of SVMs for classification as shown in Figure 4.17. The performance of the SVM based method has been extensively tested with the 54000 test cases. Table 4.21 shows the performance of the SVM based scheme. In the case of SVM also, the performance for the compensation level of 50%, for which the SVMs are trained is found to be better than those obtained at other compensation levels.

Table 4.21: Fault classification accuracy with SVM for direct pattern recognition scheme

Compensation Level	Numbers of Test Cases	Fault Type Detection Errors	Accuracy
25%	19200	419	97.85%
50%	15600	257	98.35%
75%	19200	614	96.80%
Total	**54000**	**1290**	**97.61%**

Performance of the SVM based scheme for different types of faults is shown in Table 4.22. Table 4.23 shows the performance of the scheme at different fault distances corresponding to 25%, 50% and 75% compensation levels. A detail analysis and comparison of these results are provided below.

Table 4.22: Performance of the SVM based fault classification scheme for different types of faults

Type of Fault	Numbers of Test Cases	Fault Classification Errors	Accuracy
L-g	16200	268	98.35%
L-L-g	16200	412	97.46%
L-L	16200	312	98.07%
L-L-L-g	5400	298	94.48%
Total	**54000**	**1290**	**97.61%**

Table 4.23: Performance evaluation of the SVM based pattern recognition based fault classification scheme at various fault location with different levels of compensation

Fault Distance In Km	25% Series Compensation			50% Series Compensation			75% Series Compensation		
	Test cases	Errors	Accuracy	Test cases	Errors	Accuracy	Test cases	Errors	Accuracy
Before Compensator									
60	2400	74	96.91%	1500	38	97.47%	2400	118	95.08%
120	2400	57	97.62%	2400	41	98.29%	2400	83	96.54%
138	2400	43	98.25%	1500	28	98.13%	2400	68	97.16%
147	2400	42	98.28%	2400	31	98.71%	2400	58	97.58%
After Compensator									
153	2400	39	98.38%	2400	23	99.04%	2400	56	97.66%
162	2400	47	98.04%	1500	39	97.40%	2400	68	97.16%
180	2400	48	98.00%	2400	29	98.79%	2400	72	97.00%
240	2400	69	97.12%	1500	28	98.13%	2400	91	96.20%
TOTAL	**19200**	**419**	**97.61%**	**15600**	**257**	**98.35%**	**19200**	**614**	**96.80%**

4.6.1 Comparison of ChNN, MLPNN and SVM for Pattern Recognition Based Fault Classification of Series Compensated Transmission Lines

A comparative plot for obtained accuracies at different fault length for ChNN, MLPNN and SVM based schemes is shown in Figure 4.18. As mentioned in Section 4.4, performance of the ChNN with LSLM algorithm learning is preferable over RLSFF, and as a result, for comparison of ChNN with MLPNN and SVM, the ChNN with LSLM learning has been used.

In case of linearly non-separable classes i.e. the problem considered in this chapter, both SVMs and ChNN apply non-linear projection into higher-dimensional space. In case of ChNN, Chebyshev functional expansion serves the purpose while, a kernel function is used for the same purpose with SVM. MLPNN produces non-linear classification boundary by addition of hidden layers in the structure. However, inclusion of hidden layers will increase training and classification complexity, computation burden and time required for training.

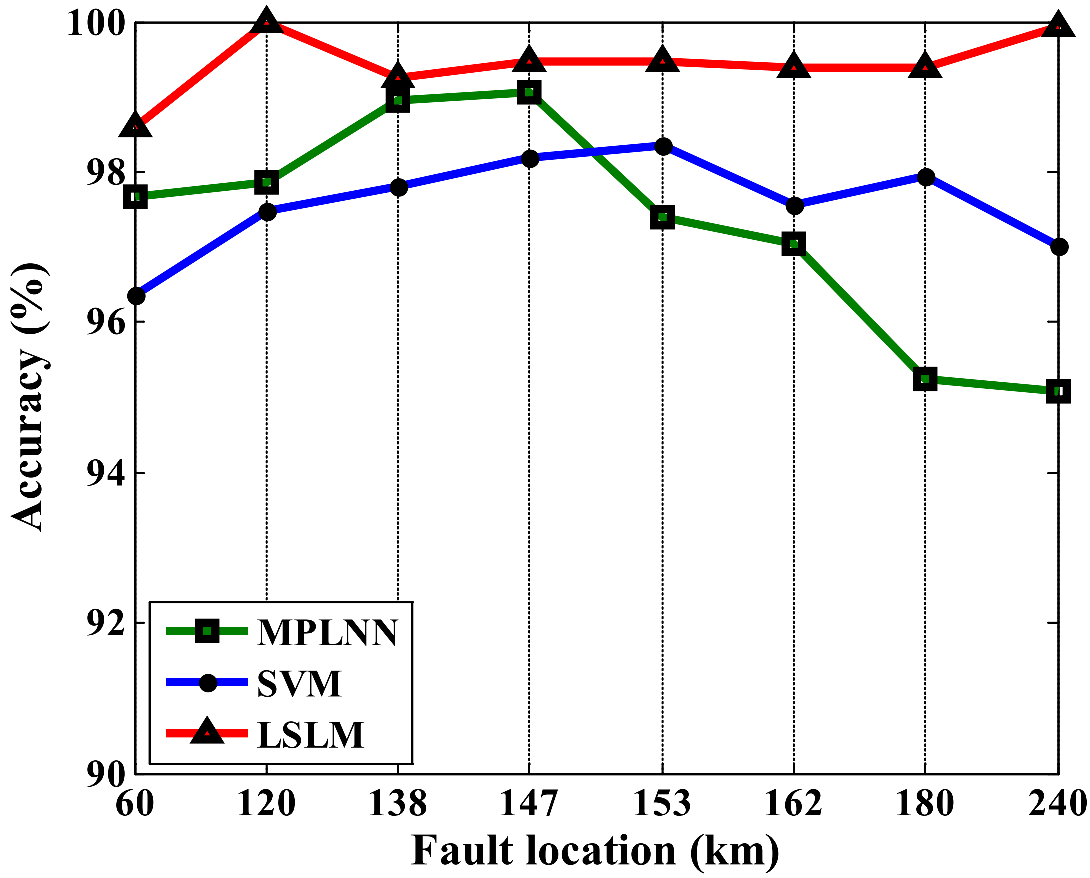

Figure 4.18: Comparison of ChNN, MLPNN and SVM for series compensated transmission line fault classification at different fault locations

The main difference to notice between SVM, MLPNN and the ChNN is the different optimization criterion. For ChNN, MLPNN and SVM, the form of the functions learned by them are typically the same. For example, a single hidden layer neural network uses exactly the same form of model as an SVM. That is:

$$Out(x) = \sum_{n=1}^{i} W_n x(i) * f(i) \qquad (4.27)$$

Where, the x = input vector and f = non-linear function.

The nonlinear functions will also have some parameters. By learning, the classifier defines number of non-linear functions, parameters for these functions and weights. The difference between SVM and ANN lies in deciding these parameters. The SVM tries to achieve this goal by defining the optimal separating hyperplane which maximizes the margin (in the feature space), while the ChNN usually tries to minimize the empirical risk associated with some loss function, typically the mean squared error.

In ChNN, the patterns are linearly separable in projected higher dimensional space due to Chebyshev expansion. This eliminates the possibility of theoretical weakness of 'local minima' of the classical MLPNN system. This gives advantage to the ChNN over MLPNN.

SVM training requires the solution of the Lagrangian dual problem. This is a quadratic optimization problem, in which the number of variables is very large, i.e., equal to the number of training samples. On the other hand, the ChNN is a single layer structure and requires calculations corresponding to basic expansions only. This reduces the computational time during learning process. Therefore, the training of the SVM is more complex than ChNN.

Another important factor should be noted here. The classification performance of the SVM largely depends on the selection of the kernel function and its associated parameters (in our application 'RBF' kernel and 'C' and 'γ'). A preferred combination of the parameters is essential for every new application of the SVM. These parameters are quite often unknown and mostly found only by a severe exercise with experiments and/or prior knowledge. The MLPNN is highly sensitive to its structure. Overall non-linear processing capability of the MLPNN is largely dependent on number of hidden layer and numbers of neurons in these layers. Being a single layer neural network, ChNN is free from design concerns. Moreover, the only classification variable that affects the performance of the ChNN is the order of Chebyshev expansion. That can be found easily with performance investigation with sample fault cases. Therefore, from this discussion, ChNN can be considered as preferable classifier for protection requirements.

4.7 EFFECT OF CURRENT TRANSFORMER SATURATION

In all the above studies, it has been assumed that the faulted current waveform is exactly reproduced at the relay terminal (i.e. the effect of the CT was neglected). However, under fault condition, it is possible that the CT of the protective relay may saturate and can no longer reproduce the faulted current waveform at the relay terminal exactly. Therefore, it is necessary to assess the performance(s) of the algorithm(s) under CT saturation. Now, in the above results, the performance of the ChNN based direct pattern recognition scheme with LSLM training algorithm was found to be the best (without considering the effect of CT saturation). Hence, in this section, the performance of this algorithm under CT saturation is investigated.

Now, the saturation of the CT is avoided by properly selecting the turns ratio, burden, and CT accuracy class. As long as the product of the secondary current and burden impedance does not exceed the saturation or knee point voltage of the CT, the CT will operate in the unsaturated region and its performance will be satisfactory for the AC component.

For this study, all 54000 fault cases used for testing the algorithm (Section 4.4.4) are re-simulated in PSCAD with current transformer. The CT has been modelled in PSCAD with Jiles-Atherton (JA) model [105, 106]. The JA-type simulation provides flexibility to make cross-sectional area of the coil relatively large, that facilitate a relatively large current. The CT is simulated as per following parameters [107] [108]:

i) CT Type: C Type
ii) CT Ratio: 2000/5 A
iii) CT selected: 5P20
iv) CT saturation voltage: 60 V

The performance of the algorithm (ChNN based direct pattern recognition scheme with LSLM training) with consideration of CT saturation for all 54000 fault cases (described in Section 4.4.4) is shown in Table 4.24.

Table 4.24: Fault classification accuracy of the developed algorithm with inclusion of CT in measurement circuit

Compensation Level	Numbers of Test Cases	Fault Type Detection Errors	Accuracy
25%	19200	106	99.45 %
50%	15600	29	99.81 %
75%	19200	186	99.03 %
Total	**54000**	**321**	**99.41 %**

It is evident from Table 4.8 and Table 4.24 that, the effect of CT saturation is very nominal (99.41 compare to 99.44) for fault classification application. As per the IEEE Standard C37.110 – 1996, the value of current for saturating CT has to be somewhere between 6 to 20 times that of rated current. In case of line protection, the chances of obtaining such a high current can only be for solid faults close to the relay location or just after the compensator. Therefore, for all practical purposes the CT saturation is not an issue of concern. Owing to this, no further investigation has been made in this thesis regarding the impact of CT saturation.

Furthermore, it is worth to note here that with recent trends in current sensing technology being adopted in power system i.e. use of Optical Current Transformer (OCT), CT saturation issue will not be there.

4.8 EFFECT OF TRANSPOSITON ON THE DEVELOPED ALGORITHM

To check effect of the transposition to the developed algorithm, a fault data set has been simulated on the same system of Figure 4.1 without transposition of the transmission line. This line has been simulated in PSCAD with Frequency Dependent Phase model with identical transmission line parameters given in Appenix – A (converted for the model). Typical steady state current waveform corresponding to line loading angle of 20° for untransposed and transposed transmission line are shown in Figure 4.19 (a) and (c). Figure 4.19 (b) and (d) show three phase current waveforms for the same A-g fault at 80% of the total transmission line length for untransposed and transposed lines. A visible difference can be seen from these figures.

Untransposed

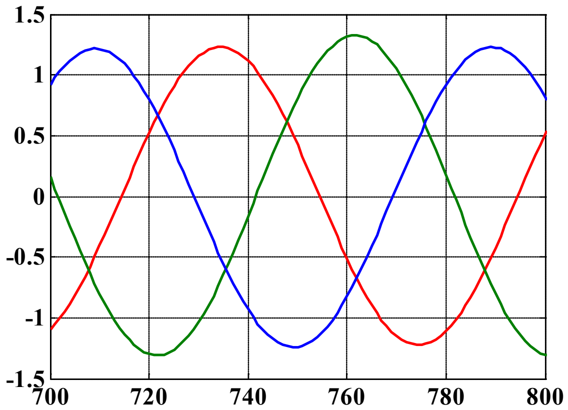

Figure 4.19 (a)

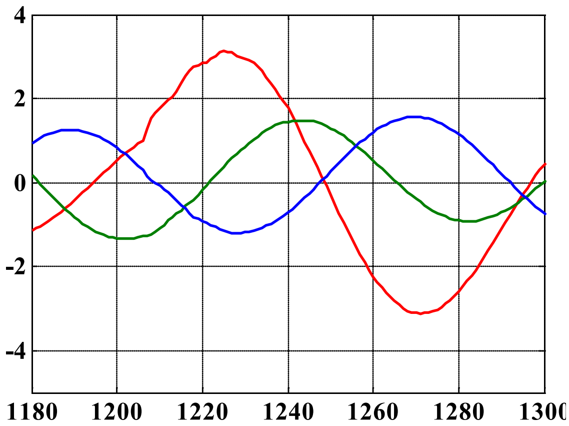

Figure 4.19 (b)

Figure 4.19: (a) and (b) Typical three phase waveform and fault current waveform without transmission line transposition.

Transposed

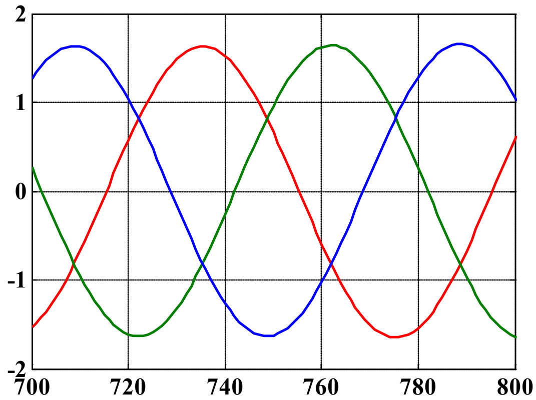

Figure 4.19 (c)

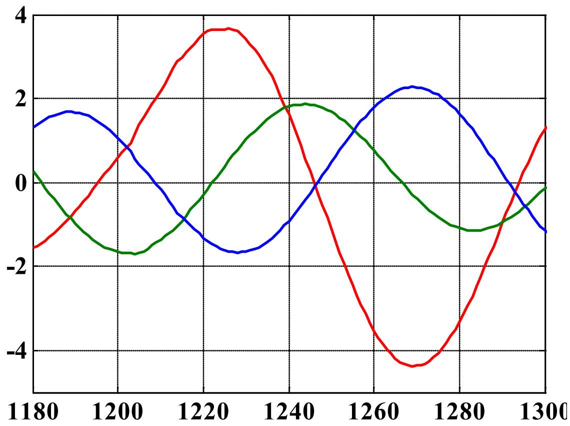

Figure 4.19 (d)

Figure 4.19: (c) and (d) Typical three phase waveform and fault current waveform without transmission line transposition.

The performance of the fault classification algorithm (ChNN based direct pattern recognition scheme with LSLM training) for untrasnposed line has been investigated on a fault data set of 19200 fault patterns corresponding to 25% compensation level (as described in Table 4.8). The results obtained are compared with already available results with consideration of fully transposed transmission line and the results are shown in **Error! Not a valid bookmark self-reference.**.

Table 4.25 : Comparison of results with properly transposed and untransposed transmission line fault data

Fault Distance in % of total line length	Number of Test Cases	Untransposed Transmission Line		Transposed Transmission Line	
		Fault Type detection Error	Accuracy	Fault Type detection Error	Accuracy
Fault at 20%	2400	15	99.37%	15	99.37%
Fault at 40%	2400	1	99.95%	0	100.0%
Fault at 46%	2400	20	99.54%	19	99.20%
Fault at 49%	2400	24	99.50%	24	99.00%
Fault at 51%	2400	17	99.16%	15	99.37%
Fault at 54%	2400	17	98.95%	15	99.37%
Fault at 60%	2400	11	99.29%	10	99.58%
Fault at 80%	2400	12	99.25%	5	99.79%
Total	**19200**	**117**	**99.37%**	**103**	**99.46%**

From Table 4.25 it is observed that with untransposed transmission line, the performance of the algorithm degraded marginally. This can be improved with inclusion of some of these cases during ChNN learning. Therefore, it can be concluded that; the effect of untransposed line on developed algorithm is negligible and no further investigation has been made for untransposed transmission line in this thesis. Further, the performance of the algorithm can be improved further for untransposed lines by including appropriate number of fault patterns during the traning process. However, this option has not been pursued in this thesis.

4.8.1 FURTHER INVESTIGATION

For investigating the performance of the ChNN based algorithm further, a second test system as shown in Figure 4.20 has been considered [[109, 110]].The system consists of three transmission lines and two generators. The middle 100 km transmission line (between bus X and bus Y) carries a fixed series compensator at the center of the line. The transmission line is protected by a relay at bus X. The system data is given in Table 4.26.

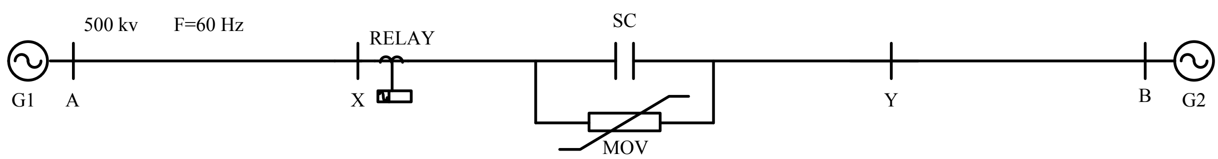

Figure 4.20: Three line transmission system

Table 4.26: System parameters

Transmission Line (Each line)		
Length	100	Km
Voltage	500	kv
Frequency	60	Hz
Positive sequence impedance	0.0185 + j0.3766	Ω/km
Zero-sequence impedance	0.3618 + j1.2277	Ω/km
Positive-sequence capacitance	0.22789	MΩ*km
Sources		
Frequency	60	Hz
Positive sequence impedance	1.43 + j 16.21	Ω
Zero-sequence impedance	3.068 +j 28.746	Ω/km

Initially, the required test cases were generated covering various system and fault conditions. For this system, the variations considered in the system parameters are:

i) Compensation level (X_C) : 25%, 50%, 75% of the total line reactance

ii) Source impedances : Three combinations of generator impedances Z_{SG1} and Z_{SG2} (100%-100%, 125%-75% and 75%-125% of GBI) (Z_{SG1} is impedance of generator G1 and Z_{SG2} is of generator G2 of Figure 4.1)

iii) Line loading angles (δ) : 10˚, 20˚, 30˚.

For each of these 27 system conditions, following fault parameter variations are considered.

i) Fault resistance (Rf) : 0 Ω, 5 Ω, 25 Ω, 50 Ω;

ii) Fault inception angle (FIA) : 0˚, 45˚, 80˚, 115˚

iii) Fault distance (L) : 10 km, 25 km, 45 km, 55 km, 75 km, 90 km

iv) Fault type : All ten types (L-g, L-L-g, L-L, L-L-L-g)

Thus, a total of 1280 fault combination have been generated for a specific system condition [(4(Rf) * 4(FIA) * 6(L) * 10(fault type) = 960]. With 27 system conditions, a total of 25920 fault cases thus have been generated for this study. Out of these 25920 fault cases, only 3240 (only 12.5%) fault cases have been used for training the ChNN. The details of the training cases are shown in Table 4.27.

Table 4.27: Fault and system parameters considered for training

Parameters								**Number of Fault Cases**
Xc	**Z_{SG1} In % of GBI**	**Z_{SG2} In % of GBI**	**δ**	**R_f (Ω)**	**FIA**	**L (km)**	Fault Type	
50%	100	100	10˚,20° & 30˚	0, 5 & 50	0, 45 & 115	10, 45, 55, 90	All ten types of fault considered	1080
50%	125	75						1080
50%	75	125						1080
Total Fault Cases								**3240**

The performance of the developed algorithm has been investigated on the remaining 22680 cases. The results are shown in Table 4.28, Table 4.29 and Table 4.30. From these tables again it is observed that for this second test system also, the developed algorithm attains quite a high level of accuracy. Table 4.28 gives the performance of the developed scheme corresponding to different compensation levels. Accuracies at all the levels of compensation are above 99% and comparable with accuracies obtained for the previous

Table 4.28: Fault classification accuracy at different compensation levels for the second system

Compensation Level	Numbers of Test Cases	ChNN Trained with LSLM algorithm	
		Fault Type Detection Errors	Accuracy
25%	8640	37	99.57 %
50%	5400	14	99.74 %
75%	8640	70	99.19 %
Total	**22680**	**121**	**99.46 %**

Table 4.29: Accuracy for different fault types for the second system

Type of Fault	Numbers of Test Cases	ChNN Trained with LSLM algorithm	
		Fault Classification Errors	Accuracy
L-g	6804	10	99.85 %
L-L-g	6804	35	99.48 %
L-L	6804	38	99.44 %
L-L-L-g	2268	38	98.32 %
Total	**22680**	**121**	**99.46 %**

Table 4.30: Detailed break-up of fault classification accuracy for the second system

Fault Distance In Km	25% Series Compensation			50% Series Compensation			75% Series Compensation		
	Test cases	Errors	Accuracy	Test cases	Errors	Accuracy	Test cases	Errors	Accuracy
Before Compensator									
10	1440	7	99.51 %	630	2	99.68 %	1440	17	98.82 %
25	1440	2	99.86 %	1440	3	99.79 %	1440	2	99.86 %
45	1440	6	99.58 %	630	0	100.00 %	1440	9	99.38 %
After Compensator									
55	1440	12	99.17 %	630	4	99.37 %	1440	21	98.54 %
75	1440	7	99.51 %	1440	3	99.79 %	1440	13	99.10 %
90	1440	3	99.79 %	630	2	99.68 %	1440	8	99.44 %
TOTAL	**8640**	**37**	**99.57%**	**5400**	**14**	**99.74%**	**8640**	**70**	**99.19%**

system (Table 4.8). Similarly, comparison of Table 4.29 (4.30) with Table 4.9 (4.10) shows that the performance of the developed algorithm is almost at the same level for both these test systems. Further, the fault classification for the second system has also been carried out with SVM and an overall accuracy of 97.32% has been obtained. Therefore, for this system also, the ChNN bases scheme outperforms the SVM.

As the performance of the ChNN based scheme is found to be almost at the same level for different test systems, in the subsequent chapters, the performances are investigated only on one test system.

4.9 COMPARISON WITH OTHER METHODS IN THE LITERATURE

A comparison of the performance obtained by ChNN (trained with LSLM technique) with some of the other reported methods in the literature are shown in Table 4.31. As can be seen from this table, the developed method gives a better accuracy than those obtained by the other methods mentioned in Table 4.31 even with a larger testing data set. Moreover, ChNN is easy to design as compared to fuzzy set [96], neuro-fuzzy system [111] or SVM [22] [25]. Absence of classification parameters makes it superior than other classifiers.

Moreover, the developed scheme gives a similar level of accuracy with variation in system and fault parameter. Therefore, it can be considered to be immune to these variations.

Table 4.31 : Performance comparison with some other methods given in the literature

Reference	Description	Method	Number of Test Cases	Accuracy
[96]	for Uncompensated Line	Fuzzy Logic	2400	98.75%
[112]	for Uncompensated Line	Wavelet Transform and ANN	276	99.26%
[22]	for fixed series compensated transmission line	Support Vector Machine	25200	98.70% (Full Cycle sample) 98.186 (Half cycle sample)
[25]	for Controllable compensated Transmission Line	SVM	200 (500 training)	95-to-97% (Half Cycle Samples)
[111]	for fixed series compensated transmission line	Wavelet Transform and Fuzzy-Neuro System	21036	99.30 (One cycle Samples)
Proposed ChNN based Pattern Recognition algorithm	**for fixed series compensated transmission line**	**ChNN with LSLM training**	**54000**	**99.44% (Half cycle samples)**

4.10 CONCLUSION

In the present chapter, two different fault classification schemes have been presented. The first one utilizes Discrete Wavelet Transform (DWT) as signal pre-processor along with ChNN used as a classifier. The second scheme applies ChNN as direct pattern recognition tool. Moreover, two different ChNN learning algorithms have been compared on the basis of the application performance.

The central theme of all these algorithms is to identify the spectral and amplitude changes in the fault currents. In the first method, this objective is accomplished by time-frequency investigation of current waveforms with help of DWT. The ChNN has been presented as an advanced classifier for DWT induced features.

However, the fact that the complexity of the two-stage fault classifier increases the operational time leads towards development of absolute pattern recognition based fault classification scheme using ChNN. The performance comparison of ChNN based fault classification scheme has been presented for two ChNN training algorithms, namely RLSFF and LSLM.

The RLSFF technique has been found to have faster convergence during training and takes necessary shape quickly, but, over-fitting to the training patterns makes it less effective. However, the ChNN with LSLM learning method was found to be better than the ChNN with RLSFF method for series compensated line fault classification application without considering the effect of CT. Further, even in the presence of an appropriately designed CT, the performance of the ChNN with LSLM learning method degrades very marginally. Lastly, the performance of this algorithm has also been investigated for untransposed line and in this case also, the performance of the algorithm has been found to be almost at the same level.

CHAPTER 5: IMPROVED FAULT ZONE IDENTIFICATION SCHEMES FOR SERIES COMPENSATED TRANSMISSION LINE

Fault detection, fault classification and fault location are three main components of any transmission line protection scheme. Inclusion of the compensator in the fault circuit alters system parameters and hence the impedance measurement subroutine of the distance based relaying scheme. Therefore, the effect of the compensator needs to be considered when included in the fault circuit. Hence, identification of fault point with respect to the compensator (fault zone identification) becomes pre-requisite for fault impedance calculations. This chapter presents improved fault zone identification schemes for series compensated transmission line in terms of accuracy and speed.

5.1 INTRODUCTION

Inclusion of SC in a transmission line improves power transfer capability, increases accuracy in regulation, damp inter-area power oscillation and moderate sub-synchronous resonance to improve transient stability. However, in the eventuality of fault circuit encompassing the series compensator, operating conditions for the protective relay become unfavorable as discussed in Chapter 2. Therefore, the positive sequence impedance measured by the traditional distance relay no longer is the genuine indicator of the fault location. The impedance calculation needs to be changed according to the series compensator equivalent operating impedance in the case when the compensator is part of the fault circuit. This necessitates the knowledge of the inclusion of the compensator in the fault circuit (fault zone identification) for faithful fault impedance calculation [5-8].

As being an important aspect of series compensated transmission line protection, efforts have been made in the literature on the fault section identification. A travelling wave based algorithm using wave equation, including non-linearity of compensation was developed in [35]. A decision tree based approach for fault zone identification scheme for fixed series compensated transmission line is presented in [113].

Many recent developments in the field of series compensated transmission line protection consider fault zone identification as a problem of pattern recognition, with the help of a signal-processing tool. Use of SVM as a pattern recognition tool for fault classification and fault zone identification has been utilized by authors of [25].

Use of WT for fault-zone identification is proposed in [114]. An algorithm developed in [56] for the fault zone detection uses DWT and SVM.

From these available literatures, it can be noticed that most of the available algorithms require at least one cycle of data after fault inception for proper zone identification. All developed algorithms in this chapter utilize only half cycle post fault data for zone identification. In fault condition, it is fairly possible that proper voltage signal may not be available. Thus all developed algorithms use three phase measured currents only at the relaying point. This in turn reduces the voltage related measurements and computations.

5.2 APPLICATION OF DISCRETE WAVELET TRANSFORM AND CHEBYSHEV NEURAL NETWORK FOR FAULT ZONE IDENTIFICATION

In this work, fault zone identification algorithm has been developed with DWT as feature extraction tool and ChNN as a classifier. The developed fault section identification algorithm has been tested on a two area transmission system with mid-line fixed capacitor compensation (shown in Figure 4.1) with a large number of test set of 54000 cases as described in Section 4.3.4.

5.2.1 Fault Zone Identification

The identification of fault zone and classification of faulted phases on a transmission line are essential for relaying decisions. It is well established that for a series compensated transmission line, the magnitude and spectral components of the fault current as seen by the relay get changed following inclusion or exclusion of the series compensator in the fault circuit. These changes are observed as the compensator impedance interferes with the spectra of the fault-induced transient.

As an example, the three phase current waveforms for an AB-g fault at 49% and 51% of the total line length (i.e. fault at either side of the compensator) with identical fault and system parameters are shown in Figure 5.1 and Figure 5.2 respectively. The following parameters have been chosen for both these faults: fault inception angle (FIA) = 45˚; fault resistance (R_f) = 5 Ω and line loading angle (δ) = 30˚.

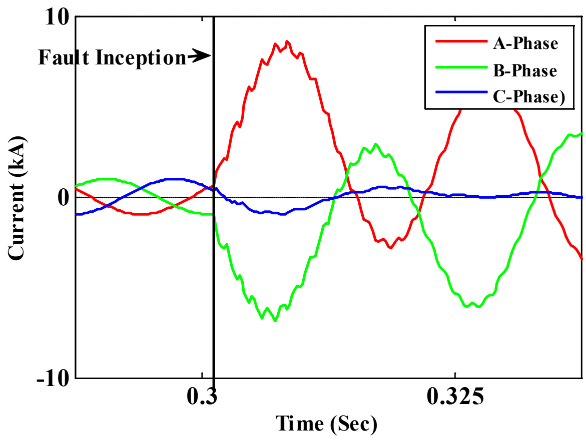

Figure 5.1: Fault currents for an A-B-g fault at 49% of the line length

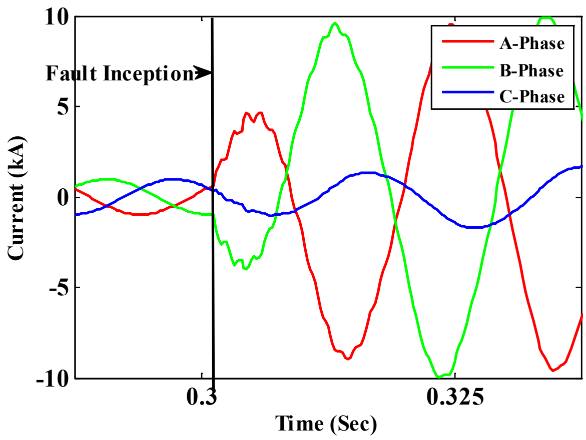

Figure 5.2: Fault currents for an A-B-g fault at 51% of the line length

It is observed from Figure 5.1 and Figure 5.2 that, both the amplitude and frequency characteristics of the fault current change with the position of the fault vis-à-vis the series capacitor. The proposed methodology in this section is based on the detection of these changes to identify the participation of the SC in the fault circuit. In this scheme, half cycle post fault current signals measured at the relaying end are first subjected to a DSP tool to generate the feature vector that enhances the pattern for classification. The feature vectors for all three phases are then subjected to a classifier to determine the position of the fault with respect to the compensating device.

The schematic block diagram of the proposed two-stage scheme is shown in Figure 5.3. The technique consists of two stages. In the first stage a suitable DWT technique is applied to extract the attributes from the three line currents. In the second stage, the extracted features are expanded with Chebyshev expansion and then passed through a ChNN to decide the fault zone. The ChNN gives an output close to '0' for a fault in the first segment of the line (before the compensating capacitor) and '1' for a fault in the line segment after the compensating capacitor.

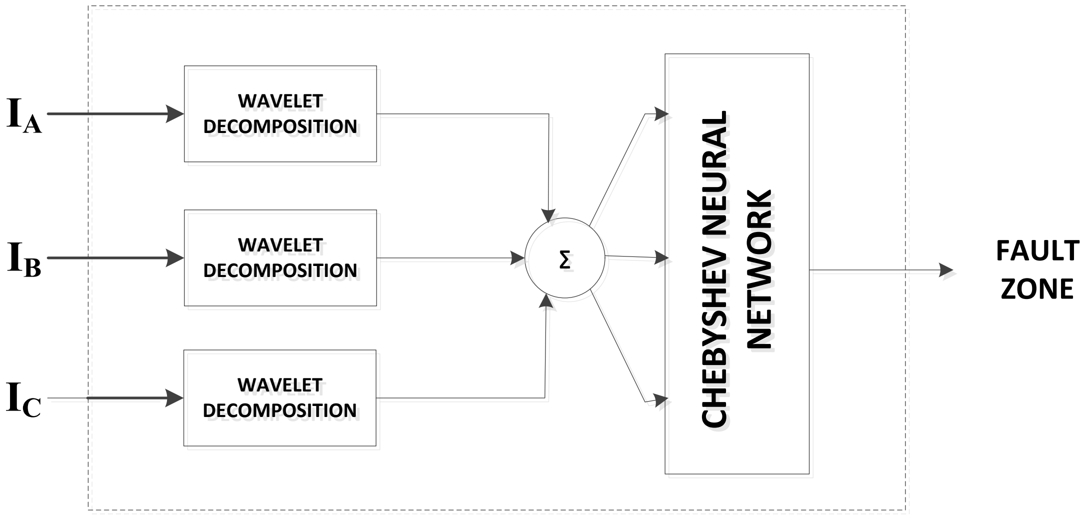

Figure 5.3: DWT and ChNN based fault zone identification scheme

As a fault is a non-stationary phenomenon, the WT is quite suitable for analyzing the faulted signals. A considerable amount of change can be noticed in the amplitude and phase of the fault current as analyzed by the WT. Figure 5.4 and Figure 5.5 show the wavelet coefficients for detail bands on first and second level of decomposition for the waveforms of Figure 5.1 and Figure 5.2 respectively. It can be inferred from these two figures that, the WT enhances the features of the measured waveforms to make the fault zone identification process easier.

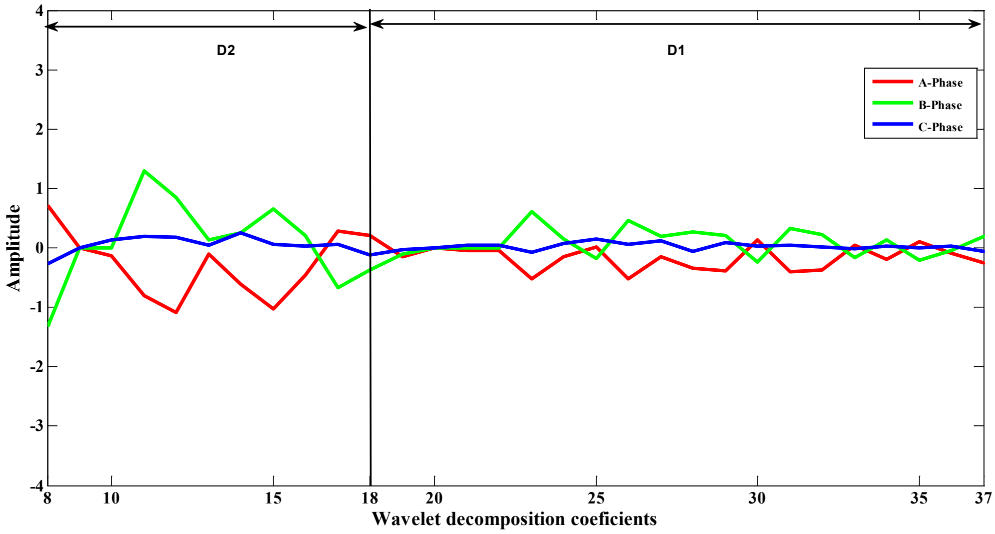

Figure 5.4: First and second level WT details of the measured waveforms for the faulted waveform given in Figure 5.1

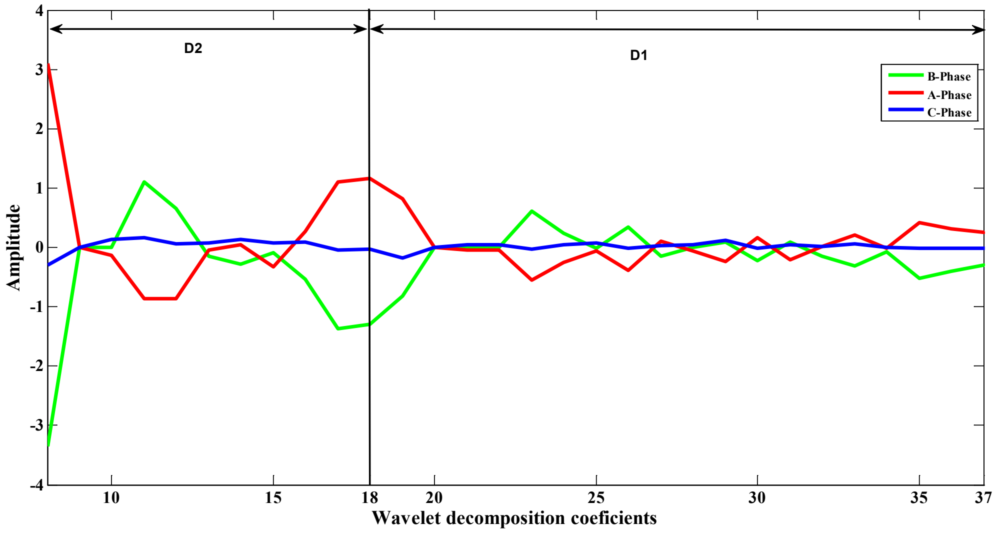

Figure 5.5: First and second level WT details of the measured waveforms for the faulted waveform given in Figure 5.2

5.2.2 ChNN Based Classification

The schematic diagram of the proposed algorithm for fault zone identification with the help of DWT and ChNN is shown in

Figure 5.3. As already described in Chapter 4, a sampling frequency of 4 kHz has been used in this work. Further, for fault zone identification application, the mother wavelet 'db1' has been found to be best suitable and hence has been used in the present work. Also, different levels of the wavelet decomposition provide information about various signal

frequency components. The minimum number of scaling has an effect on the computations required to decompose the signal. In the present work, the second level decomposition details have been found to be necessary and sufficient for proper classification application.

The decomposed components are expanded with Chebyshev expansion and subsequently fed to a single layer ChNN with single output indicating the involvement/non-involvement of the compensating capacitor in the fault circuit. Numbers of input to the ChNN depend on the degree of Chebyshev expansion. The neural network is trained with a supervised back-propagation learning algorithm with LSLM optimization.

Fault zone identification logic

Initially, discrete wavelet decomposition on the current signals with "db1" mother wavelet with second level of resolution is performed. The produced wavelet decomposition vector 'C' which carries total 2 sub bands (one wavelet sub band and one approximation sub band) is then used as a feature vector for classification with ChNN. The ith element of this decomposition vector can be given as

$$C_p^{dwt} = \frac{1}{n_i}\sum_{j=1}^{n_i} w_{i,j}^2 \tag{5.1}$$

In equation (5.1), p denotes particular phase, n_i is the number of samples in an individual sub band and $w_{i,j}^2$ is the j^{th} coefficient of the i^{th} sub band. The feature vectors for all the three phases (A,B,C) are calculated and are then subjected to ChNN. This DWT feature vector is given by,

$$\boldsymbol{V}^{dwt} = [C_A^{dwt}, C_B^{dwt}, C_C^{dwt}] \tag{5.2}$$

This feature vector is then expanded with Chebyshev functions for generating the Chebyshev vector as,

$$\mathbf{T_{n+1}(x)} = 2x\mathrm{T_n}(x) - \mathrm{T_{n-1}}(x) \tag{5.3}$$

where, n = degree of expansion and x=$\boldsymbol{V}^{dwt}$.

This Chebyshev Vector is then subjected to pre-trained ANN. The ANN identifies the involvement/non-involvement of the compensating device in the fault circuit and accordingly gives the output (0 for fault before capacitor and 1 for fault after capacitor).

5.2.3 Results and Discussion

To decide the appropriate level of Chebyshev expansion for fault zone identification, the proposed scheme has been tested for various levels of Chebyshev expansions. The ChNN has been trained with 5400 fault patterns generated on the system shown in Figure 4.1. The details of these fault patterns are given in Table 5.1. It is to be noted that the number of training patterns shown in Table 5.1 is more than that shown in Table 4.3 (used in fault classification task). This is due to the fact that the discriminative variation in fault currents between a low impedance fault just before compensator and a high impedance fault after the compensator is marginal. Therefore, the ChNN is required to develop classification plane which are adjacent to each other. Thus the number of training cases is higher for fault zone identification problem than that used for fault classification problem. The proposed algorithm is tested over remaining 52200 fault cases out of 57600 fault patterns generated and described in Section 4.3.4. Therefore, none of the fault pattern used during training has been considered for testing.

Table 5.1: System and fault variable used for training patterns

<table>
<tr><th rowspan="2">Case</th><th colspan="7">Parameters</th><th rowspan="2">Number of Test Cases</th></tr>
<tr><th>Z_{G1} %</th><th>Z_{G2} %</th><th>x_c %</th><th>R_f Ω</th><th>FIA</th><th>δ</th><th>L (%)</th></tr>
<tr><td>1</td><td>100</td><td>100</td><td>50</td><td rowspan="5">0, 5 & 50</td><td rowspan="5">0, 45 & 115</td><td rowspan="5">10 & 30</td><td rowspan="5">20%, 40%, 49%, 51%, 60% & 80%</td><td>1080</td></tr>
<tr><td>2</td><td>100</td><td>75</td><td>50</td><td>1080</td></tr>
<tr><td>3</td><td>100</td><td>125</td><td>50</td><td>1080</td></tr>
<tr><td>4</td><td>125</td><td>100</td><td>50</td><td>1080</td></tr>
<tr><td>5</td><td>75</td><td>100</td><td>50</td><td>1080</td></tr>
<tr><td colspan="7">Total Training Cases</td><td></td><td>5400</td></tr>
</table>

To identify the suitable level of Chebyshev expansion for fault zone identification, the training and testing has been performed with identical fault data sets for various levels of Chebyshev expansions. Table 5.2 shows the accuracy of the proposed methodology for fault zone identification for different degrees of Chebyshev expansion in ChNN. The inputs to the ChNN are DWT feature vector generated with equation (5.2). It is evident from the results that, the developed methodology provides highest level of accuracy at 5^{th} order of Chebyshev expansion. Therefore, the fifth order of functional expansion has been utilized in this work. However, overall accuracies at other levels are also comparable with those obtained with other methods reported in the literature [25, 56, 113].

Table 5.2: Accuracy of the DWT and ChNN based scheme for different order of Chebyshev expansions

Order of ChNN	**Accuracy Level Observed at % Level of Compensation**			**Total Accuracy Obtained**
	25%	**50%**	**75%**	
Third	93.53	98.30	96.79	95.90 %
Fourth	93.48	96.66	98.00	96.51 %
Fifth	96.51	98.99	98.17	97.78 %
Sixth	94.64	98.78	97.85	96.86 %
Seventh	95.20	99.76	92.61	95.30 %

As can be seen from the above table, overall fault zone identification accuracy obtained with 5th degree of Chebyshev expansion is 97.78%. The details of accuracies for different levels of compensation and fault types are given in Table 5.3 and Table 5.4 respectively.

Table 5.3: Fault zone identification accuracy at different compensation levels

Level of compensation	Numbers of Test Cases	Fault Zone Identification Errors	Accuracy
25%	19200	670	96.56 %
50%	13800	139	99.90 %
75%	19200	350	98.09 %
Total	**52200**	**1159**	**97.77 %**

From Table 5.3, it can be observed that, the proposed scheme provides excellent results at different levels of compensations. The ChNN acquires quite a necessary characteristic in the classification plane to give excellent results for 50% compensation level, as the ChNN training patterns are obtained at this compensation level. However, a dip in the performance is observed with 25% compensation level. This is due to the fact that, the parameter changes introduced by the compensator at 25% compensation level is of lower order than those at 50% compensation level, for which the ChNN training has been performed. This drawback can be eliminated by introducing few of the training cases corresponding to this compensation level. However, it is worth to notice here that, the accuracy at 25% compensation level is still higher than those obtained by other methods reported in the literature [25, 56, 113].

The breakup of the accuracy according to the type of faults is given in Table 5.4. From this table, the accuracy for LLL-g fault can be observed to be little less as compared to those obtained for other types of faults. However, probability of LLL-g fault is least in the system [20] and the overall accuracy of the proposed system is better than those obtained by other methods reported in the literature [25, 56, 113].

Table 5.4: Fault zone identification accuracy for all possible types of faults

Type of Fault	Numbers of Test Cases	Fault Classification Errors	Accuracy
L-g	15660	229	98.54%
LL-g	15660	312	98.01%
L-L	15660	376	97.60%
LLL-g	5220	242	95.36%
Total	**52200**	**1159**	**97.77%**

Fault zone identification accuracies for faults at various fault distances on a series compensated transmission line are presented in Table 5.5. From this table it can be observed that the minimum level of accuracy is always more than 95% and as a result, the performance of the proposed scheme can be considered to be reasonably satisfactory.

Table 5.5: Fault zone identification accuracies at various fault distances

Fault Distance In Km	25% Series Compensation			50% Series Compensation			75% Series Compensation		
	Test cases	Errors	Accuracy	Test cases	Errors	Accuracy	Test cases	Errors	Accuracy
Before Compensator									
60	2400	94	96.08 %	1500	23	98.47 %	2400	49	97.96 %
120	2400	78	96.75 %	2400	17	98.87 %	2400	46	98.08 %
138	2400	87	96.38 %	1500	19	99.21 %	2400	42	98.25 %
147	2400	64	97.33 %	2400	12	99.20 %	2400	36	98.50 %
After Compensator									
153	2400	69	97.13 %	2400	14	99.07 %	2400	35	98.54 %
162	2400	82	96.58 %	1500	19	99.21 %	2400	41	98.29 %
180	2400	94	96.08 %	2400	15	99.00 %	2400	52	97.83 %
240	2400	102	95.75 %	1500	20	98.67 %	2400	49	97.96 %
TOTAL	**19200**	670	96.51 %	**15600**	139	98.99 %	19200	350	98.18 %

5.3 DWT AND SVM BASED SCHEME

The basic arrangement of this scheme is same as that shown in Figure 5.3 with the only difference is that the ChNN is replaced with SVM. The scheme applies identical procedure for fault zone identification as that with DWT and ChNN based scheme. The feature vector identical to that used in previous scheme (given in equation (5.2)) is used for fault zone identification for each fault with the help of SVM. The same set of training and testing fault cases has been employed for the performance evaluation.

The SVM has been implemented with Lib-SVM [104] software under windows environment. The classification process with SVM is sensitive to classification parameters. Proper selection of parameters is necessary for successful application of SVM. In the absence of the parameter selection procedure in the literature, the kernel function and values of C and γ are decided by cross-validation process as already discussed in Section 4.6. A sample data set of 1000 fault cases has been considered for identification of proper values. It has been found that for ‘C=1000’ and ‘γ=0.0000025’, the performance of the SVMs is best and therefore, these values have been used for fault zone identification. Identical values of these parameters have been used for all four SVMs used in this method.

Table 5.6 describes the performance of the DWT and SVM based scheme at various levels of compensation. For better comparison of the performances of the ChNN and SVM based schemes, the results given in Tables 5.3 and 5.6 are shown as bar charts in Figure 5.6. From this figure it is observed that, the performance of the ChNN based scheme is superior than that obtained by the SVM based scheme at all compensation levels.

Table 5.6: Performance of the DWT and SVM based scheme for fault zone identification

Level of compensation	Numbers of Test Cases	Fault Zone Identification Errors	Accuracy
25%	19200	848	95.58 %
50%	13800	213	98.43 %
75%	19200	560	97.08 %
Total	**52200**	**1159**	**96.89 %**

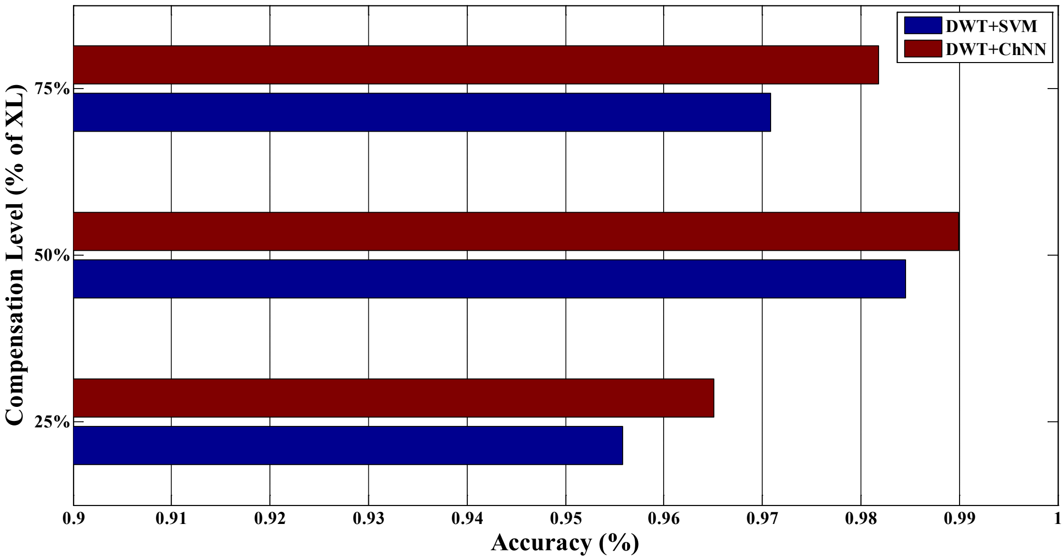

Figure 5.6: Comparison of SVM and ChNN for fault zone identification with help of DWT

Table 5.7 shows the performance of the DWT and ChNN based scheme for different types of faults. Performance of SVM is normally found superior than that of conventional ANN classifiers. However, due to Chebyshev functional expansion, the generalisation ability of the neural network increases manifold and provides substantially higher fault zone prediction accuracy compared to SVM for all possible type of faults. Again, for better comparison of the performances of the ChNN and SVM based schemes, the results given in Tables 5.4 and 5.7 are shown as bar charts in Figure 5.7. From this figure it is observed that, the performance of the ChNN based scheme is superior than the SVM based scheme for all types of faults.

Table 5.7: Fault zone identification accuracy for possible types of faults for DWT and SVM based system

Type of Fault	Numbers of Test Cases	Fault Classification Errors	Accuracy
L-g	15660	336	97.85%
LL-g	15660	488	98.01%
L-L	15660	502	96.88%
LLL-g	5220	295	94.35%
Total	**52200**	**1621**	**96.89%**

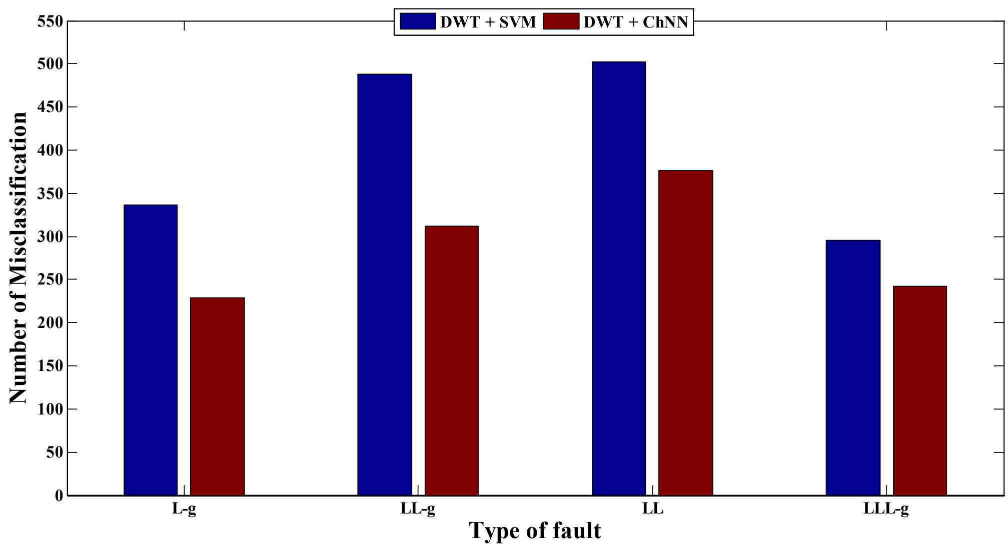

Figure 5.7:Misclassification comparison of SVM and ChNN based schemes for all possible types of faults

Table 5.8 presents the accuracies of the proposed scheme for faults at different points on the transmission line. The fault generated spectrum is quite different for faults at line ends than the faults occurring near the compensating capacitor. Therefore, accuracies towards the end of the line are slightly lower, and are almost same for both classifiers (please refer Table 5.5 and Table 5.8). The ChNN proved to be more suitable at every fault location than SVM due to its higher adaptability to the variation in the training samples.

Table 5.8: Accuracies of fault zone identification schemes at different fault length

Fault Distance In Km	25% Series Compensation			50% Series Compensation			75% Series Compensation		
	Test cases	Errors	Accuracy	Test cases	Errors	Accuracy	Test cases	Errors	Accuracy
Before Compensator									
60	2400	88	96.33 %	1500	18	98.80 %	2400	61	97.46 %
120	2400	103	95.71 %	2400	29	98.07 %	2400	78	96.75 %
138	2400	128	94.67 %	1500	32	98.67 %	2400	84	96.50 %
147	2400	107	95.54 %	2400	37	97.53 %	2400	82	96.58 %
After Compensator									
153	2400	98	95.92 %	2400	19	98.73 %	2400	52	97.83 %
162	2400	137	94.29 %	1500	27	98.88 %	2400	77	96.79 %
180	2400	101	95.79 %	2400	31	97.93 %	2400	68	97.17 %
240	2400	86	96.42 %	1500	20	98.67 %	2400	58	97.58 %
Total	**19200**	**848**	**95.58 %**	**15600**	**213**	**98.46 %**	**19200**	**560**	**97.08 %**

5.4 APPLICATION OF UDWT FOR FAULT ZONE IDENTIFICATION

The Undecimated Discrete Wavelet Transform (UDWT) is a type of the wavelet transform that is both linear and time-invariant. The transform is said to be linear if the sum of two signals is sum of transform of individual signal.

The fault-induced transients may have wide frequency bandwidth with inclusion of series compensator in the fault circuit. For analyzing a signal within a specific bandwidth, the DWT has been proved to be quite efficient tool as discussed in the previous sections. However, as discussed in Chapter 3, the major drawback of the DWT technique is its non-invariance in time and space [70]. The time-invariance property is important in statistical signal processing applications such as variation detection and parameter estimation with unknown inception time as encountered in case of a fault [115]. In this regard, the UDWT provides a better approximation property as compared to DWT. This is due to the fact that, the UDWT is a redundant, shift invariant and linear transformation method. The UDWT gives denser approximation to the continuous wavelet transform than the approximation provided by the orthonormal DWT [116, 117].

Therefore, using the advantages of UDWT, the ChNN based fault zone identification scheme is proposed in this section. The basic arrangement of this scheme is same as that shown in Figure 5.3 with the only difference is that the DWT is replaced with UDWT. With identical training and testing cases, a detailed comparison between DWT and UDWT based scheme is presented in this section.

5.4.1 Fault Zone Identification Scheme

As already described in Section 3.6, the original signal is not decimated after each level of decomposition with UDWT. Instead, UDWT modifies the filters at each level, by padding them out with zeroes [70]. Essentially the UDWT technique upsamples the coefficients of the low-pass and high-pass filters at each level of decomposition (Figure 3.7). The upsampling operation is equivalent to dilation of the wavelets. Therefore, the approximation and detail coefficients are of same length at each level of resolutions. Details about UDWT can be found in Section 3.6.

The samples of fault current signals for half-cycle duration (after the fault inception) have been taken as input to the developed system. The sampling frequency for this work is same as 4 kHz as that used earlier. The same half cycle duration post fault samples are processed using UDWT with the same 'db1' mother wavelet.

The detail sub-bands generated after UDWT of the current signal for phase 'p' are used for calculating the representative feature of phase 'p' (p = a, b, c) as:

$$C_p^{UDWT} = \frac{1}{n^2}\sum_{j=1}^{n} w_j^2 \tag{5.4}$$

In the above equation, C_p^{UDWT} is the representative feature of phase 'p', 'n' is the number of samples in the wavelet sub-bands and w_j is the j^{th} co-efficient of the wavelet sub-band.

The first level of decomposition has been found to be sufficient with UDWT for fault zone identification in this work. The first level decomposition with UDWT generates detailed sub-band CD1 of the same length as that of the input vector (i.e. 40). The D1 coefficients of a-phase current for an A-G fault at four different locations (20%, 49%, 51%, 80%) of the line are shown in Figure 5.8. These faults have been created with the following fault parameters: FIA = 45˚, R_f = 5 Ω, and loading angle (δ) = 20˚. Figure 5.9 zooms on the last ten coefficients of the UDWT. As observed from Figure 5.9, the last 10 co-efficients are sufficient to clearly classify the position of the fault vis-à-vis the SC. Therefore, this set of last 10 co-efficients only has been used for further processing with ChNN. As only 10 co-efficients are used, both memory requirement and computational burden of ChNN would be reduced for real time implementation as compared to that required for DWT.

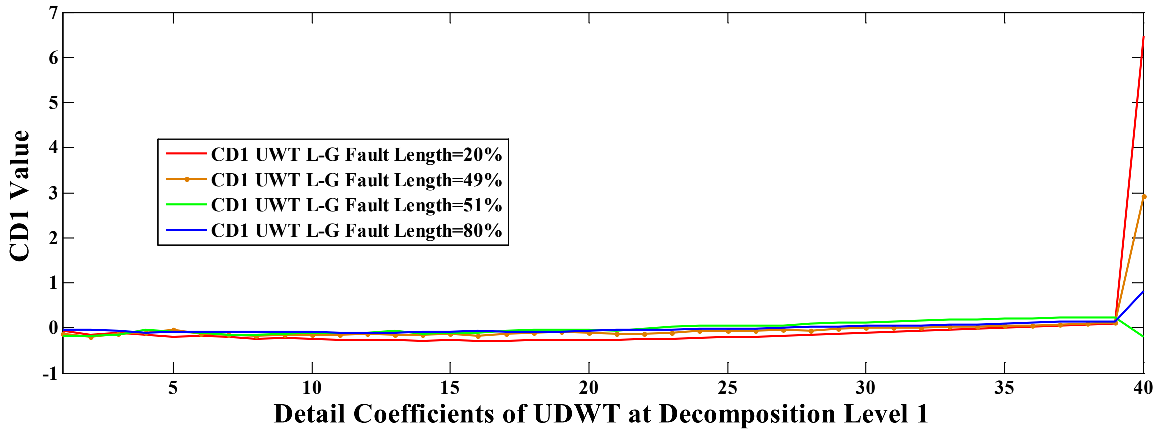

Figure 5.8: First level UDWT decomposition coefficients

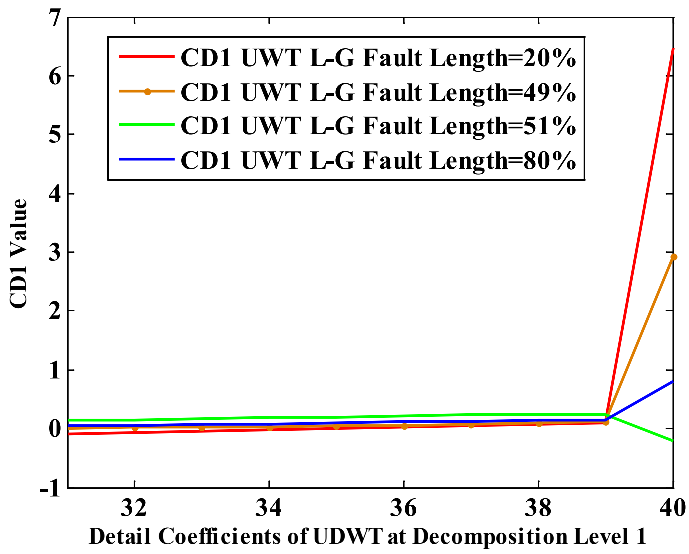

Figure 5.9: Last ten coefficients of first level UDWT decomposition

For comparison with UDWT, a second order DWT decomposition of A-phase half cycle post fault current for the same A-g faults considered in Figure 5.8 are presented in Figure 5.10. From this figure it is observed that these coefficients also indicate the fault position vis-à-vis the SC. However, DWT requires 30 coefficients (as opposed to 10 coefficients for UDWT) for proper discrimination. More exhaustive performance comparison of UDWT and DWT schemes is given in the next section.

Once the representative features for all the three phases are calculated, the feature vectors of UDWT are formed as

$$\boldsymbol{V}^{UDWT} = \{C_A^{UDWT}, C_B^{UDWT}, C_C^{UDWT}\} \tag{5.5}$$

With 10 co-efficients of D1 per phase, the vector V^{UDWT} consists of total 30 coefficients. On the other hand, with 30 coefficients per phase, the feature vector of DWT consists of 90 components.

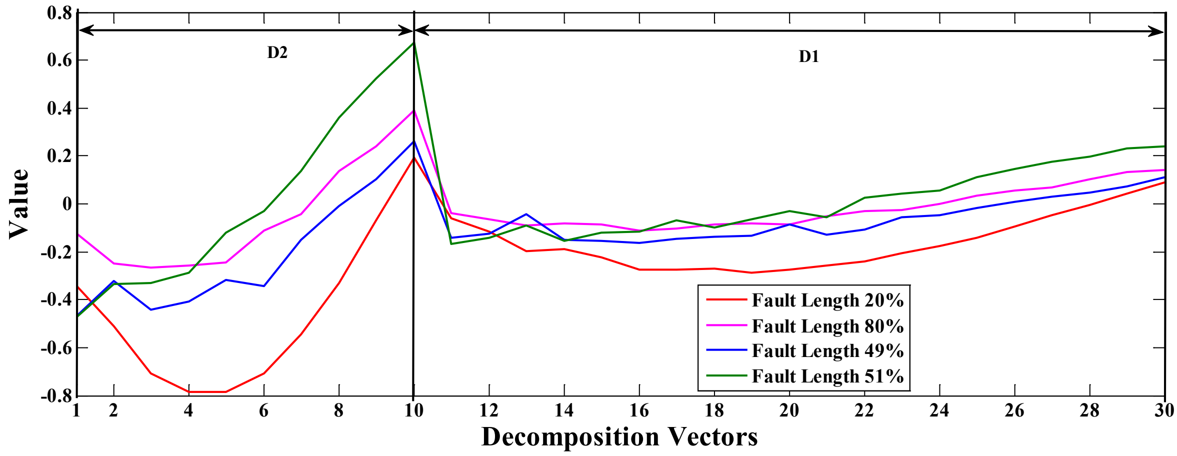

Figure 5.10: First and second level DWT decomposition coefficients

Using the identical procedure as used in the DWT based scheme, the extracted feature vector obtained with UDWT has been given to a ChNN. In this case, the third order Chebyshev expansion has been found to be sufficient for proper zone identification. Once the ChNN is well trained, it is expected to produce an output of '1' if the compensator is included in the fault circuit and '0' for otherwise.

5.4.2 Results and Comparison with DWT Based Scheme

Table 5.9 summaries the results for performance testing with UDWT and ChNN based schemes for fault zone identification. The performance of the DWT with ChNN based scheme has been found to be superior than that obtained by the SVM based scheme. Hence, the performance of the DWT+ChNN based scheme has been compared with UDWT and ChNN based scheme in this section. From Table 5.3 and Table 5.9, it can be observed that the performance of the UDWT scheme is better than that obtained by DWT based scheme. This is due to the absence of down-sampling operation in UDWT. Further, the overall accuracy of UDWT is quite satisfactory (98.62%) also. From these two tables, it can also be observed that the highest level of accuracy is obtained at 50% compensation level. This is due to the fact that the ChNN has been trained with fault cases from this compensation level (refer Table 5.1). However, at other compensation levels also, the accuracy is reasonably acceptable.

Table 5.9: Fault zone identification accuracy for UDWT and ChNN based scheme

Level of compensation	Numbers of Test Cases	Fault Zone Identification Errors	Accuracy
25%	19200	411	97.86 %
50%	13800	85	99.38 %
75%	19200	187	99.02 %
Total	**37800**	**521**	**98.69 %**

To further analyze the performance of this scheme, the detailed breakup of the accuracies for different fault locations corresponding to different compensation levels are shown in Table 5.10. From this table, it is observed that for each fault location at any compensation level, the performance of the UDWT based scheme varies marginally and provides almost equal level of accuracies.

Table 5.10: Fault zone identification accuracies for UDWT and ChNN based scheme for different fault length for different compensation levels

Fault Length (% of L)	25% Compensation			50% Compensation			75% Compensation		
	Number of Test Cases	Error	Accuracy	Number of Test Cases	Error	Accuracy	Number of Test Cases	Error	Accuracy
20%	2400	**65**	**97.29%**	1500	12	**99.20%**	2400	**28**	**98.88%**
40%	2400	**50**	**97.91%**	1500	11	**99.26%**	2400	**27**	**98.87%**
46%	2400	**43**	**98.20%**	1500	14	**99.41%**	2400	**25**	**98.95%**
49%	2400	**46**	**98.08%**	1500	10	**99.33%**	2400	**26**	**98.91%**
50%	**Compensator**								
51%	2400	**33**	**98.62%**	1500	7	**99.53%**	2400	**12**	**99.50%**
54%	2400	**48**	**98.00%**	1500	12	**99.50%**	2400	**20**	**99.16%**
60%	2400	**57**	**97.62%**	1500	8	**99.46%**	2400	**21**	**99.12%**
80%	2400	**69**	**97.12%**	1500	11	**99.26%**	2400	**28**	**98.83%**

The breakup of the accuracy according to the type of faults is given in Table 5.11. From this table it is observed that for any type of fault, the performance of UDWT based scheme is better than that obtained by DWT based scheme. Further, it is observed that the accuracy of the algorithm marginally reduces for three-phase to ground faults. However, as the possibility of this type of fault in the system is least, this marginal reduction is of very little consequence.

Table 5.11: Accuracies according to type of faults

Type of Fault	Numbers of Test Cases	DWT and ChNN		UDWT and ChNN	
		Fault Zone Detection Errors	Accuracy	Fault Zone Detection Errors	Accuracy
L-g	15660	229	**98.54%**	138	**99.11%**
L-L-g	15660	312	**98.00%**	246	**98.43%**
L-L	15660	376	**97.60%**	172	**98.90%**
L-L-L-g	5220	242	**95.36%**	127	**97.56%**
Total	**52200**	**1159**	**97.77%**	**683**	**98.69%**

An overall comparison of the performances of all three proposed schemes at different fault distances for the mid-point series compensated transmission line is presented in Figure 5.11. All three methods indicate improvement in fault zone identification as compared to the techniques reported in the literature [25, 56]. Further, a higher level of accuracy is noted just after the series compensator. This is due to the fact that, highest spectral and magnitude variations are observed for the faults just after the compensator. During training, the ChNN adjusts its weights properly to work with lower order variations in frequency and magnitude to classify the fault zone accurately for line end faults. This enables higher degree of classification accuracy for higher variations in input parameters on either side of the compensator.

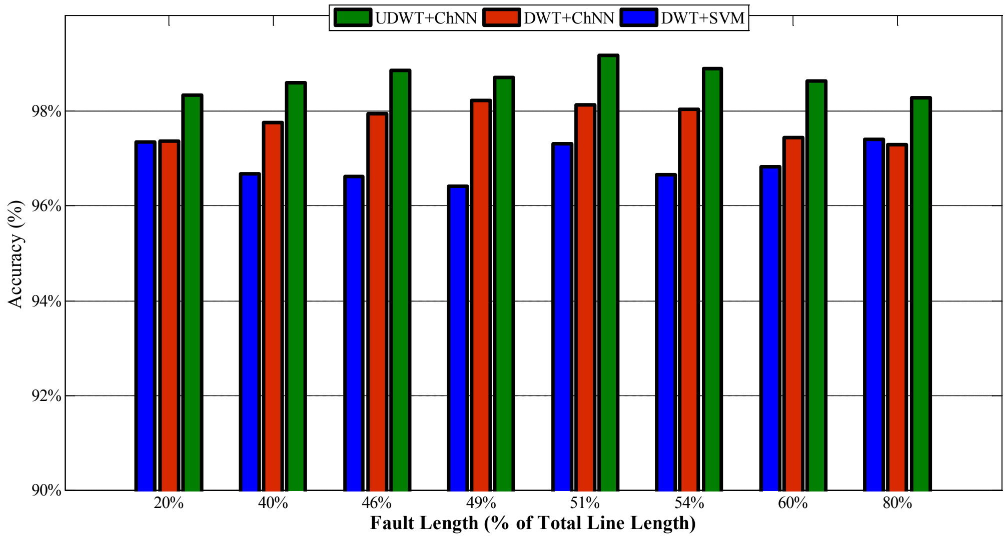

Figure 5.11: Fault zone identification performance with different schemes

It is to be noted that, the ChNN took 150 epochs to converge (during training) with the features extracted by UDWT. On the other hand, when DWT is used to extract the features, the training of ChNN require about 270 epochs to converge.

From the above results, it is found that the UDWT based scheme outperforms the DWT based scheme in every aspect. In fact even for practical application, the UDWT based scheme is advantageous as compared to the DWT based scheme as can be seen from Table 5.12. This is due to the fact that while UDWT based scheme requires 30 coefficients (10 from each phase), the DWT based scheme requires 90 coefficients to be processed by ChNN. Therefore, the memory requirement of the UDWT based scheme is certainly less than that of the DWT based scheme. Simultaneously, for UDWT based scheme, the co-efficients obtained after first level of decomposition are found to be sufficient. On the other hand, in the DWT based scheme, the co-efficients obtained after second level of decomposition are also necessary for proper zone identification. Thus, the execution time for UDWT based scheme is also less than that required by the DWT based scheme.

Table 5.12: Comparison of implementation parameters for fault zone identification schemes

	DWT+SVM	**DWT + ChNN**	**UDWT+ChNN**
Epoch for learning convergence	--	About 270	About 150
Classifier inputs	90	90	30
Level of decomposition	Second	Second	First
Training	Complex	Back-propagation	Back-propagation
Accuracy	96.89 %	97.77 %	98.69 %

The above comparison clearly establishes the superiority of UDWT and ChNN based scheme over the other schemes. Therefore, the performance of this scheme has also been compared to those obtained by two recent methods reported in [56] and [25]. Both of these methods have been chosen as the investigation of the performances of the algorithms proposed in these works had been carried out with reasonably higher numbers of fault cases as compared to the other methods reported in the literature. The comparison is shown in Table 5.13. From this table, it is observed that the performance of the proposed UDWT based method is clearly superior to those described in [56] and [25]. Further, it is to be noted that the 52200 fault test cases used in this work also include the 25200 test cases used in [56].

Table 5.13: Performance comparison with previously reported methods

	UDWT + ChNN method	**Method of [56]**	**Method of [25]**
Post Fault Data Requirement	Half cycle	Full cycle	Half cycle
Testing Cases	52200	25200	200
Fault Zone Identification Accuracy	98.69%	93.917%	95.09%

5.5 CONCLUSION

In this chapter, three methods are proposed for fault zone identification in a series compensated transmission line. The first two methods employ DWT with AI classifiers of ChNN and SVM. The third scheme involves application of UDWT along with ChNN.

Based on large number of fault simulation studies under wide variation in different parameters, the following conclusions can be drawn.

- Accuracies of all three demonstrated schemes in this chapter are higher than those obtained by the existing methods in the literature.
- The methods proposed in this chapter use samples for only half cycle duration for fault zone identification. Therefore, they are quite suitable for digital protection application.
- All three methods presented in this chapter work on current measurement only thereby reducing the measurement and computational burden.
- As compared to the DWT based method, the UDWT based scheme has less memory requirement and more execution speed for practical implementation.
- As compared to other recent methods proposed in the literature, the UDWT-ChNN based method is faster and more accurate simultaneously.

CHAPTER 6: FAULT LOCATION ESTIMATION ON SERIES COMPENSATED TRANSMISSION LINES

In this chapter development and evolution of the fault location schemes for protecting the EHV transmission line with series compensation is reported. The chapter starts with the review of fault location process in transmission line in literature. These concepts leads towards requirements and concepts for fault locations on series compensated transmission lines. Phasor estimation techniques and compensator modeling procedures are presented in brief for fault location calculations. Fault location processes based on these techniques are presented with description and comparative studies. Finally, an artificial intelligence and signal processing technique based fault location scheme is presented as further improvement in fault location studies. In addition, the scheme reveals several key advantages offered by ChNN such as: ability to learn from a set of examples and the robustness in approximating any complex function using a set of learning data sets.

6.1 INTRODUCTION

In the absence of accurate fault distance measurements, many research efforts were directed to develop dedicated fault location schemes based on impedance/ reactance measurements from the relaying end. Introduction of series compensation makes fault location estimation still more difficult due to change in system parameters. Normally, the fault location algorithm is developed assuming the line to be properly transposed. Thus any unbalance or unsymmetry in line parameters and measurements amplify with inclusion of series compensation thereby making the estimate erroneous. Most of the fault locator algorithms consider lumped parameter model of the line. However, in reality, line parameters are distributed so this assumption also introduces error in the fault distance calculation.

6.2 OVERVIEW OF FAULT LOCATION TECHNIQUES IN SERIES COMPENSATED TRANSMISSION LINE

Depending on the locations of the measurements, fault location techniques can broadly be classified as:

1) One-end measurement algorithms [48, 118, 119]
2) Two-end measurement algorithms [32, 33]
3) Multi-end measurement algorithms [120, 121]

The single end algorithm has an advantage as it calculates the fault distance based on the measurements taken on the relaying end only. Two end and multi end algorithms need measurements from each end of line. Moreover, these algorithms require a communication channel for data transmission between the ends for calculating the fault distance. Therefore, the single end measurement algorithms are the most convenient methods and lead to reduced computational burden. However, it lacks in accuracy. Two and multi end algorithms gain an advantage as measurements from either side of the fault eliminate the effect of fault impedance and compensation voltage drop on distance calculations.

Another classification of fault location techniques for series compensated transmission line in literature can be made based on their working methodology as:

- Phasor based approaches
- Differential equation based models
- Travelling wave based method to solve faulted network equations
- Signal processing based methods on the basis of the high-frequency transients generated by the faults
- Other specially developed methods

Phasor based approach is the most fundamental method for estimating the location of fault in a transmission line [32, 118]. However, during the period of fault, the voltage and current signal are not purely sinusoidal; and therefore, the fault location accuracy gets affected. This problem gets aggravated with the introduction of non-linear series compensating devices. Time-domain algorithms have been developed with single-circuit networks to overcome the problems in phasor estimation based schemes [33]. Time duration between two successive thigh frequency travelling waves is indication of the fault distance. The travelling wave equations can be modified to include series compensation as well. Accurate and faithful measurement of time domain signal is prime requirement for this method. Use of modern analysis and classification tool such as ANN [48], SVM [122-124], etc. are also reported in the literature.

A single ended fault location algorithm using phasor coordinates has been proposed in [118]. The method calculates two different synchronized voltages from either ends of the line with the help of a distributed time model. An approach to estimate the voltage across compensation devices for estimating the fault location with the help of this voltage has been developed in [32]. However, in these methods, shunt and mutual capacitances of the line are ignored. This limits the accuracy of final distance calculations. In [125] a high speed numerical method is proposed on directional comparison principle. The method uses a dedicated communication channel and measurements from either side of the line to estimate the fault location.

Application of modern single processing techniques and artificial intelligence for fault location are reported in the literature. Use of ANN for fault location has been explored for fixed capacitor compensated line in [48] and for controllable compensated line in [126]. In [122] wavelet packet decomposition and support vector regression based fault location algorithm using half cycle post fault data is presented. However, use of sampling frequency of 12.8 kHz is considered to be too high for practical implementation. Moreover, it should be noted that training and testing is done for same fault data set. Thus the accuracy cannot be guaranteed for other systems. In [33] a fault locator algorithm by dividing the transmission line in three separate circuits is developed. The authors presented the fault resistance calculation by LSE [127]. This scheme works on data measurements obtained from both ends of the line. This makes the algorithm independent of compensator type and its mode of operation. However, it also requires a dedicated communication channel and results in heavy computational burden.

6.3 INTRODUCTION TO PHASOR ESTIMATION

A fast, reliable and automatic fault location is prime requirement in transmission line protection. The correct operation of the modern day numerical relays depends on the correct estimation of the location of the fault.

Fault location techniques normally process the power frequency components of the fault signals to calculate the position of the fault on a transmission line [4, 6]. The main advantage of this method is that, it can be applied using actual power network measurements. However, in the event of a fault, the voltage and current signals are severely distorted. The fault signal may contain harmonics, decaying dc and decaying ac components besides the power frequency components. This increases the difficulty in fast and accurate phasor estimation required for estimating the fault location.

6.4 PHASOR ESTIMATION TECHNIQUES

The phasor estimation algorithm estimates the amplitude and phase of the desired frequency component of the measured signal being fed to the numerical relay. The phasor estimation makes use of the sampled values over a specified data window. The continuous sliding data window technique is used to carry out continuously updated phasor estimation [128]. This process is called estimation because the true value of the desired component is not known upfront. The quality of the estimated phasor largely depends upon the method used.

The phasor estimation techniques can broadly be divided into following categories:

i) Non recursive short window algorithms: (Miki and Mikano, Mann and Morrison [129], Rockfeller and Udren, Golbert and Shivelin, etc. [130, 131]).
ii) Non-recursive long window algorithms: (DFT, LSE, etc.).
iii) Recursive algorithms: (Kalman filtering, recursive least square error, etc.)

The non-recursive long window algorithms are most widely used for phasor estimation.

This section describes some of the phasor estimation techniques used in this work for finding the location of the fault. In this work, three phasor estimation methods have been used for finding the location of the fault. These three methods are: DFT, DWT and LSE based technique. All these three methods have been implemented using 80 samples of measurement data (i.e. number of samples in a one cycle window with measurement frequency of 4 kHz for 50 Hz system).

6.4.1 DFT Based Phasor Estimation

The DFT uses Fourier series to represent a given set of the measurement samples in terms of sine and cosine components for the desired range of the frequency. Basically, DFT is a transform that converts a sequence of time samples to another sequence of frequency samples. Let us consider 'N' discrete samples obtained with sampling frequency of '*fs*'. With sampling window length of '*n*Δt*' ('*Δt*'= sampling time on the time axis = '*1/fs*'), the FFT of the acquired time samples *x(n),n=0,1,2,….N-1*, (where N is an even quantity) can be given as:

$$X(k)=\sum_{n=0}^{N-1}x(n)e^{-j\frac{2\pi}{N}kn} \qquad \textit{Where, } k = 0,1,\ldots,N\text{-}1 \tag{6.1}$$

The number of frequency samples $X(k)$ are same as that of time samples $x(n)$. However, only half of the frequency samples are relevant. The index k indicates the multiple of fundamental frequency, also called harmonic number, from zero up to $N/2$. The remaining index values above $N/2$ have the following relationship [132],

$$\begin{aligned} X(N-k) &= \sum_{n=0}^{N-1}x(n)e^{-j\frac{2\pi}{N}(N-k)n} \\ &= \sum_{n=0}^{N-1}x(n)e^{+j\frac{2\pi}{N}kn}e^{-j2\pi n} \\ &= \sum_{n=0}^{N-1}x(n)e^{+j\frac{2\pi}{N}(N-k)n} \\ &= X(k)^* \end{aligned} \tag{6.2}$$

In equation (6.2), $X(k)^*$ is the complex conjugate of $X(k)$. This indicates that any half of the total outputs is significant for the phasor estimation and the outputs in the other half are complex conjugate of the respective outputs in the first-half.

Fundamental frequency phasor estimation consists of first calculating the DFT components. For any specific frequency, the real and imaginary components can be calculated separately by calculating the cosine and sine components. By using the Fourier series expansion method, the cosine component for any harmonic order k (= 1,..., $N/2$-1) of interest can be obtained through the definition of the DFT elements.

The sine component gives the imaginary part of the estimation and is given as [133]:

or,

$$\frac{1}{N} j\left(X(k)+X(k)^*\right)=\frac{1}{N}\sum_{n=0}^{N-1} x(n)\left[e^{-j\frac{2\pi}{N}kn}+e^{+j\frac{2\pi}{N}kn}\right]$$
$$-\frac{2}{N}\mathrm{Im}\{X(k)\}=\frac{2}{N}\sum_{n=0}^{N-1} x(n)\sin\left(\frac{2\pi}{N}kn\right) \tag{6.3}$$

The magnitude of the estimated phasor will be equal to the peak value of the fundamental frequency component of the signal analyzed. For the number of samples to be an integer number (say N samples per cycle), a sample synchronization process is required, which keeps track of the changes in the frequency of the power system and adjusts the sampling rate accordingly.

6.4.2 Fault Location Estimation with Reactance Method

Normally, any fault location technique measures the apparent impedance up to the fault point. In reactance based method, the fault locator estimates the fault location with the help of the ratio of the measured reactance to the reactance of the entire line. The same system as shown in Figure 4.1 has also been used in this chapter. To introduce some extra variables used in connection with estimation of fault location, this system is again shown in

Figure 6.1. As shown in this figure, a fault is simulated at distance 'm' from the relaying end.

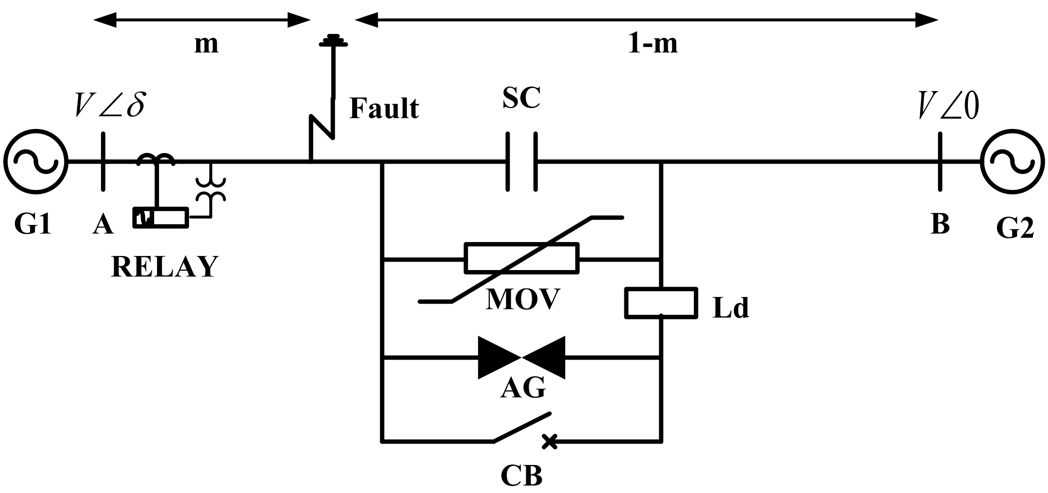

Figure 6.1: Single line diagram of the considered system with fault before compensator

Figure 6.2 represents the equivalent circuit of the considered transmission system in this study. In this figure Z_{G1} *and* Z_{G2} represent the generator impedances. Further, Z_L is the line impedance between terminals A and B, I_{G1} is the line current at terminal A, R_F is the fault resistance and I_F is the total fault current.

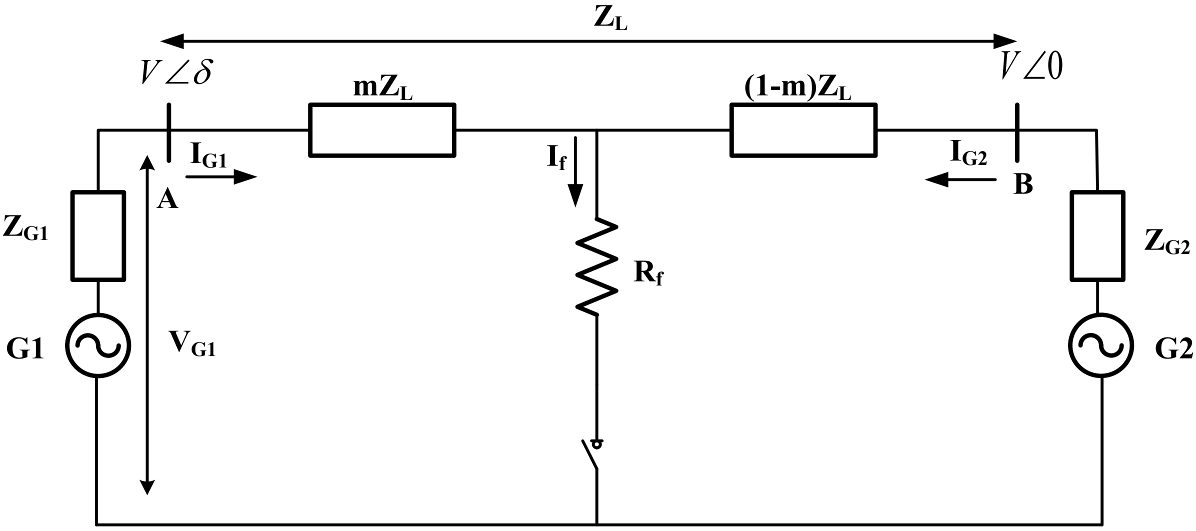

Figure 6.2: Equivalent circuit for fault on the system of Figure 6.1

The per unit distance to a three phase fault can be given as:

$$m = \frac{\operatorname{Im}(V_{G1} / I_{G1})}{\operatorname{Im}(Z_L)} \tag{6.4}$$

For a line-to-ground (a-g) fault, the calculation would be as:

$$m = \operatorname{Im}\left[\frac{V_{G1A}}{I_{G1A} + k_0 I_R}\right] / \operatorname{Im}(Z_{1L}) \tag{6.5}$$

In equation (6.5), Z_{1L} is the positive sequence impedance of the line and $k_0 = (Z_{0L} - Z_{1L}) / 3Z_{1L}$. Further, Z_{0L} is the zero sequence impedance of the line. Moreover, the residual current is defined as $I_R = 3I_0$ [134].

Based on the above fundamental concept of fault location estimation, a single ended impedance based fault location technique has been implemented with the help of phasors computed by DFT. With the computation of fundamental phasors of current and voltage from one cycle post fault measurements, the locations for all types of faults can be estimated as the ratio of the imaginary part of the calculated impedance (shown in Table 6.1) to the total reactance of the line [13].

Table 6.1: Calculated positive sequence impedance for various types of fault

Fault type	Imaginary part of the impedance equation
A-g	$\frac{V_a}{I_a + k_0 IR}$
B–g	$\frac{V_b}{I_b + k_0 IR}$
C–g	$\frac{V_c}{I_c + k_0 IR}$
AB or AB-g	$\frac{V_{ab}}{I_{ab}}$
BC or BC-g	$\frac{V_{bc}}{I_{bc}}$
CA or CA-g	$\frac{V_{ca}}{I_{ca}}$
ABC-g	Any of the following: $\frac{V_{ab}}{I_{ab}}, \frac{V_{bc}}{I_{bc}}, \frac{V_{ca}}{I_{ca}}$

6.4.2.1 Fault location estimation before compensator

As shown in Figure 6.1, the series compensator is installed at the middle of the transmission line. The series compensation device divides the transmission line into two equal sections. The compensator is equipped with highly non-linear over-voltage protection device and hence, adversely affects the fault location estimation as discussed earlier. Therefore, the fault location estimation task has been divided in two sub-routines in this work according to the inclusion/non-inclusion of the compensator in the fault circuit.

Location of any fault before the compensator can be estimated with the help of DFT based phasor estimation discussed earlier. The calculations for estimating the locations of the faults have been implemented with MATLAB software in this work. Further, as the fault resistance plays significant role on the accuracy of the fault location algorithms [135-138], its variation has also been considered in this study.

Fault location errors have been calculated as a percentage of the fault distance of the line, and are given as:

$$\%error = \frac{Actual\ Fault\ Location - Measured\ Fault\ Location}{Actual\ Fault\ Location} * 100 \qquad (6.6)$$

It is worth noticing here that, most of the available literature represents the percentage error in fault location as measured against the total length of the transmission line, i.e.

$$\%error = \frac{Actual\ Fault\ Location - Measured\ Fault\ Location}{Total\ Line\ Length} * 100 \qquad (6.7)$$

This approach effectively reduces the value of percentage fault location errors at any point on the transmission line. Therefore, it gives an over-optimistic value of the error and hence the fault location errors have been calculated against the actual fault location in this work.

6.4.2.2 Fault location estimation after compensator

The non-linear impedance of the compensator creates problem for fault location estimation when it is included in the fault circuit. Due to the presence of the compensator in the fault circuit, the estimated voltage magnitude and phase differ from their respective actual values. The highly non-linear nature of the compensator is mainly due to the presence of MOV. The MOV is normally applied for overvoltage protection of the series compensator. A highly non-linear resistive characteristic of the MOV provides effective protection to the capacitor against overvoltage. The MOV also facilitates quick insertion of the SC in the line with higher reliability and lower maintenance requirements.

As already mentioned, the distance protection scheme for transmission line protection calculates the fault impedance inaccurately due to the voltage drop across the compensator. This problem can be addressed by calculating this voltage drop with measured quantities. One of the methods is to develop an equivalent compensator model for calculations.

The MOV modeling is normally considered as a non-trivial task as the device conducts the current only for a part of each half cycle. Therefore, the SC is neither in the circuit continuously, nor is entirely bypassed during fault. Thus, development of an accurate SC-MOV model is quite difficult. In [19] a practical linearized SC-MOV model for calculating the system parameters in fault conditions is presented. This model provides an approximation of the actual value only. However, this model is widely used by the researchers as it is fairly simple in application. Based on [19], in [9] a quasi-linear model of SC-MOV combination to be used in simulation studies is reported. These models are used widely by various researchers for series compensated line protection and have been found to be very useful in calculating the SC-MOV impedance and hence for voltage estimation [10, 16, 20, 28-34].

A non-linear model of parallel combination of SC and MOV has been developed in [20]. The model utilizes the compensator current as an input parameter. This necessitates a dedicated communication channel with real-time measurements in case of mid-line compensation. Further, the model uses interpolation technique during final calculations, which reduces the prediction accuracy. In [31] an algorithm for estimating the SC-MOV impedance by calculating two different impedances across the compensator is presented. The first impedance is calculated with the measured voltage and current while the second impedance is calculated with measured current and calculated compensation voltage by using 2nd order Gear Differentiation Rule (GDR).

However, as already discussed, the model developed by Goldsworthy is fairly simple in application. For the same reason, this model has also been used in this work.

According to this model, the approximate compensator impedance is given as:

$$Z_c = R_c + X_c \tag{6.8}$$

where,

$$R_c = X_{co}(0.0745 + 0.49e^{-0.243I_{pu}} - 35\,e^{-0.8566I_{pu}} - 0.6e^{-1.4I_{pu}}) \tag{6.9}$$

and

$$X_c = X_{co}(0.1010 - 0.005749I_{pu} + 2.088e^{-0.8566I_{pu}}) \tag{6.10}$$

In the above equations, X_{co} is the nominal value of reactance of the capacitor bank. Further, equations (6.9) and (6.10) are applicable for $I_{pu} > 0.98$ where I_{pu} is per unit value of the compensator current I_c with respect to the capacitor protective level current (I_{pr}) as given below. I_{pr} is considered as twice the rated current of the SC.

$$I_{pu} = \frac{I_c}{I_{pr}} \tag{6.11}$$

For all other values of the fault current, the reactance of capacitor is taken as the overall impedance of the compensator. Finally, the estimated fault location is corrected with this impedance.

6.4.2.3 Performance evaluation of the DFT based method

The performance of the DFT based method has been evaluated with all the 57600 fault cases simulated with PSCAD/EMTDC as described in Section 4.2. Sampled values of the voltages and currents measured for one cycle duration after fault inception are provided to the algorithm to estimate the fault location. The accuracy of the fault location has been calculated as a percentage of the actual fault distance as shown in equation (6.6). The overall fault location estimation performance at different compensation levels for all considered fault cases is shown in Table 6.2.

From Table 6.2, it can be observed that comparatively large errors are present in the estimations of the fault locations. Decaying dc component and harmonics present in the system at the time of fault are major factors for these errors. Fault estimation errors (in absolute values) are higher for faults occurring after the compensator (as observed from the relay); however, due to higher distance from the relay, the percentage error is less as the denominator is relatively large in equation (6.6). Erroneous estimation of the compensator impedance is a major source of errors after the compensator.

Table 6.2: Performance of DFT based method for fault location estimation

Type of Fault	25% Compensation		50% Compensation		75% Compensation	
	Absolute Average Error (%)	Absolute Maximum Error (%)	Absolute Average Error (%)	Absolute Maximum Error (%)	Absolute Average Error (%)	Absolute Maximum Error (%)
	Before Compensator					
A-g	3.5479	5.2963	3.8148	6.3605	4.5918	5.5989
B-g	3.1827	6.2792	2.4928	5.5593	3.4874	7.1086
C-g	3.8197	4.2590	4.8248	6.1827	4.9780	5.6855
AB-g	2.1548	4.6426	2.9715	3.9824	3.5855	4.8955
AC-g	2.5140	7.5001	2.9370	5.8743	3.8815	12.1590
BC-g	3.1579	6.6896	3.5479	5.8015	3.9960	9.5628
ABC	4.0246	4.1856	4.2146	8.2537	4.2480	18.3259
AB	2.4559	5.2979	3.5798	6.6879	4.0583	7.2568
AC	2.4190	4.8256	3.4365	6.0146	4.1250	9.6487
BC	2.1796	4.1897	3.8151	3.8593	3.8715	4.6850
	After Compensator					
A-g	4.2489	5.9359	4.7259	6.8826	4.7950	6.4549
B-g	3.5110	8.2196	3.6827	7.0006	3.8110	7.0543
C-g	4.0579	6.2875	4.2893	6.9596	4.8330	6.0744
AB-g	2.9252	5.1199	3.8830	5.1684	4.0487	6.4821
AC-g	3.2489	7.7326	3.5595	8.2860	4.1790	7.6985
BC-g	3.6130	5.9358	3.4498	7.7144	4.4359	8.1795
ABC	4.1962	8.5971	4.8630	9.5880	4.6773	6.2598
AB	3.1143	5.0598	3.4585	6.9673	3.8465	7.2658
AC	3.1920	5.7157	3.3740	6.2899	3.9173	8.5874
BC	3.0498	5.3236	3.2759	4.3594	4.1688	5.2977

Figure 6.3 shows the absolute average errors calculated for all types of faults at different fault distance on the 300 km transmission line considered in this study. The absolute average error is the absolute value of the average error for 960 fault cases for each fault type at every level of compensation [i.e. there are 57600/2 = 28800 fault cases before/after compensator; with 10 fault types, there are 2880 cases for each fault type and finally there are 2880/3 = 960 fault cases for each level of compensation corresponding to any particular type of fault]. The average errors have been calculated with all types of fault with different fault and system parameters. It can be observed from this figure that, the average error is on

the higher side for faults after the compensator (as observed from the relay). This is mainly due to the errors introduced by the imperfect compensator modeling as described earlier. Moreover, the absolute average error reduces with increase in the fault distance because of relatively large denominator (actual fault distance) in equation (6.6).

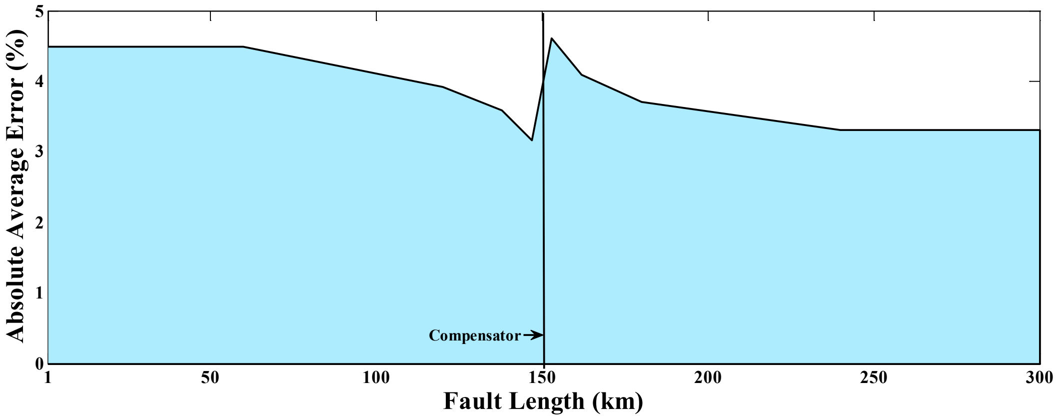

Figure 6.3: Absolute average error obtained with DFT based fault location technique

The corresponding maximum fault location errors at different fault distances are shown in Figure 6.4. Higher fault location errors are observed for faults closer to the relaying end. This is due to the fact that, errors have been calculated against actual fault location (equation (6.6)). As the actual fault distances are on lower side for faults closer to the relaying end, the percentage errors are higher for these faults.

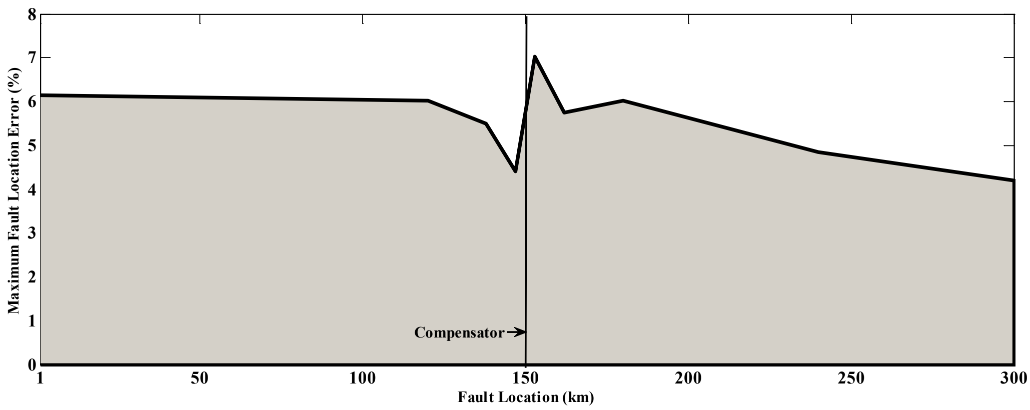

Figure 6.4: Maximum fault location error with DFT based fault location technique

6.4.3 Wavelet Based Phasor Estimation

Fourier analysis of any waveform relies on a single basis function. However, with wide functional forms of the WT, many researchers anticipated application of WT for phasor calculations [139]. As discussed in Section 3.2 of this thesis, this analysis is based upon the selection of an appropriate 'mother wavelet' and performing analysis using shifted and dilated versions of this wavelet. In contrast to the FT, in WT, the wavelet can be chosen with very desirable frequency and time characteristics. With variable windowing analysis, the WT is capable of providing more information than FT.

As explained in Section 3.2.2, the WT can be implemented with wavelet tree structure as shown in Figure 3.3. Table 6.3 gives the frequency range of the decomposed signal at 4 kHz sampling frequency, used throughout in this thesis.

Table 6.3: Frequency band for different levels of wavelet decomposition for sampling frequency of 4 kHz.

Level	**Detail coefficients**	**Frequency Band (Hz) (HP)**	**Approx. coefficients**	**Frequency Band (Hz) (LP)**
1	D1	1000-2000	A1	0-1000
2	D2	500-1000	A2	0-500
3	D3	250-500	A3	0-250
4	D4	125-250	A4	0-125
5	D5	62.5-125	A5	0-62.5

The decomposition vector A5 contains the fundamental frequency component (50 Hz) of the signal. Therefore, theoretically the current and voltage phasors should be estimated from A5 only. However, the WT filter does not involve ideal cutoff frequencies. Therefore, a margin on either side of the desired frequency is essential in case of WT. Moreover, to reduce the effect of 'aliasing' in WT, an identical spectral margin on either side of the desired frequency should be maintained. For this reason, a down-sampling by 5 has been performed on the measured data before being processed through the WT. The down-sampling operation effectively reduces the measurement frequency to 800 Hz. Detailed frequency segmentation at various levels of decomposition for this sampling frequency is shown in Table 6.4.

Table 6.4: Frequency band for different levels of wavelet decomposition for sampling frequency of 800 Hz.

Level	**Detail coefficients**	**Frequency Band (Hz) (HP)**	**Approx. coefficients**	**Frequency Band (Hz) (LP)**
1	D1	200-400	A1	0-200
2	D2	100-200	A2	0-100

With 800 Hz sampling frequency, the second-level decomposition vector A2 provides a resolution corresponding to 0 to 100 Hz. The fundamental frequency of the considered system (50 Hz) lies at the middle of the approximation output of this second-level decomposition. Therefore, the phasor (magnitude and angle) of each measurement signal can be estimated using approximate coefficient vector A2 as discussed below.

Phasor estimation for voltage and current signals at any specific frequency can be made by using unity amplitude sinusoidal reference signal. In this work, a signal with unity magnitude at power frequency (50 Hz) has been utilized as the reference signal (R_{unity}) as shown in Figure 6.5. The reference signal is also sampled at the same sampling frequency of 800 Hz as used for the measured signal. For each data window, the sinusoidal reference signal and the measured signals are decomposed into two levels of decomposition using "db1" mother wavelet.

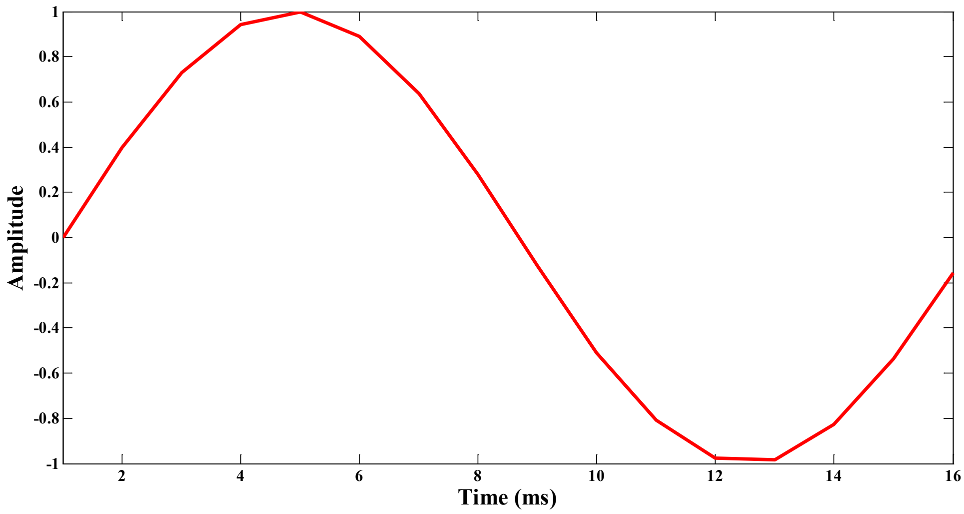

Figure 6.5: Unity reference signal (R_{unity}) for wavelet based phasor estimation

Let, $A2_m$ and $A2_r$ be the vectors that present the approximation coefficients of the measured signal and the reference signal respectively. If the mother wavelet function forms an orthogonal basis, then the angle between $A2_m$ and $A2_r$ is the angle between the fundamental component of the measured signal and reference (Figure 6.6). The angle between them can be obtained by inner product as given below:

$$\theta = \cos^{-1} \frac{\left(\left\langle A2_r, A2_m \right\rangle\right)}{\left|A2_r\right|\left|A2_m\right|} \tag{6.12}$$

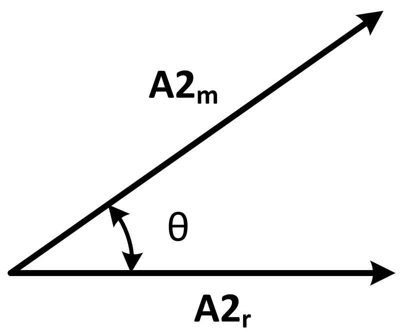

Figure 6.6: The DWT representation of the measured and reference signal

In the above equation, $(\langle A2_r, A2_m \rangle)$ denotes the dot product of these vectors and, $|A2_r|$ *and* $|A2_m|$ are their magnitudes respectively. In order to compute the magnitude, a new sine function with unity magnitude is constructed with a phase shift equal to the measured angle 'θ' as shown below:

$$R_2(t) = \sin(2 * \pi * 50 * t + \theta) \tag{6.13}$$

The new reference signal R_2 is sampled at the previously used sampling frequency of 800 Hz and is decomposed up to 2nd level of decomposition with the same mother wavelet to generate $A2_{r2}$. Using $A2_{r2}$ and $A2_m$, the magnitude of the measured signal can be estimated as:

$$x = \frac{|A2_m|}{|A2_{r2}|} \tag{6.14}$$

The same procedure can be repeated for all the other measured signals to estimate their phasors.

6.4.3.1 Performance of Wavelet based fault location estimation

Table 6.5 shows the average and maximum fault location errors at different level of compensations for various types of faults. The performance has been evaluated for all the fault cases described in Section 4.3.4. The compensator modeling as discussed in the previous section has been used in this case also.

Figure 6.7 shows the absolute average fault location errors (in % of fault distance) with respect to the fault distance with wavelet phasor estimation based fault location method. From this figure it is observed that the maximum value of the absolute average error is roughly equal to 5%. Figure 6.8 shows the maximum absolute fault estimation error computed through wavelet based phasor estimation approach for various fault distances. From this figure it is observed that the maximum absolute error is almost 12% by this WT based method.

Table 6.5: Performance evaluation of the wavelet phasor estimation based fault location estimation algorithm

Type of Fault	25% Compensation		50% Compensation		75% Compensation	
	Absolute Average Error (%)	Absolute Maximum Error (%)	Absolute Average Error (%)	Absolute Maximum Error (%)	Absolute Average Error (%)	Absolute Maximum Error (%)
	Before Compensator					
A-g	2.0498	5.1007	2.2730	5.3475	4.1700	6.0479
B-g	1.0800	5.1480	0.5400	6.2880	0.4700	6.8147
C-g	3.8190	5.5655	4.1700	6.4725	3.4920	7.2174
AB-g	0.7100	3.2871	2.0430	3.4441	1.7580	3.9859
AC-g	1.4900	5.4936	4.9200	5.9748	4.8790	6.5790
BC-g	0.4700	6.6048	1.6600	5.9715	2.1800	6.8173
ABC	3.9100	6.7379	3.6100	7.7359	4.1850	11.8725
AB	1.0500	5.0048	0.8260	6.1875	1.2500	6.5479
AC	1.9400	5.0514	2.8900	5.9957	3.1200	6.1792
BC	2.8900	6.7958	4.0100	6.6895	3.9540	7.2279
	After Compensator					
A-g	2.1900	4.8257	3.1478	6.5738	3.9100	7.0191
B-g	3.8700	5.3591	3.4600	6.1143	2.1500	6.4357
C-g	4.5600	6.4798	4.5900	7.0180	5.2300	8.1497
AB-g	2.8700	3.1498	3.8120	3.8957	3.8450	4.2059
AC-g	3.9400	6.2799	3.9900	6.1796	4.2890	7.0249
BC-g	2.8900	4.2791	3.1950	5.8459	4.1700	6.2179
ABC	2.2700	7.1774	3.4700	7.7543	4.4500	8.9143
AB	3.7200	5.4787	3.4900	6.7255	3.9250	6.8478
AC	1.5800	5.5549	2.0010	5.3799	2.4900	6.8547
BC	2.4250	4.1798	2.6210	5.4798	4.1800	7.1254

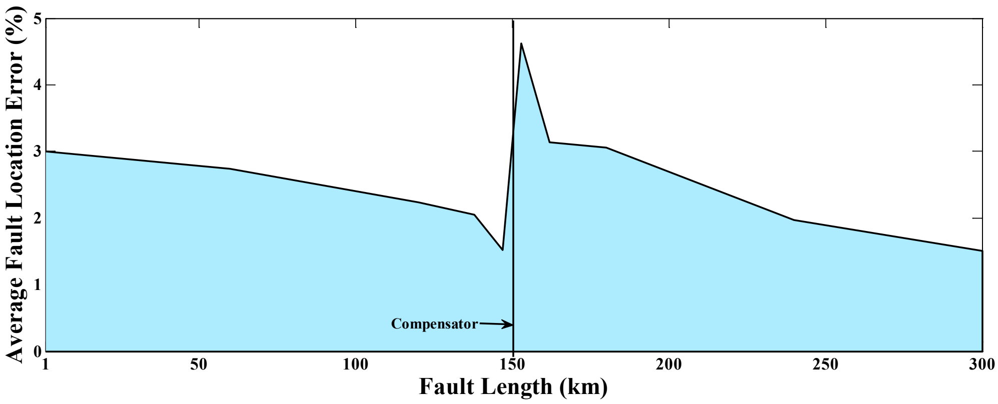

Figure 6.7: Absolute average error for wavelet based fault location technique

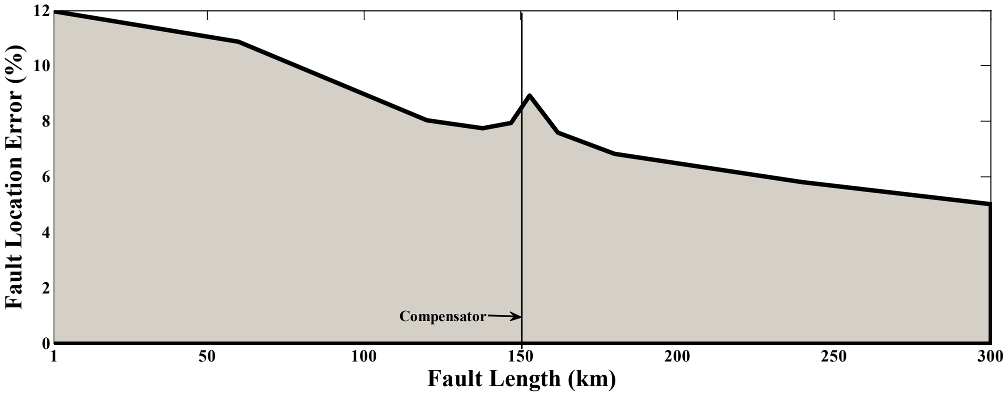

Figure 6.8: Absolute maximum error for wavelet based fault location technique

6.4.4 The Least Square Error Solution

The Least Square Error (LSE) phasor measurement is based on the fitting of a pre-selected curve to a set of measurements as close as possible. As mentioned in Section 6.4.1, by considering '*N*' sample points with sampling frequency of '*fs*', the samples will be given as *x(n), n=0,1,2,….N-1.* The fitting process consists of finding the value of the parameters of the curve that minimize the sum of squares of the differences between the measurements and the fitted curve.

6.4.4.1 Curve fitting

In this work, the sine function with fundamental frequency of the system (50 Hz) has been chosen as the pre-selected curve. The difference between the curve selected and the measurements is assumed to be the noise ε as shown below.

$$x(t) = Y\sin(\omega_o t + \theta) + \varepsilon(t) \tag{6.15}$$

Equation (6.15) can be represented as the combination of a sine and cosine signal as:

$$\begin{aligned} x(t) &= Y\cos(\theta)\sin(\omega_o t) + Y\sin(\theta)\cos(\omega_o t) + \varepsilon(t) \\ &= Y_R\sin(\omega_o t) + Y_I\cos(\omega_o t) + \varepsilon(t) \end{aligned} \tag{6.16}$$

Hence, the reference sine curve is decomposed into two orthogonal sine and cosine functions of unknown amplitudes Y_R and Y_I . These amplitudes also represent the real and imaginary part of the desired estimated phasor [140].

Equation (6.16) is applied to each of the N discrete measurement individually to find out the least square solution for measured signal. This results in a set of linear equations, which can be arranged in a matrix form as shown below:

$$\begin{bmatrix} x(t_0+0\Delta t) \\ x(t_0+1\Delta t) \\ . \\ . \\ x(t_0+[N-1]\Delta t) \end{bmatrix} = \begin{bmatrix} \sin(\omega_0 0\Delta t) & \cos(\omega_0 0\Delta t) \\ \sin(\omega_0 1\Delta t) & \cos(\omega_0 1\Delta t) \\ . & \\ . & \\ \sin(\omega_0 [N-1]\Delta t) & \cos(\omega_0 [N-1]\Delta t) \end{bmatrix} \begin{bmatrix} Y_R \\ Y_I \end{bmatrix} + \begin{bmatrix} \varepsilon(t_0+0\Delta t) \\ \varepsilon(t_0+1\Delta t) \\ . \\ . \\ \varepsilon(t_0+[N-1]\Delta t) \end{bmatrix} \tag{6.17}$$

The left side of the equation represents the vector of N measurements (*vector b*) as a function of the sampling time. The right-hand side of the equation contains a summation of two terms. The first term represents a matrix with sine and cosine coefficients multiplied with vector of unknown magnitudes of Y_R and Y_I *(matrix Y)*. The second term represents the vector of errors (*vector* ε). Therefore, equation (6.17) can be represented as:

$$[b] = [A][Y] + [\varepsilon] \tag{6.18}$$

The least squares solution for this equation that minimizes the sum $\left[[\varepsilon]^T[\varepsilon]\right]$ is obtained using the left pseudo-inverse of [*A*] as:

$$[Y] = \left[[A]^T[A]\right]^{-1}[A]^T[b] \tag{6.19}$$

The solution provides the real and imaginary part of the considered signal at fundamental power frequency.

6.4.4.2 Performance evaluation of LSE based fault locator

A major advantage gained by the least square method over DFT and WT based methods is that, the LSE does not need to evaluate (curve fit) the considered signal with respect to sine function only. In this regard, the least square method is more general and accurate for phasor estimation. Moreover, LSE method takes care of DC offset and harmonics to provide more accurate fault location estimation.

The performance of the LSE method for estimating the fault locations is shown in Table 6.6. Table 6.5 and Table 6.6 show that a considerable improvement in average as well as maximum fault location errors is achieved in LSE method as compared to wavelet based method for all types of faults.

The performance enhancement is also evident in average and maximum errors for different fault distances as shown in Figure 6.9 and Figure 6.10 respectively. Moreover, the LSE method does not impose the necessity of integer number of samples per cycle as compared to the other signal processing tools. This advantage gives an edge to LSE for phasor estimation based fault location estimation method.

Table 6.6: Performance evaluation of the least square estimation based fault location estimation algorithm

Type of Fault	25% Compensation		50% Compensation		75% Compensation	
	Absolute Average Error (%)	Absolute Maximum Error (%)	Absolute Average Error (%)	Absolute Maximum Error (%)	Absolute Average Error (%)	Absolute Maximum Error (%)
	Before Compensator					
A-g	1.4285	2.4590	1.5478	3.3874	1.7925	4.1583
B-g	0.8410	3.2483	1.1525	3.6626	1.6201	4.2487
C-g	1.7572	4.1162	1.8610	5.4932	2.1500	4.2473
AB-g	0.5820	1.2512	0.9577	2.0651	1.1183	2.6147
AC-g	0.7748	4.8215	0.8360	5.4789	1.5850	5.9725
BC-g	1.0440	2.9446	1.4743	3.2498	1.5147	3.5912
ABC	1.4749	5.2872	1.5300	5.5540	2.4713	6.0821
AB	0.6140	4.0178	0.8860	5.2120	0.9473	5.7468
AC	0.7718	3.5715	0.8019	3.9326	1.5257	4.5236
BC	1.8652	2.5193	1.3540	2.9957	1.4844	3.5859
	After Compensator					
A-g	1.4890	3.5489	1.6869	3.1498	1.9270	4.1498
B-g	1.1028	4.0146	1.3470	4.2512	1.8663	4.3582
C-g	1.8245	2.6748	1.9920	2.5478	2.1281	2.9835
AB-g	0.5538	4.0105	0.9680	5.1895	1.6000	5.7814
AC-g	0.9420	4.4478	1.1352	4.8480	1.3383	5.2725
BC-g	1.5279	4.1790	1.2052	4.2478	1.8472	4.8975
ABC	1.7330	5.1489	1.9551	3.2145	2.3352	7.0245
AB	0.4193	3.8598	0.9440	4.2234	1.0388	4.5400
AC	0.8677	4.9715	1.0493	5.5529	1.2491	6.4158
BC	1.4524	4.5553	1.2018	4.7486	1.6229	5.0478

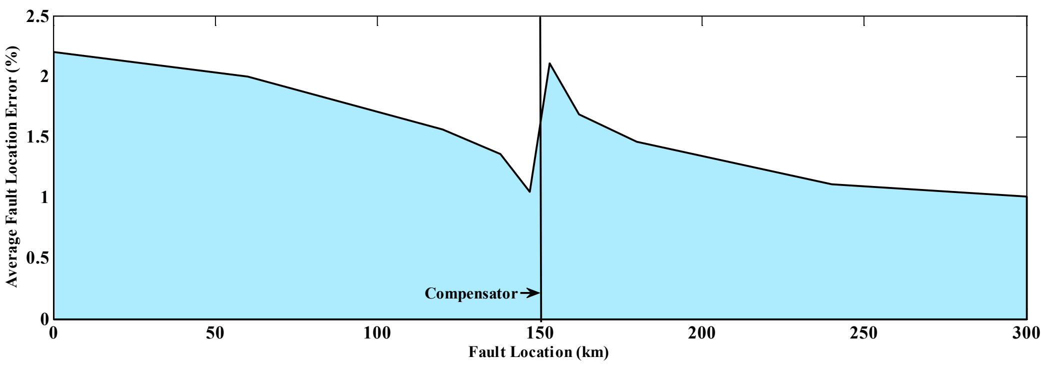

Figure 6.9: Absolute average error for LSE based fault location scheme

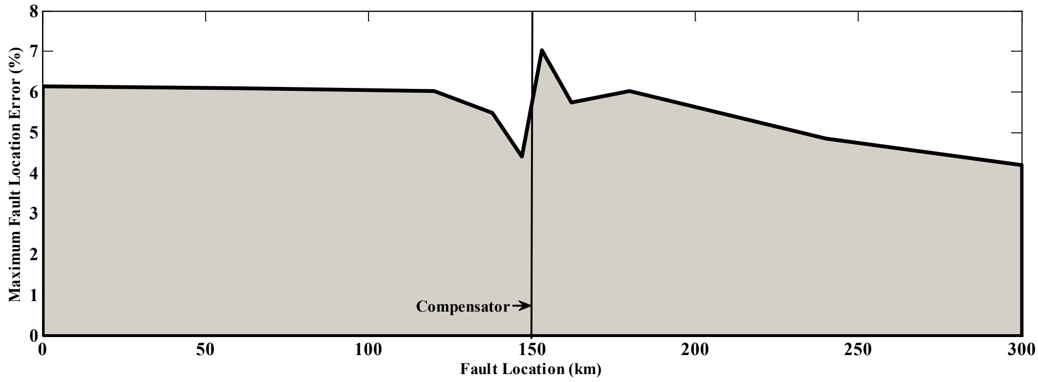

Figure 6.10: Maximum errors for LSE based fault location scheme with respect to fault distance

6.4.5 Comparison of the Phasor Estimation Based Fault Location Schemes

Fourier, Wavelet and LSE phasor estimation based one-ended fault location algorithms for series compensated transmission line have been described in the previous sub-sections. All these algorithms have been implemented in MATLAB for evaluating the accuracy of fault estimation with a large fault data set of 57600 fault cases dynamically generated with PSCAD/EMTDC.

A comparative performance of these algorithms is shown in Figure 6.11 and Figure 6.12. From these two figures, the performance of the LSE method is found to be superior to that of the other two methods for faults at different locations and for various compensation levels as well.

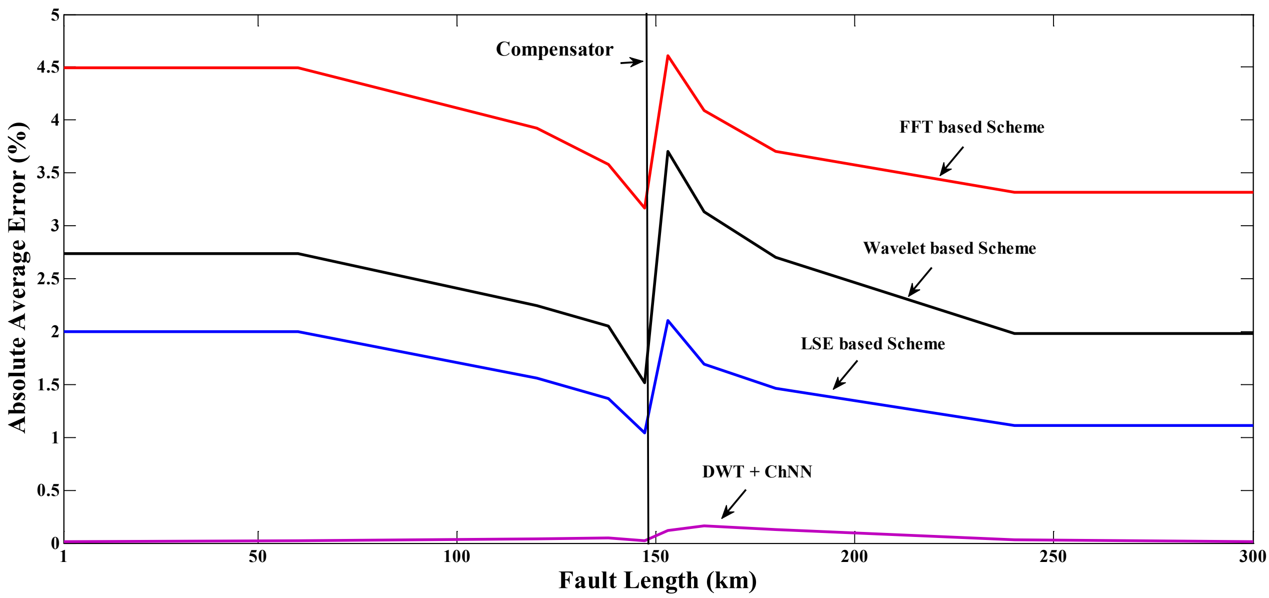

Figure 6.11: Absolute average error for various fault loation schemes

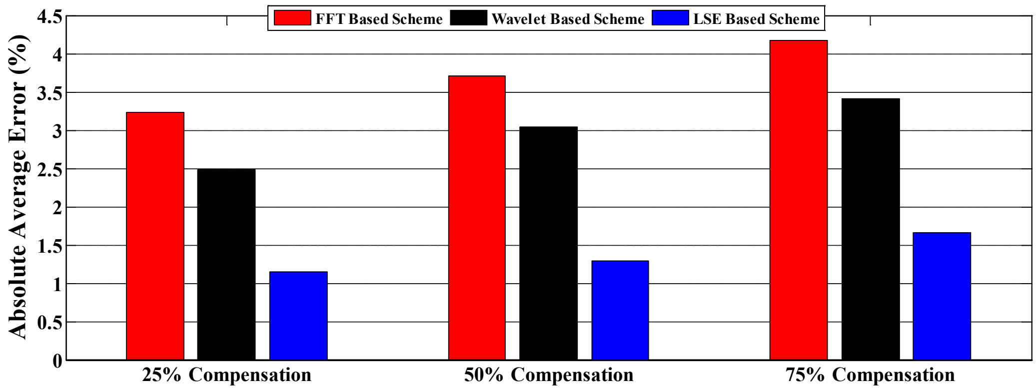

Figure 6.12: Average absolute error for various fault location schemes

6.5 APPLICATION OF DSP AND AI FOR FAULT LOCATION ESTIMATION

As discussed in the previous sections, the compensator exhibits highly non-linear behavior during fault. This non-linearity presents difficulty in formulation of the accurate and practical mathematical model for estimating the location of the fault as large number of variables are involved. Therefore, the models so far reported in the literature for compensator modeling are too complex and/or are less accurate to represent compensator impedance.

This fact can be verified with conventional phasor estimation based methods presented above. These methods are although designed with some good attributes for estimating the fault distances, they have not performed well overall. The performance of these methods lacks in accuracy for some specific fault type or ranges of fault parameters due to inadequate models.

However, it is well-known that the faulted voltage and current waveforms contain the required information for fault location which is difficult to extract otherwise. Thus an algorithm needs to be developed that can learn from the supplied examples, contains non-linear regression capability, can accommodate system parameter variations and is fast as well. Such a technique, combining DWT and ChNN, is described in the next subsection.

6.6 WAVELET AND CHNN BASED FAULT DISTANCE ESTIMATION SCHEME

Basically, in this method, DWT is used to extract the features from the post fault current and voltage waveforms which are subsequently used by the ChNN for estimating the fault distance. To deciding the appropriate architecture of the scheme, the change in current and voltage patterns for an A-g fault at different fault distances are shown in Figure 6.13 and Figure 6.14. All these faults have been simulated with fault resistance of 5 Ω, FIA of 0° and line loading angle of 10˚. From these figures, following points can be observed:

- A considerable difference exists between the fault current patterns on different sides of the compensator and the same can be observed from Figure 6.13 (a) and (d).
- Fault current and voltage patterns for faults before the compensator carry similar patterns as can be seen in Figure 6.13 (a), (b), (c) and Figure 6.14 (a), (b), (c). These matching patterns differ in amplitudes according to the fault distances.

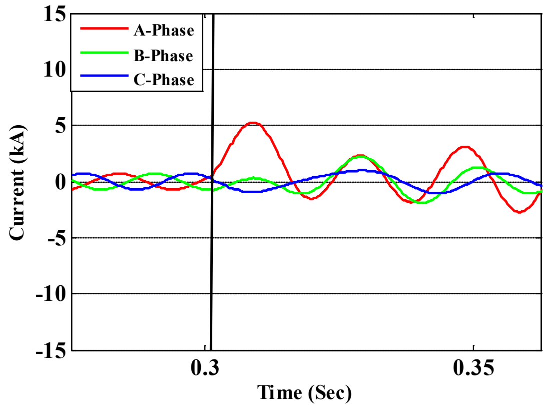

(a) : 49% of line length

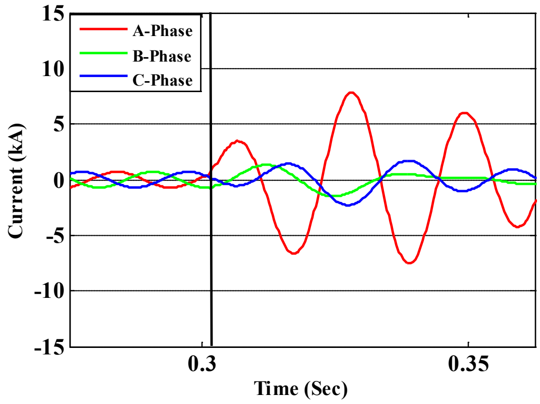

(d) : 51% of line length

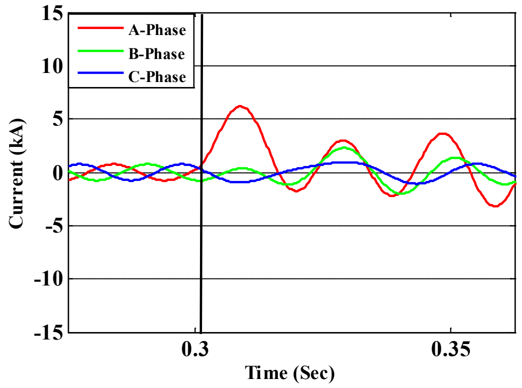

(b) : 40% of line length

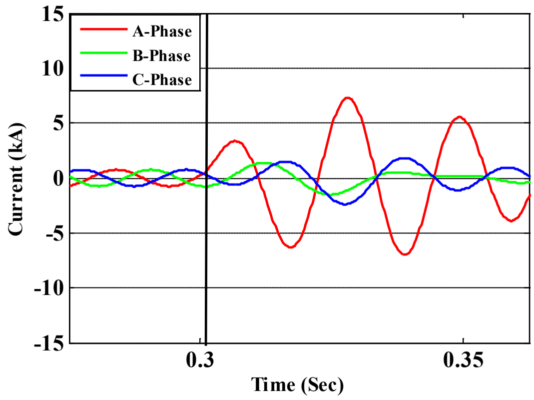

(e) : 60% of line length

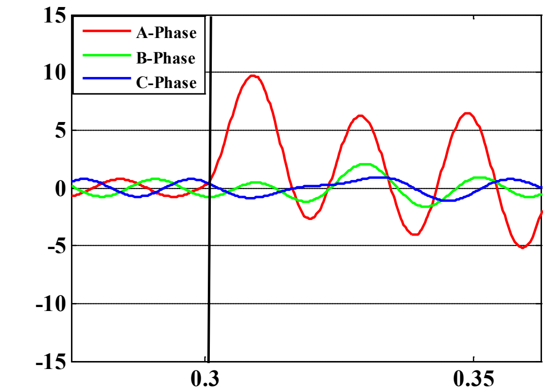

(c): 20% of line length

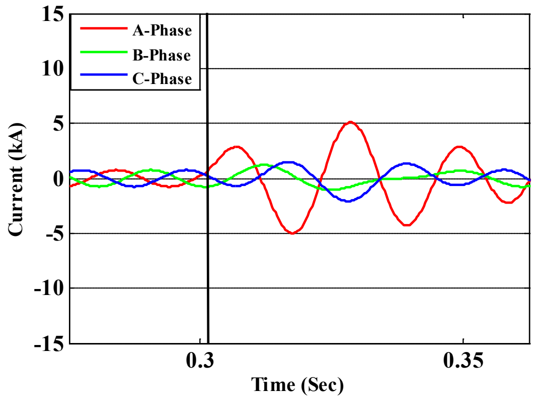

(f) : 80% of line length

Figure 6.13: Changes observed in current waveforms for an A-g fault at various fault distances

- Moreover, current and voltage patterns for faults after the compensator also carry resembling wave shapes with discriminatory amplitude changes according to fault distance (Figure 6.13 (d), (e), (f) and Figure 6.14 (d), (e), (f)).

From this discussion it is clear that, separate identifiers are required for faults on either side of the compensator.

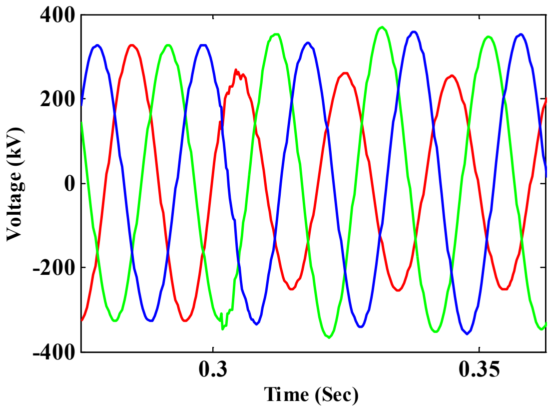

(a) : 49% of line length

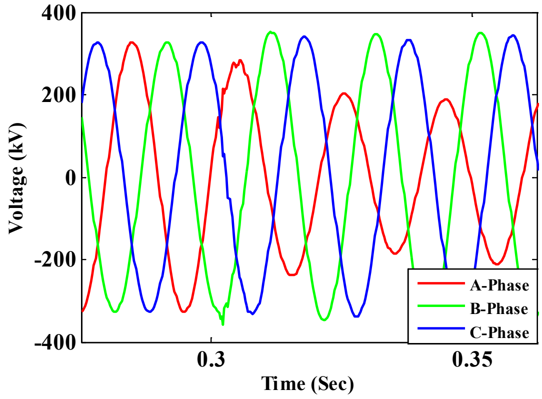

(d) : 51% of line length

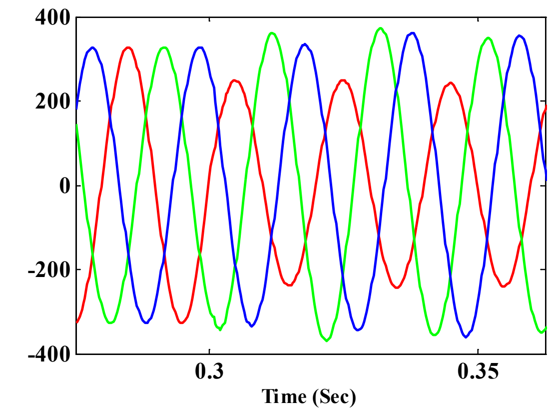

(b) : 40% of line length

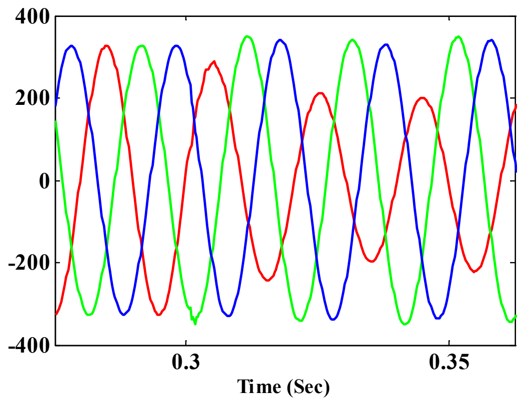

(e) : 60% of line length

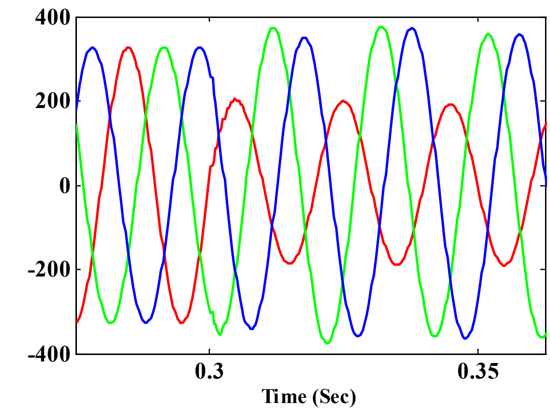

(c): 20% of line length

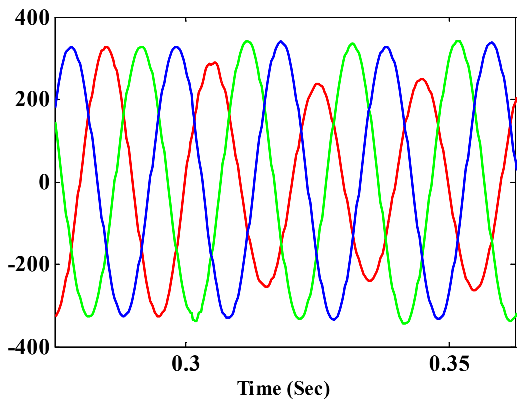

(f) : 80% of line length

Figure 6.14: Changes observed in voltage waveforms for an A-g fault at various fault distances

Since each of the ten possible fault types have their own distinct fault pattern, a separate ChNN was found to be necessary to be employed for each type of fault under consideration. Therefore, a total of 20 ChNNs have been used for fault distance estimation in this work. ChNNs are divided in two distinct groups according to the position of fault relative to the compensator as given in Table 6.7. With the knowledge of the fault type and zone, the required DWT feature information is passed to the appropriate network to achieve correct estimation of the location of the fault.

Table 6.7: ChNN fault zone identification groups

Group 1 **Fault Before Compensator**	**Group 2** **Fault After Compensator**
1-ChNN-A-g	2-ChNN-A-g
1-ChNN-B-g	2-ChNN-B-g
1-ChNN-C-g	2-ChNN-C-g
1-ChNN-AB-g	2-ChNN-AB-g
1-ChNN-AC-g	2-ChNN-AC-g
1-ChNN-BC-g	2-ChNN-BC-g
1-ChNN-ABC-g	2-ChNN-ABC-g
1-ChNN-AB	2-ChNN-AB
1-ChNN-AC	2-ChNN-AC
1-ChNN-BC	2-ChNN-BC

The identical feature vector calculated in Section 4.3 for fault classification is used in this work for fault location estimation. However, an additional DWT voltage vector is also included in estimating the location of the fault. The identical wavelet function ‘db1’ has been used for feature extraction at fourth level of decomposition as described in Section 4.3. The generated DWT vectors for voltage and currents for all three phases $\mathbf{V}^{dwt}$ (as in equation (4.3)) have been used in this work. The detailed diagram of the proposed scheme is shown in Figure 6.15.

6.6.1 Implementation

The developed algorithm uses transient voltage and current data at the relaying end (Bus-A) of the system considered (Figure 6.1). Any fault in the network produces transients in the currents and voltages. The distortions change with the type of fault, inclusion of the series compensator in the fault circuit, distance of the fault to the system, etc. Therefore, knowledge of the phases involved in the event of fault and the position of the fault with respect to the compensator are pre-requisites for the developed algorithm.

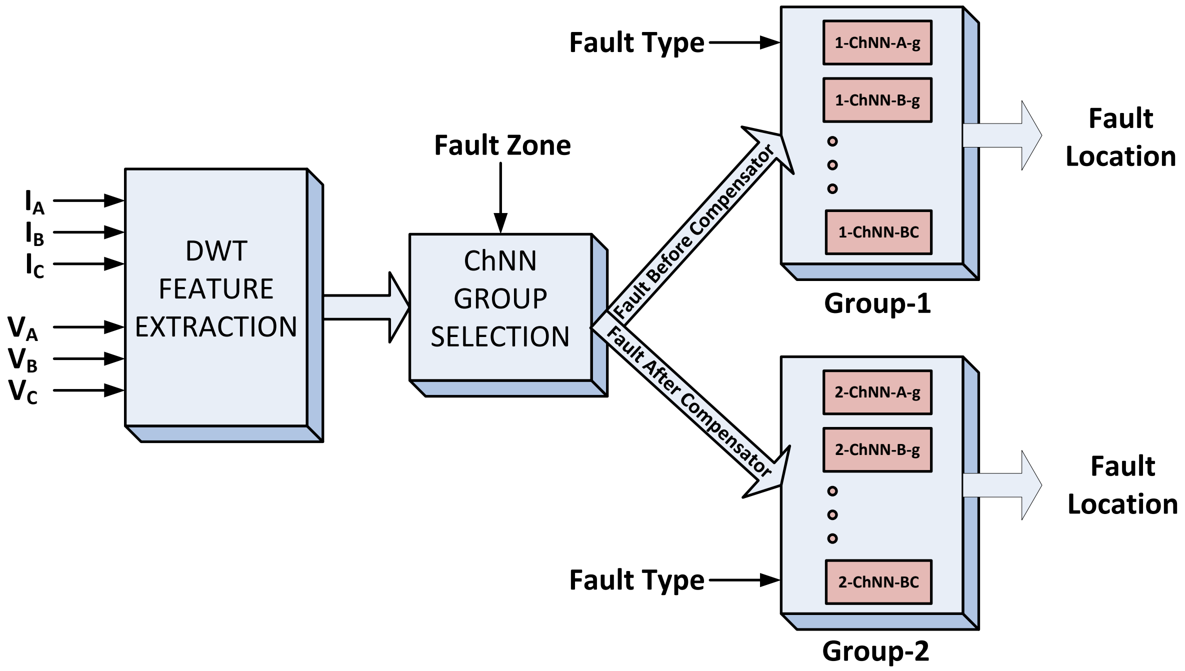

Figure 6.15: Modular structure of DWT and ChNN based 'fault location estimation' scheme

6.6.2 Input Selection - Feature Extraction

Being a single-layer structure, the ChNN is capable to generate output in a short span of time. However, the ChNN implementation necessitates Chebyshev functional expansion. Complexity of the computation and computational time largely depends on the length of input vector and the order of functional expansion. This demands that the input vector should contain relevant and discriminatory information only. This information should help the ChNN to understand the regression requirement as a whole. Therefore, feature extraction forms an integral part of the fault location estimation strategy.

Being a better signal feature extraction tool, the time-frequency analysis of the fault current and voltage with help of DWT has been employed in this work. Since the fault location task is based on offline post-fault analysis, one cycle post fault data with a sampling frequency of 4 kHz has been used in this work. The samples of three phase currents and voltages have been decomposed with DWT for fault distance estimation.

Figure 6.16 shows all four DWT decomposition vectors of A-phase current and voltage for an A-g fault at 40% of the line length with fault resistance of 5Ω, FIA of 45° and line loading angle of 10°. Figure 6.17 shows the DWT vectors of A-phase for AB-g fault for identical fault location and conditions of fault of Figure 6.16. A detailed investigation of these figures shows that, even when the A-phase quantities (current and voltage) only are decomposed in either case, the resulting vectors are quite different for two types of faults.

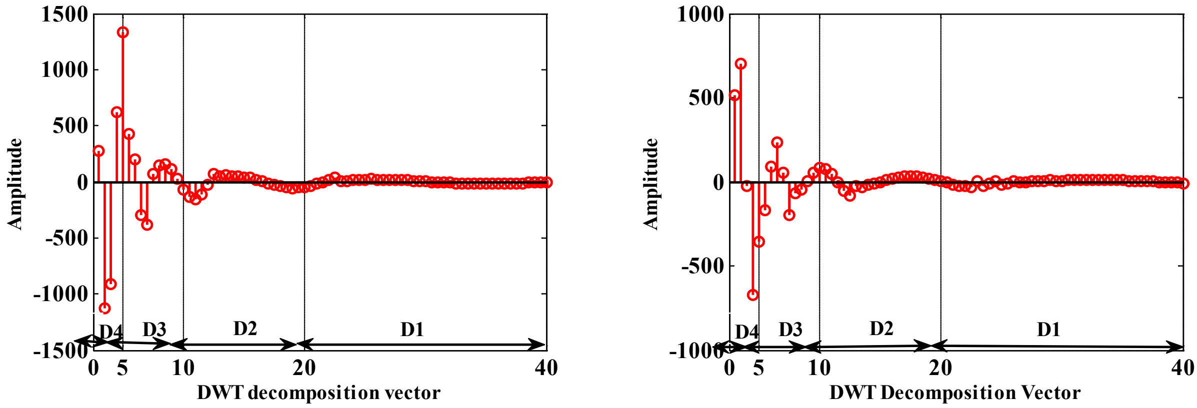

(a): A-Phase Current (b): A-Phase Voltage

Figure 6.16: DWT decomposition vectors for A-g fault up to 4th level of resolutions

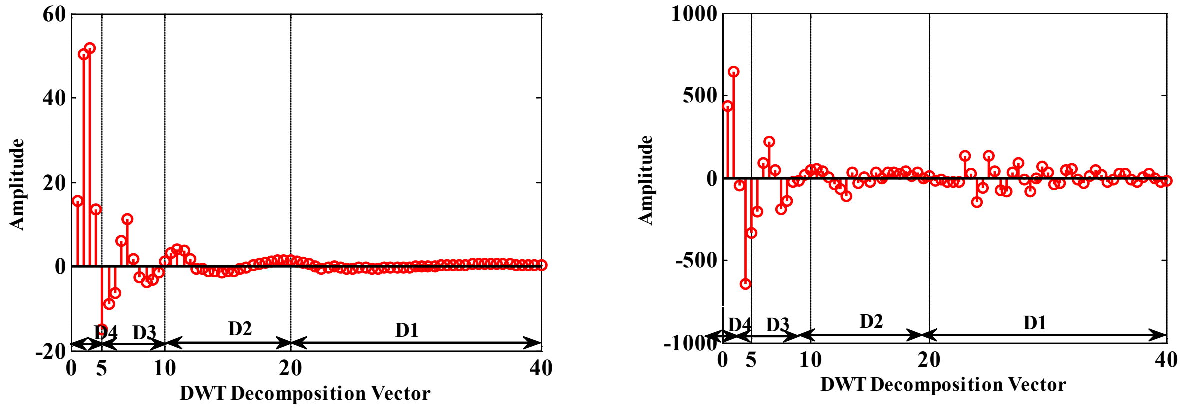

(a): A-Phase Current (b): A-Phase Voltage

Figure 6.17: DWT decomposition vectors for AB-g fault up to 4th level of resolutions

With the shown input vector dimensions in Figure 6.16 and Figure 6.17, the dimension of the input vector comprising of the decomposed vectors of all the three phase currents and voltage is rather large. With Chebyshev expansion, the size of single layer input increases as well. To make the ChNN fast and effective with acceptable accuracy, only a smaller portion of interest with high frequency band are found to be appropriate as features of the fault to be applied to ChNN. Detailed investigation reveals that, third and fourth order wavelet resolutions (D3 and D4) can be used to represent the whole of the feature space. Furthermore, assuming that the type of fault is readily available, only those phase(s) / ground involved in the fault need to be evaluated with DWT and ChNN. Hence, every ChNN will receive inputs according to the type of fault identified. The details about inputs to the ChNN are presented in Table 6.8.

Table 6.8: Input selection for ChNN with DWT

FAULT TYPE	BEFORE COMPENSATOR	AFTER COMPENSATOR	Current			Voltage		
			I_A	I_B	I_C	V_A	V_B	V_C
A-g	1-ChNN-A-g	2-ChNN-A-g	✓			✓		
B-g	1-ChNN-B-g	2-ChNN-B-g		✓			✓	
C-g	1-ChNN-C-g	2-ChNN-C-g			✓			✓
AB-g	1-ChNN-AB-g	2-ChNN-AB-g	✓	✓		✓	✓	
AC-g	1-ChNN-AC-g	2-ChNN-AC-g	✓		✓	✓		✓
BC-g	1-ChNN-BC-g	2-ChNN-BC-g		✓	✓		✓	✓
ABC-g	1-ChNN-ABC-g	2-ChNN-ABC-g	✓	✓	✓	✓	✓	✓
AB	1-ChNN-AB	2-ChNN-AB	✓	✓		✓	✓	
AC	1-ChNN-AC	2-ChNN-AC	✓		✓	✓		✓
BC	1-ChNN-BC	2-ChNN-BC		✓	✓		✓	✓

Therefore, the complete fault location estimation system proposed in this work can be expressed in the form of flow chart as shown in Figure 6.18.

The order of Chebyshev expansion for solving the pattern recognition problem largely affects the decision boundary developed by ChNN. The process to determine the optimum number of Chebyshev expansion is largely experimental, involving training and testing different order network configurations. With consideration of generalization capability and computational complexity, third order expansion has been found to be sufficiently effective for fault location application.

6.6.2.1 Training and testing of ChNN

The same set of 57600 fault cases generated in Section 4.3.4 has been used for training and testing of the ChNN based fault location scheme. As described earlier, dedicated pair of ChNNs is provided for each fault type. One is used for faults before the compensator and another for fault after the compensator. Therefore, a set of 2880 fault pattern are available for every fault type (on either side of the compensator) for training and testing of the ChNNs. A set of 270 (less than 10%) fault pattern for each type of fault has been used for training. Therefore, a total of 270*20 = 5400 fault cases have been used for training the group of 20 ChNNs. Remaining 52200 (57600 – 5400) patterns have been used for testing of the ChNN. Details of the training data for each ChNN is given in Table 6.9. It is worth noting here that, the testing patterns do carry many parameters that were not used by ChNNs during learning.

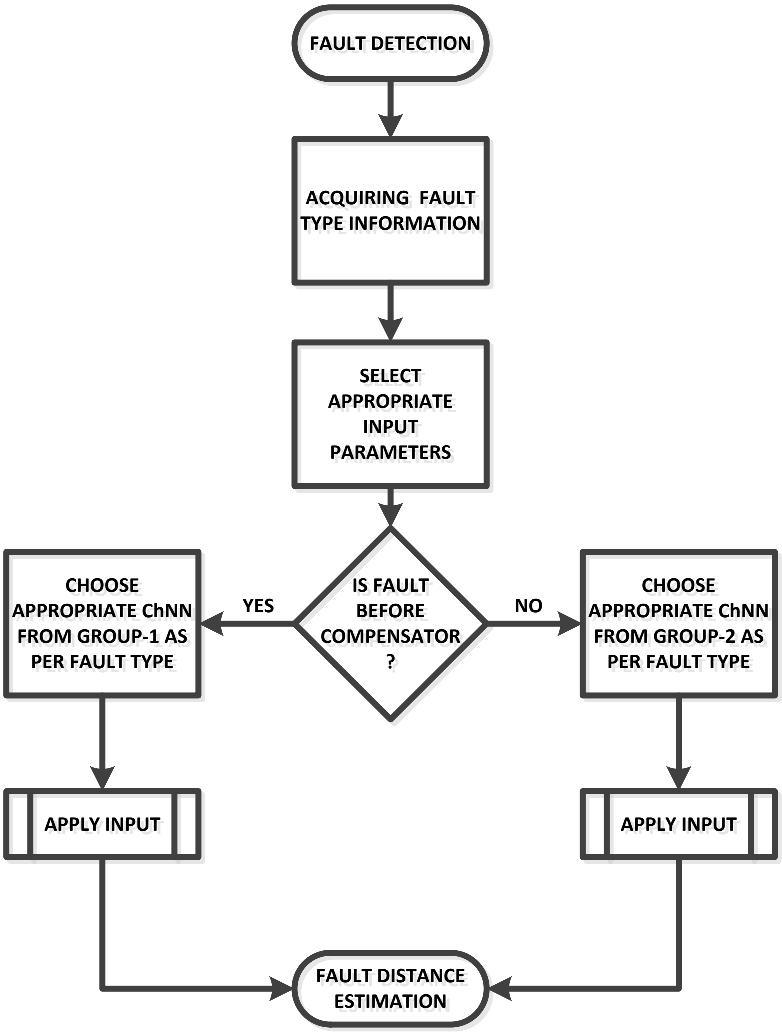

Figure 6.18: Flow chart of fault distance estimation

Table 6.9: Training data used for each ChNN

Parameters								**Number of Fault Cases**
Xc	**Z_{SG1} In % of GBI**	**Z_{SG2} In % of GBI**	**δ**	**R_f (Ω)**	**FIA**	**L (km)**	**Fault Type**	
50%	100	100	10˚ & 30˚	0, 5 & 50	0, 45 & 115	60, 120, 147	Associated with ChNN	54
50%	100	75						54
50%	100	125						54
50%	125	100						54
50%	75	100						54
Total Fault Cases								**270**

Neural Network Toolbox in Matlab Environment [141] has been used to implement the ChNNs. For fault location estimation, the ChNN would generate a large range of outputs to represent the predicted fault location. This variation is possible in regression mode of ChNN.

In the regression mode of ChNNs, outputs are normalized to facilitate quick and easy training. Therefore, in training mode, outputs of the fault location system have been normalized. However, the input vector set has been kept to be the same to increase the sensitivity of the ChNN. During testing, ChNN generated outputs are in normalized form which is subsequently converted into total fault distances.

The ChNNs have been trained by using back-propagation LSLM learning algorithm. The training is repeated until the squared error is reduced up to the predefined threshold of 1×10^{-25}.

6.6.3 Performance Evaluation of DWT and Chnn Based Scheme

In order to examine the performance of the DWT and ChNN based fault location estimation algorithm, the trained set of ChNNs are tested with remaining 52200 distinct fault patterns. Each of the ChNN has been tested with 2610 distinct fault patterns, which are different from those patterns used during training.

Traditional ANN based approaches suffer large errors in fault location estimation due to the presence of DC offsets which occur with variation in fault inception angles [49, 119, 142]. However, due to selection of only higher frequency components as inputs, the proposed scheme proved to be immune to any fault or system parameter variation as shown in Figure 6.19. This figure shows the fault location errors as a function of fault distance for A-g fault corresponding to all 2610 test fault cases. It is worth to note here that, the maximum difference between the actual fault location and predicted fault location is around 4 km. However, it is less than 1 km for majority of the fault cases. Similar fault location error has been observed for all other considered fault types also.

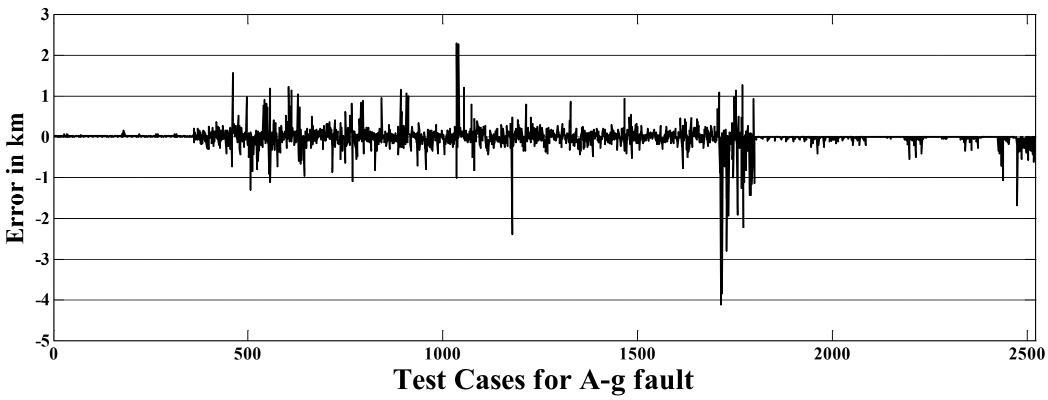

Figure 6.19: Fault location errors in km for A-g type of faults

The absolute maximum and absolute average fault location errors for all considered fault types at various fault locations are shown in Figure 6.20 and Figure 6.21. The maximum error observed during testing is 2.5%. This error has been observed for a fault located just after the compensator. This is due to the fact that the variation in frequency spectrum is maximum for a fault just after the compensator. For most of the fault distances, maximum error is less than 1%. Moreover, from Fig. 6.21, an average error of less than 0.2% has been observed (corresponding to all 52200 fault patterns). Thus, the suggested technique has been proven to be insensitive to the fault inception time, compensation level, fault resistances and pre-fault power flow level. Figure 6.22 and Figure 6.23 show the absolute average errors for each type of fault.

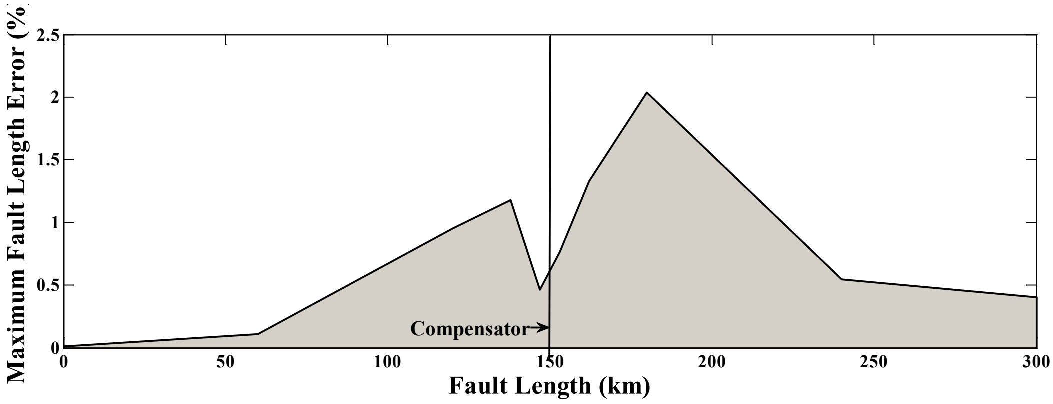

Figure 6.20: Absolute maximum fault location errors with DWT-ChNN approach

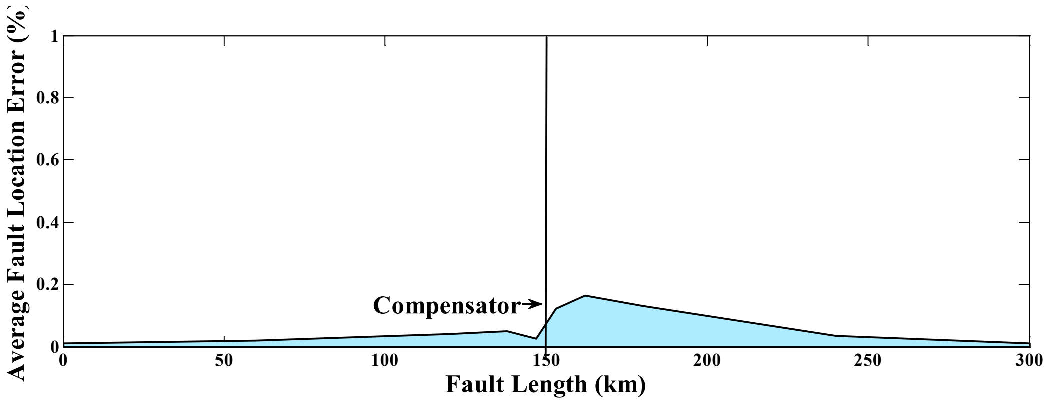

Figure 6.21: Absolute average fault location errors with DWT-ChNN approach

Error! Not a valid bookmark self-reference. shows the detailed break-up of average and maximum errors for 2610 fault cases for each considered fault type at various levels of compensations.

Table 6.10: Performance Evaluation of the DWT and ChNN based fault location algorithm

Type of Fault	25% Compensation		50% Compensation		75% Compensation	
	Absolute Average Error (%)	**Absolute Maximum Error (%)**	**Absolute Average Error (%)**	**Absolute Maximum Error (%)**	**Absolute Average Error (%)**	**Absolute Maximum Error (%)**
	Before Compensator					
A-g	0.0231	0.4393	0.0308	1.3756	0.0449	0.7956
B-g	0.0089	2.8067	0.0060	0.1865	0.0083	0.1355
C-g	0.0445	0.7833	0.0438	0.7068	0.0472	0.8208
AB-g	0.0065	0.1949	0.0129	0.8250	0.0167	1.0176
AC-g	0.0361	0.3967	0.0552	1.2493	0.0625	1.7058
BC-g	0.0061	1.0633	0.0164	1.2920	0.0223	1.1667
ABC-g	0.0145	0.8956	0.0212	0.7535	0.0258	0.9793
AB	0.0066	0.2088	0.0113	0.3723	0.0136	0.3746
AC	0.0806	0.8105	0.1117	1.4491	0.1130	1.7462
BC	0.0404	2.2826	0.0335	0.7360	0.0403	1.8633
	After Compensator					
A-g	0.1559	2.1239	0.2020	2.3300	0.2214	3.4549
B-g	0.0140	0.7174	0.0135	0.1768	0.0251	0.7054
C-g	0.1381	2.1773	0.1544	2.4889	0.1845	3.0944
AB-g	0.0133	0.6767	0.0134	0.6725	0.0252	1.1415
AC-g	0.0123	0.4806	0.0165	1.4164	0.0296	1.9000
BC-g	0.0397	0.5481	0.0437	0.7237	0.0559	1.5749
ABC-g	0.0216	2.1628	0.0406	2.1796	0.0446	3.8206
AB	0.0449	0.5650	0.0425	0.4563	0.0468	0.4100
AC	0.0236	1.4283	0.0389	1.7003	0.0536	1.3373
BC	0.4643	2.8733	0.6704	3.5459	0.5204	3.1089

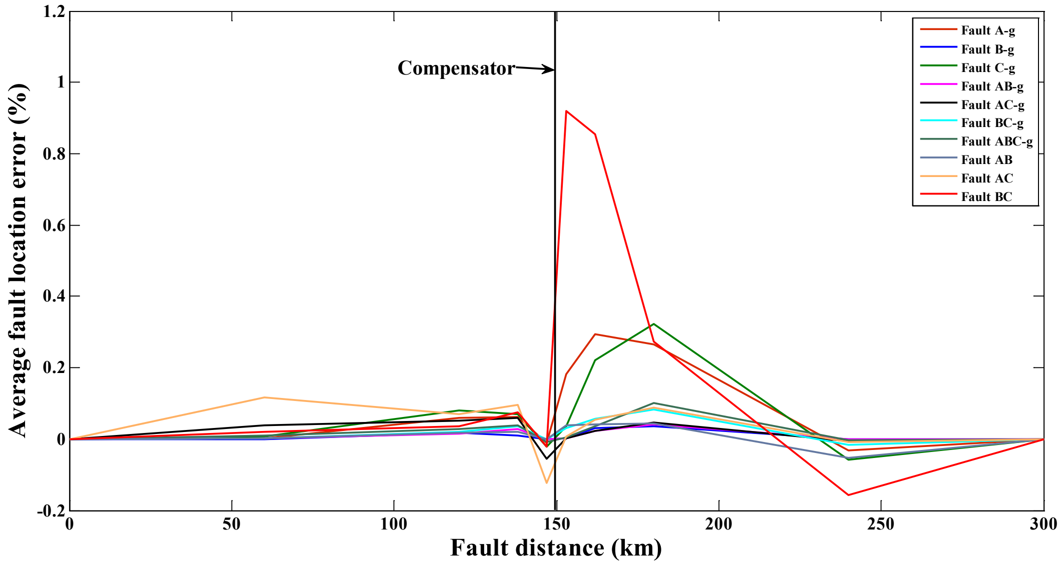

Figure 6.22: Absolute average fault location error corresponding to each fault type with DWT-ChNN approach

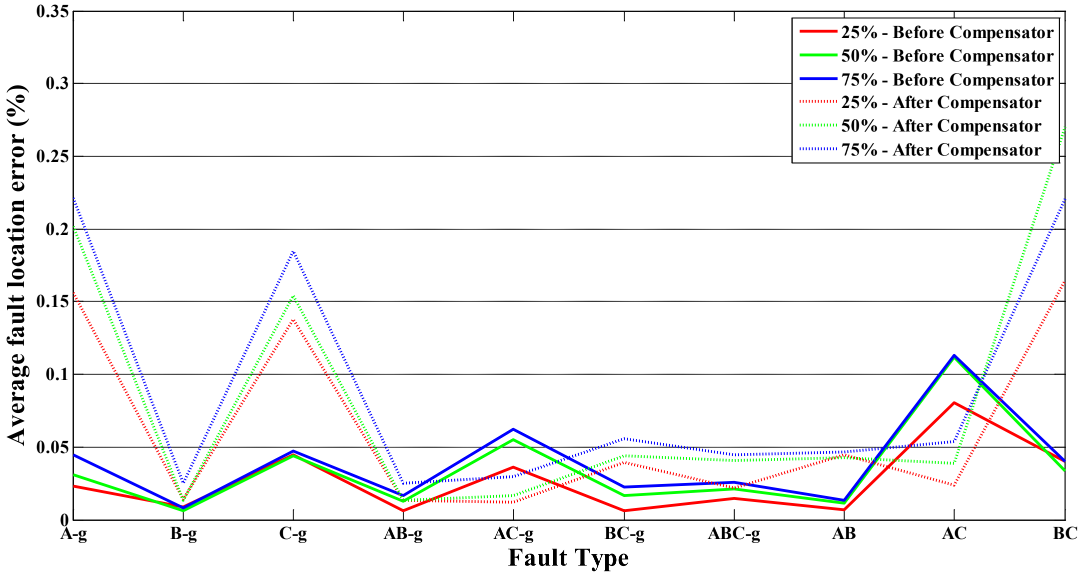

Figure 6.23: Average error for each type of fault

6.7 PERFORMANCE COMPARISON WITH PHASOR ESTIMATION BASED FAULT LOCATION METHOD

Four different fault location approaches for series compensated transmission lines have been described and implemented in this chapter. Initial three approaches used phasor estimation method for fault location calculations, while, the fourth one applies DWT and ChNN based approach.

The results obtained from the DWT and ChNN based algorithm have been compared with those obtained by the other three fault location schemes. The comparative results are summarized in Figure 6.24. From this figure it is observed that the DWT and ChNN based algorithm is best in comparison to the phasor estimation based methods. Further, the comparative performances of the DWT and ChNN based method and the LSE based method for all types of faults are shown in Fig. 6.25. From this figure it is again observed that irrespective of the type of fault, the DWT and ChNN based scheme always outperforms the LSE based scheme. Further, the DWT and ChNN based approach is more robust to provide almost equal level of accuracies for all considered fault types.

The ChNN method with DWT applies single layer neural structure only, which is simple in design and training. Moreover, a well-trained ChNN eliminates the requirement of online computation necessary for phasor estimation approaches.

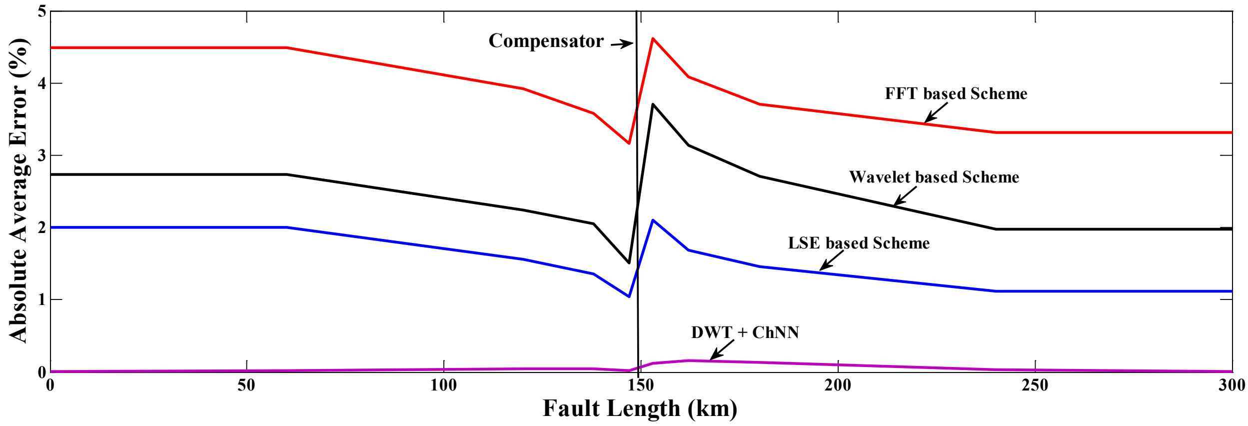

Figure 6.24: Average fault location errors at various fault distances for different fault location estimation methods

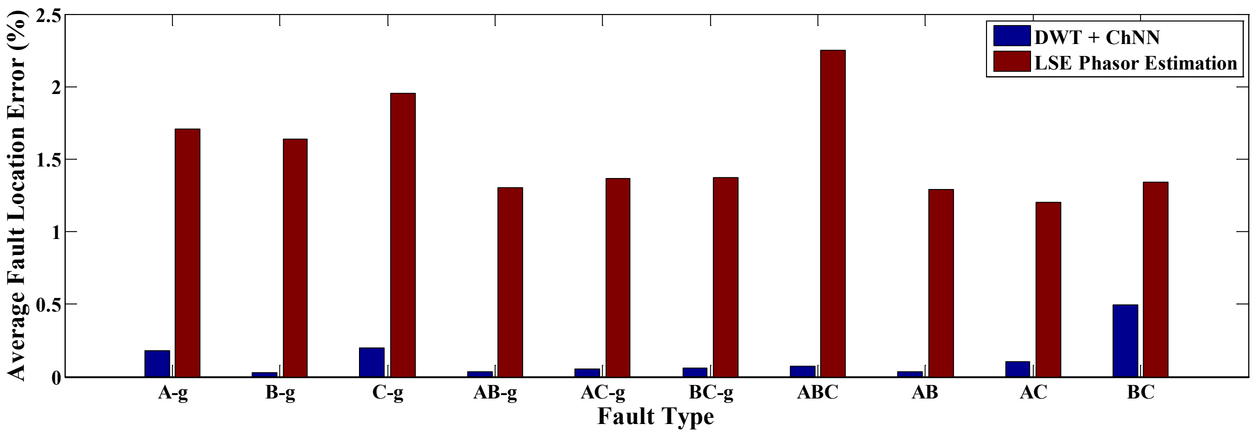

Figure 6.25: Comparison of LSE and DWT+ChNN based schemes for absolute average fault location errors

6.8 EFFECT OF INACCURACIES OF FAULT TYPE AND ZONE IDENTIFICATION ON FAULT LOCATION

The accuracy of fault location estimation is largely dependent on correctly identified fault type and zone in this scheme. An error in fault zone identification results in wrong selection of the ChNN group, which ultimately results in a huge error. Further, because of erroneous fault classification, an improper ChNN in a particular group would be selected.. It is observed from Table 4.8 that, the maximum fault classification accuracy obtained with ChNN based pattern recognition scheme is 99.44%. A total of 300 fault cases are incorrectly classified in this method. On the other hand, for 683 fault cases, incorrect fault zones have been determined (Table 5.11). Further, for few fault cases, both the fault zone and the fault type have been identified incorrectly. Table 6.11 shows average and maximum fault location estimation errors obtained for three cases: i) erroneous fault type, ii) erroneous fault zone and iii) erroneous fault type and zone. The level of inaccuracy is very high in all these cases. Therefore, an accurate fault type and fault zone identification scheme is a pre-requisite for correct estimation of the location of the fault.

Table 6.11: Errors in fault location estimation with erroneous fault type and zone identification

	Number of fault cases	**Average Fault location error**	**Maximum fault location error**
Error in fault classification only	187	8.5273%	17.1348%
Error in fault zone identification only	570	17.5795%	38.1682%
Error in both fault type and zone identification	113	22.1057%	41.1859%

6.9 CONCLUSION

Three phasor based fault location estimation methods on series-compensated transmission line have been studied and evaluated. All considered methods utilize voltage and current phasors from relaying end only. However, results reveal many drawbacks of phasor estimation for fault location.

A large amount of harmonics and exponentially decaying DC component in fault generated transient affects phasor estimation adversely. With quarter cycle delay, DWT produces better results for fault location estimation than DFT. However, LSE based fault location method performs best among all the phasor based approaches. However, overall accuracy reveals requirement of a more accurate fault location estimator.

A new artificial intelligence based fault location estimation method has been proposed in this chapter. The method integrates DWT and ChNN for fault location estimation. Two sets of ChNN subroutines are developed to predict the possible locations of the fault on either sides of the series compensator. Evaluation studies for a large fault data set have demonstrated that the proposed fault location algorithm is highly accurate.

However, for all fault location algorithms for series compensated transmission line, prior knowledge of fault type and fault zone are essential. Any error related to them results in higher error in fault location estimation.

CHAPTER 7: VERSATILE RELAYING ALGORITHM FOR DETECTION AND CLASSIFICATION OF FAULTS ON UNCOMPENSATED AND SERIES COMPENSATED TRANSMISSION LINES

Inclusion of series compensation in transmission line necessitates significant change in protection methodology. Therefore, the practical transmission line protection domain is presently divided into two distinct areas; protection of uncompensated transmission line and protection of series compensated transmission lines. At least, a new relay setting is always required to accommodate addition of the series compensator in a transmission line. Conversely, protection system designed for series compensated transmission line faces difficulty during the maintenance or bypass operation of the compensator. This necessitates the requirement of a transmission line protection algorithm that can provide effective protection for a transmission line irrespective of the presence or absence of series compensation, without any change in the methodology. A new, fast and versatile real time transmission line protection algorithm is presented in this chapter. The proposed method is capable of providing fault detection and classification for uncompensated as well as fixed series compensated transmission line with different levels of series compensations; without any functional customization and with the same level of accuracy. The algorithm has been developed with three-phase current measurements only that eliminates the requirement of voltage measurement and reduces the computational burden.

7.1 INTRODUCTION

Transmission line protection with series compensation is considered to be one of the difficult tasks for protection engineers. Protection and control of the transmission line need to be adapted to the alteration introduced by these devices.

As already discussed in Chapter 2, inclusion of series compensation increases power transfer capacity of the transmission line and helps to improve the transient stability of the system. In addition, it improves the voltage control, power flow control and reduces the line losses. The integration of the series capacitor into the transmission line makes the line protection more complex due to the changes in line parameters as described in Chapter 2.

Over the years, considerable efforts have been devoted for the development of transmission line protection. With development of digital processing techniques and Artificial Intelligence (AI), the protection system has become faster and accurate. The modern protection schemes utilize fault information to aid the calculations of impedance by the impedance relays. In an initial approach for application of AI technique for fault classification, Dalstein et al. [24] and Aggarwal et al. [143] established the use of multilayer ANN. The fuzzy logic based scheme has been explored in [96]. Potential of WT for application in protection system has been established in [42, 144]. Applications of WT with AI techniques for fault analysis have been demonstrated in the literature, such as with WT and ANN [145], WT and SVM [124], WT and fuzzy in [146].

In an early approach for protection of series compensated line, developed a protection algorithm based on travelling waves has been developed in [35]. Use of WT for fault analysis has been proposed in [114] and [97]. An application of ANN for adaptive protection scheme (for determining the fault type and estimating the distance) of series compensated transmission line has been made in [50]. Application of WT along with various AI techniques for protection of series compensated transmission line has also been proposed in the literature. WT with SVM has been applied for fault classification in series compensated transmission line in [22]. In yet another implementation of WT, fuzzy logic has been applied for fault type identification in [23].

7.2 MOTIVATION FOR DEVELOPMENT

The problem of fault detection, classification and fault distance calculation on a transmission line has been investigated for a very long time. It has been one of the major concerns of the power industry, and a systematic development pattern can be noticed in the literature. As discussed in the previous section, a significant improvement in terms of accuracy and speed in transmission line protection has been obtained with development of digital processing techniques and AI.

However, it is noticeable from the literature review that, the development efforts for protection of a transmission line so far, are normally split into two domains,

i) Protection of a normal two terminal transmission line.
ii) Protection of series compensated transmission line.

In this scenario, it is evident that a new setting is required for a relay on uncompensated transmission line with introduction of series compensation. On the other hand, during maintenance or bypass operation of the compensator the settings of the relay need to be changed. This necessitates the development of a protection scheme which is capable of providing protection to both types of transmission lines without changing the relay settings. The proposed algorithm of this chapter works efficiently for normal two terminal uncompensated overhead EHV line and needs no alteration in methodology, when this line is subjected to different levels of fixed series compensations.

Being a non-stationary phenomenon, the information about particular spectral components in the currents and voltages at the time of fault is very important. An ability to analyze the signal in time and frequency domain simultaneously makes DWT a better processing tool (as discussed in Chapter 3) and is used in this method. The spectral energy (at different frequency band) of the windowed current signals obtained with the help of DWT is utilized for fault detection and classification.

Being a shift variant transform, most implementations of the DWT works on sampling and analysis of a full cycle data [42, 147]. The use of a full cycle data for fault detection makes the protection system slower. This indicates the necessity of a fault detection system which requires reduced amount of data.

During the last decade, digital relaying scheme has been greatly benefited from the development of AI techniques. The application of classifier is continuously increasing for solving classification problems. The fuzzy classifiers have been proven to be efficient for protection purpose [23, 96, 111]. However, introduction of the non-linear components with inclusion of the series compensation makes the fuzzy system difficult to design. In the absence of an appropriate mechanism for deciding the classification parameters, the SVM is also difficult to apply. In this scenario, the generalization and fault tolerance capability makes the ANN a potential classifier for protection requirements. However, in the absence of an appropriate methodology for designing the ANN, the performance of ANN cannot be guaranteed. This indicates the requirement of a classifier that is independent of the topology of the ANN and also insensitive to the parameter variation.

The above discussion indicates the requirement of a transmission line protection system with the following characteristics:

1. The protection system should be able to provide effective protection when series compensation is introduced in the line.
2. The relaying mechanism for series compensated transmission line should not get affected by fault or bypass operation of the capacitor bank.
3. The protective relay should be fast enough to clear the fault at the earliest. Therefore, it should require minimum amount of post fault data.

7.3 PROPOSED FAULT DETECTION AND CLASSIFICATION SCHEME

The proposed algorithm has been developed with an objective to make it work for both uncompensated and series compensated transmission lines without any change in the methodology. The literature suggests that lower frequency components of fault current transients are least affected, when series compensation is introduced into the transmission line [114]. Therefore, in this algorithm, lower frequency components of the three-phase fault currents at the relaying end are captured and processed to generate a wavelet energy factor. This energy factor is utilized for fault detection and fault type identification.

Most implementations of the DWT work on sampling and analysis of a full cycle data as discrete wavelet transform is shift variant [42, 147]. To accelerate the fault detection process, the proposed algorithm has been developed with sliding window method for data processing and a data hold circuit that stores results for most recent processed data. A sliding window of one cycle (20 ms for 50 Hz supply frequency) and slide size of 1 ms per sweep has been chosen for the implementation. Therefore, data corresponding to 1 ms of new measurement is included in the current iteration while data corresponding to oldest 1 ms of the just finished sweep is removed. Figure 7.1 (a) shows this sliding window concept. Since the comparison of energy is made with respect to the previous cycle, the previous cycle is shown in Figure 7.1 (b).

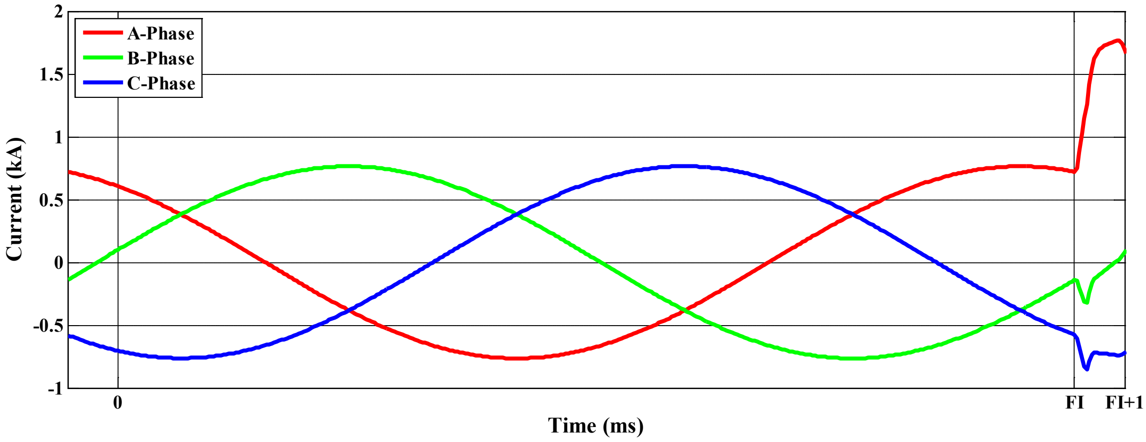

Figure 7.1 (a)

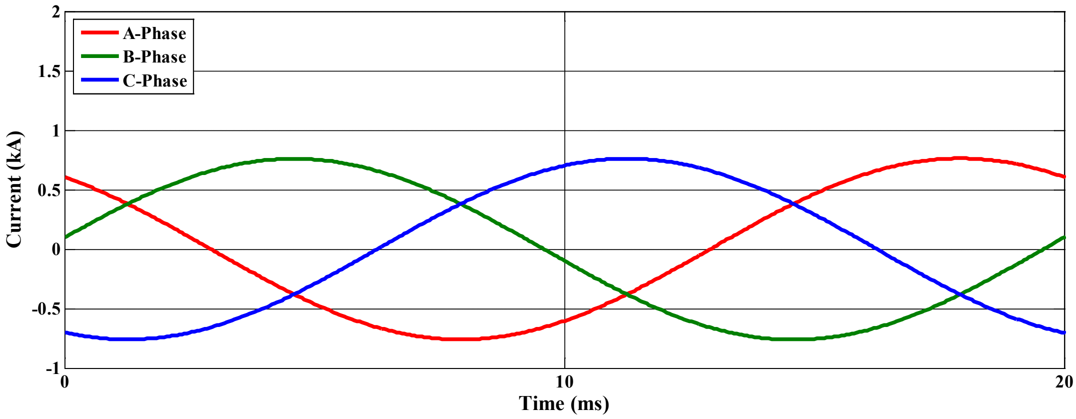

Figure 7.1 (b)

Figure 7.1: (a) Fault instance (FI) waveforms of current for fault inception

Figure 7.1: (b) Pre-fault current waveforms corresponding to identical phase angles

The schematic block diagram of the proposed scheme for fault detection is shown in Figure 7.2. The three phase current signals (corresponding to a given window) measured at the relaying end are passed through a low-pass filter to eliminate the higher-frequency components from the waveforms. A suitable DWT technique decomposes these filtered current signals to analyze it in a time-frequency domain. For this purpose, the ‘db4’ mother wavelet has been used in this work. The spectral wavelet energy at each level of the decomposition is then extracted to derive the sum of spectral energy. The overall energy derived from the decomposition is used as a measure for fault detection. Details are provided in the next section.

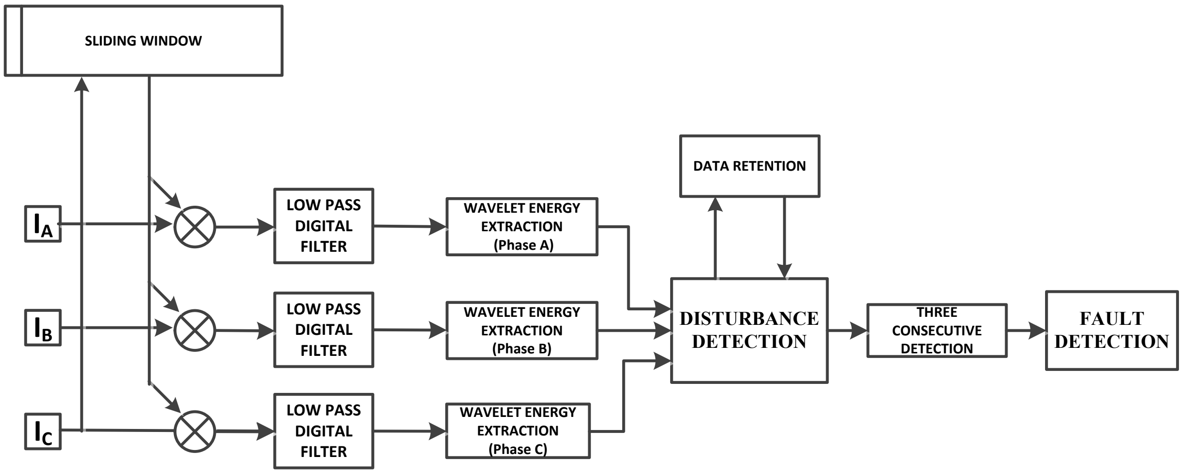

Figure 7.2: Versatile fault detection scheme

When the signal energies are computed for two consecutive cycles with current samples corresponding to identical phase angles (in both the cycles), in normal operating condition, energy extracted in the current cycle matches the energy calculated in the previous cycle. Any major deviation in their energies indicates the presence of a non-healthy condition. However, this may be due to transitory situations, as fresh data corresponding to only 1 ms period are included. To avoid erroneous tripping under such momentary transients, trip decision is taken only if such abnormality is detected in three consecutive comparative assessments of the signal energy. Figure 7.3 (a) shows a fault case with three consecutive windows showing change in normal values and Figure 7.3 (b) shows the signal in the previous cycle corresponding to the same phase angles as of current cycle, which will be used as base value for comparison purpose.

Moreover, the energy sum of these three consecutive mismatches for each phase forms the base scalar value to be used for fault type classification. A major deviation in the spectral energy value for any phase indicates a probability of the fault in the corresponding phase. As the sum of all three phase currents represents the zero sequenc current, higher value of summation of three phase wavelet energies suggests the involvement of the ground in the fault. The Chebyshev neural network has been trained in this case for automatic identification of the phases/ground involved in the fault.

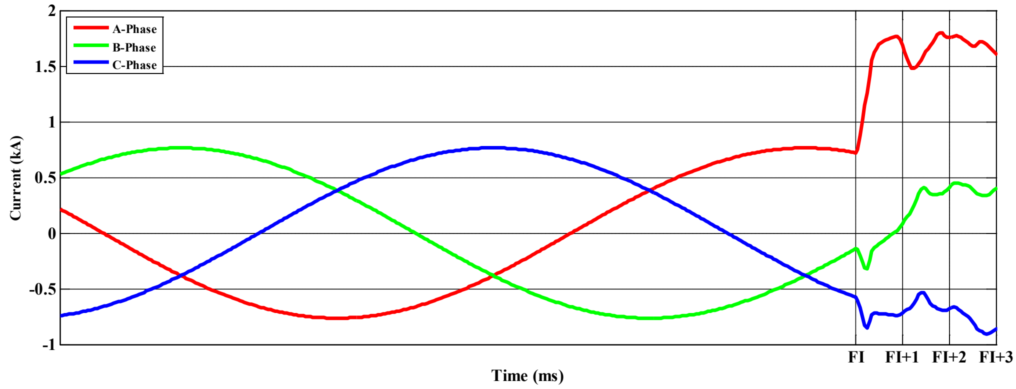

Figure 7.3 (a) : Three-phase current waveforms at the instant of the fault

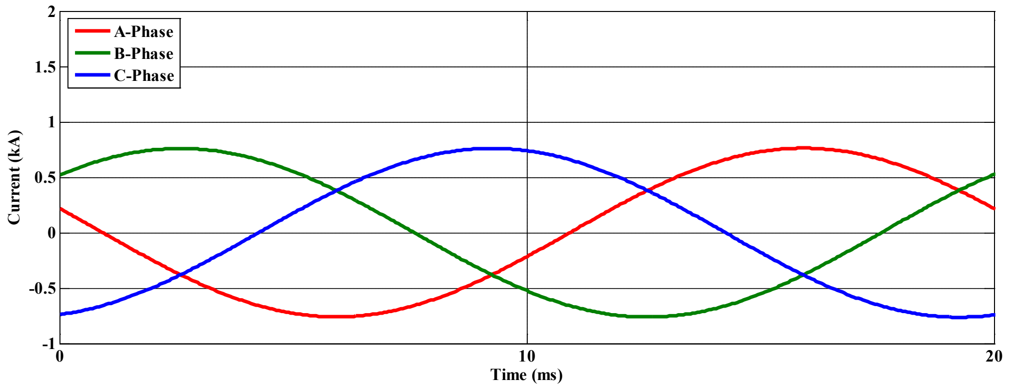

Figure 7.3: (b) Pre-fault three-phase current waveforms corresponding to identical phase angles

7.3.1 Fault Detection

The schematic flow chart of fault detection logic of the developed algorithm that works for both uncompensated and series compensated line with same accuracy without any functional modification is given in Figure 7.4. The fault detection logic has been developed using a sampling frequency of 5 kHz. The fault detection logic developed in this work operates with sliding window of one cycle (100 samples at 5 kHz sampling frequency); with 1 ms (5 samples) sliding size for each sweep as described in the previous section. Therefore, each new window carries 95 latest samples of the previous window along with 5 samples of most recent measurements. This windowed full cycle signal is then subjected to a low pass butterwort digital filter that eliminates any higher-frequency components above 250 Hz (5^{th} harmonic). As mentioned earlier, higher-frequency components of fault signal are more affected by inclusion of series compensation and therefore, only lower frequency components (up to 5^{th} harmonics) are utilized in this method. DWT on reconstructed three phase signals up to fourth level of resolution is performed with 'db4' as mother wavelet to extract the spectral components for further analysis.

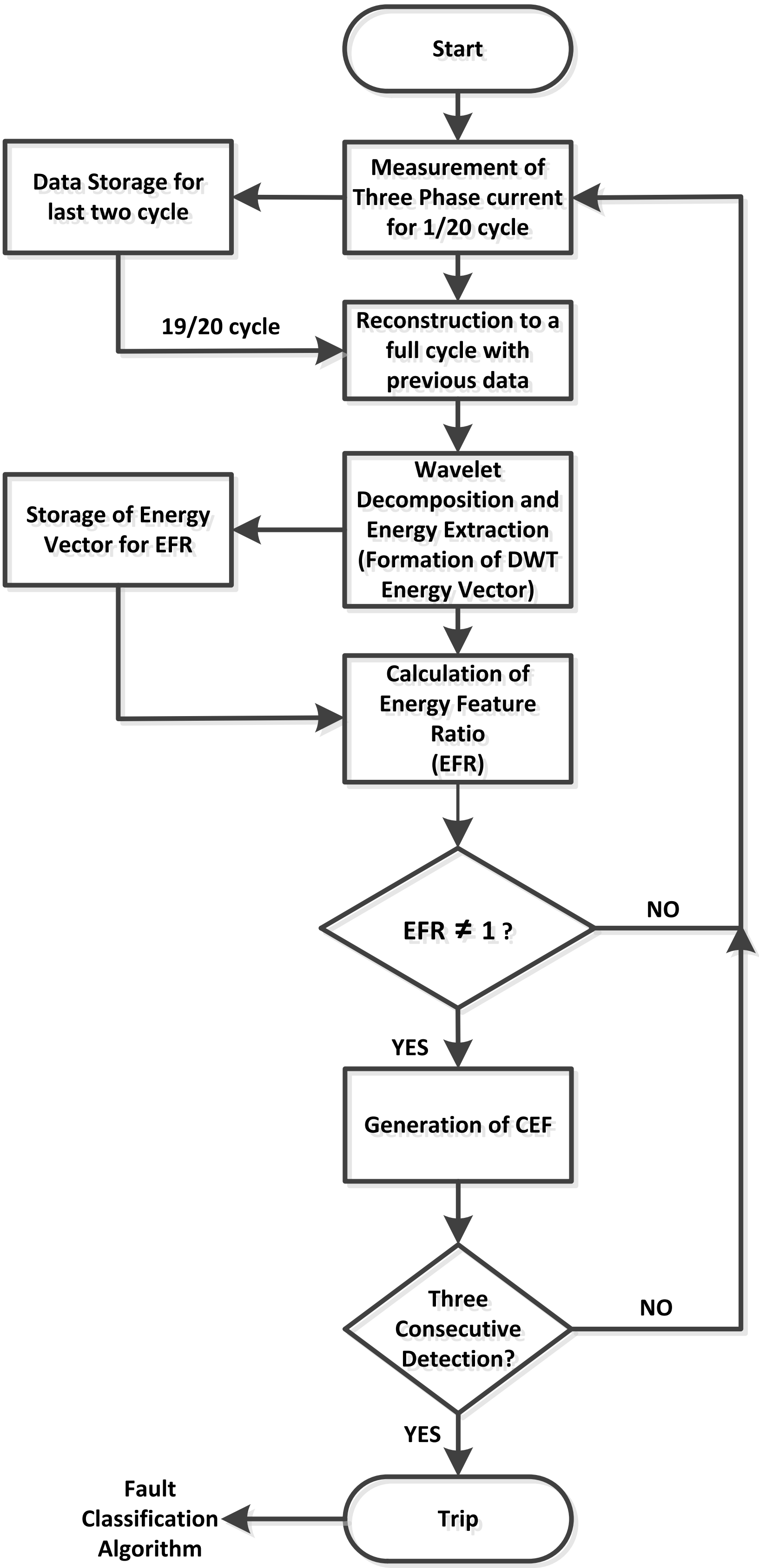

Figure 7.4: Flow chart of fault detection logic

In a case when wavelets form an orthogonal basis, according to Parseval's theorem, the energy of the each expansion components are related to their wavelet coefficients. The energy contained within the transform vector at all stages of the multi-resolution decomposition remains constant and can be given by equation (3.8). For ready reference it is reproduced here as equation (7.1).

$$E = \sum_{i=0}^{N-1} (W_i^m)^2 \tag{7.1}$$

An average energy content of the coefficients given by equation (7.1) at each resolution is computed. A feature vector $(k_{i,n}^{dwt})$ is proposed with four wavelet (detailed) sub bands as the approximate sub-bands do not give distinguishable change. The ith element of the feature vector for nth window is given by:

$$k_{i,n}^{dwt} = \frac{1}{c_i} \sum_{j=1}^{c_i} w_{i,j}^2 \qquad \text{Where, i=1,2,3,4} \tag{7.2}$$

Here, c_i represents the number of samples in an individual sub band and $w_{i,j}^2$ is the j^{th} coefficient of the i^{th} sub band. As a result, a DWT feature vector for each phase 'p' is formed and given by,

$$\mathrm{K}_{\mathrm{p,n}}^{\mathrm{dwt}} = \{ k_{1,n}^{dwt}, k_{2,n}^{dwt}, k_{3,n}^{dwt}, k_{4,n}^{dwt} \} \tag{7.3}$$

As discussed previously, the generated feature vector is compared with a feature vector generated from the samples (corresponding to the same phase angle) of the last full cycle window. This feature vector $\left(K_{p,n-1}^{dwt}\right)$ is stored in the memory. A ratio of these two energy vectors forms "Energy Feature Ratio (EFR)" for each phase:

$$EFR_{p,n} = \frac{\sum_{i=1}^{4} k_{i,n}^{dwt}}{\sum_{i=1}^{4} k_{i,n-1}^{dwt}} \tag{7.4}$$

The EFR is a numeric value and represents ratio of wavelet energy content for each phase. In normal operating condition, this ratio should be unity. A sum of EFRs for all three phases and ground gives the "Fault Detection Ratio" (FDR) for present window ('*n*') as:

$$FDR_g = \sum_{p=A,B,C,N} EFR_{p,g} \tag{7.5}$$

In the steady state, the value of FDR_n should be 4. A major deviation in FDR from this value indicates a probability of fault in the system. After several studies using the proposed algorithm, it was concluded that a fault condition in the series compensated transmission line can be detected in a reliable way when the value of FDR deviates from 4. To eliminate the possibility of erroneous fault detection in case of switching or any other transient, the succeeding formations of FDRs $\left(FDR_{n+1}, FDR_{n+2}\right)$ are continued for next two measurements (1/20th of the cycle each) after the first detection. Deviations of FDR for three consecutive measurements confirm the presence of a fault condition in the system, and algorithm issues signal for fault detection (Figure 7.4). The fault detection has been performed with summation of these three consecutive values of FDRs.

$$FDR_{n,3} = FDR_n + FDR_{n+1} + FDR_{n+2} \tag{7.6}$$

Here, $FDR_{n,3}$ represents summation of FDR for three consecutive windows from the n^{th} window (when first variation in FDR is detected). Third measurement after fault inception (FDRn+2,3 =18.0624)

Figure 7.5 shows the waveforms of an A-g fault with 0 Ω fault resistance, fault inception angle = 45˚, line loading angle (δ) = 10˚ occurring at 180 km distance of the 300 km mid-point compensated transmission line given in Figure 4.1. The compensation level has been set at 50% of the total line inductive reactance. Figure 7.5(a) shows a healthy condition in the power system. The waveforms corresponding to the current window and those corresponding to the previous window almost match each other thereby giving a value of FDR equal to 12 in steady state. Figure 7.5(b) includes the last measurement that carries a fault condition with it. A clear deviation in the current signal can be identified due to an A-g fault. In this and subsequent figures, the acronym 'FI' denotes the fault instant. This deviation takes the FDRs to a higher value of $FDR_{1,3}$ = 12.5472 for three consecutive windows (window 1,2,3), starting from window 1, when first deviation in FDR is detected. As mentioned earlier, the process continues for next two measurements that give FDR values of $FDR_{2,3}$ = 15.6173 and $FDR_{3,3}$ = 18.0624 ($FDR_{2,3}$ and $FDR_{3,3}$ represents summations of FDRs for windows 2,3,4 and 3,4,5 respectively). Three successive FDR variations confirm the presence of a fault in the system. In this case, the fault detection has been made with three successive measurements that take 1 ms each. Therefore, the fault is detected after minimum time of 3 ms only.

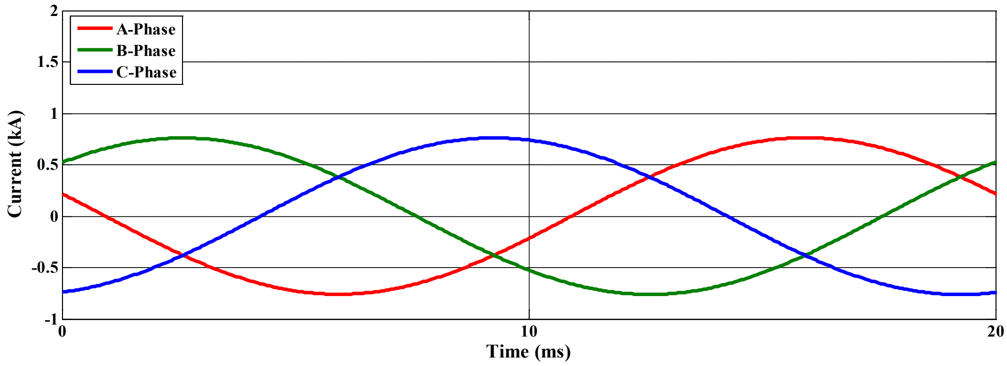

Figure 7.5 (a) Healthy condition, measurements match with stored waveform in memory (FDR=12)

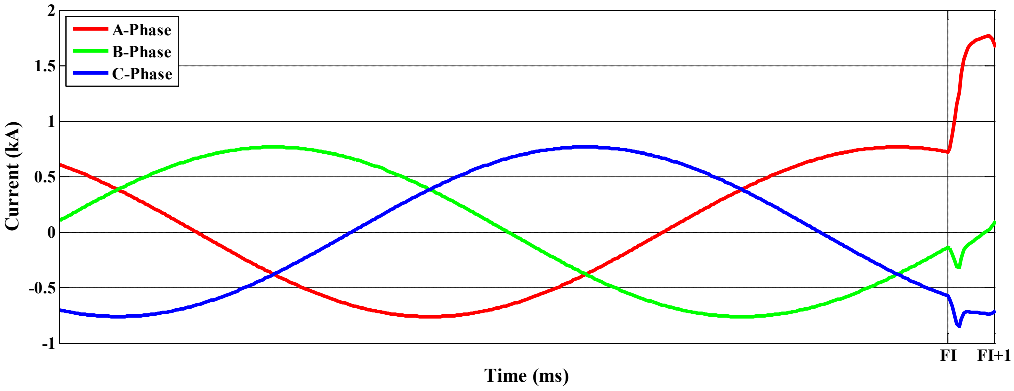

Figure 7.5 (b) First measurement after fault inception ($FDR_{n,3}$ = 12.5472)

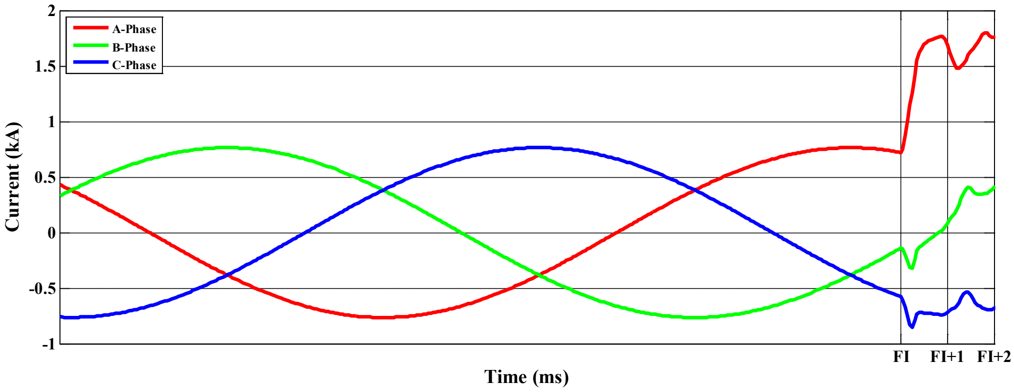

Figure 7.5 (c) Second measurement after fault inception ($FDR_{n+1,3}$ = 15.6173)

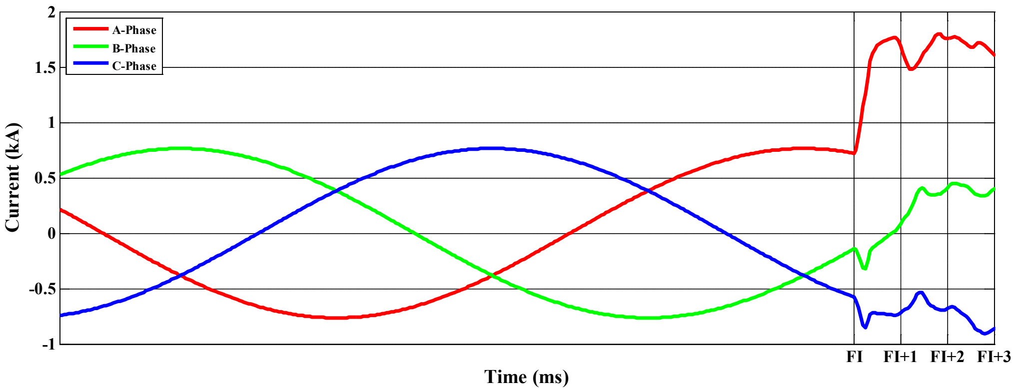

Figure 7.5 (d) Third measurement after fault inception ($FDR_{n+2,3}$ =18.0624)

Figure 7.5: Fault Detection process for a A-g Fault

The FDR for three consecutive detections for different type of faults at different fault locations, with different fault resistances, fault inception angle and line loading angle are shown in Table 7.1.

Table 7.1: Variation of FDR and detection time for compensation levels

Fault Type	X_c	Fault Resistance (Ω)	FIA	(δ)	Value of FDR			Fault Detection Time (ms)
					$FDR_{1,3}$	$FDR_{2,3}$	$FDR_{3,3}$	
Fault at 60 km from relaying end and 90 km before compensator								
A-g	No	25	45	10	12.4069	13.4938	17.5480	4
A-g	25%	25	45	10	12.3277	13.4418	16.8643	4
A-g	50%	50	45	10	13.3923	16.2873	18.7667	5
B-g	75%	50	45	20	12.8171	14.4775	15.5191	3
C-g	50%	50	80	30	12.5248	13.5974	15.2629	7
AB-g	No	150	135	20	13.2625	16.1081	15.9130	6
AC-g	75%	100	10	20	12.9174	13.9432	15.3826	4
BC	50%	150	10	10	12.3365	14.7105	19.1366	7
ABC-g	50%	25	45	10	12.7243	13.7919	20.7401	4
AB	50%	25	80	20	12.3019	14.3512	18.2197	6
Fault at 120 km from relaying end and 30 km before compensator								
A-g	No	25	10	10	12.6289	14.0213	16.5299	3
C-g	No	50	10	20	12.5577	12.8242	12.4674	4
BC-g	25%	100	45	30	12.8332	13.7009	14.5703	7
BC-g	25%	150	45	10	12.454	12.3338	14.1951	5
AC-g	50%	0	45	20	13.1975	15.6019	19.4325	5
AC	50%	25	80	30	13.2904	15.5719	18.1961	7
AB	75%	25	80	10	14.5554	19.0199	19.8769	7
AB-g	75%	50	80	20	13.0012	14.4520	14.2988	7
BC	25%	50	135	30	13.1572	15.3655	18.9933	8
BC	No	100	135	10	12.4368	12.6634	12.3029	6
Fault at 180 km from relaying end and 30 km after compensator								
A-g	No	25	10	10	12.4464	13.5838	15.8508	3
C-g	No	50	10	20	12.4408	12.6542	12.4012	4
BC-g	25%	100	45	30	12.6057	13.1660	13.9127	7
BC-g	25%	150	45	10	13.4574	15.0117	15.5033	7
AC-g	50%	0	45	20	12.6490	14.1470	15.7812	7
AC	50%	25	80	30	12.9764	14.6314	15.9101	7
AB	75%	25	80	10	13.4006	15.9946	16.5818	7
AB-g	75%	50	80	20	12.4975	13.0433	12.6490	7
BC	25%	50	135	30	12.9497	14.5655	16.8538	8
BC	No	100	135	10	12.3501	12.6318	12.1697	6

Fault at 240 km from relaying end and 90 km after compensator								
A-g	25%	0	10	10	13.1944	15.1014	18.2646	4
B-g	50%	25	10	20	12.4358	13.1739	13.5517	3
C-g	75%	50	45	30	12.5080	12.6836	12.6072	8
AB-g	No	100	45	10	12.9799	15.4409	17.9015	5
AC-g	25%	150	80	20	12.7396	13.6050	13.4699	7
BC-g	50%	0	80	30	12.7934	14.1663	16.2288	8
ABC-g	75%	25	135	10	12.6877	15.4320	18.9825	6
AB	No	50	135	20	12.7994	15.3911	17.9155	6
AC	25%	100	45	30	13.3256	14.4900	14.6479	6
BC	50%	150	45	10	12.5511	12.8075	12.8453	5

As mentioned earlier, three consecutive detections are found necessary and sufficient for fault detection to avoid mal-operation during transient conditions. For some faults, detection of three consecutive mismatches over threshold value takes more window sweeps (Table 7.1) and therefore more detection time is necessary. The time of operation depends on fault current variation from its base value. This deviation largely depends on type, location, severity, fault resistance and inception angle of the fault.

7.3.2 Fault Classification

As discussed earlier, the developed algorithm does not require any further measurement or data other than those used during the fault detection process. Figure 7.6 shows the schematic flow-chart of the fault classification scheme. During fault detection process, aggregation of three consecutive EFRs for each phase is performed to generate a "Fault Classification Ratio" (FCR) to identify the involvement of phases in the fault as shown in equation (7.6).

$$FCR_p = EFR_{p,n} + EFR_{p,n+1} + EFR_{p,n+2} \tag{7.7}$$

The FCR represents the total wavelet energy in the specific phase. A deviation in energy from its normal value of 12 (4*unity*(3 consecutive detection) = 12) indicates the presence of fault in the specific phase. Therefore, FCR is calculated as variation from its normal value of 12 :

$$FCR_p = (EFR_{p,n} + EFR_{p,n+1} + EFR_{p,n+2}) - 12 \tag{7.8}$$

It is worth to note here that the FCR is a scalar value. To identify the involvement of ground in the fault, the FCR for ground is calculated in the same way as for other phases, except that the input to the DWT is zero sequence current given in equation (7.9).

$$I_g = I_A + I_B + I_C \tag{7.9}$$

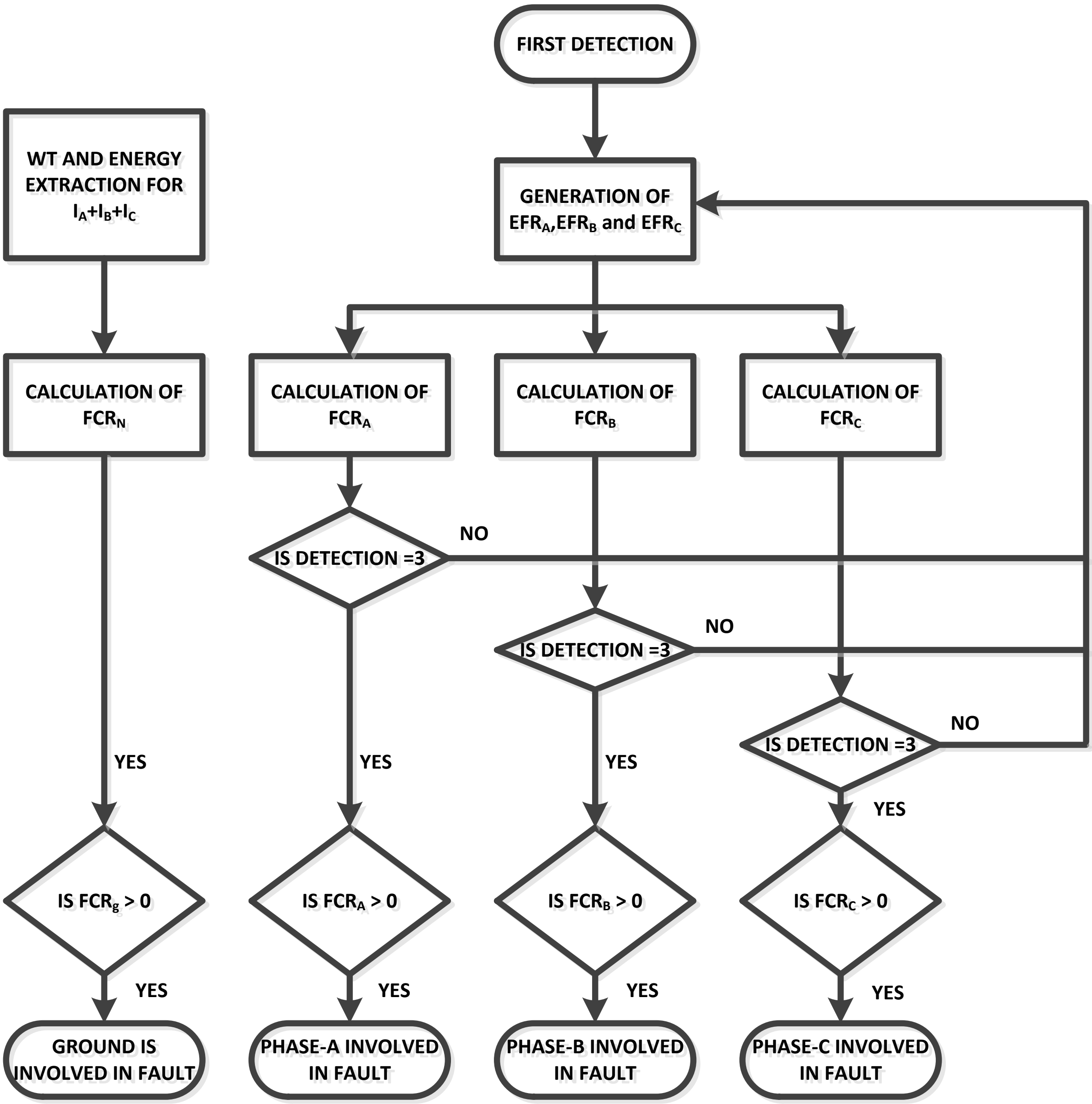

Figure 7.6: Flow chart for fault classification

The zero sequence current is subjected to DWT energy analysis and the FCR for ground is calculated as in equation (7.7). Any higher positive value of FCR_N indicates the involvement of ground in the fault circuit. Figure 7.6 shows the schematic flow chart for fault classification in the developed algorithm.

Figure 7.7 (a) shows the waveforms for an A-g fault occurring at 180 km from the relaying end, with a fault resistance of 50 Ω and fault inception angle of 45˚ at line loading angle of 10°. The fault provides FDR values of 12.4412, 13.4200 and 15.0518 for three consecutive windows. Fault detection is achieved here at 3 ms after fault inception. The

FCRs generated for this fault are: 4.57166 (A-phase), -0.18129 (B-phase), -0.2142 (C-phase) and 21.6059 (ground). This clearly indicates that, the FCR of the faulty phase is quiet higher as compared to those of the other two healthy phases.

Similar observation is noticed with an B-C-g fault occurring at 120 km from the relaying end with line loading angle of 20°, fault resistance of 25 Ω and same fault inception angle of 45° as shown in Figure 7.7 (b). FDRs for this fault for consecutive detections are 14.1462, 18.8493 and 20.7251. The FCR for A, B and C phases are (-0.157), (9.811) and (7.3167) respectively while that for the ground is 20.0547. It is again clear that phase-B and Phase-C are involved in the fault as their indices are higher than that for phase-A which is near to its nominal value.

Table 7.2 gives some representative FCR values for the same faults used for fault detection in Table 7.1.

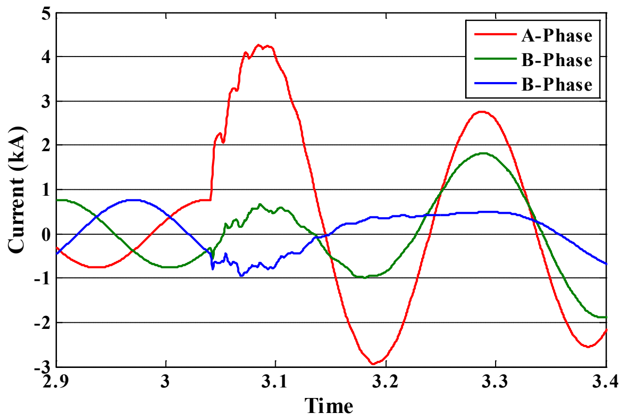

Figure 7.7 (a): Three phase current waveforms for A-g fault at 60% of the line with 50Ω fault resistance and 45 degrees of fault inception angle.

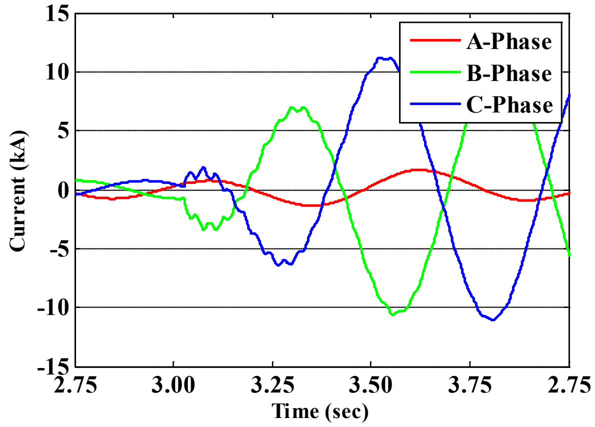

Figure 7.7 (b): Three phase current waveforms for B-C-g fault at 40% of the line with 25Ω fault resistance and 45 degrees of fault inception angle.

Table 7.2: Variation of FCR at various compensation levels and system conditions

Fault Type	X_c	Fault Resistance (Ω)	FIA	(δ)	FCR for Classification			
					FCR_A	FCR_B	FCR_C	FCR_N
Fault at 60 km from relaying end and 90 km before compensator								
A-g	No	25	45	10	6.9134	-0.1327	-0.0819	711.8089
A-g	25%	25	45	10	6.1716	-0.1674	-0.1204	60.8618
A-g	50%	50	45	10	11.9706	-0.1751	-0.0989	5.29950
B-g	75%	50	45	20	-0.1579	6.4544	-0.2327	251.7145
C-g	50%	50	80	30	-0.1955	-0.2086	5.0394	127.2183
AB-g	No	150	135	20	7.2687	1.4682	-0.2033	1251.2520
AC-g	75%	100	10	20	5.3714	-0.1952	0.3170	276.0343
BC	50%	150	10	10	-0.2410	6.3150	3.3597	-10.6628

ABC-g	50%	25	45	10	6.6115	3.6926	0.2022	-10.7121
AB	50%	25	80	20	4.7163	3.6492	-0.2428	-10.3935
Fault at 120 km from relaying end and 30 km before compensator								
A-g	No	25	10	10	6.6433	-0.0489	-0.1641	891.8113
C-g	No	50	10	20	-0.1004	-0.1448	1.3447	122.55331
BC-g	25%	100	45	30	-0.1708	0.3649	4.1604	607.2173
BC-g	25%	150	45	10	-0.0754	1.5586	0.7506	76.8194
AC-g	50%	0	45	20	11.2818	0.4199	-0.2197	184.7421
AC	50%	25	80	30	3.7795	-0.2296	6.7584	-10.4673
AB	75%	25	80	10	7.3647	9.5277	-0.1902	-3.1538
AB-g	75%	50	80	20	3.4082	1.8152	-0.2213	987.3954
BC	25%	50	135	30	-0.2360	3.1583	7.8437	-0.5739
BC	No	100	135	10	-0.2484	0.1170	0.7845	1.4956
Fault at 180 km from relaying end and 30 km after compensator								
A-g	No	25	10	10	5.4372	-0.0872	-0.2188	1225.0966
C-g	No	50	10	20	-0.1475	-0.1803	1.0742	101.6720
BC-g	25%	100	45	30	-0.1739	0.1614	2.9470	349.8913
BC-g	25%	150	45	10	-0.0833	2.1567	5.1491	36.9716
AC-g	50%	0	45	20	-0.1827	1.2065	4.8035	613.7088
AC	50%	25	80	30	2.3361	-0.2303	4.6621	-7.9056
AB	75%	25	80	10	4.0274	5.3909	-0.1911	-6.5913
AB-g	75%	50	80	20	1.3198	0.2765	-0.1565	526.6582
BC	25%	50	135	30	-0.2355	2.3822	5.4724	-5.0225
BC	No	100	135	10	-0.2482	0.0419	0.6079	-4.7320
Fault at 240 km from relaying end and 90 km after compensator								
A-g	25%	0	10	10	10.1106	-0.1380	-0.1620	46.2006
B-g	50%	25	10	20	-0.1786	2.8145	-0.2244	31.7543
C-g	75%	50	45	30	-0.2183	-0.1727	1.4400	1802.8994
AB-g	No	100	45	10	8.2433	1.5262	-0.1972	422.7778
AC-g	25%	150	80	20	1.4225	-0.2165	1.8588	14.6599
BC-g	50%	0	80	30	-0.2092	0.9689	5.6789	112.2757
ABC-g	75%	25	135	10	6.3835	1.5520	2.4168	-11.0501
AB	No	50	135	20	6.4499	3.1531	-0.2469	-3.9495
AC	25%	100	45	30	3.4902	-0.2401	2.4636	-6.1034
BC	50%	150	45	10	-0.2065	0.2392	1.4213	-10.7178

7.3.3 Application of Artificial Intelligence Classifier for Fault Type Identification

Fault classification is an on-line procedure, in which the faulty phase identification must be performed in a very short time span at the beginning of the fault. This leads towards the requirement of an online classification system that can identify the involvement of particular phase or ground in the fault.

Machine Learning (ML) is well-suited to deal with this type of task in an efficient way, as they can be trained off line and used on-line to classify fault types due to their generalization capabilities. Therefore, the task is to design a decision rule that is easy to compute which will also minimize the probability of misclassification. This leads to an artificial intelligence classifier. In a classifier, with the help of already classified examples, the optimal decision rule is formed for proper classification of the unseen pattern.

ANN, SVM and Fuzzy system have shown great promise as a classifier in the area of power system protection [23, 41, 49, 56, 96, 126]. However, single-layer Chebyshev functional expansion has the advantages of structural simplicity, faster speed of execution and insensitivity towards the classification variables. Therefore, ChNN has been used for the classification task in this work. The detail of ChNN is already given in Chapter 3, Section 3.7.3. The LSLM training method has been used for training in this work. The ChNN has been trained with less than 10% of the total number of generated fault data. The details of training and testing data sets are given in the following section.

7.4 DETAILS OF DATA GENERATION

To generate the fault data for training and testing of the ChNN, the system shown in Figure 4.1 has again been considered. By considering variations of different system and fault parameters, a total of 23400 fault cases have been generated. The details of these fault cases are given in Table 7.3.

Table 7.3: Details of the generated fault data

Level of Compensation	Fault Resistance (Ω)	Load Angle (Degree)	Type of Fault	FIA (Degree)	Fault Location (% of total line length)	Total Fault Cases
25%	0,25,50, 100,150	10,20, 30	A-g, B-g, C-g, A-B, A-C, B-C, AB-g, AC-g, BC-g, ABC-g (All ten)	0,45, 80, 115	10, 20, 30, 40, 49, 51, 60, 70, 80, 90	6000
50%	0,25,50, 100,150	10,20, 30	A-g, B-g, C-g, A-B, A-C, B-C, AB-g, AC-g, BC-g, ABC-g (All ten)	0,45, 80,115	10, 20, 30, 40, 49, 51, 60, 70, 80, 90	6000
75%	0,25,50, 100,150	10,20, 30	A-g, B-g, C-g, A-B, A-C, B-C, AB-g, AC-g, BC-g, ABC-g (All ten)	0,45, 80,115	10, 20, 30, 40, 49, 51, 60, 70, 80, 90	6000
0%	0,25,50, 100,150	10,20, 30	A-g, B-g, C-g, A-B, A-C, B-C, AB-g, AC-g, BC-g, ABC-g (All ten)	0,45, 80,115	10, 20, 30, 40, 50, 60, 70, 80, 90	5400
Total						**23400**

Out of these total 23400 fault cases, a set of 2280 fault patterns shown in Table 7.4 have been used for ChNN training. All remaining cases have been used for testing of the developed algorithm. It is clear from Table 7.3 and Table 7.4 that, the system parameters used for testing are different than those used for training.

Table 7.4: Details of training data set

Level of Compensation	Fault Resistance	Load Angle	Type of Fault	FIA	Fault Location (% of total line length)	Total Fault Cases
50%	0,50,150	10,30	A-g, B-g, C-g, A-B, A-C, B-C, AB-g, AC-g, BC-g, ABC-g (All ten types)	0,80	10%, 20%, 30%, 40%, 49%, 51%, 60%, 70%, 80%, 90%	1200
0%	0,50,150	10,30	A-g, B-g, C-g, A-B, A-C, B-C, AB-g, AC-g, BC-g, ABC-g (All ten types)	0,80	10%, 20%, 30%, 40%, 50%, 60%, 70%, 80%, 90%	1080
Total						**2280**

7.5 CHEBYSHEV NEURAL NETWORK IMPLEMENTATION

For AI based classification, as mentioned in Section 7.3.2, the ChNN has been implemented. The generated FCR for any fault pattern is subjected to a cluster of four pre-trained ChNN for fault classification; three ChNNs for each phase and fourth one for the ground. The overall fault detection and classification scheme is shown in Figure 7.8.

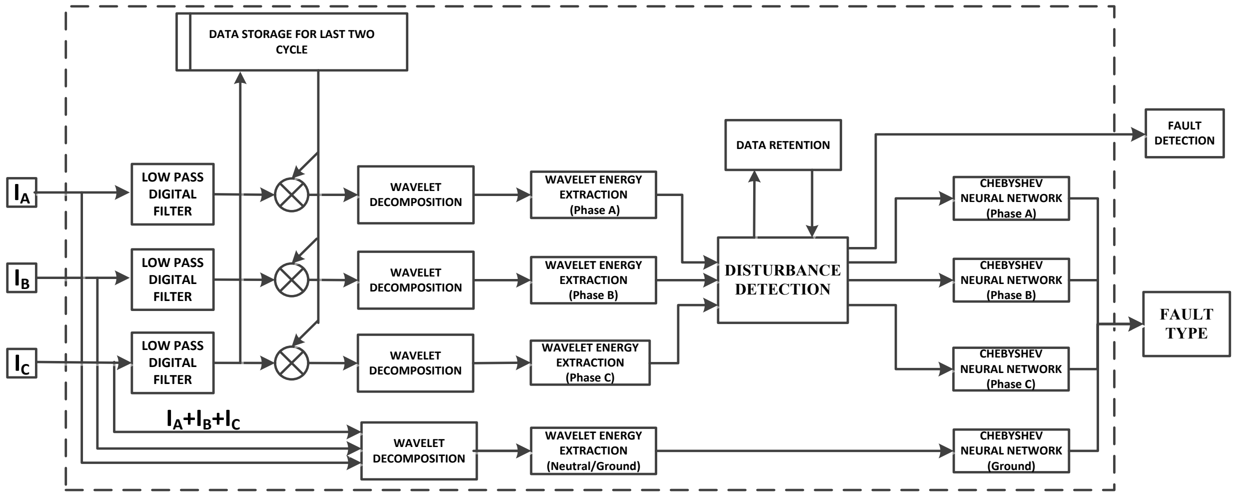

Figure 7.8 : Wavelet energy- ChNN based fault detection and classification scheme

A well-trained ChNN generates '1' as the output if the phase is involved in the fault, else generates '0'. A minor rounding off may be require in the final output. The sum of three phase currents is given as an input to the fourth ChNN to detect involvement of ground in fault. The ChNNs have been trained with 2280 training patterns as described in Table 7.4.

The training has been completed with default learning parameters and LM back propagation algorithm with Neural Network toolbox in MATLAB environment.

To decide the order of Chebyshev expansion in the neural network input, performance of the ChNN has been checked for various orders of expansion. If the order of Chebyshev expansion is higher, the nonlinear processing capability is stronger. However, this would result in heavy computational burdens [148, 149]. The level of accuracies for various levels of the Chebyshev expansion is given in Table 7.5. Maximum accuracy is observed at fourth level Chebyshev expansion. Therefore, the order of the Chebyshev functional expansion has been chosen to be 4 [148, 149].

Table 7.5: Performance of the ChNN based scheme for various levels of expansions

Level of Chebyshev Expansion	Numbers of Test Cases	Fault Classification Errors	Accuracy
Level Two	21120	425	97.98 %
Level Three	21120	402	98.09 %
Level Four	**21120**	**351**	**98.33 %**
Level Five	21120	359	96.30 %
Level Six	21120	401	98.10%

Therefore, the three dimensional input pattern of FCR $[FCR_{A,} FCR_B, FCR_C]$ (m=3, Chapter 3, Section 3.7.3) has been expanded up to fourth order of Chebyshev expansion to generate [(m*n +1) = 13] dimensional feature space (Figure 3.12).

Figure 7.9 shows the ChNN inputs (3 for each fault) for 20 arbitrary selected faults. This input is subjected to the Chebyshev expansion and the reusting expanded inputs are supplied to the single-layer neural network. The 2^{nd} order Chebyshev expansion of the same 20 fault patterns of Figure 7.9 are shown in Figure 7.10. It can be seen from these two figures that, the Chebyshev expanded inputs provide more discrimination in input values for phases with faults. This distinction ability of the Chebyshev expansion helps in classification and improves the accuracy.

7.6 SIGNIFICANCE OF THE LOW-PASS FILTER

The method proposed in this work uses a low-pass filter as a signal pre-conditioning measure before applying the WT to extract the energy measures. This is due to the fact that, the effect of the introduction of the series compensation is least with lower frequency components of fault current transient signals [114].

Figure 7.11 (a) represents the three-phase current waveforms for an A-g fault created at 49% of the total line length (147 km from the relaying end and 3 km before compensator), with 25 Ω fault resistance, fault inception angle of 45˚ at the line loading angle of 10˚. Figure 7.11 (b) gives the value of the FCR of the fault currents of Figure 7.11(a) for all three phases. Figure 7.12 (a) shows the three-phase current waveforms at 51% of the total line length (153 km from the relaying end and 3 km after compensator) with identical system and fault parameters of the Figure 7.11 (a). Figure 7.12 (b) represents the values of FCR for the waveforms of Figure 7.12 (a).

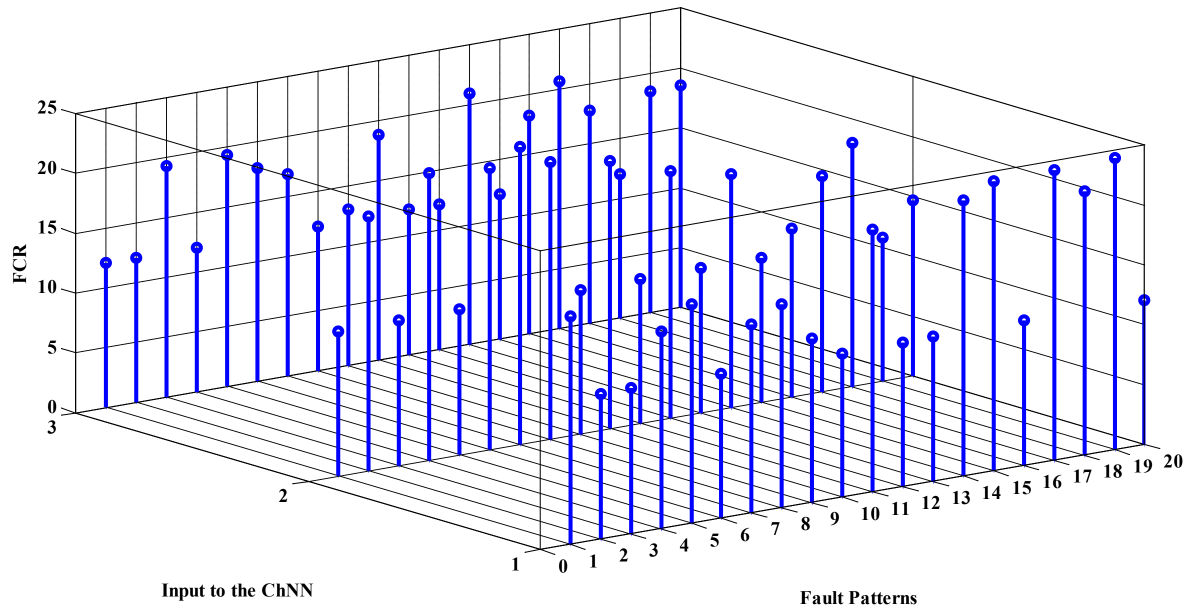

Figure 7.9: Chebyshev neural network inputs

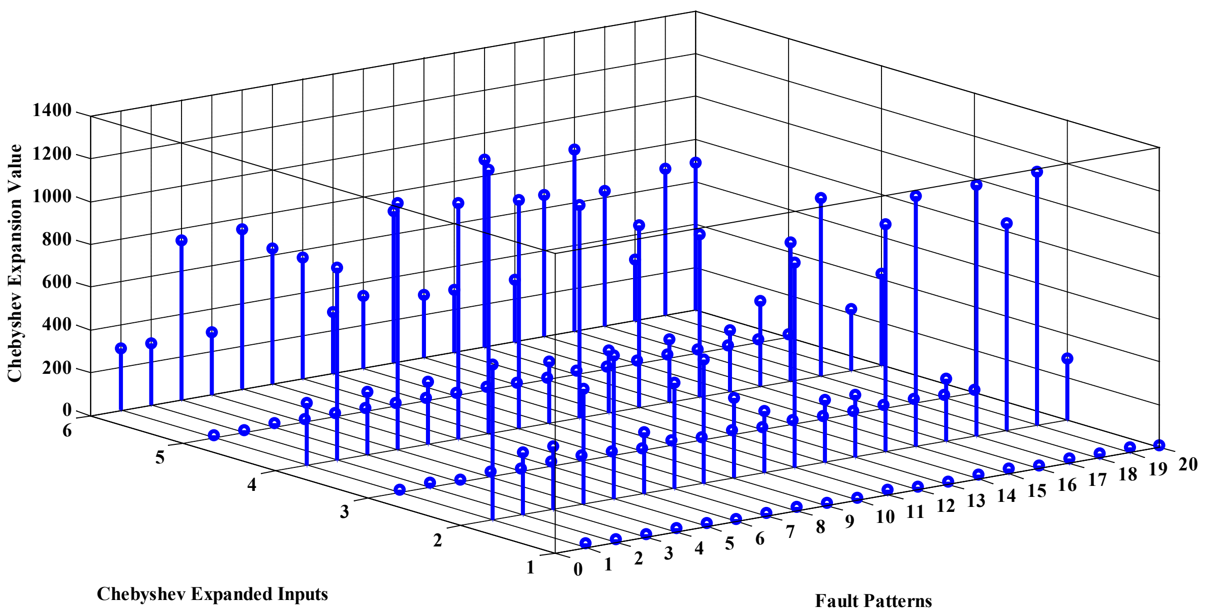

Figure 7.10: Chebyshev expanded inputs

It is evident from Figure 7.11 (a) and Figure 7.12 (a) that, a considerable difference exists in the fault current(s) with inclusion of the series compensation in the fault circuit. The capacitive reactance of the compensator reduces the line impedance that boosts the fault current magnitude and includes few more frequency components in the fault currents. However, addition of the filter in the signal-processing circuit eliminates the higher-frequency components. As a result, almost same values of FCR for faults are generated just before and after the capacitors as given in Figure 7.11 (b) and Figure 7.12 (b).

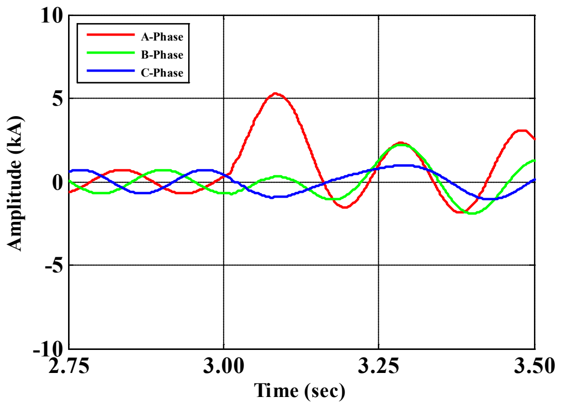

Figure: 7.11 (a): Three phase current waveforms for an A-g fault just before the compensator

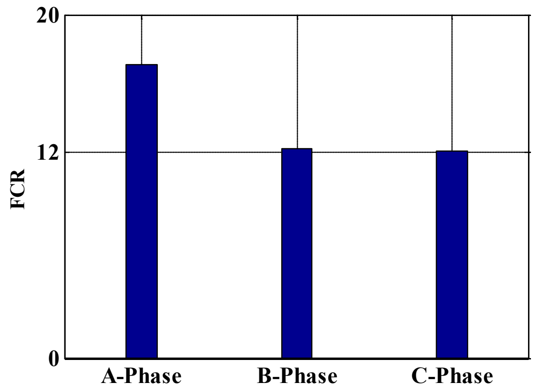

Figure 7.11 (b): FCR for an A-g fault of Figure 7.11 (a)

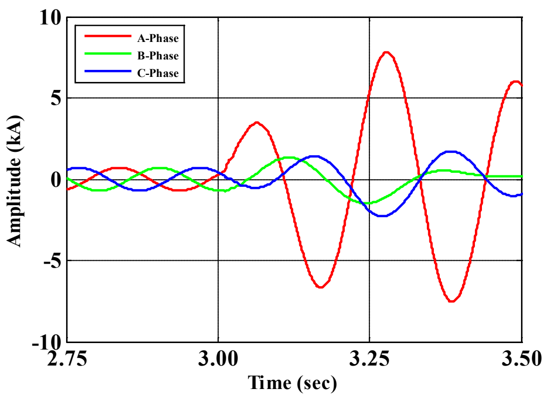

Figure 7.12 (a): Three phase current waveforms for an A-g fault just after the compensator

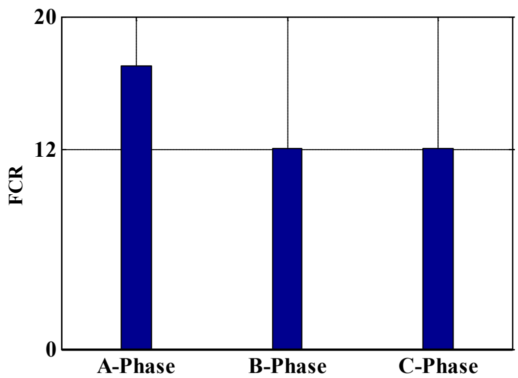

Figure 7.12 (b): FCR for an A-g fault of Figure 7.12 (a)

Figure 7.13 shows the variation in the values of FCR for all possible ten types of the faults occurring at 60% of the line length of the series compensated transmission line of Figure 4.1. For the results shown in this figure, the low pass filter has not been included in the calculation. All of these faults have been created with fault resistance of 5 Ω, fault inception angle of 0˚, and line loading angle of 20˚. An abrupt variation can be seen in the values of FCR in Figure 7.13. On the other hand, the values of FCR for the same faults have also been computed by including the low pass filter in the calculation and are shown in Figure 7.14. It is observed that the abrupt variations present in Fig. 7.13 are absent in Fig. 7.14 and as a result, the data represented in Figure 7.14 are more suitable for fault classification application than those in Figure 7.13.

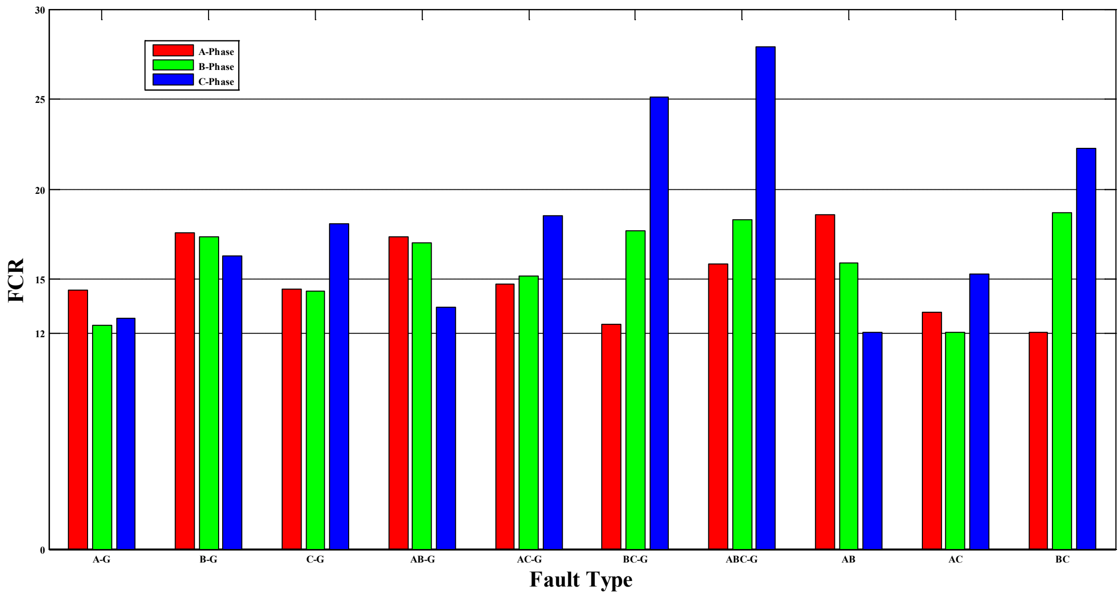

Figure 7.13: Variation in FCR for all possible type of faults without low pass filter

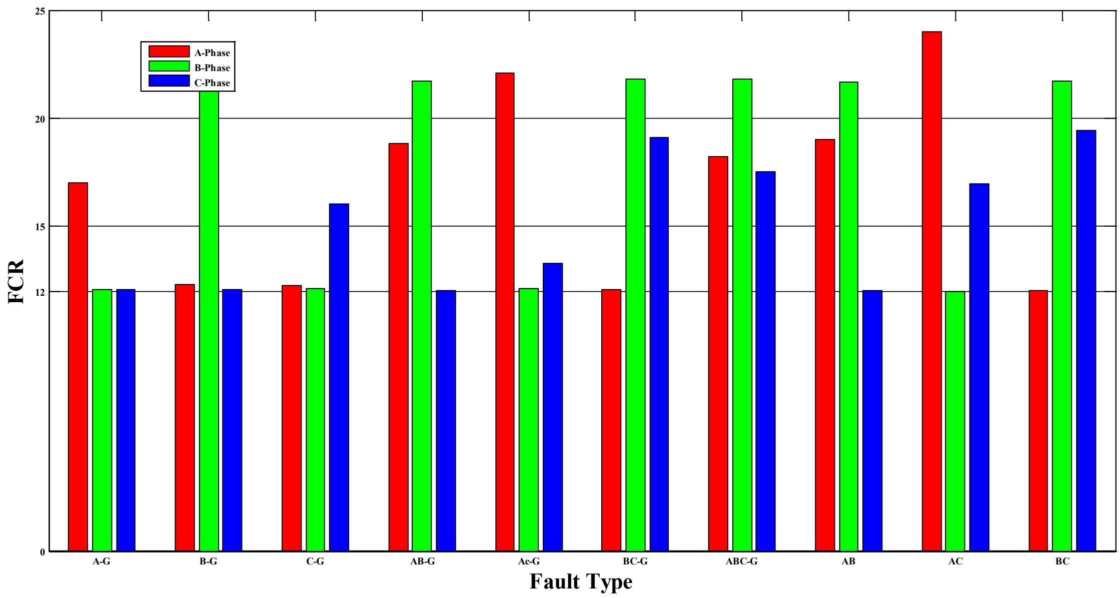

Figure 7.14: Variation in FCR for all possible type of faults with low pass filter

7.7 RESULTS AND DISCUSSION

The effectiveness of the proposed algorithm has been tested on 21120 distinct fault cases (Table 7.3 and Table 7.4). The algorithm is successful to detect fault in about half cycle duration. The overall fault classification accuracy obtained is 98.33%.

Figure 7.15 (a) and Figure 7.15 (b) show the plots for FCR at different fault resistances for A-g fault and A-B fault with 45˚ FIA, created at 60% of the total line length at line loading angle of 10°. It is clear from these plots that, as fault resistance increases, value of FCR decreases continuously. The FCR also decreases for an increase in length of the fault circuit, as shown in Figure 7.16. The faults shown in this figure have been simulated with 0 Ω fault resistance, 45° fault inception angle at line loading angle of 10°. This will help the algorithm to restrict its operation speed for far end fault or for a fault on the next line.

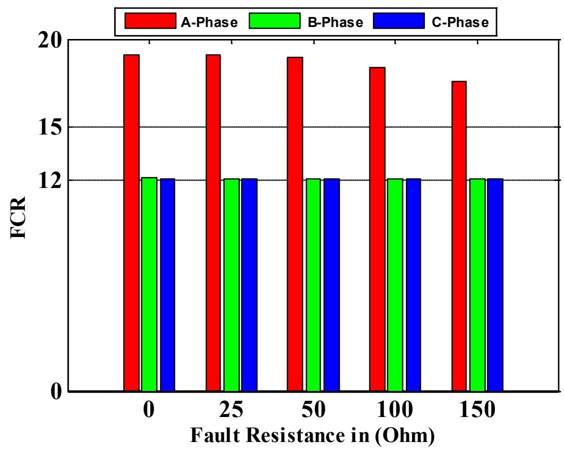

Figure 7.15 (a): Change in FCR with fault resistance for an A-g fault

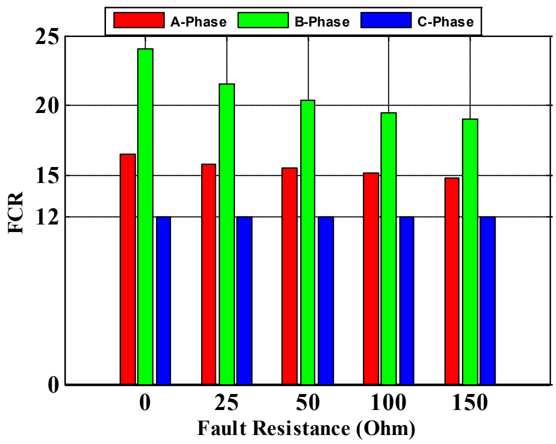

Figure 7.15 (b): Change in FCR with fault resistance for a A-B fault

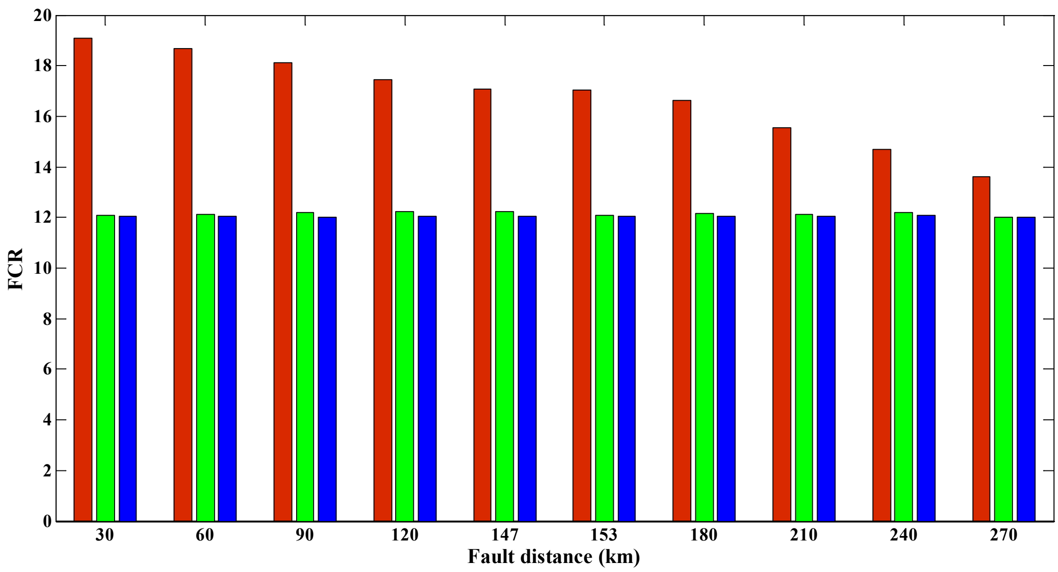

Figure 7.16: Variation in FCR with respect to fault distance for an A-g fault

Figure 7.17 (a) and Figure 7.17 (b) show the plots for FCR at different fault inception angles considered in this study for A-g and A-C-g fault. Both of these faults have been simulated at 51% of the total line length with 25 Ω fault resistance and line loading angle of 10°. It is clear from these graphs that the value of FCR varies with change in FIA. However, the variation is sufficient to allow proper fault classification.

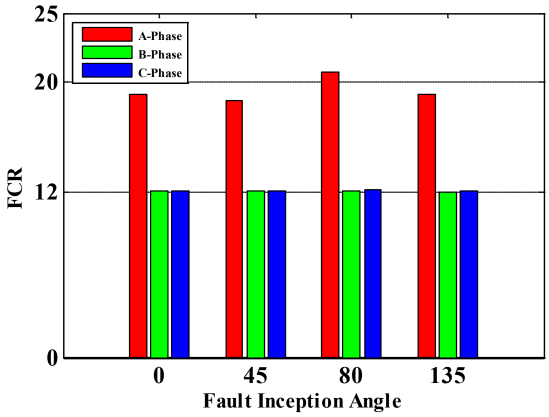

Figure 7.17 (a): Change in FCR with inception angle for a A-g fault

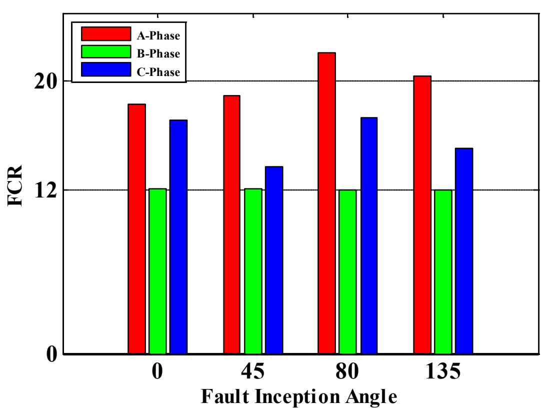

Figure 7.17 (b): Change in FCR with fault inception angle for a A-C-g fault

The effect of loading on the transmission line can also be observed on fault induced transients. A variation in FCR for all three-phase currents at line loading angle of 10˚, 20˚ and 30˚ is shown in Figure 7.18 for a B-C-g fault. The fault has been simulated at 40% line length with no fault resistance and at fault inception angle of 45°. It is clear from the plot that, the FCR changes with change in line loading angle. However, the values of FCR remain well in a range at which these are classifiable for all line loading conditions.

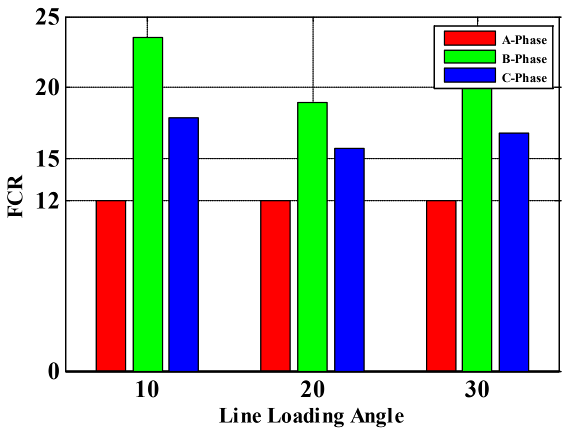

Figure 7.18: Variation of FCR for a B-C-g fault with different line loading angles

Table 7.6 provides the results for fault detection and classification for different levels of compensations. Table 7.7 gives the detailed break-up of fault classification accuracy for various types of faults. It is to be noted that in Table 7.6 and Table 7.7, the term “fault classification errors” denotes the number of testing cases (patterns) for which the fault has been classified incorrectly. The accuracy has been computed for any case as:

$$\eta = \frac{\text{Number of correct detections}}{\text{Number of total considered test cases}} * 100 \qquad (7.10)$$

Table 7.6: Fault Detection and Classification Accuracy

Level of compensation	Numbers of Test Cases	Fault Classification Errors	Fault Classification Accuracy	Fault Detection Errors	Fault Detection Accuracy
25%	6000	63	98.95%	0	100%
50%	4800	70	98.54%	0	100%
75%	6000	162	97.30%	0	100%
0%	4320	56	98.73%	0	100%
Total	**21120**	**351**	**98.33%**	**0**	**100%**

Performance of the proposed scheme can be considered to be suitable for protection requirement for uncompensated line as given in Table 7.6. Moreover, it provides same level of accuracies for different compensation levels also. Fault classification accuracies at different compensation levels are of same order which indicates the capability of ChNN to achieve acceptable level of classification accuracy irrespective of the compensation levels. However, slightly inferior performance is observed at 75% compensation level. This is due to the fact that, the algorithm is trained for 50% and 0% compensation levels only. Accuracy at 75% compensation can be enhanced by including some fault cases for 75% compensation level in the training set. However, this option has not been pursued in this work further.

Table 7.7: Fault type detection accuracy for different types of faults

Type of Fault	Numbers of Test Cases	Fault Classification Errors	Accuracy
L-g	6336	113	98.21 %
L-L-g	6336	60	99.05 %
L-L	6336	61	99.03 %
L-L-L-g	2112	117	96.36 %
Total	**21120**	**351**	**98.33 %**

From Table 7.7, accuracy for LLL-g fault can be considered a bit on the lower side. However, probability of LLL-g fault is least in the system and the overall accuracy of the proposed algorithm is better than those reported in the literature [22, 57, 96]. Table 7.8 represents the overall breakup of the fault classification accuracy with respect to the various fault distance considered in this study. Figure 7.19 shows the graphical representation of the percentage accuracy of fault classification for various fault distances at different compensation levels.

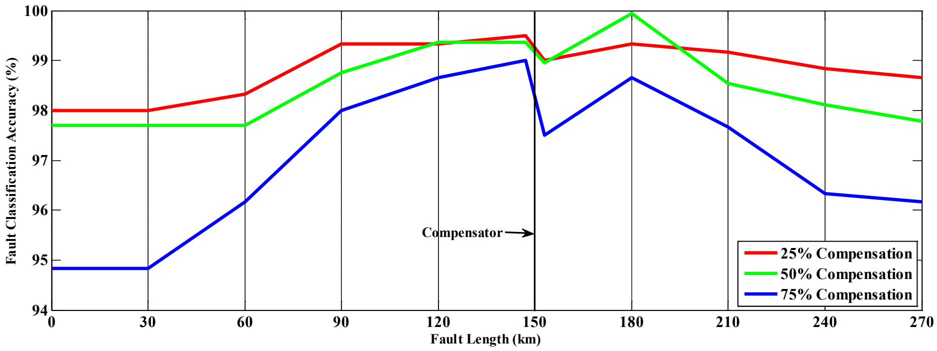

Figure 7.19: Fault classification accuracy at different fault distances

Table 7.9 shows the average time required in ms for the proposed algorithm to converge on the fault detection for various fault locations at different fault resistances. Figure 7.20 and Table 7.9 present average time required by the developed algorithm to detect the fault for various fault distances. It can be observed from the table that, average time required for final decision is half cycle (10 ms) or less in most of the cases. It is also evident from this table that the fault detection time of the relay is less for the faults closer to the relay (high current fault); the fault detection time increases for remote fault from the relay location (as observed in the columns of Table 7.9). It can also be observed that, at any fault location, the operating time increases with increase in fault resistance (rows of Table 7.9). This can be related to the fault current, which reduces with either increase in fault resistance or fault distance. Normally, the transmission line protection schemes are expected to operate quickly for close-in high current faults and can allow more time for remote low current faults. The fault detection time in the developed algorithm increases with increase of fault distance from the relay and with fault resistance; as required for a transmission line protection system.

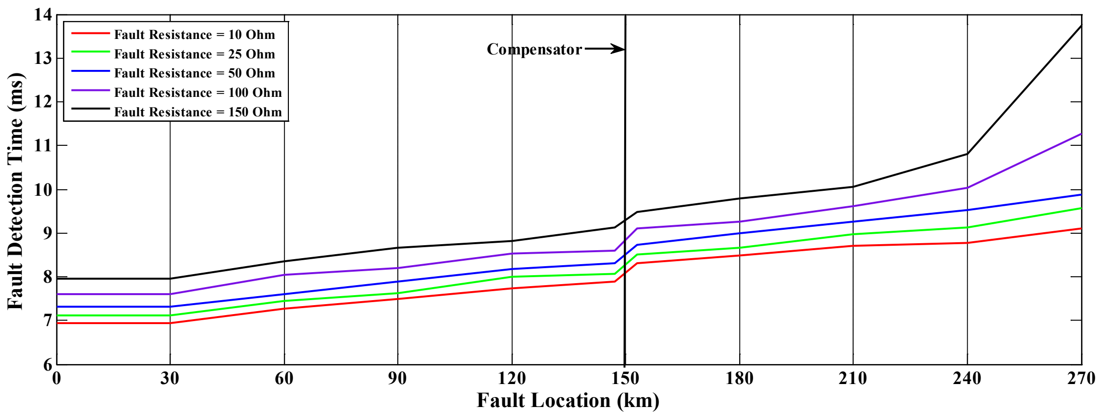

Figure 7.20: Average time for fault detection for developed algorithm

Table 7.8: Fault classification accuracy for various fault distances

Fault Distance (% of Total Line Length)	25% Series Compensation			50% Series Compensation			75% Series Compensation			No Compensation		
	Test cases	Errors	Accuracy	Test cases	Errors	Accuracy	Test cases	Errors	Accuracy	Test cases	Errors	Accuracy
Before Compensator												
10	600	12	98.00%	480	11	97.70%	600	31	94.83%	480	10	97.91%
20	600	10	98.33%	480	11	97.70%	600	23	96.16%	480	9	98.12%
30	600	4	99.33%	480	6	98.75%	600	12	98.00%	480	4	99.16%
40	600	4	99.33%	480	3	99.37%	600	8	98.66%	480	3	99.37%
49	600	3	99.50%	480	3	99.37%	600	6	99.00%	480	4	99.16%
After Compensator												
51	600	6	99.00%	480	5	98.95%	600	15	97.50%			
60	600	7	99.33%	480	5	99.95%	600	8	98.66%	480	5	98.95%
70	600	5	99.16%	480	7	98.54%	600	14	97.66%	480	6	98.75%
80	600	7	98.83%	480	9	98.12%	600	22	96.33%	480	6	98.75%
90	600	8	98.66%	480	10	97.79%	600	23	96.16%	480	9	98.12%
TOTAL	**6000**	**63**	**98.95%**	**4800**	**70**	**98.54%**	**6000**	**162**	**97.30%**	**4320**	**56**	98.70%

Table 7.9: Average Time in ms for fault detection at various line lengths for different fault resistances

Fault Distance (in % of Total Line Length)	**Fault Resistance**				
	10 Ω	**25 Ω**	**50 Ω**	**100 Ω**	**150 Ω**
10%	6.945833	7.1125	7.304167	7.595833	7.954167
20%	7.279167	7.445833	7.604167	8.045833	8.3625
30%	7.4875	7.620833	7.8875	8.204167	8.654167
40%	7.745833	8.004167	8.1875	8.529167	8.820833
49%	7.895833	8.0625	8.3125	8.5875	9.120833
51%	8.304167	8.5125	8.720833	9.095833	9.470833
60%	8.495833	8.6625	9.004167	9.254167	9.779167
70%	8.704167	8.9625	9.254167	9.620833	10.04583
80%	8.779167	9.129167	9.529167	10.02917	10.79583
90%	9.095833	9.5625	9.8875	11.2625	13.75417

7.8 PERFORMANCE IN TRANSIENT CONDITION

To demonstrate the stability (non-operation) of the algorithm for different switching transient conditions, following transient models have been created on the system of Figure 4.1.

7.8.1 Capacitor Switching

A 10 MVAR capacitor is switched 'ON' at bus B at 3.025 sec on phase A in the presence of an active load of 20 MW as shown in Figure 7.21, which generates switching transient. Three different capacitor switching transients have been generated at line loading angles of 10˚, 20˚ and 30˚. Three-phase currents measured at the relaying end (Bus- A) due to the switching of the capacitor at line loading angle of 10˚ are shown in Figure 7.22.

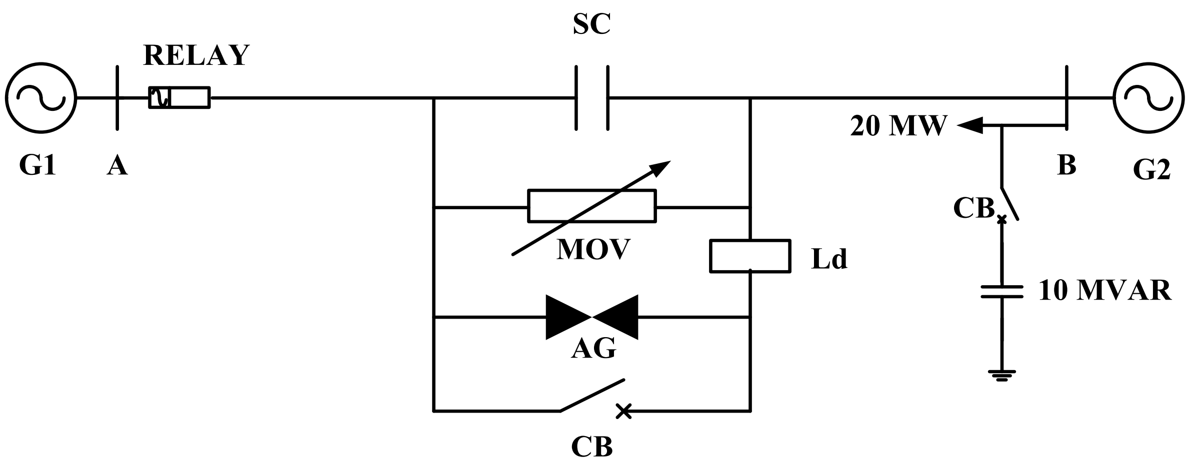

Figure 7.21: Capacitor switching to study effect of transients

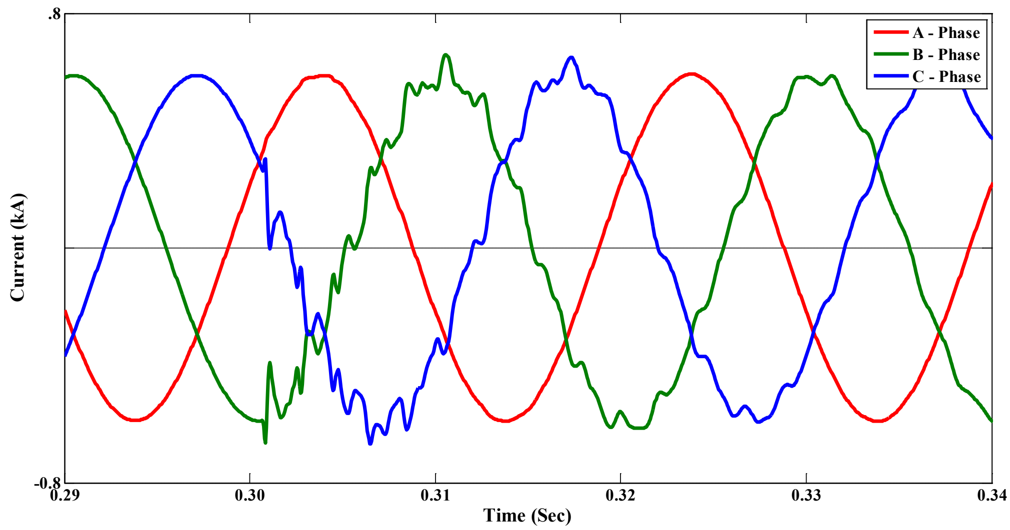

Figure 7.22: Three phase capacitor switching current at line loading angle of 10°

7.8.2 Reactive Compensation Switching With a Teed Line

A 20 MVAR capacitive compensator is switched 'ON' at 0.3025 sec to the system with active load of 45 MW on a teed line as shown in Figure 7.23. The teed line carries identical parameters of the transmission line as given in Appendix-A. The load point has been considered at 15 km from the tee point. A capacitor at the point of loading is switched 'ON' with help of the circuit breaker. The transients in the three-phase currents measured at the relaying end during switching can be seen clearly in Figure 7.24.

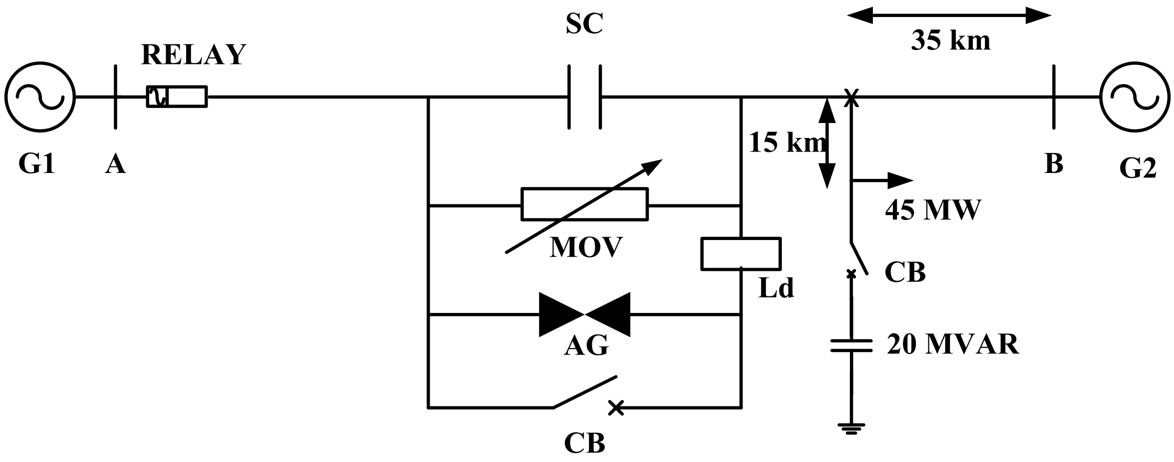

Figure 7.23: Reactive compensation switching with a teed line

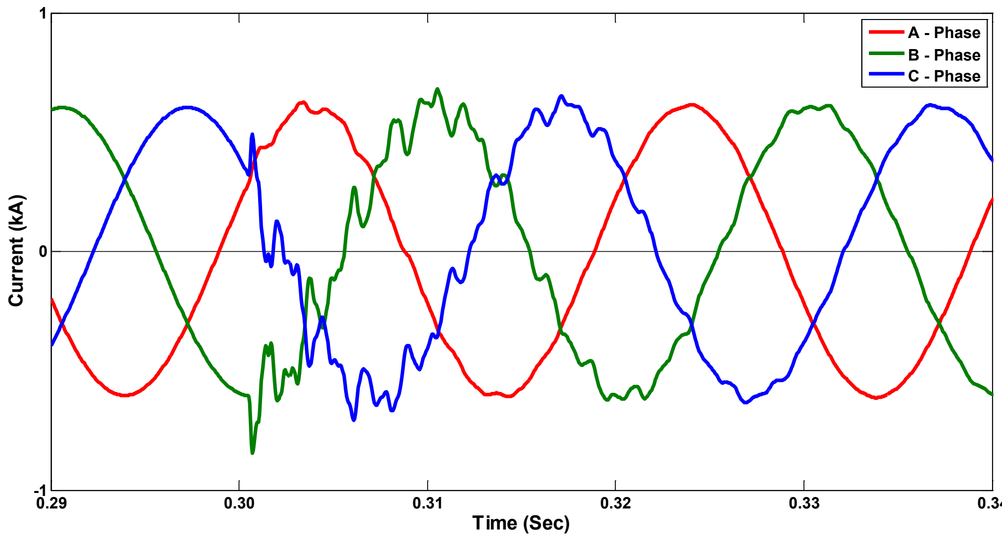

Figure 7.24: Three Phase waveform of reactive compensation switching with teed line at line loading angle of 10˚

7.8.3 Switching Of Active and Reactive Load

A load comprising of active and reactive component is switched ‘ON’ at two different locations to generate 12 different switching transients as shown in Figure 7.25. A continuous load of 110 MW + 30 MVAR has been considered on bus B during these switching operations. Particulars of the load are as follows:

Load Locations	: i) Bus B and ii) Teed Line
Loading	: i) 10 MW and 10 MVAR inductive and
	ii) 10 MW and 10 MVAR capacitive
Generator Loading Angles	: i) 10°, ii) 20° and iii) 30° (In degrees)

Figure 7.26 shows the measured three phase current waveforms at the relaying end for switching of 10 MW active load along with 10 MVAR inductive load at busbar B at generator loading angle of 20 degrees.

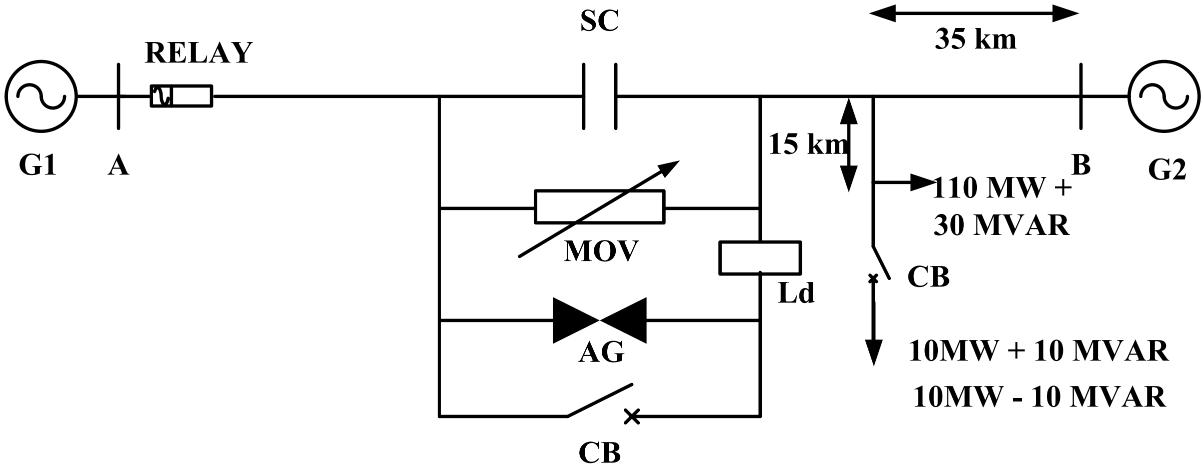

Figure 7.25: Connection of load to generate switching transients

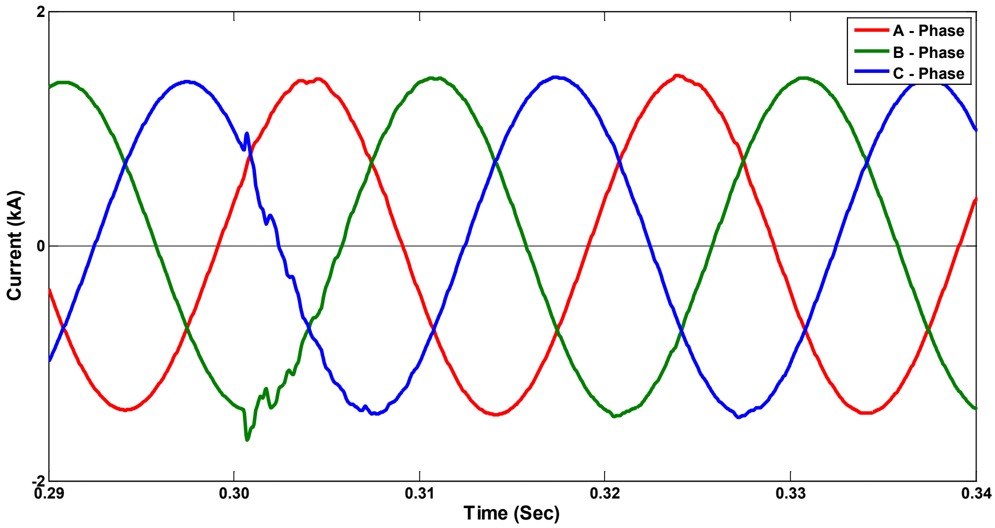

Figure 7.26: Three phase currents at connection of load at generator load angle of 20°

The algorithm has been tested with these 18 different transient cases. During this testing phase, the algorithm never converged to detect the fault and proved to be immune to these transients. In many out of these cases, an initial detection is observed, but three consecutive detections (hysteresis) required for establishing final fault detection have never been achieved.

7.9 PERFORMANCE COMPARISON

Normally available transmission line protection algorithm in literature, are either intended for uncompensated transmission line or for series compensated transmission lines. The presented algorithm performs fault detection and classification task for series compensated line and for uncompensated line also with the same level of accuracy. Therefore, it is first of its kind that can be used for either type of line without any functional modification. In the absence of any method providing protection to both uncompensated and series compensated transmission lines, the performance of the developed methodology has been compared (Table 7.10) with those obtained by recent methods for only uncompensated or only series compensated line with an adequate number of test cases (2400 for [96], 1080 for [57]) for comparison with this method.

Table 7.10: Performance comparison

	Developed Algorithm	**Reference [57]**	**Reference [96]**
Objective	Fault Detection and Classification	Fault Classification	Fault Classification
Number of Test Cases	21120	1080	2400
Post Fault Data Requirement	Half Cycle or Less	One Cycle	Half Cycle
Level of compensation	**Fault Classification Accuracy**		
25%	98.95%	------	97.68%
50%	98.54%	------	98.75%
75%	97.30%	------	93.66%
0%	98.73%	94.72%	-------

The work described in [57] represents fault classification with WT-SVM based approach for uncompensated transmission line. As mentioned in the Table 7.10, the developed methodology performs better fault classification and that is also with higher number of test patterns. The developed method uses only half cycle post fault data, compared to the full cycle data required in [57].

Further, in contrast to the fuzzy based scheme [96] for fault classification, in which the accuracy variation is observed with change in compensation levels, the generalization capability of the ChNN is quite sufficient to produce same level of accuracies for different compensation levels. The proposed scheme works on only three phase current measurement, that reduces computational and measurement burdens.

7.10 CONCLUSION

A new versatile algorithm for fault detection and classification with DWT energy and a two-stage algorithm with DWT and ChNN for fault type identification has been suggested in this chapter. The algorithm is first of its kind that gives identical performance for uncompensated overhead transmission line and for series compensated line as well. Moreover, it provides a comparable level of fault detection and classification accuracy at various levels of compensations. The algorithm in this chapter does not require any functional modification during fault detection and classification process for various levels of compensation. The effectiveness of the algorithm has been established by testing over 21200 fault cases with distinct system conditions; the algorithm provides 100% fault detection accuracy with 98.33% fault type identification precision. Moreover, the algorithm has been proven to be immune to the switching transients generated by various switching phenomena.

From testing over a large fault data cases, following salient points can be brought out for this algorithm:

1. The use of the lower frequency components of fault transient for protection of a transmission line has been explored in this method. From the results, it is observed that the proposed technique is un-affected by the presence of the series compensator.
2. As the algorithm uses only 1/20th of fresh cycle data for analysis, three consecutive fault detections are found necessary and sufficient to remove the possibility of fault detection in transient conditions.

The required data for fault classification has been generated during the fault detection algorithm only. This removes the need of any additional data after fault detection. This enables employment of the fast digital protection schemes.

CHAPTER 8: TCSC COMPENSATED TRANSMISSION LINE PROTECTION

The Thyristor Controlled Series Capacitor (TCSC) are the most widely used FACTS devices today. The initial part of this chapter introduces the TCSC. The subsequent part of this chapter addresses the issues related to the protection of line containing it. The problems faced by the impedance based protection scheme have been discussed in detail with basic modelling using the dynamic power system simulator PSCAD. Improved fault classification and fault zone identification schemes are presented with their relative merits and demerits.

8.1 INTRODUCTION

In recent times, transmission systems worldwide are undergoing continuous restructuring due to increasing stress of power demand. For economic and regularity constraints, the developments of transmission networks are restricted. The development of the Flexible AC Transmission Systems (FACTS) offers an effective means to meet the requirements of the ever-growing power market.

Different FACTS devices are available with their relative merits and limitations. There are series and shunt power compensators [3]. Thyristor Controlled Series Compensator (TCSC) is a series compensation device that provides a fast control of the active power through a transmission line. The TCSC provides this control by effectively inserting the inductive or capacitive reactance in series with a transmission line.

In view of the benefits offered by TCSC, they have found increasing applications. It is therefore, imperative that relevant protection approaches be developed along with the primary system developments.

To understand the impact of TCSC in various operating conditions effectively, an appropriate model is a prerequisite. In this respect, time domain simulations render a means of analyzing the dynamic behavior of the TCSC especially when investigating the impact of these devices on a system under different fault conditions. The next section presents a brief discussion of the theoretical aspects of the TCSC as well as the TCSC modeling considerations that will serve as the platform for the fault study.

8.2 TCSC OPERATION

The TCSC utilizes power electronic devices to control the effective impedance of the transmission line. In a way, the TCSC is an efficient device for controlling the power network by continuous variation of the transmission line impedance. The TCSC uses thyristors that switch successively in every half cycle to provide impedance variation. As a result, it exhibits a non-linear impedance characteristic.

The concept and control strategies of TCSC have been significantly developed in the recent years. Various models for the TCSC are presented by different researchers in [128, 132, 133, 139, 140]. These models have been developed for various applications and therefore, carry different levels of complexity and details. In practice, simplified linear models incorporating the necessary transition characteristics are found sufficient with minimal simulation time and reasonable complexity of the model.

A basic TCSC module consists of a fixed capacitor in series with the line and a bi-directional thyristor pair in series with an inductor (Thyristor Controlled Reactor (TCR)) connected in parallel to the capacitor as shown in Figure 8.1. A MOV is also provided for over-voltage protection of the capacitor along with a back up protection in the form of air-gap surge protector and circuit breaker. The TCSC module typically comprises of an array of the arrangement shown in Figure 8.1. Moreover, the inductor can also be split into two halves to avoid thyristor damage in the case of short-circuit.

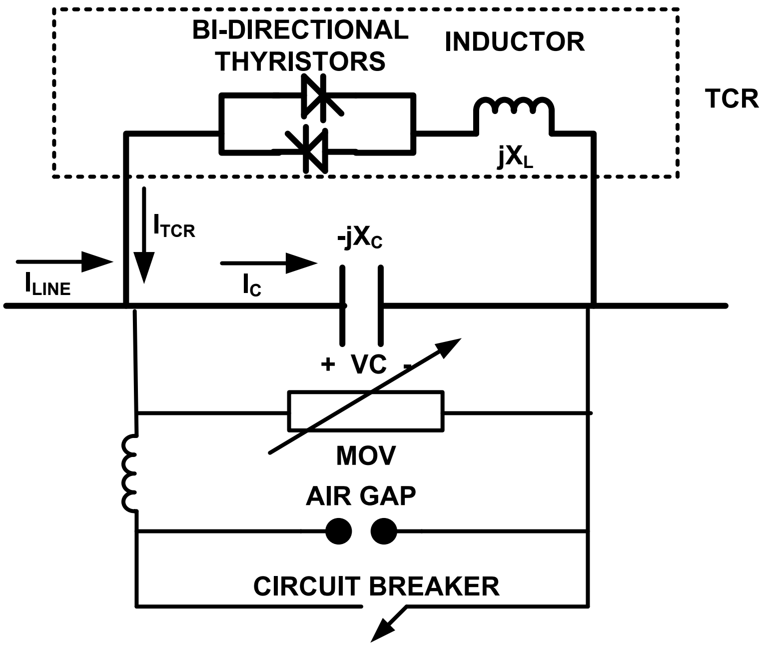

Figure 8.1: Basic TCSC configuration

The TCSC can be visualized as a variable reactance series compensator during operation. The TCSC works on the principle of charge injection. According to the conduction of the thyristors, an injected current I_{TCR} is added to the line current as shown in the Figure 8.1. This current modifies the voltage across the series capacitor. The voltage developed across the capacitor is in quadrature with the line current and could be inductive or capacitive depending upon the conduction of TCR.

The equivalent reactance offered by the TCR for a firing angle α can be given as [3]:

$$X_L(\alpha) = X_L \frac{\pi}{\pi - 2\alpha - \sin 2\alpha} \tag{8.1}$$

Therefore, the operating mode of the TCSC can be described according to the firing angle α, or thyristor conduction angle σ, where, $\pi = 2\alpha + \sigma$. Therefore, an appropriate current and hence voltage across the series capacitor can be achieved through the variation of the firing angle α. The overall equivalent impedance at fundamental frequency can be given by:

$$X_{TCSC} = -jX_C \left[1 + \frac{2}{\pi} * \frac{\lambda^2}{\lambda^2 - 1} * \left\{ \frac{2\cos^2\left(\frac{\sigma}{2}\right)}{\lambda^2 - 1} \left(\lambda \tan\left(\frac{\lambda\sigma}{2}\right) - \tan\left(\frac{\sigma}{2}\right) \right) - \frac{\sigma}{2} - \sin\left(\frac{\sigma}{2}\right) \right\} \right] \tag{8.2}$$

Where,

$$\lambda = \sqrt{\frac{X_C}{X_L}}$$

In the above equation, X_C and X_L denote the reactances of the capacitor and the inductor respectively.

8.2.1 Modes Of Operation

As mentioned in the previous section, the equivalent impedance of the TCSC depends on the thyristor firing angle. According to the conduction, the TCSC operation can be classified in following basic modes [3] :

1) Capacitive boost ($\alpha_{c\lim} > \alpha > \pi$)
2) Inductive boost ($\frac{\pi}{2} > \alpha > \alpha_{L\lim}$)
3) Bypass ($\alpha = \pi$)
4) Blocking ($\alpha=\pi/2$)

8.3 SIMULATION OF THE TCSC

The TCSC operation and its equivalent reactance largely depend on thyristor firing angle α. Therefore, the TCSC design necessitates a means to control and synchronize the thyristor firing. The TCSC control system plays a crucial role in providing trigger control signals to the thyristors to obtain the desired compensation levels. Control strategies used with TCSC can broadly be divided into open loop and close loop strategies.

A number of works have been reported in the literature for modeling of TCSC for power system studies [128, 150, 151]. Many of these models presented are of discretized natures. Discretize models involve complicated design and more computational burden [150]. Few other models are designed to reduce the overall complexity. Therefore, a TCSC model with phase locked loop (PLL) control is used in this work. This closed loop control model has a reasonable accuracy for dynamic study and can be used with any normal ac system [151]. The model is utilized with a SVC modeling as a subsystem of the TCSC module [152].

The steady-state model parameters are initiated for TCSC with its fundamental frequency model. With assumption of the constant fundamental frequency current through the TCSC, the voltage across the capacitor 'V_C' carries controlled and uncontrolled components [3]. With a controlled and uncontrolled components the TCSC control has been designed as shown in Figure 8.2 [151].

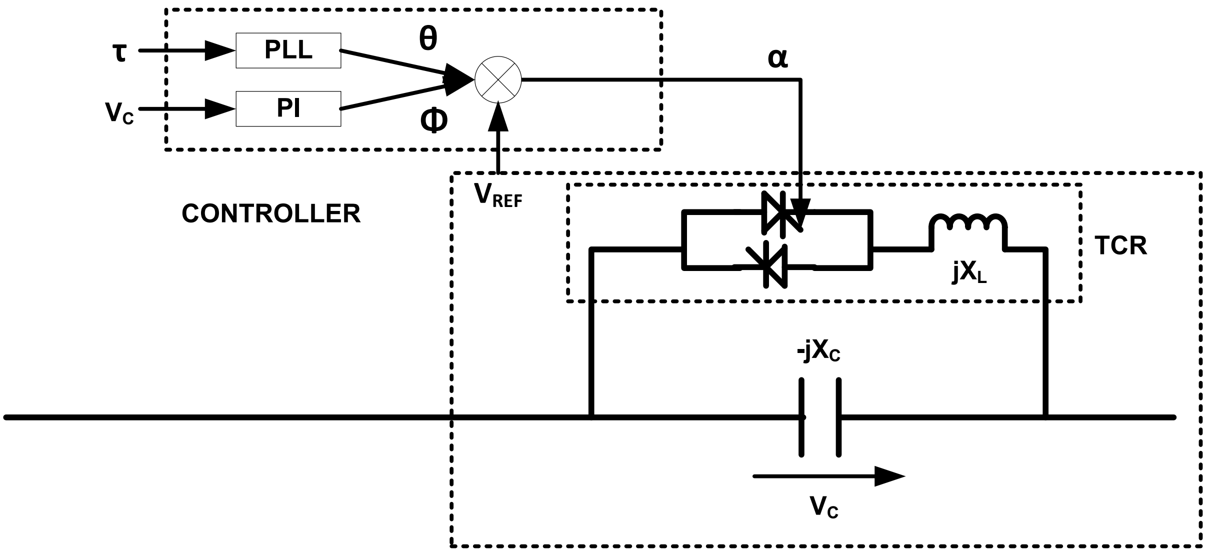

Figure 8.2: TCSC close loop control strategy

The voltage developed across the series capacitor ('V_C') has been used as reference to estimate the current passing through the TCSC and is supplied to the control circuit for synchronization and control reference. The voltage PI controller ('PI' in Figure 8.2) calculates the required firing angle 'Φ' for the thyristor circuit. With TCSC current phase angle 'τ', the PLL provides a ramp output to generate the reference angle 'θ' for the TCSC firing. The PLL uses the trigonometric multiplication identities to form an error signal that tracks the variation in phase-locked oscillator, to match the phase of the input. The actual thyristor firing angle 'α' is provided by considering the reference angle provided by the PLL with calculated firing angle Φ' from the PI voltage controller as shown in Figure 8.2.

The embedded power electronic switches and the associated TCSC control system have been modeled in PSCAD/EMTDC [153]. The TCSC is assumed to operate with the open loop control system with constant impedance configuration as shown in Figure 8.2. The control system has been designed as a sub-model of the TCSC module.

8.4 SYSTEM UNDER CONSIDERATION

This section describes the simulation study used to generate the fault data for development of fault classification and zone identification algorithms for a TCSC compensated transmission line. The simulation study of the power system with TCSC has been performed using PSCAD environment [153]. A sampling frequency of 4 kHz has been used in this work.

The transmission line is equipped with a TCSC at the middle of the line as shown in Figure 8.3. The TCSC is aided with a fixed series compensator (Cf_1). The TCSC and the fixed series compensator are protected against overvoltage by MOV as shown in Figure 8.3. The transmission line parameters are identical as used in the previous chapters and given in Appendix-B. Overvoltage protection is provided with MOV to the compensators with maximum permissible current rating of 2.5 times rated current (Chapter 4).The fixed series compensator (Cf_1) is providing 30% compensation to the total line length. The TCSC provides variable capacitive compensation with variation of the firing angle (α) form 153˚ to 180˚.

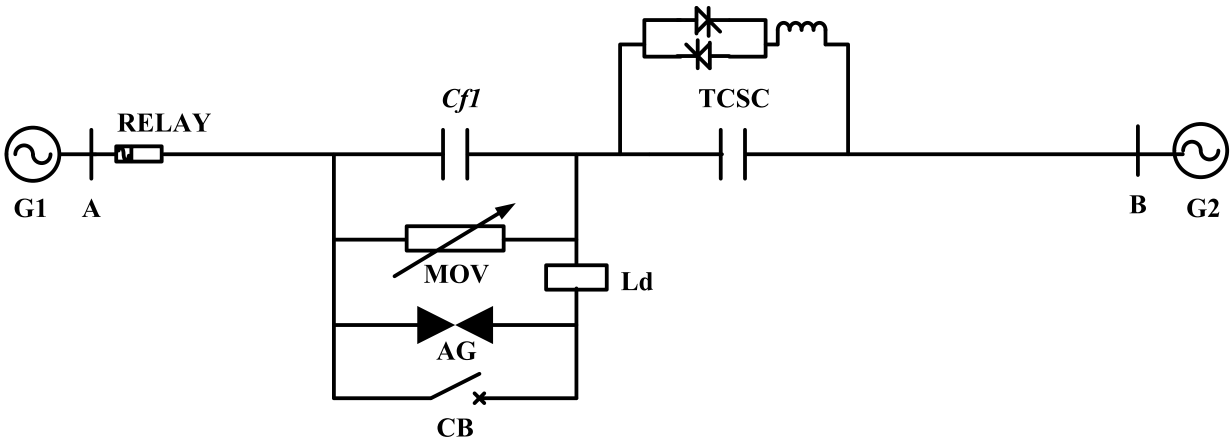

Figure 8.3: System used for simulation

For training and evaluation of the developed algorithms in this chapter, a large data set of faults with wide variation of system and fault parameters have been generated. These variations in system conditions are created by varying the system parameters such as source impedances (Z_{SG1} and Z_{SG2}), TCSC firing angle (α) and line loading angle (δ) as given in Table 8.1.

Table 8.1: Different system conditions considered for TCSC bulk data generation

Source Impedance Variation	TCSC firing angle (α)	Line Loading Angle (δ)	System Conditions
(Z_{SG1}-Z_{SG2})	180˚,160˚,144˚	10˚,20˚,30˚	1-9
(0.75Z_{SG1}-Z_{SG2})	180˚,160˚,144˚	10˚,20˚,30˚	10-18
(1.25Z_{SG1}-Z_{SG2})	180˚,160˚,144˚	10˚,20˚,30˚	19-27
(Z_{SG1}-0.75Z_{SG2})	180˚,160˚,144˚	10˚,20˚,30˚	28-36
(Z_{SG1}-1.25Z_{SG2})	180˚,160˚,144˚	10˚,20˚,30˚	37-45

As mentioned in Table 8.1, combination of these variations creates 45 system conditions. Furthermore, with variation in different fault parameters, a number of fault cases have been created under each of these system conditions. The considered variations in these parameters are:

i) Fault Inception Angle (FIA) : 0˚, 45˚, 115˚.

ii) Fault Resistance (R_f) : 0 Ω, 5 Ω, 25 Ω, 50 Ω.

iii) Fault Distance : 60 km, 120 km, 138 km, 162 km, 180 km, 240 km.

iv) Type of faults : L-g, L-L-g, L-L, L-L-L. (All ten types of faults).

For every specific system condition, combination of these fault parameters creates 720 [3 (FIA) * 4 (R_f) * 6 (Line Distance) * 10 (Fault Types)] distinct fault cases. Therefore, for 45 system conditions, a sum total of 32400 fault cases have been generated with PSCAD.

8.5 WT AND CHNN BASED FAULT TYPE CLASSIFICATION SCHEME

8.5.1 WT Feature Extraction and Quantification

To identify the type of fault effectively, the changes in spectral components of the measured voltage and currents can be used effectively as shown in Chapter 4. The faulted signal carries non-fundamental decaying frequency components, odd harmonics due to conduction of MOV and high-frequency components caused by resonance between line capacitance and line inductance. The algorithm in this section utilizes these spectral changes to identify the faulted phase with the help of DWT and ChNN.

Figure 8.4(a) represents the current waveforms for all three phases for A-g fault occurring at 60% of total line length. This fault has been simulated with fault resistance of 5 Ω, fault inception angle of 135˚ and line loading angle of 20˚. The coefficients of first-order WT of half cycle duration of these waveforms are represented in Figure 8.4(b). Figure 8.4(c) represents the three-phase current waveforms for a A-C-g fault occurring at 40% of the line length. The fault has been simulated with fault resistance of 25 Ω, fault inception angle of 45˚ and line loading angle of 10˚. The WT decomposition vector for this fault is shown in Figure 8.4(d). It is clear from these figures that, a significant amplitude and spectral difference exist between faulted and healthy phase which can be used for fault classification. The schematic block diagram of the proposed scheme is shown in Figure 8.5. Samples of three phase post fault currents of half cycle duration are subjected to WT for feature extraction and generated wavelet coefficients are subjected to a cluster of four ChNNs for fault type classification.

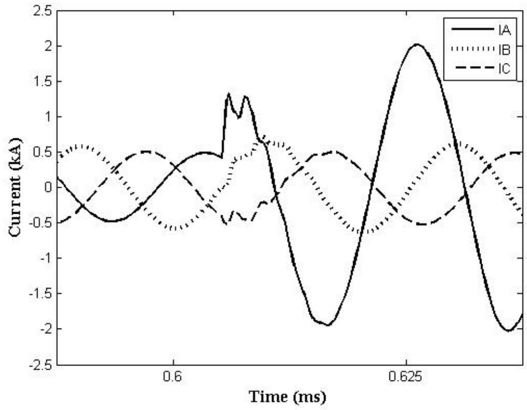

Figure 8.4(a)

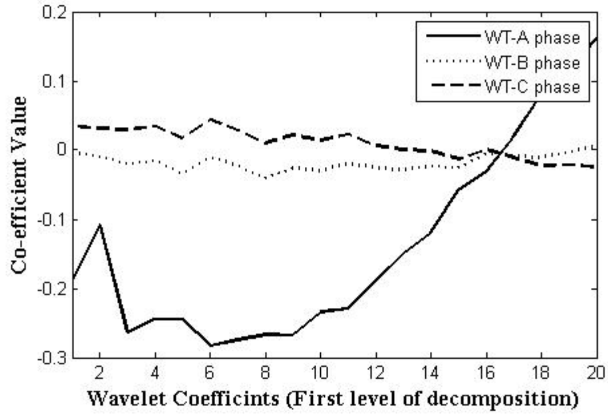

Figure 8.4(b)

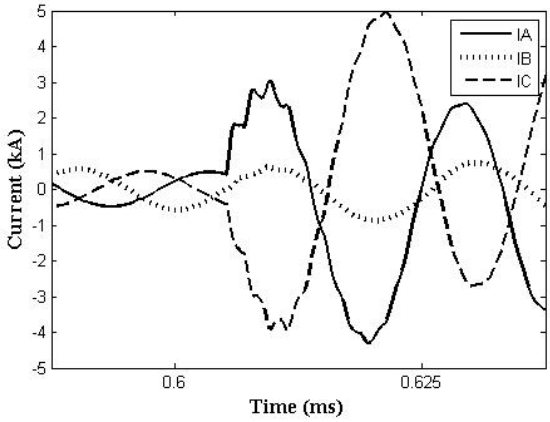

Figure 8.4(c)

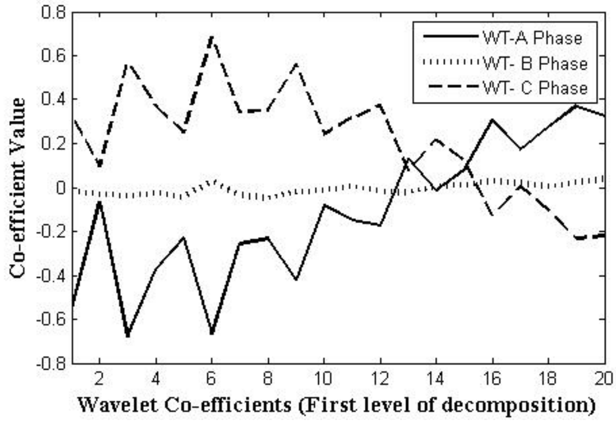

Figure 8.4(d)

Figure 8.4 : Current waveforms and wavelet transform coefficients for A-g and A-C-g fault

8.5.2 Fault Type Identification Logic and Computation

The three-phase post fault currents measured at Bus-A (Figure 8.3) with a sampling frequency of 4 kHz gives 40 samples per phase for half cycle duration. Discrete wavelet decomposition is performed on these samples with “db1” as mother wavelet (as described in Section 4.3.2) at first level of resolution. The resulting decomposition vector ***P*** for each phase carries two sub-bands, detail and approximation, each with 20 resolutions. The detail wavelet sub-band carrying 20 resolutions per phase is used for further processing. The decomposition vector for any phase can be given as:

$$v_p^{dwt} = \frac{1}{n_i} \sum_{j=1}^{n_i} b_{i,j}^2 \tag{8.3}$$

Where, *i* = level of decomposition, in this work, i=1

p shows phase, A, B or C, and

n_i = the number of samples in an individual sub band and $b_{i,j}^2$ is the j^{th} coefficient of the i^{th} sub band. Thereafter, the wavelet feature vector $\boldsymbol{Q}^{dwt}$ is generated with decomposition vector of all three phases v_A^{dwt}, v_B^{dwt} *and* v_C^{dwt}. This vector $\boldsymbol{Q}^{dwt}$ has 60 coefficients which in turn is processed with a set of three ChNNs (ChNN-A, ChNN-B, ChNN-C of Figure 8.5).

$$\boldsymbol{Q}^{dwt} = \{v_A^{dwt}, v_B^{dwt}, v_C^{dwt}\} \tag{8.4}$$

To evaluate the participation of ground in the fault, the WT of half cycle zero sequence post fault current (40 samples) is performed and the generated wavelet feature vector for ground $Q_G^{dwt} = \{v_G^{dwt}\}$ is subjected to ChNN-N assigned to identify the participation of ground in the fault. It is to be noted that the $\boldsymbol{Q}_G^{dwt}$ vector has a total of 20 co-efficients.

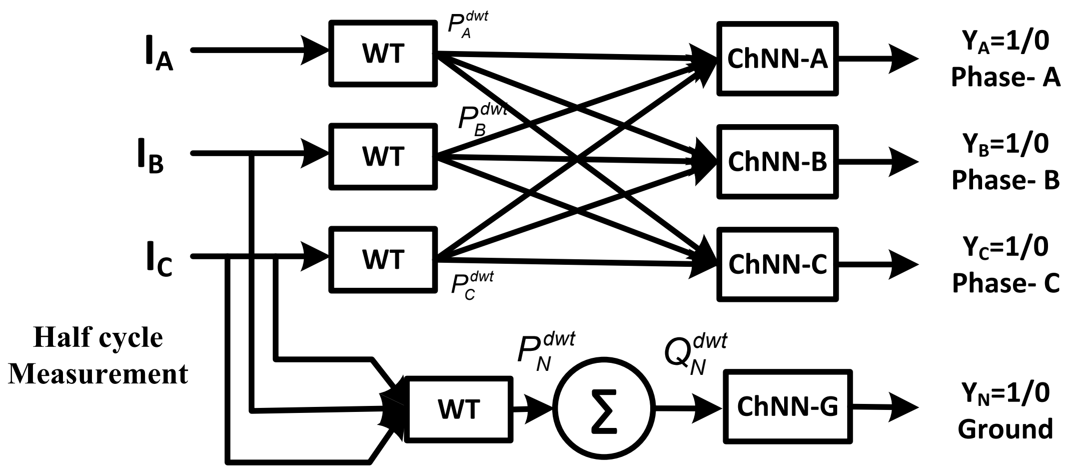

Figure 8.5: DWT and ChNN based fault classification scheme block diagram

The ChNN requires learning for the classification task. Moreover, for establishing its robustness the ChNN should be tested with fault cases which are different from the training cases. With this objective, a set of 2400 fault patterns as given in Table 8.2 are used for training of the ChNN (which are not used during testing of the ChNN).

Table 8.2 : - Parameters used for training fault data generation

Fault/System Parameter	**Value used for training**
Source Impedance Variation	All five considered
TCSC Firing Angle (α)	160˚
Fault Resistance (R_f)	0Ω, 5Ω, 50Ω
Load Angle (δ)	10˚, 30˚
Fault Inception Angle	0˚, 45˚
Fault Location	60 km, 120 km, 180 km, 240 km
Total Test Cases	2400

The DWT resolution vector of $\boldsymbol{Q}^{dwt}$ (60 coefficients as per (equation 8.4)) is processed through the pre-trained bunch of three ChNNs meant to identify the involvement of the corresponding phase in fault (Figure 8.5). The vector $\boldsymbol{Q}_G^{dwt}$ is supplied to the fourth ChNN. The ChNN generates '1' as output $(y_A, y_B, y_C \; or \; y_n)$, if the respective phase/ground are involved in fault, otherwise the output is '0'.

The non-linear classification capability of the ChNN increases with an increase in order of Chebyshev polynomial expansion. However, higher-order expansion results in larger size of the network and results in increased computational burden. The third-order expansion has been found to be sufficient in this work for fault classification with acceptable accuracy and moderate computational burden. Therefore, the Chebyshev expansion is limited to third order for fault classification in this work. With third order Chebyshev expansion, the vector $\boldsymbol{Q}^{dwt}$ is expanded to Φ_F (181 expanded NN inputs) for processing through ChNN-A, ChNN-B, ChNN-C, ChNN-N (Figure 8.5) to identify the involvement of each phase.

$$\Theta_F(x) = ([1, v_{i1}(x_1), v_{i2}(x_1), \ldots\ldots\ldots v_{i60}(x_3)]^T)_{i=A,B,C} \tag{8.5}$$

In the above equation '*x*' denotes specific input sample. $[v_{i1}, v_{i2}, \ldots v_{i60}]$ are wavelet coefficients for the current samples as defined in equation (8.3). The ChNN designated to find out involvement of the ground during fault, expands the ground vector $\boldsymbol{Q}_G^{dwt}$ to $\boldsymbol{\Phi}_G$ (61 samples for third order Chebyshev expansion) as:

$$\Theta_G(x) = ([1, v_{g1}(x_1), v_{g2}(x_1), \ldots\ldots\ldots v_{g20}(x_3)]^T) \tag{8.6}$$

$[v_{N1}, v_{N2}, \ldots v_{N20}]$ are wavelet coefficients for the zero sequence current samples as defined in equation (8.3). All four ChNN have been trained with 2400 fault patterns described in Table 8.2 in Matlab environment using Neural Network Toolbox [141]. The training accomplishes in [40, 43, 139 and 62] iterations for the respective ChNNs for Phase-A, Phase-B, Phase-C and Ground. The testing of this scheme is described in the following section.

8.5.3 Performance Evaluation of The DWT and Chnn Based Scheme

The fault classification method proposed for TCSC compensated transmission line in this work has been evaluated using 30000 fault patterns. As mentioned in Section 8.4, these testing fault patterns are distinct from the fault cases used for training. The WT and ChNN based method gives significantly improved performance in terms of accuracy, similar level of performance for various levels of compensation and robustness to accommodate parameter variations than those reported in the literature [58, 154].The fault classification performance of the proposed algorithm for different firing angles are given in Table 8.3.

Table 8.3: Fault classification performance of DWT and ChNN based scheme at different TCSC firing angles

TCSC Firing Angle (α)	No of test cases	Misclassification	Successful classification	Accuracy
153˚	10800	53	10747	99.51%
160˚	8400	39	8361	99.54%
180˚	10800	49	10751	99.55%
Total	**30000**	**141**	**29859**	**99.53%**

The accuracy of the proposed method is almost same for different TCSC firing angles although, it has been trained with a firing angle of 160˚ only. A higher level of accuracy is obtained at a TCSC firing angle of 180˚. At any other firing angle than 180˚, due to partial conduction in a cycle, the change in spectral components at the time of fault is higher. The separation plane of the ChNN has been created with 160˚ firing angle (for higher amount of spectral change). With reduced amount of spectral changes at 180˚, the ChNN performs better classification. The overall accuracy obtained in this method shows marked improvement as compared to other methods reported in the literature [43, 46, 51, 155].

Table 8.4 shows the fault classification accuracy for various fault distances at different TCSC firing angles. It is observed from these results that, the algorithm proved to be consistent for various fault distances on transmission line. It is worth noticing here that fault cases with different system operating parameters occurring at 46% of line length (138 km from relaying end) and 54% of line length (162 km from relaying end) are never used during training. However, accuracy observed for these faults are also quite similar with those obtained at other fault locations. This proves the robustness of ChNN for fault classification.

Table 8.4: Distribution of fault classification accuracy for DWT and ChNN based scheme

Fault Distance (% of Total Line Length)	TCSC Firing Angle = 153˚			TCSC Firing Angle = 160˚			TCSC Firing Angle = 180˚		
	No of test cases	Errors	Accuracy	No of test cases	Errors	Accuracy	No of test cases	Errors	Accuracy
Before TCSC									
20	1800	11	99.39%	1200	6	99.50%	1800	12	99.33%
40	1800	7	99.61%	1200	5	99.72%	1800	6	99.67%
46	1800	6	99.67%	1800	2	99.83%	1800	5	99.72%
After TCSC									
54	1800	10	99.44%	1800	9	99.25%	1800	9	99.50%
60	1800	7	99.61%	1200	8	99.56%	1800	6	99.67%
80	1800	12	99.33%	1200	9	99.25%	1800	11	99.39%
TOTAL	**10800**	**53**	**99.51%**	**8400**	**39**	**99.54%**	**10800**	**49**	**99.55%**

Table 8.5 summarize the test results corresponding to the type of faults considered in this study. Accuracy obtained for each fault type in Table 8.5 is on higher side as compared to those obtained by other methods in literature [43, 155] and indicates the usefulness of the ChNN for fault classification application. The moderate reduction in performance is observed for L-L-L-g fault as fault energy is distributed in all the three phases. However, the possibility of this fault is least in the power system and accuracy is above 99% in these cases also [156].

Table 8.5: Fault classification for different types of fault

Type of Fault	Numbers of Test Cases	Fault Type Detection Errors	Accuracy
L-g	9000	37	99.58%
L-L-g	9000	52	99.42%
L-L	9000	23	99.87%
L-L-L-g	3000	29	99.03%
TOTAL	**30000**	**141**	**99.53%**

8.5.4 Comparison of Chnn Based Algorithm with MLPNN and SVM Based Methods Using DWT

To demonstrate the superiority of ChNN + DWT based fault classification performance for TCSC compensated line, fault classification task has also been carried out with DWT + SVM and DWT + MLPNN based schemes. Both of these schemes are implemented identically as DWT and ChNN based scheme, except the fact that the ChNN is replaced with SVM/MLPNN. The schematic diagram of the fault type identification schemes either with SVM or MLPNN is shown in Figure 8.6. Identical feature vectors described in the previous sub-sections have also been used for these schemes. These decomposed components (equation (8.4)) are then subjected to i) the SVM) or ii) MLPNN for classification.

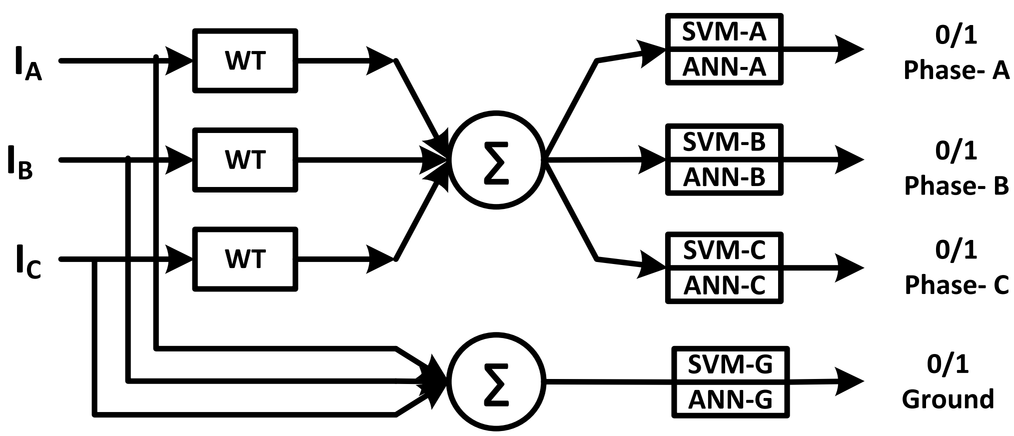

Figure 8.6: SVM/MLPNN based classification scheme

8.6 FAULT TYPE IDENTIFICATION WITH DWT + MLPNN AND DWT + SVM

For comparison, identical set of fault cases that has been used for ChNN based scheme is also used for these two schemes. The generated feature vector $\mathbf{v}^{\mathbf{dwt}}$ is subjected to pre-trained bunch of MLPNNs and SVMs. The classifier for each phase identifies the involvement of the corresponding phase in the fault. Fourth classifier identifies the involvement of the ground in the fault circuit with ground feature vector $\boldsymbol{v}_g^{dwt}$ as its input. The MLPNN/SVM gives '+1' as output if the associated phase or ground is involved in the event of fault, else '-1'.

The MLPNN is trained with the back-propagation algorithm with LSLM approach. After checking performance with different architecture of neural nets, a structure with 20 hidden layer neurons has been chosen because of its higher accuracy. The LibSVM 3.11 package [157] has been used in this work for training and testing of the SVM. Due to its better performance, Gaussian Kernel has been used with values of C=100000 and γ=0.0000045 for all four SVMs.

8.6.1 Performance Comparison

After decomposition with first level of wavelet transform, the clusters of SVM and MLPNN are trained with the data set of 2400 fault cases described in Table 8.2. Fault type identification accuracy for SVM and MLPNN based schemes are given in Table 8.6. As can be seen in Table 8.6, the accuracies of the both these methods are inferior to that obtained by ChNN based method at various levels of compensation with different firing angles.

Table 8.6: Performance of MLPNN and SVM based scheme for fault classification task on TCSC compensated transmission line

		SVM		MLPNN	
Fining Angle (α)	**No of test cases**	**No of fault cases misclassified**	**Accuracy**	**No of fault cases misclassified**	**Accuracy**
153˚	10800	287	97.34%	119	98.90%
160˚	8400	88	98.95%	54	99.36%
180˚	10800	175	98.38%	87	99.19%
Total	**30000**	**550**	**98.17%**	**260**	**99.13%**

Figure 8.7 shows the comparison of classification accuracies at different TCSC firing angles. It is worth to notice here that, ChNN provides equal level of accuracies at all firing angles considered in this work. However, a considerable amount of performance variation can be noticed for MLPNN and SVM based schemes. This indicates over fitting of MLPNN and SVM to the training cases. The ChNN has taken quite a necessary shape in the classification plane such that it gives identical accuracy for all TCSC firing angles. This is

because of the fact that ChNN has the potential to handle very large feature spaces. The training of ChNN has been carried out so that the dimension of classified vectors does not have distinct influence on the performance of ChNN. This makes ChNN efficient in large classification problems. From this discussion, it can easily be noticed that, non-linear capability of the ChNN is higher than that of MLPNN and SVM, which gives advantage to ChNN over MLPNN and SVM for fault type classification in controllable compensated environment.

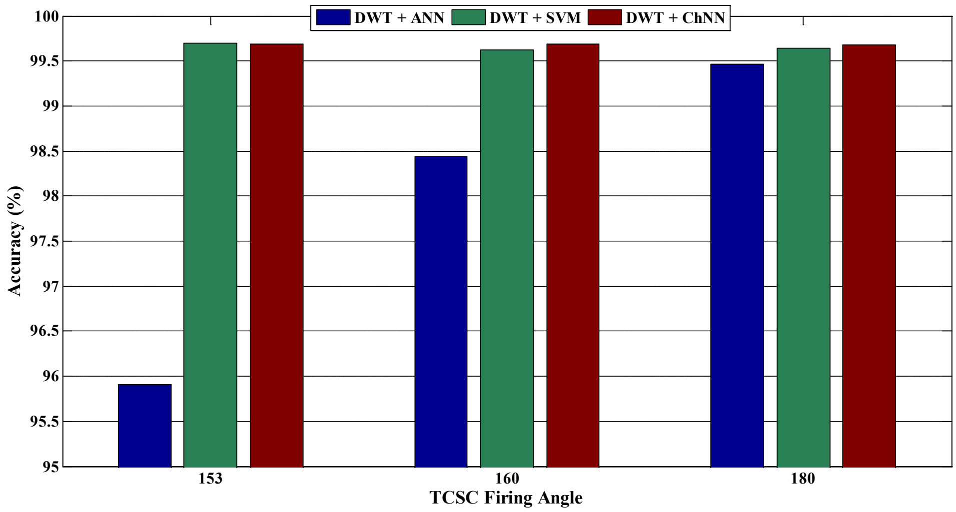

Figure 8.7 : Performance comparison of MLPNN, SVM and ChNN with DWT at various TCSC firing angles

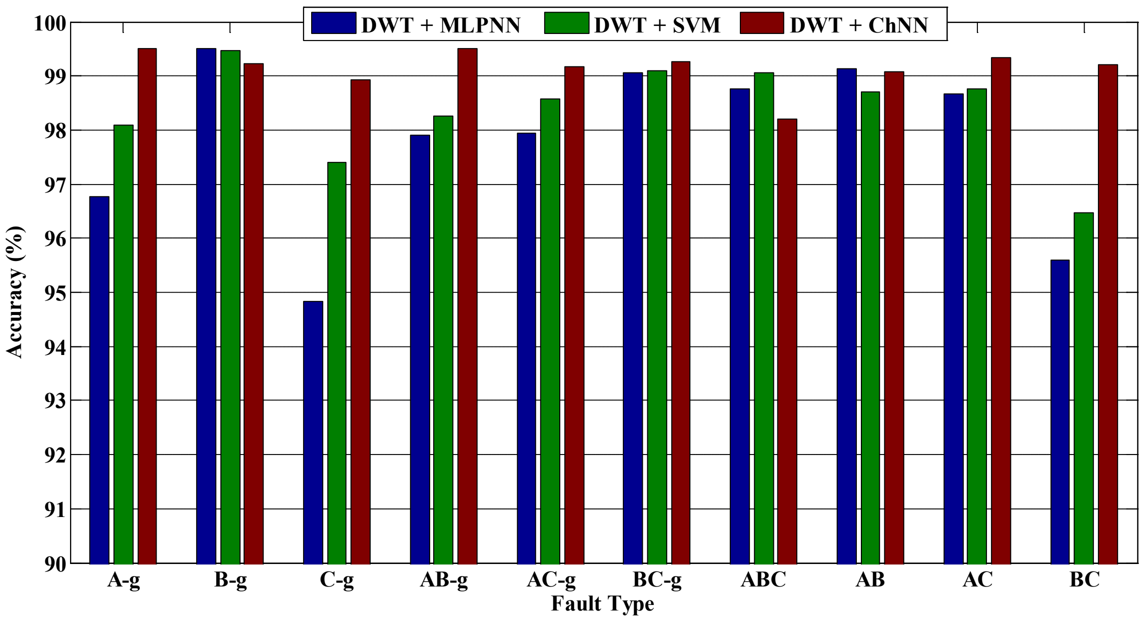

Figure 8.8: Comparison of MLPNN, SVM, ChNN for fault classification for different types of faults

Figure 8.8 compares all three considered classifiers for different type of faults. The result establishes ChNN as a better classifier which is able to produce the same level of accuracy for various types of faults. This is due to the better generalization capacity of ChNN compared to conventional classifiers such as SVM and MLPNN.

Table 8.7 shows other parameters to be considered for MLPNN, SVM and ChNN for practical implementation. Hidden layer in MLPNN increases the number of inter connection weights in the structure. With 60 inputs (20 detailed sub-bands for each phase) the total interconnection weights is 1220 [60*20 = 1200 (between input and hidden layer) + 20 (between hidden to output layer)]. These interconnections are bound to increase with either increase in hidden layer neurons or number of hidden layers. Thus use of MLPNN requires a significantly large amount of memory and calculations. This large structure makes back-propagation learning a very heavy computational task with high number or training cycles and computational time. In contrast to this, the SVM uses kernel based expansion for the classification task. The final vector structures (support vector) are very less compared to MLPNN and are obtained within very few numbers of training cycles. This improves the response time in real time. However, the performance of the SVM largely depends on the choice of Kernel function and classification parameters. A change in the classification parameter results in a major variation in classification boundary and hence the accuracy. With higher generalization capability, ChNN outperforms MLPNN and SVM for fault classification task.

Table 8.7: Comparison of application parameters for MLPNN, SVM and ChNN

	Neural Nets (Matlab Platform)	**SVM (LibSVM platform)**	**ChNN (Matlab platform)**
Training (2400 fault cases)	About 3 minutes	About 20 seconds	About 30 seconds
Testing (For any fault case)	Average 0.1 Sec	Average 0.1 Sec	Average 0.1 Sec
Classifier Structure	Nos. of NN weights A- Phase=1220, B- Phase=1220, C- Phase=1220, Ground =60	Nos. of Support vector A-Phase=52, B-Phase=38, C-Phase=14, Ground=6	Nos. of Weights A-Phase=60, B-Phase=60, C-Phase=60, Ground=20

8.7 APPLICATION OF DWPTE AND CHNN FOR FAULT TYPE CLASSIFICATION

DWPTE stands for Discrete Wavelet Packet Transform Entropy. As the name itself suggests, it involves entropy after DWPT decomposition. DWPT is an extension of DWT in which all nodes in the tree structure are allowed to split further at each level of decomposition

(Section 3.4, Chapter 3). The DWPT can describe the signal under consideration more efficiently than DWT [66].

The entropy is one of the quantitative measures associated with digital signal processing. The entropy provides valuable information for analysis of the time-varying signals, i.e. fault signals when associated with wavelet analysis. Different types of entropy such as log, norm, Shannon, sure, and threshold can be used to characterize the current signals. Shannon's entropy equation enables searching for the smallest entropy expansion of a signal [158]. Therefore, Shannon entropy has been utilized for this study (Section 3.5, Chapter 3). Entropy analysis of a signal with DWPT is capable of providing more valuable information than DWT.

The measured half cycle post-fault current signals (40 samples at 4 kHz) at the relaying end are preprocessed through DWPT. Second level of decomposition has been found necessary and sufficient for proper classification. The DWPT generates identical frequency resolutions for any level of decomposition. The decomposition frequency band generated by DWPT is shown in in Table 8.8.

The entropy value for each of the three phases are then calculated (equation (3.15)). This generates an entropy vector $\boldsymbol{G_p}$ (equation (8.7)) for all four decompositions corresponding to every phase *p* at sample 'k' as:

$$\boldsymbol{G_p} = [S_{DA}^{(k)}, S_{DD}^{(k)}, S_{AA}^{(k)}, S_{AD}^{(k)}]; \tag{8.7}$$

Table 8.8: Frequency resolution of DWPT

Decomposition Level	Number of Coefficients in the level	Detail Coefficients	Approximate Coefficient	Frequency Resolution
First	40	0-1 kHz	1-2 kHz	25 Hz
Second	20	0-500 Hz	500-1000 Hz	25 Hz

Each of the entropy is represented by a scalar value; therefore, the vector $\mathbf{G_P}$ is of length 4. A combination of entropy vector $\boldsymbol{G_p}$ for all the three phases generates the classification vector $\boldsymbol{V}$ for the specific fault case:

$$\mathbf{V = [G_A, G_B, G_C]} \tag{8.8}$$

With four entropy elements in the component vector of every phase, the length of the vector **V** is 12. The DWPE vector $\boldsymbol{V}$ is processed using AI techniques for training and testing of the algorithm to classify fault. The overall scheme is shown in Figure 8.9.

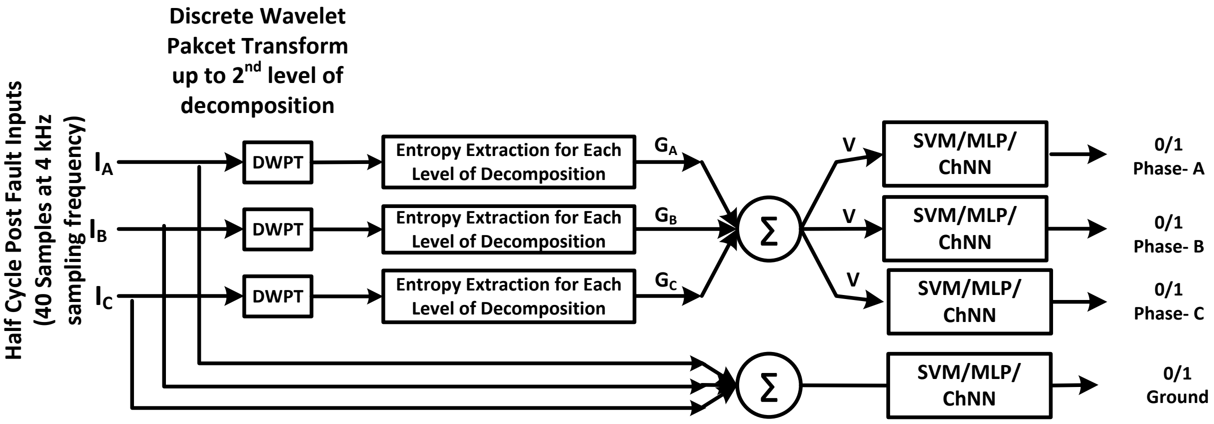

Figure 8.9 : DWPETE based fault classification scheme

Figure 8.10(a) represents variation in DWP entropy (S_{DD}) of the 'Detail' coefficient of the 'Detail' sub-band on first level decomposition for an A-g fault with change in fault resistances. The energies are represented for an A-g fault occurring at a distance of 120 km for loading angle of 10˚, fault inception angle of 45˚ and source impedance values of Z_{SG1} and Z_{SG2} tiven in Appendix – B respectively. It is clear from the plot that, a significant difference in DWP entropy exists to identify the faulty phase. The difference in entropy reduces with increase in fault resistance, which may lead to errors in classification. To eliminate these errors of classification wavelet packet entropy of other sub-bands can be utilized. Figure 8.10(b) represents the variation in DWP entropy of 'Approximate' sub-band (H_{AA} of Figure 3.4). It is basically derived from decomposition of 'Approximate' sub-band of first level decomposition for same fault conditions of Figure 8.10(a).

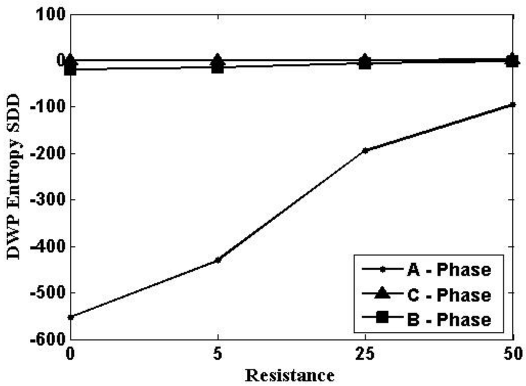

Figure 8.10 (a)

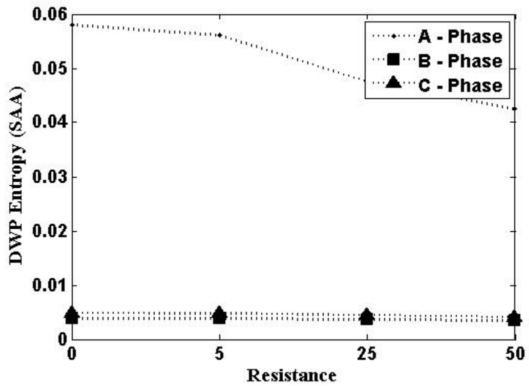

Figure 8.10 (b)

Figure 8.10 (a): Change in DWPE of S_{DD} with fault resistance, Figure 8.10 (b): Variation in DWPE for S_{AA} with fault resistances at FIA of 45 degrees, line loading angle of 10 degrees

Figure 8.11(a) represents the variation in S_{DD} with fault resistance for an A-B-g fault with same system condition as that of Figure 8.10(a). Figure 8.11 illustrates the changes in

S_{DD} due to variation in fault distance for an A-B-g fault with fault resistance of 25Ω, FIA = 85° and line loading angle of 30°.

The DWPE feature vector '***V***' (having 12 components, equation 8.8) is supplied to ChNN. For comparison, identical training and testing has also been performed with SVM and MLPNN . In the case of ChNN, the input vector '***V***' having 12 components is enhanced to an enhanced vector having 37 inputs with third level Chebyshev expansion.

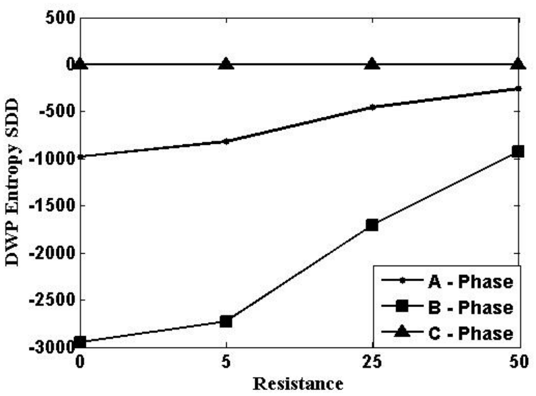

Figure 8.11 (a)

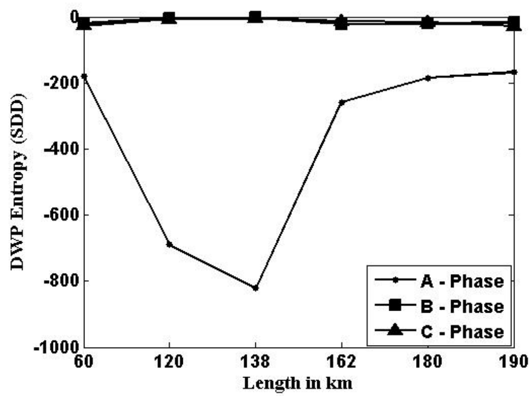

Figure 8.11 (b)

Figure 8.11 (a): Variation in DWPE of S_{DD} with fault resistance for A-B-g fault,
Figure 8. 11 (b): Variation in S_{DD} with change in fault distance

All three classifiers have been trained with identical 2400 fault patterns (as mentioned in Table 8.2) and testing has been performed with the same 30000 fault patterns. The optimal structure of the MLPNN, with 16 hidden layer nodes, has been chosen based on trial and error procedure. The DWPE, MLPNN, and ChNN have been implemented in Matlab [159] environment. The SVMs for all the three phases and ground have been designed with Radial Basis kernel function having C = 10000000, and gamma (γ) = 0.0000045. These parameters have also been chosen based on trial and error procedure. The SVM has been implemented in this study with support vector calculator of LibSVM [157].

8.7.1 Results and Discussion

In this study, ability of the ChNN for fault classification is compared with those of MLPNN and SVM. The DWPT entropy resolutions of half cycle post fault currents have been used for this purpose. After decomposition by WPT up to second level of resolution, Shannon entropy corresponding to each decomposition has been acquired and used by classifier for fault type identification. Table 8.9 shows the comparative performances of MLPNN and ChNN. From this table it is observed that the ChNN with third level of expansion gives the best accuracy. In this table, the term "fault classification errors" denotes the number of testing cases (patterns) for which the fault has been classified incorrectly. The "fault classification accuracy" has been computed as:

$$\eta = \frac{\text{Number of Correct Detection}}{\text{Total number of Test Cases Connsidered}} \text{x100}$$

Table 8.9 : Accuracy with TCSC firing angle variation for MLPNN and ChNN with 2nd and 3rd level of expansion

	Number of samples	MLPNN		ChNN with 2^{nd} order expansion		ChNN with 3^{rd} order expansion	
		Fault Classification errors	**Fault Classification Accuracy**	**Fault Classification errors**	**Fault Classification Accuracy**	**Classification errors**	**Accuracy**
153˚	10,800	287	97.34%	157	98.54%	53	99.51%
160˚	8,400	88	98.95%	64	99.23%	39	99.54%
180˚	10,800	175	98.38%	124	98.85%	49	99.55%
Total	**30,000**	**550**	98.17%	**345**	**98.85%**	**141**	**99.53 %**

Table 8.10 shows structural and other parameters to be considered for comparison of MLPNN with ChNN. With 12 inputs (4 sub-band entropies for each phase) the total number of interconnection weights for MLPNN is 208 [= (12*16 (between input and hidden layer) + 16 (between hidden to output layer)]. Thus, this MLPNN structure requires large amount of memory and computational time for both training and detection stage. In the absence of hidden layer, the ChNN inputs are directly connected to the output, which reduces computational and memory burden. Moreover, large structure of MLP makes back-propagation learning a very heavy computational task that increases the number of training cycles and training time as compared to the ChNN that trains efficiently and faster with back-propagation algorithm due to the absence of hidden layer as given in Table 8.10. The increase in Chebyshev expansion level increases the ability of the classifier as shown in Table 8.9, however, it increases the computation burden as well. In view of these issues, the order of Chebyshev expansion has been limited to three in this work.

Table 8.10: Structural comparison of MLPNN and ChNN

	Neural Nets	**ChNN 2^{nd} Order**	**ChNN 3^{rd} Order**
Hidden Layer	1	0	0
Hidden Layer Neurons	16	0	0
Classifier Structure	Nos. of NN weights A-Phase=208, B-Phase=208, C-Phase=208, Ground=208,	Nos. of NN weights A-Phase=36, B-Phase=36, C-Phase=36, Ground=36,	Nos. of NN weights A-Phase=48, B-Phase=48, C-Phase=48, Ground=48,
Training (2400 fault cases)	About 3 minutes	About 1 minute	About 1 minute

Comparative performances of SVM and ChNN are shown in Table 8.11 for various TCSC firing angles. As is evident from Table 8.11, the accuracies of both the methods are quite satisfactory at various levels of compensation with different firing angles. A higher level of accuracy is observed at 160˚ firing angle, as the SVM and ChNN are trained with data generated corresponding to this firing angle. The accuracy levels of both classifiers at other firing angles are almost same and satisfactory. This indicates the ability of ChNN to take required shape in the classification plane that gives identical accuracy for all TCSC firing angles. Like SVM, the training of ChNN has been carried out in such a way that, the classification weights do not have significant effect on the performance of classifier.

Table 8.11: Performance comparison of SVM and ChNN

TCSC Firing Angle	Number of samples	Support Vector Machine		ChNN with 3rd order expansion	
		Fault Classification errors	Fault Classification Accuracy	Fault Classification errors	Fault Classification Accuracy
180˚	10,800	119	98.90%	53	99.51%
160˚	8,400	54	99.36%	39	99.54%
153˚	10,800	87	99.19%	49	99.55%
Total	**30,000**	**260**	**99.13%**	**141**	**99.53 %**

Table 8.12 provides a comparison of the performances of MLPNN, SVM and ChNN with respect to faults occurring at various distances. The results show the adaptability of the ChNN to produce a similar level of accuracy for all fault distance, including those for which it is not trained.

Figure 8.12 compares the accuracies of the classifiers for different types of faults. Again from this figure it is observed that the accuracies obtained by ChNN remain almost same for all the fault types while the accuracies obtained by SVM and MLPNN reduce for some fault types.

Table 8.12: Performance evaluation at different fault Distance

Fault Distance	Number of samples	MLPNN		Support Vector Machine		ChNN with 3rd order expansion	
		Classification errors	Accuracy	Classification errors	Accuracy	Classification errors	Accuracy
60 km	4800	79	98.35 %	35	99.27 %	29	99.40 %
120 km	5400	83	98.27 %	55	98.85 %	18	99.67 %
138 km	4800	92	98.30 %	39	99.28 %	13	99.73 %
162 km	4800	91	98.31 %	44	99.19 %	28	99.42 %
180 km	5400	109	97.73 %	40	99.17 %	21	99.61 %
240 km	4800	96	98.00 %	47	99.02 %	32	99.33 %
Total	**30000**	**550**	**98.17 %**	**260**	**99.13 %**	**141**	**99.53 %**

8.8 PATTERN RECOGNITION BASED FAULT CLASSIFICATION FOR TCSC COMPENSATED TRANSMISSION LINE

As discussed in previous chapter, a scheme using DSP for feature extraction requires a numbers of filters for relaying applications that makes it slow for implementation. The two-staged DSP and AI based scheme require additional implementation of AI classifier after

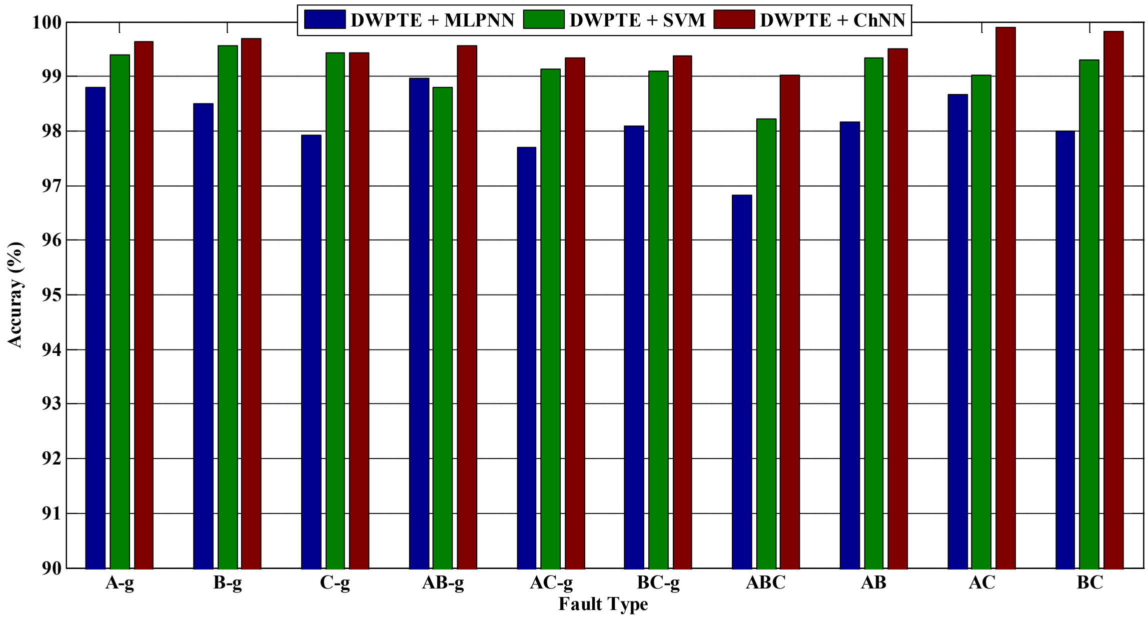

Figure 8.12 : Performance comparison of MLPNN, SVM and ChNN for TCSC compensated line fault classification with DWPE

DSP. In this scenario, the AI based pattern recognition techniques hold an edge for development. This section presents ChNN as a better pattern recognition tool for fault classification of the transmission line equipped with TCSC. Performance comparisons with MLPNN and SVM for identical fault cases are also presented. The proposed algorithm utilizes only half cycle post fault data at relaying end to determine the fault type. This makes the algorithm fast and practical.

The magnitude and spectra of the measured current change with inception of fault in a transmission line. The algorithm proposed in this section is based on recognition of these changes with ChNN used as a pattern recognition tool. The algorithm has been developed with measurements at relaying end (bus-A) of the considered system shown in Figure 8.3. The three-phase currents measured at this end are considered for pattern recognition with a cluster of four ChNNs.

Figure 8.13 (a) shows the current waveforms for all three phase for an A-g fault occurring at 180 km fault distance with 5 Ω fault resistance and 45° fault inception angle. The fault has been simulated with line loading angle of 20° with TCSC operating at firing angle (α) = 160°. Figure 8.13 (b) shows the three phase currents for an A-B-g fault with same system and fault conditions as in Figure 8.13 (a).

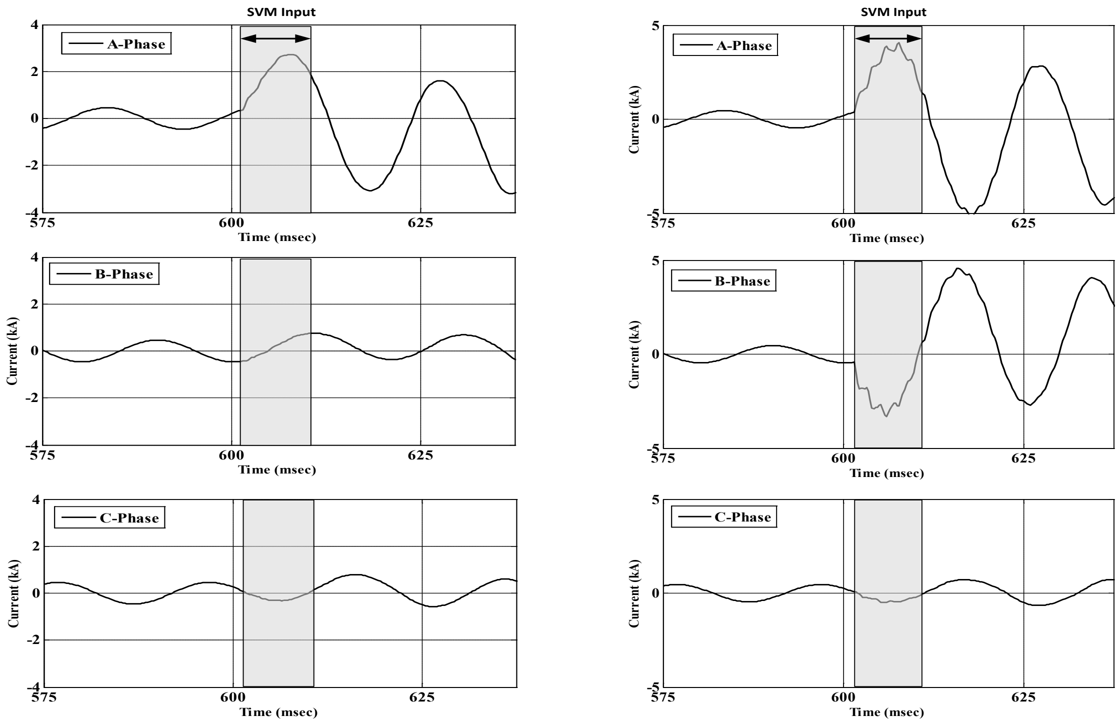

(a) (b)

Figure 8.13: ChNN inputs for (a) A-g fault and (b) A-B-g fault

The pattern recognition based fault classification scheme is shown in Figure 8.14. The three-phase currents measured at the relaying end are sampled with sampling frequency of 4 kHz. A half cycle post fault data (40 samples) from each phase is supplied to three ChNNs responsible for identifying the involvement of corresponding phase in the fault. With these samples from all the three phases, a classification vector is formed as given in equation (8.9).

$$V_{phase} = [C_A, C_B, C_c] \tag{8.9}$$

Where, $\mathbf{C_p}$ (p = A, B, C) is a vecor of 40 samples corresponding to phase p. To recognize the involvement of ground in fault, the fourth ChNN is supplied with a vector ($\boldsymbol{V_{ground}}$) representing summation of all three current samples (40 samples).

$$V_{neutral} = (C_A + C_B + C_c) \tag{8.10}$$

The input vectors are given to the ChNNs which give an output '+1', if the respective phase/ground is involved in the fault, otherwise the output is '-1'. The training of each ChNN has been performed with same data set of 2400 cases presented in Table 8.2. With higher amount of accuracies (99.59%), fourth order Chebyshev expansion is chosen for this work. The ChNN gives 98.98%, and 99.14% accuracies for second and third order of Chebyshev expansions. Moreover, higher level of expansion does not show a considerable improvement in accuracy. Therefore, fourth order ChNN is chosen in this work.

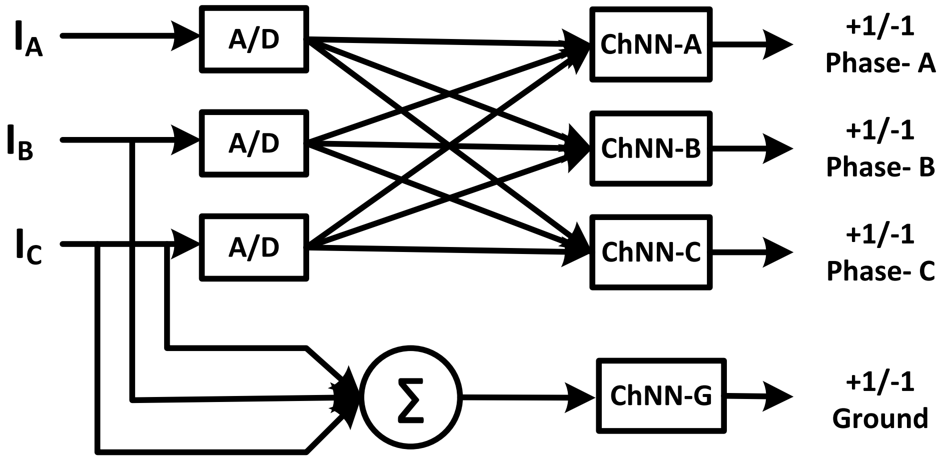

Figure 8.14: Direct pattern recognition application block diagram

To demonstrate the ability of the ChNN as a classifier, a comparative study has been conducted with MLPNN and SVM with identical fault cases. A typical feed-forward neural network with a single hidden layer has been considered for this evaluation. The number of hidden layer neurons, in the absence of any decisive algorithm for the architecture, has been chosen based on application performance. After checking the performance with different architecture of MLPNN, a structure of [(40-14-1) for A-Phase MLPNN, (40-18-1) for B-Phase MLPNN, (40-20-1) for C-Phase MLPNN and (40-4-1) for ground MLPNN have been chosen.

For SVM implementation, the Gaussian kernel has been found to be suitable for all four SVMs in this work. The literature reveals that in the absence of classification parameters (cost function 'C' and 'γ') governing mechanism, they are supposed to be finely adjusted for each SVM separately for appropriate classification. In this work, common values of these parameters are determined from implementation experiences for all four SVMs for fault type classification. The value of C=10000 and γ=0.0000042 have been chosen for all four SVMs. The trained SVM with these variables and Gaussian kernel carries 10, 47, 39, and 09 support vectors for Phase-A, Phase-B, Phase-C and ground respectively. The LibSVM 3.11 software has been used for implementation of SVMs [104, 160].

The identical classification vectors of $\boldsymbol{V_{phase}}$ and $\boldsymbol{V_{ground}}$ generated in equations (8.9) and (8.10) are used for classification with MLPNN and SVM. Both are trained with same training set of Table 8.2, which has been used for training of the ChNN.

8.8.1 Performance Evaluation for Direct Pattern Recognition Scheme

The direct pattern recognition algorithm has been tested with the same data set of 30000 fault cases used earlier in this chapter. Fault type identification accuracies for ChNN, SVM and MLPNN based schemes at different TCSC firing angles are given in Table 8.13. As can be seen in Table 8.13, accuracy of all these methods is quite satisfactory at various levels of compensation with different firing angles.

Table 8.13 : Accuracy with TCSC firing angle variation for MLPNN, SVM and ChNN

	Number of samples	MLPNN		Support Vector Machine		Chebyshev Neural Network	
		Fault Classification errors	Fault Classification Accuracy	Fault Classification errors	Fault Classification Accuracy	Classification errors	Accuracy
153˚	10,800	442	95.91%	169	98.44%	58	99.46%
160˚	8,400	25	99.70%	32	99.62%	30	99.64%
180˚	10,800	30	99.72%	34	98.69%	35	99.68%
Total	**30,000**	**497**	98.34%	**235**	**99.22%**	**123**	**99.59 %**

The accuracy of the proposed method with ChNN is almost same for different firing angles (level of compensations). However, a considerable variation in accuracy with TCSC firing angle can be seen with MLPNN. This indicates over-fitting of the training to the training cases. Moreover, performance of SVM and ChNN are almost same at various firing angles. It proves the abilities of SVM and ChNN to take intuitive shape in the multi-dimensional classification plane to give same level of accuracy for various TCSC firing angles; however these have been trained with TCSC angle of 160˚ only. Training of ChNN and SVM are carried out so that the dimension of classified vectors does not have distinct influence on the performance. This makes them efficient in large classification problems. The fault waveforms carry number of features that can be used for fault classification, and use of ChNN and SVM in this case becomes advantageous.

Table 8.14 shows the level of accuracies for different fault distances on the transmission line. The results establish ChNN as a better trained classifier which is able to produce same level of accuracy for various fault distances. This is due to the better generalization capacity of ChNN.

Table 8.14: Performance evaluation of at different fault distance

Fault Distance	Number of samples	MLPNN		Support Vector Machine		ChNN with 3^{rd} order expansion	
		Classification errors	Accuracy	Classification errors	Accuracy	Classification errors	Accuracy
60 km	4800	92	98.08 %	37	99.23 %	21	99.56 %
120 km	5400	86	98.41 %	34	99.37 %	13	99.76 %
138 km	4800	74	98.46 %	37	99.23 %	14	99.71 %
162 km	4800	61	98.73 %	33	99.31 %	26	99.46 %
180 km	5400	88	98.37 %	40	99.26 %	18	99.67 %
240 km	4800	96	98.00 %	54	98.88 %	31	99.35 %

Figure 8.15 shows the performance of all three methods with all three Artificial Intelligence classifiers. Performance of the SVM is almost same as that obtained with ChNN based schemes and for all types of faults. However, SVM is sensitive to its classification

parameters. This necessitates heuristic approach to identify classification parameters for each change in line configuration. In this scenario, the ChNN has been found to be a potential AI technique that is robust and free of classification variables.

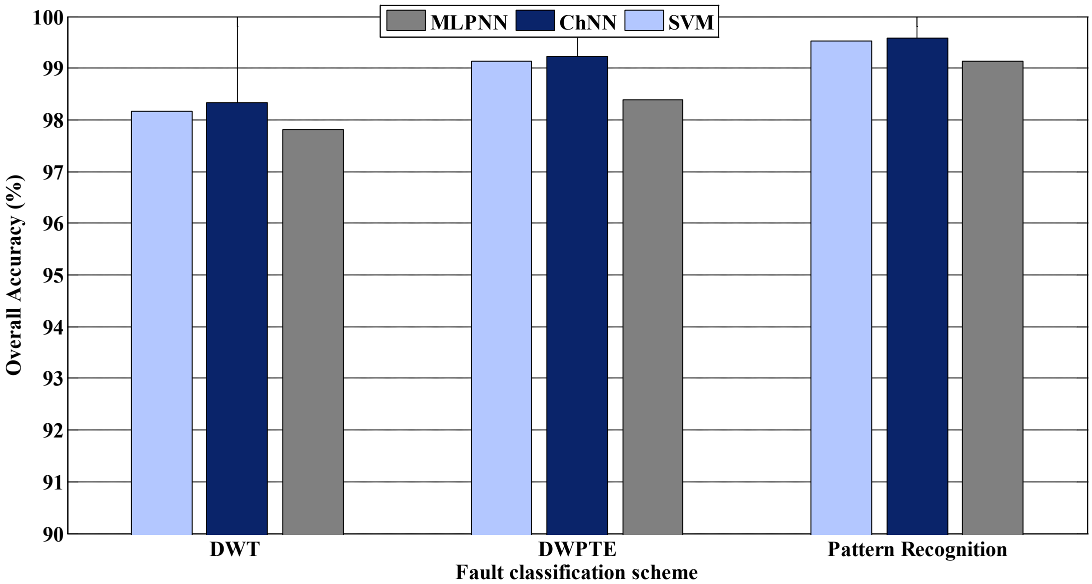

Figure 8.15: Comparison of classifier performance with DWT, DWPTE and pattern recognition application

Figure 8.16 shows the performances of pattern recognition based fault classification schemes for TCSC compensated transmission line for different types of faults. Superiority of ChNN can be seen in this figure also.

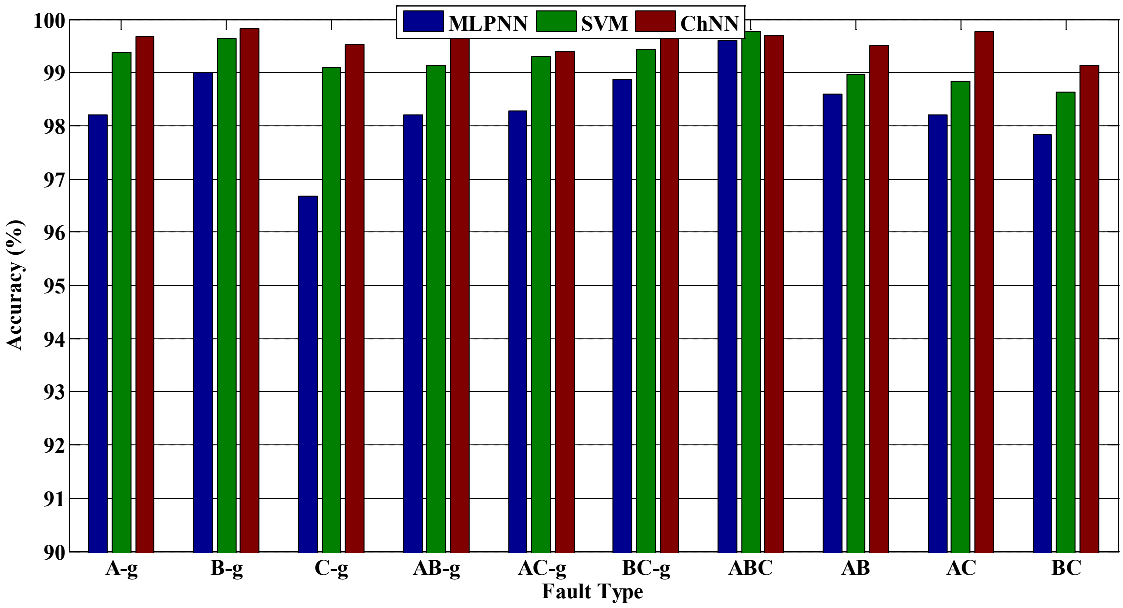

Figure 8.16: Comparison of fault classification accuracy for various fault types

8.9 DWT AND CHNN BASED FAULT ZONE IDENTIFICATION SCHEME

Spectral characteristics of fault current get modified with the inclusion of the TCSC in the fault circuit. This is due to the inclusion of equivalent TCSC impedance in the circuit. The fault zone identification in this work depends on the detection of this spectral change in the fault induced currents with the help of the DWT and ChNN.

Figure 8.17(a) and (b) show the current waveforms for all three phases for A-B-g fault at 40% and 60% of the line lengths respectively. Both of these faults have been simulated with fault resistance of 5 Ω, fault inception angle of 45˚ and line loading of 10˚ with generator impedances of Z_{SG1} and Z_{SG2} (given in Appendix – B). Figure 8.17(c) and (d) represent the first-level decomposition values of detail coefficients for fault currents represented in Figure 8.17(a) and (b) respectively. It is evident from the Figure 8.17(c) and (d) that, the presence of TCSC makes a considerable change in the pattern of wavelet detail coefficients.

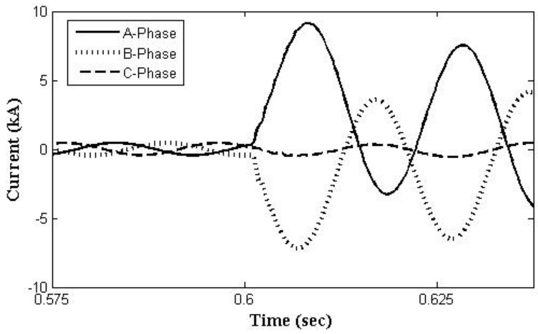

Fig. 8.17(a)

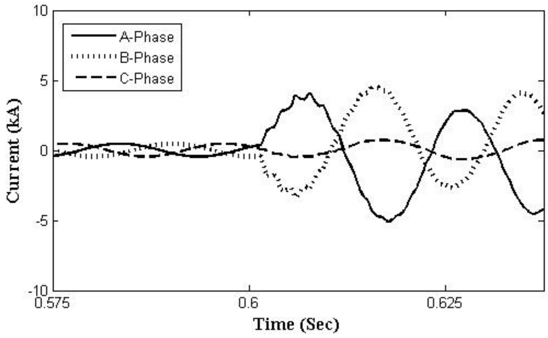

Fig. 8.17(b)

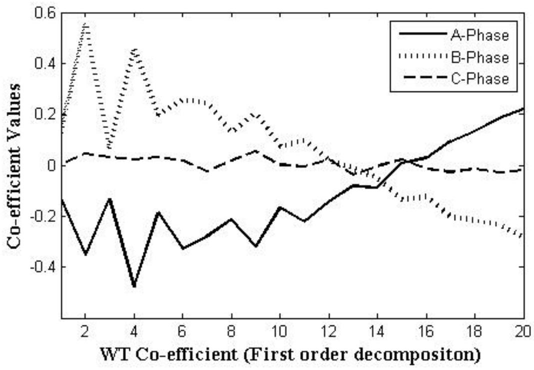

Figure 8.17(c)

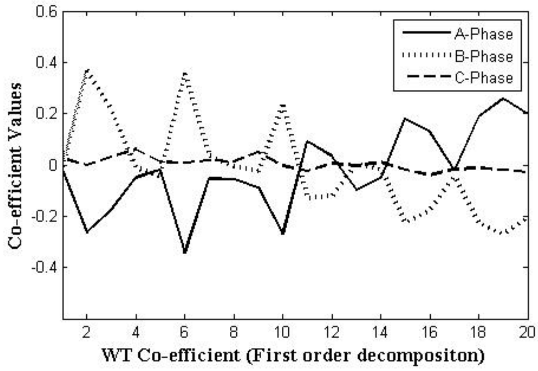

Figure 8.17(d)

Figure 8.17 (a):A-B-g fault at 40% of the line length
Figure 8.17 (b): A-B-g fault and 60% of the line length
Figure 8.17 (c): Detail coefficients for DWT for waveforms in Figure 8.16 (a)
Figure 8.17 (d): Detail coefficients for DWT for waveforms in Figure 8.16 (b)

Figure 8.18 represents the schematic diagram of fault zone identification scheme for TCSC compensated transmission line with DWT and ChNN. The vector $\boldsymbol{Q^{dwt}}$ (equation (8.4)) has been utilized for fault zone identification process. Due to highly non-linear nature of TCSC because of its control circuitry, a higher-order Chebyshev expansion is needed for successful classification. During implementation process, fifth order Chebyshev functional expansion has been found to be necessary for significantly accurate classification in this work.

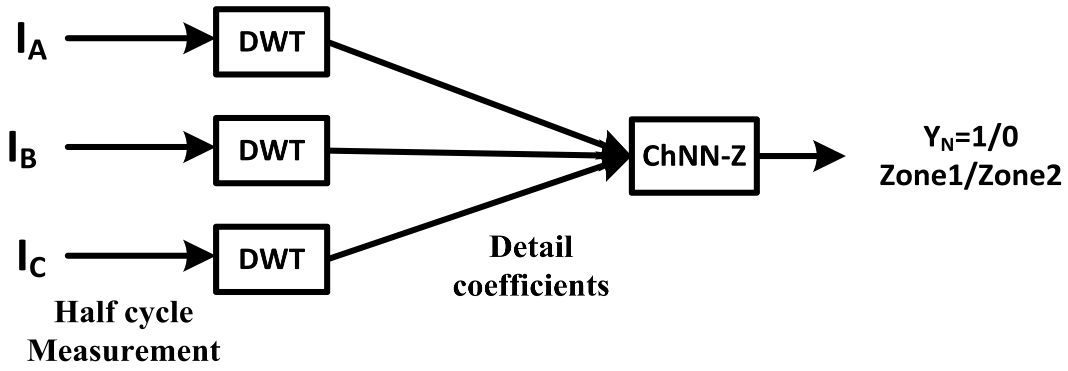

Figure 8.18: Block diagram of fault zone identification scheme

The fault zone classification vector $\boldsymbol{Q}^{dwt}$ consists of 60 detail resolutions per fault pattern (20 coefficients per phase). This extracted fault feature pattern is then subjected through a well-trained ChNN for fault zone identification. The fault zone classification vector $\boldsymbol{Q}^{dwt}$ (60 resolutions) is expanded to Θ_Z (301 samples) as:

$$\Theta_Z(x) = ([1, v_{i1}(x_1), v_{i2}(x_1), ... v_{i60}(x_5)]^T)_{i=A,B,C} \tag{8.11}$$

The same training set of 2400 fault cases (Table 8.2) has been used for training of ChNN-Z. This ChNN yields '0' for fault before the TCSC and '1' if the fault circuit includes the TCSC. The detailed results for fault zone identification with 30000 fault cases are given in the following section.

8.9.1 Performance Evaluation

The ChNN-Z used in this method has been trained with identical 2400 fault cases used for training the ChNNs used for fault classification. Table 8.15 shows the results for fault zone identification at various firing angles and faults at different locations. From Table 8.15 one can observe that the fault zone identification accuracy is almost same for all fault distances except for faults at 20% distance. This can be attributed to the fact that at this distance, the fault is quite close to the relay and therefore, fault current is of larger magnitude. A larger fault current means larger amplitude and spectral changes at the time of fault. As these significantly larger variations in magnitude and frequency are not presented to the classifier during training periods, it experiences some difficulty in the presence of large spectral changes during classification.

Table 8.15: Distribution of fault zone accuracy

Fault Distance (% of Total Line Length)	TCSC Firing Angle = 153˚			TCSC Firing Angle = 160˚			TCSC Firing Angle = 180˚		
	No of test cases	Classification Errors	Accuracy	No of test cases	Classification Errors	Accuracy	No of test cases	Classification Errors	Accuracy
Before TCSC									
20	1800	92	94.88%	1200	56	95.33%	1800	87	95.16%
40	1800	18	99.00%	1200	6	99.55%	1800	4	99.77%
46	1800	32	98.22%	1800	13	99.38%	1800	12	99.33%
After TCSC									
54	1800	37	97.94%	1800	17	99.05%	1800	14	99.22%
60	1800	35	98.05%	1200	3	99.77%	1800	3	99.83%
80	1800	3	99.83%	1200	0	100.00%	1800	2	99.88%
TOTAL	**10800**	**217**	**97.99%**	**8400**	**95**	**98.94%**	**10800**	**122**	**98.87%**

However, overall fault zone identification accuracy is on the higher side than that reported in the literature [43, 154]. The accuracy for fault zone identification in the line length between 40 to 60% (for mid-point compensation) is considered as a critical region for series compensated line protection scheme. The fault zone identification accuracy of the proposed algorithm is acceptably good in this zone as well and comparable to the accuracy obtained for other fault distances. This is despite the fact that samples corresponding to this zone are not used in training. However, a dip in accuracy is observed for firing angle of 153˚ as higher amount of spectral variations are observed compared to 160˚, at which the training has been performed. Fault zone detection results for all types of transmission line faults are presented in Figure 8.19. From this table, it can be inferred that the accuracies for all fault types are higher than that is reported in the literature.

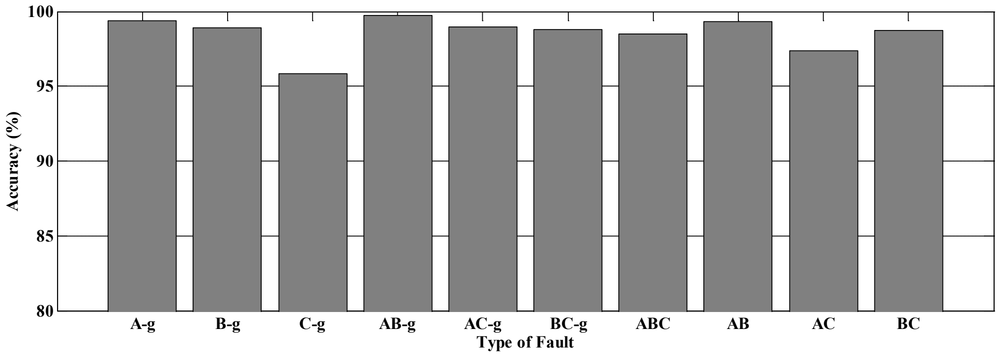

Figure 8.19: Fault zone detection accuracies for various types of faults

8.10 COMBINED FAULT TYPE AND FAULT ZONE IDENTIFICATION SCHEME WITH DWT AND CHNN

A fast, advanced and successful application of ChNN with DWT feature extraction has been described in Section 8.5 for fault type identification for TCSC compensated transmission line. A fault zone identification scheme based on the same DWT feature vector has been discussed in Section 8.9 of this chapter. As both schemes utilizes identical post fault DWT analyzed data, they can be represented as two-subroutines of a combined system. Figure 8.20 shows the flow diagram of the combined system for fault classification and fault zone identification.

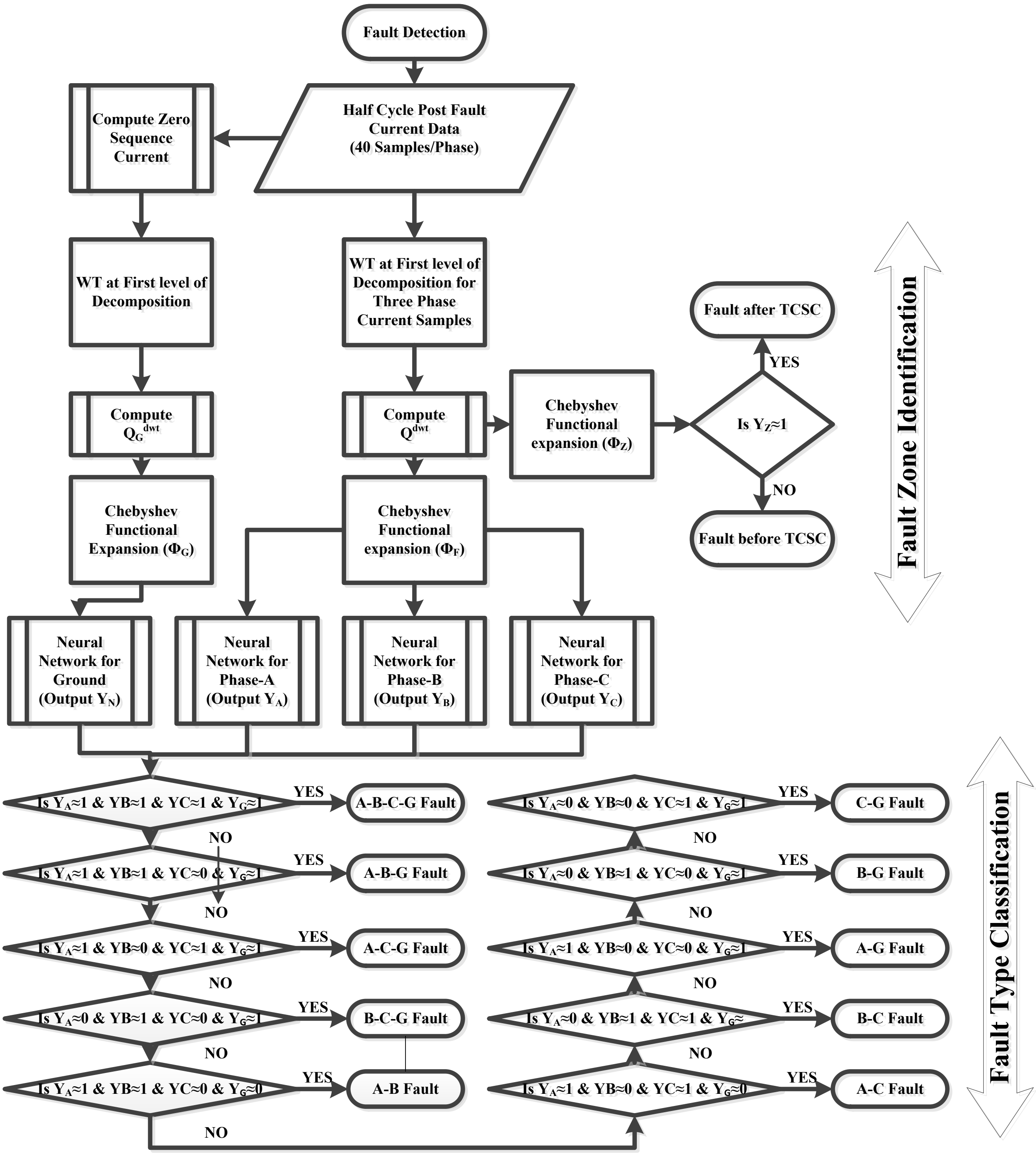

Figure 8.20: DWT and ChNN based combined fault classification and fault zone identification scheme

A typical fault pattern of three phase currents for an A-g fault occurring at 60% of the line length (fault after compensator) with fault resistance of 5 Ω, FIA of 45° and line loading angle of 10° is shown in Figure 8.21(a). The output of the all of ChNNs of the fault classification scheme are shown in Figure 8.21(b) while the output of the ChNN of the zone identification scheme is also seen in Figure 8.21(c) are also presented for the same time period for illustration.

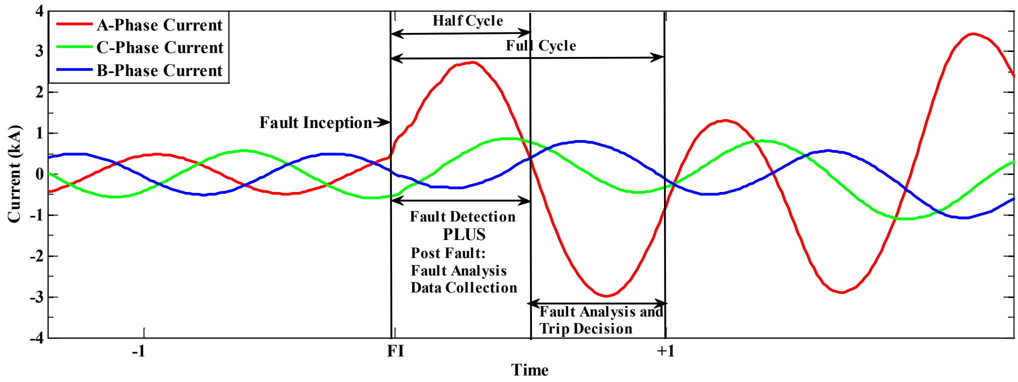

Figure 8.21 (a)

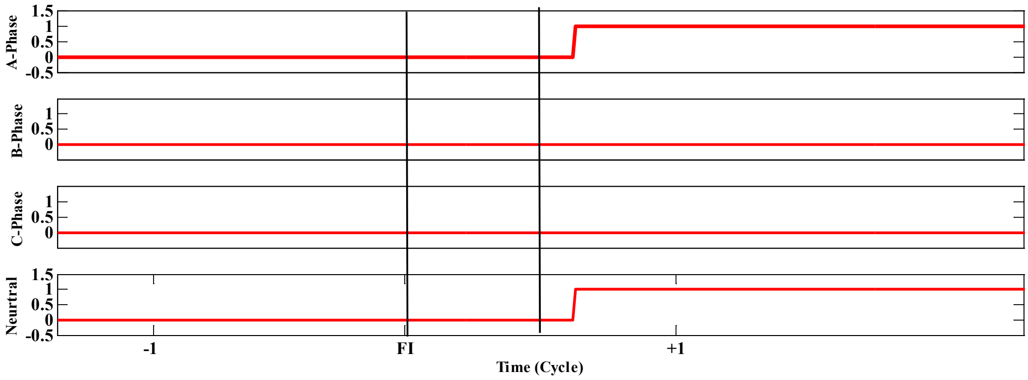

Figure 8.21 (b)

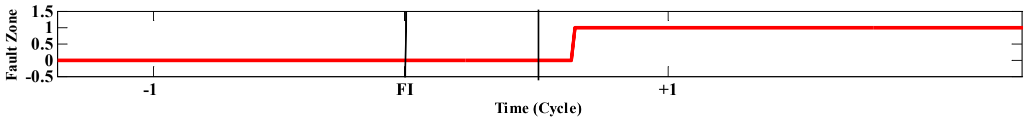

Figure 8.21 (c)

Figure 8.21: Three phase TCSC current and corresponding ChNN outputs for a A-g fault at 60% of the series compensated transmission line.

8.11 CONCLUSION

Fault classification and fault zone identification schemes for TCSC compensated transmission line have been presented in this chapter. The investigations made in this chapter infer that ChNN is a better classifier for protection analysis in controlled compensation environment.

Out of three schemes presented for fault classification, first two are of two-stage. First uses DWT and second uses DWPT for fault feature extraction. However, the third applies ChNN as direct pattern recognition tool. All three methodologies utilizes only half cycle post fault current data. Testing of the developed algorithm for different fault and system conditions has been carried out with a large set of simulated fault data obtained by simulation the system on a dynamic power system simulator PSCAD/ EMTDC.

Proposed methods are found to be capable to classify the fault and identify the fault zone with better accuracy and speed for wide system parameter variations. The results clearly establish the ability of Chebyshev Neural Network for non-linear regression and to take intuitive shape in the classification plane to provide improved results.

9.1 CONCLUSION

Long EHV transmission lines have a very important function in modern power systems. With inclusion of series compensation, their protection represents a critical task to maintain both stability and reliability of the power system.

This work has focused on fundamental issues in the protection of series compensated transmission lines, namely, fault detection, fault classification, fault zone identification and estimation of fault location. Although solutions do exists for these problems, new approaches have been proposed in this work which have been found to be advantageous over the existing methods reported in the literature.

Fault signals on series compensated transmission line are arbitrary in nature and carries variations in their time-frequency structures. Such signals are produced from highly non-linear components such as compensator on the line. Capability of the wavelet to approximate the piecewise signal effectively made it the first choice in this work. To capture these time-frequency variations, wavelets and their variants have been used for all the four problems considered in this work.

Being free from structural constraints and insensitive to parameter variations, the ChNN possess several advantages over existing artificial intelligence techniques used in protection system. Therefore, the ChNN has been used for all the four tasks in this work and the performance of the ChNN based scheme has been found to be better than the performances obtained by other existing techniques in the literature. A comparative study of ChNN based scheme with MLPNN and SVM based schemes has also been made for many applications for identical fault cases. The ChNN proved to be better in all of these investigations. Considerable improvement in term of accuracy and time of operation has been achieved with newly developed fault type identification algorithms. Spectral components of the fault generated transients on time-scale are extracted to generate the feature pattern for classification with the help of DWT. Application of ChNN to recognize these pattern shows considerable improvements in accuracies than those reported in the literature. Moreover, direct application of ChNN for recognizing the fault current pattern improves the performance further. Also, it was observed that the performance of the DWT-ChNN scheme is better than those obtained by DWT-SVM and DWT-MLPNN schemes.

Training is a very important aspect of ChNN implementation. The success of the recall process relies on the ability of the training set to reflect the characteristic features of each specific separable category. Therefore, two ChNN learning algorithms, namely, RLSFF and LSLM have been compared for fault classification performance. However, when the ChNN is trained with limited number of training patterns, the performance of the RLSFF method has been found to deteriorate with variation in system and fault parameters. Therefore, the ChNN with LSLM learning has been found to be more suitable over the ChNN with RLSFF method for series compensated line fault classification application.

An accurate fault zone identification algorithm of series compensated transmission line is developed in this work. This is achieved by integrating UDWT and ChNN. It shows an improvement in performance as compared to another developed method using DWT along with ChNN. However, performance of DWT and ChNN based method also shows improvement in terms of accuracy and execution time as compared to the other methods already available in literature.

In the later stage of this work, fault classification and fault zone identification algorithms developed for fixed series compensated line are improved to address the changes which occur due to the presence of TCSC instead of fixed series capacitor. Application of ChNN proved to be superior for fault classification and fault zone identification as compared to SVM and MLPNN based methods which utilize enhanced DWT feature vector. Extraction of DWPEM further enhances the fault classification accuracies.

All the above fault location and fault zone identification algorithms have been implemented with local (relaying end) current measurements of half cycle duration (post fault) only. Requirement of only half cycle post fault measurements makes all the developed algorithms quite fast in response. Moreover, application of three phase current measurements only eliminates the voltage measurements and related computations.

With contineous development in power networks, any transmission line stretches for hundreds of kilometers over complex geographic terrain. Precise and timely fault location information speeds up the restoration of the line which, in turn, and reduces the revenue losses. In this thesis some of the phasor estimation based fault location approaches are investigated for their accuracies. However, due to errors in phasor estimation procedure, they give larger fault location errors. The fault location estimation scheme presented in this thesis overcome the shortcoming of the phasor estimation and other existing methods by introducing a novel AI based regression method using ChNN along with DWT feature vector extraction. It was observed that the developed methodology is robust and immune to fault and system parameter variations.

One major advantage of the newly developed technique over existing methods is its ability to work without any communication channel for estimating the location of the fault. This enables considerable cost saving in capital and operating cost of the protection system.

9.2 THESIS OUTCOME

After investigation of all the developed algorithms with a large number of fault cases with all possible types of faults, faults parameters and system parameters variations, following outcomes of this work can be listed:

- The fault classification, fault zone identification and fault location algorithms developed in this work show considerable improvement in terms of accuracy compared to the methods available in the literature.
- All algorithms in this work are developed for single end measurement only. This eliminates the requirement of measurements from other end, communication channel and synchronization.
- All fault classification and fault zone identification algorithms are developed to work with measurements of three phase currents only. This eliminates the requirement of voltage related measurements and computation.
- All fault classification and fault zone identification algorithms designed in this work are developed to work with half cycle post fault measurements only. This reduces the processing time of the algorithms thereby making them quite fast for practical implementation.
- Among SVM, MLPNN and ChNN, ChNN has been found to be most accurate and fast classifier for protection application.
- UDWT and DWPEM have been found to be quite effective and useful time-frequency analysis tools that improve accuracies of the protection scheme.
- DWT and ChNN based fault location estimation scheme proposed in this work provides highly accurate scheme for estimating the fault location. It shows a considerable improvement in performance as compared to the fault location estimation accuracies reported in the literature.
- Application of lower frequency components of fault generated transients proved to be immune to the effect of series compensator, even at various compensation levels. The fault detection and classification algorithm developed with lower frequency components have been found to give very high level of accuracies for both uncompensated and series compensated transmission lines.
- Fault classification and fault zone identification algorithms have been modified and improved to take into account the TCSC related changes thereby providing higher level of accuracies than those reported in the literature.

9.3 FUTURE SCOPE

Some of the suggestions for the future work in this research area are as follows:

- An accurate model of the compensator provides a great advantage in designing the protection system for series compensated transmission line, as voltage across the compensator can be estimated by the model. However, most widely used compensator model does not replicate the non-linearity of the compensator accurately. This indicates the requirement of more sustained efforts in this direction.
- Few of phasor based fault location approaches are considered in this work. However, more accurate one-ended phasor estimation can improve the fault location estimation. Further, development of an effective fault location scheme for TCSC compensated line also needs to be investigated.
- A novel protection algorithm for fault detection and classification has been developed in this work using lower frequency transient components. This algorithm is equally capable to provide wqually effective fault detection and classification to both uncompensated and series compensated transmission line. However, an integrated algorithm including fault detection, classification, zone identification and location will be a welcome step in this direction.

  It would be quite useful to design protection systems for other series compensating devices such as SSSC, TSSC and GCSC.

PUBLICATIONS FROM THE WORK

Journals

1. B. Vyas, R. P. Maheshwari and B. Das, "Protection of series compensated transmission line: Issues and state of art," *Electric Power Systems Research,* vol. 107, pp. 93-108, 2014.

2. B. Vyas, R. P. Maheshwari and B. Das, "Improved fault analysis technique for protection of Thyristor controlled series compensated transmission line," *International Journal of Electrical Power & Energy Systems,* vol. 55, pp. 321-330, 2014.

3. Bhargav Vyas, Rudra Prakash Maheshwari, and Biswarup Das, "Evaluation of Artificial Intelligence Techniques for Fault Type Identification in Advanced Series Compensated Transmission Lines," *IETE Journal of Research,* vol. 60, no. 1, pp. 85-91, 2014/01/02 2014

4. B. Vyas, R. P. Maheshwari and B. Das, "Investigation for Improved Artificial Intelligence Techniques for Thyristor-controlled Series-compensated Transmission Line Fault Classification with Discrete Wavelet Packet Entropy Measures," *Electric Power Components and Systems,* vol. 42, pp. 554-566, 2014.

5. Bhargav Vyas, Biswarup Das, and Rudra Prakash Maheshwari, "An improved scheme for identifying fault zone in a series compensated transmission line using undecimated wavelet transform and Chebyshev Neural Network," *International Journal of Electrical Power & Energy Systems,* vol. 63, no. pp. 760-768, 2014.

6. B. Y. Vyas, B. Das, and R. P. Maheshwari, "Improved Fault Classification in Series Compensated Transmission Line: Comparative Evaluation of Chebyshev Neural Network Training Algorithms," *IEEE Transactions on Neural Networks and Learning Systems,* vol. PP, no. 99, pp. 1-1, 2014.

7. B. Vyas, R. P. Maheshwari and B. Das, “Versatile Relaying Algorithm for Detection and Classification of Faults on Uncompensated and Series Compensated Transmission Lines” Under review with IET, Generation, Transmission and Distribution since December, 2013

International conferences

8. Bhargav Vyas, Rudra Prakash Maheshwari, Biswarup Das, “Fault Analysis of Controllable Series Compensated Transmission Line with Wavelet Transform and Support Vector Machine”
2012 Nirma University International Conference on Engineering, NUiCONE-2012, 06-08 December, 2012, pp- 1-5

9. Bhargav Vyas, Rudra Prakash Maheshwari, Biswarup Das , “Support Vector Machine based Fault classification scheme for Thyristor Controlled Series Compensated Transmission Lines”
Int. Conf. on Soft Computing, Artificial Intelligence, Pattern Recognition, Biomedical Engineering and Associated Technologies (SAP-BEATS) 2013, February 23-24, 2013, pp- 203-207.

10. Bhargav Vyas, Rudra Prakash Maheshwari, Biswarup Das , "Fault Detection and Fault Type Identification in Uncompensated and Series Compensated Transmission Line Using Discrete Wavelet Transform," *Power Systems Conference (PSC 2013), Clemson University, March 12 – 15, 2013. pp. 1-5*

[1] C. R. Masson, *The Art and Science of Protective Relaying*: John Wiley & Sons, Inc.

[2] L. M. Wedepohl, "Polarised mho distance relay New approach to the analysis of practical characteristics," *Proceedings of the Institution of Electrical Engineers,* vol. 112, no. 3, pp. 525-235, 1965

[3] N. G. Hingorani and L. Gyugyi, *Understanding FACTS*, First Indian Edition ed.: IEEE Press, 2001.

[4] Y. Hu, D. Novosel, M. M. Saha, and V. Leitloff, "An adaptive scheme for parallel-line distance protection," *IEEE Transactions on Power Delivery,* vol. 17, no. 1, pp. 105-110, 2002.

[5] B. S. Ashok Kumar, K. Parthasarathy, F. S. Prabhakara, and H. P. Khincha, "Effectiveness of Series Capacitors in Long Distance Transmission Lines," *IEEE Transactions on Power Apparatus and Systems,* vol. PAS-89, no. 5, pp. 941-951, 1970.

[6] R. Gruenbaum, "Series capacitors improve the line efficiency transmission," in *ABB power systems, Vasteras, Sweden*, 1988.

[7] S. Jamali, A. Kazemi, and H. Shateri, "Measured impedance for inter phase faults in presence of TCSC considering MOV operation," in *Electric Power Conference, 2008. EPEC 2008. IEEE Canada*, pp. 1-7, 2008.

[8] J. Woodworth, "MOV Protection of Series Capacitor Banks," in *Arrester Factors008*, 2008.

[9] M. Coursol, C. T. Nguyen, R. Lord, and X-D Do, "Modeling MOV-protected series capacitors for short-circuit studies," *IEEE Transactions on Power Delivery,* vol. 8, no. 1, pp. 448-453, 1993.

[10] B. Kasztenny, "Distance protection of series compensated lines–problems and solutions," in *Proceedings of the 28th Annual Western Protective Relay Conference, Spokane, WA*, 2001.

[11] B. Vyas, R. P. Maheshwari, and B. Das, "Protection of series compensated transmission line: Issues and state of art," *Electric Power Systems Research,* vol. 107, no. 1, pp. 93-108, 2014.

[12] P. K. Dash, A. K. Pradhan, and G. Panda, "Apparent Impedance Calculations for Distance-Protected Transmission Lines Employing Series-Connected FACTS Devices," *Electric Power Components and Systems,* vol. 29, no. 7, pp. 577-595, 2001.

[13] D. Novosel, A. Phadke, M. M. Saha, and S. Lindahl, "Problems and solutions for microprocessor protection of series compensated lines," in *Sixth International Conference on Developments in Power System Protection*, pp. 18-23, 1997.

[14] S. Wilkinson, "Series Compensated Line Protection Issues," in *GE Power Management*.

[15] G. E. Alexander, J. Mooney, and W. Tyska, "Advanced application guidelines for ground fault protection," in *Schweitzer Engineering Laboratories, Inc*, 2001.

[16] S. G. Srivani and K. P. Vittal, "Adaptive distance relaying scheme in series compensated transmission lines," in *Joint International Conference on Power Electronics, Drives and Energy Systems (PEDES) & 2010 Power India*, pp. 1-7, 2010.

[17] E. O. Schweitzer III and J. Roberts, "Distance relay element design," in *46th Annual Conference for Protective Relay Engineers, Texas A&M University, College Station, Texas*, 1993.

[18] H. J. Altuve, J. B. Mooney, and G. E. Alexander, "Advances in Series-Compensated Line Protection," in *62nd Annual Conference for Protective Relay Engineers*, pp. 263-275, 2009.

[19] D. L. Goldsworthy, "A linearized model for MOV-protected series capacitors," *IEEE Transactions on Power Systems,* vol. 2, no. 4, pp. 953-957, 1987.

[20] E. Rosolowski, J. Izykowski, P. Pierz, M. Fulczyk, P. Balcerek, and M. M. Saha, "High voltage series-compensated transmission line-evaluation of new distance protection," in *International Conference on High Voltage Engineering and Application (ICHVE), 2010*, pp. 513-516, 2010.

[21] Y. H. Song, A. T. Johns, and Q. Y. Xuan, "Artificial neural-network-based protection scheme for controllable series-compensated EHV transmission lines," *IEE Proceedings- Generation, Transmission and Distribution,* vol. 143, no. pp. 535-540, 1996.

[22] U. B. Parikh, B. Das, and R. P. Maheshwari, "Fault classification technique for series compensated transmission line using support vector machine," *International Journal of Electrical Power & Energy Systems,* vol. 32, no. 6, pp. 629-636, 2010.

[23] A. K. Pradhan, A. Routray, S. Pati, and D. K. Pradhan, "Wavelet fuzzy combined approach for fault classification of a series-compensated transmission line," *IEEE Transactions on Power Delivery,* vol. 19, no. 4, pp. 1612-1618, 2004.

[24] T. Dalstein and B. Kulicke, "Neural network approach to fault classification for high speed protective relaying," *IEEE Transactions on Power Delivery,* vol. 10, no. 2, pp. 1002-1011, 1995.

[25] P. K. Dash, S. R. Samantaray, and G. Panda, "Fault classification and section identification of an advanced series-compensated transmission line using support vector machine," *IEEE Transactions on Power Delivery,* vol. 22, no. 1, pp. 67-73, 2007.

[26] N. K. Saia, "The importance of site selection for series compensation," in *58th Annual Conference for Protective Relay Engineers*, pp. 201-210, 2005.

[27] M. E. Mandour and A. A. El-Alaily, "Swivelling characteristic for the protection of series compensated lines," *Electric Power Systems Research,* vol. 18, no. 1, pp. 31-35, 1990.

[28] R. K. Gajbhiye, B. Gopi, P. Kulkarni, and S. A. Soman, "Computationally efficient methodology for analysis of faulted power systems with series-compensated transmission lines: A phase coordinate approach," *IEEE Transactions on Power Delivery,* vol. 23, no. 2, pp. 873-880, 2008.

[29] R. Grünbaum, K. Wikström, and G. Strömberg, "On Series Compensation Impact on Line Protection and TRV," in *North American Power Symposium (NAPS)*, Västerås, Sweden, pp. 1-5, 2009.

[30] S. G. Srivani and K. P. Vittal, "Integrated Adaptive Reach Setting of Distance Relaying Scheme in Series Compensated Lines," *International Journal on Electrical Engineering and Informatics,* vol. 2, no. 4, pp. 291-297, 2010.

[31] M. M. Saha, B. Kasztenny, E. Rosolowski, and J. Izykowski, "First zone algorithm for protection of series compensated lines," *IEEE Transactions on Power Delivery,* vol. 16, no. 2, pp. 200-207, 2001.

[32] M. Al-Dabbagh and S. K. Kapuduwage, "Using instantaneous values for estimating fault locations on series compensated transmission lines," *Electric Power Systems Research,* vol. 76, no. 1, pp. 25-32, 2005.

[33] J. Sadeh and A. Adinehzadeh, "Accurate fault location algorithm for transmission line in the presence of series connected FACTS devices," *International Journal of Electrical Power & Energy Systems,* vol. 32, no. 4, pp. 323-328, 2010.

[34] A. Damnjanovic, D. Dayton, and G. Ferguson, "Assessment Modeling of Series Capacitors Protected by Metal Oxide Varistors in Power System Studies," in *Power Engineering Society General Meeting, 2007. IEEE*, pp. 1-5, 2007.

[35] D. W. P. Thomas and C. Christopoulos, "Ultra-high speed protection of series compensated lines," *IEEE Transactions on Power Delivery,* vol. 7, no. 1, pp. 139-145, 1992.

[36] Jun-Zhe Yang and Chih-Wen Liu, "A precise calculation of power system frequency and phasor," *IEEE Transactions on Power Delivery,* vol. 15, no. 2, pp. 494-499, 2000.

[37] Jyh-Cherng Gu and Sun-Li Yu, "Removal of DC offset in current and voltage signals using a novel Fourier filter algorithm," *IEEE Transactions on Power Delivery,* vol. 15, no. 1, pp. 73-79, 2000.

[38] C-S Yu, J-Z Yang, and C-W Liu, "New Fourier filter design for fault current filtering of series compensated lines," *International journal of power & energy systems,* vol. 28, no. 2, pp. 203-211, 2008.

[39] D. Gottlieb and Chi-Wang Shu, "On the Gibbs phenomenon and its resolution," *SIAM review,* vol. 39, no. 4, pp. 644-668, 1997.

[40] G. Helmberg, "The Gibbs phenomenon for Fourier interpolation," *Journal of Approximation Theory,* vol. 78, no. 1, pp. 41-63, 1994.

[41] A. K. Pradhan, A. Routray, and B. Biswal, "Higher order statistics-fuzzy integrated scheme for fault classification of a series-compensated transmission line," *IEEE Transactions on Power Delivery,* vol. 19, no. 2, pp. 891-893, 2004.

[42] D. C. Robertson, O. I. Camps, J. S. Mayer, and W. B. Gish, "Wavelets and electromagnetic power system transients," *IEEE Transactions on Power Delivery,* vol. 11, no. 2, pp. 1050-1058, 1996.

[43] P. K. Dash and S. R. Samantray, "Phase selection and fault section identification in thyristor controlled series compensated line using discrete wavelet transform," *International Journal of Electrical Power & Energy Systems,* vol. 26, no. 9, pp. 725-732, 2004.

[44] A. M. El-Zonkoly and H. Desouki, "Wavelet entropy based algorithm for fault detection and classification in FACTS compensated transmission line," *International Journal of Electrical Power & Energy Systems,* vol. 33, no. 8, pp. 1368-1374, 2011.

[45] S. R. Samantaray and P. K. Dash, "Pattern recognition based digital relaying for advanced series compensated line," *International Journal of Electrical Power & Energy Systems,* vol. 30, no. 2, pp. 102-112, 2008.

[46] S. R. Samantaray, L. N. Tripathy, and P. K. Dash, "Differential energy based relaying for thyristor controlled series compensated line," *International Journal of Electrical Power & Energy Systems,* vol. 43, no. 1, pp. 621-629, 2012.

[47] Z. Moravej, M. Khederzadeh, and M. Pazoki, "New Combined Method for Fault Detection, Classification, and Location in Series-compensated Transmission Line," *Electric Power Components and Systems,* vol. 40, no. 9, pp. 1050-1071, 2012.

[48] D. Novosel, B. Bachmann, D. Hart, Y. Hu, and M. M. Saha, "Algorithms for locating faults on series compensated lines using neural network and deterministic methods," *IEEE Transactions on Power Delivery,* vol. 11, no. 4, pp. 1728-1736, 1996.

[49] B. Bachmann, D. Novosel, D. Hart, Y. Hu, and M. M. Saha, "Application of artificial neural networks for series compensated line protection," in *International Conference on Intelligent Systems Applications to Power Systems*, pp. 68-73, 1996.

[50] Q. Y. Xuan, Y. H. Song, A. T. Johns, R. Morgan, and D. Williams, "Performance of an adaptive protection scheme for series compensated EHV transmission systems using neural networks," *Electric Power Systems Research,* vol. 36, no. 1, pp. 57-66, 1996.

[51] Y. H. Song, Q. Y. Xuan, and A. T. Johns, "Protection scheme for EHV transmission systems with thyristor controlled series compensation using radial basis function neural networks," *Electric Machines and Power Systems,* vol. 25, no. 5, pp. 553-565, 1997.

[52] A. M. Ibrahim, M. I. Marei, S. F. Mekhamer, and M. M. Mansour, "An artificial neural network based protection approach using total least square estimation of signal parameters via the rotational invariance technique for flexible AC transmission system compensated transmission lines," *Electric Power Components and Systems,* vol. 39, no. 1, pp. 64-79, 2011.

[53] A. Y. Abdelaziz, A. M. Ibrahim, M. M. Mansour, and H. E. Talaat, "Modern approaches for protection of series compensated transmission lines," *Electric Power Systems Research,* vol. 75, no. 1, pp. 85-98, 2005.

[54] Guang-Bin Huang, Qin-Yu Zhu, and Chee-Kheong Siew, "Extreme learning machine: theory and applications," *Neurocomputing,* vol. 70, no. 1, pp. 489-501, 2006.

[55] V. Malathi, N. S. Marimuthu, S. Baskar, and K. Ramar, "Application of extreme learning machine for series compensated transmission line protection," *Engineering Applications of Artificial Intelligence,* vol. 24, no. 5, pp. 880-887, 2011.

[56] U. B. Parikh, B. Das, and R. P. Maheshwari, "Combined wavelet-SVM technique for fault zone detection in a series compensated transmission line," *IEEE Transactions on Power Delivery,* vol. 23, no. 4, pp. 1789-1794, 2008.

[57] B. R. Bhalja and R. P. Maheshwari, "Wavelet-based fault classification scheme for a transmission line using a support vector machine," *Electric Power Components and Systems,* vol. 36, no. 10, pp. 1017-1030, 2008.

[58] P. Tripathi, G. N. Pillai, and H. O. Gupta, "New method for fault classification in TCSC compensated transmission line using GA tuned SVM," in *IEEE International Conference on Power System Technology (POWERCON), 2012*, pp. 1-6, 2012.

[59] H. S. Carslaw, "A historical note on Gibbs' phenomenon in Fourier's series and integrals," *Bulletin of the American Mathematical Society,* vol. 31, no. 8, pp. 420-424, 1925.

[60] A. J. Jerri, *The Gibbs phenomenon in Fourier analysis, splines and wavelet approximations* vol. 446: Springer, 1998.

[61] S. Mallat, *A wavelet tour of signal processing*: Academic press, 1999.

[62] *Wavelet Toolbox user's guide,* : The MathWorks, Inc, 2007.

[63] S. Mallat, "A theory for multiresolution signal decomposition: the wavelet representation," *IEEE Transactions on Pattern Analysis and Machine Intelligence,* vol. 11, no. 7, pp. 674-693, 1989.

[64] R. R. Coifman, Y. Meyer, and V. Wickerhauser, "Wavelet analysis and signal processing," in *In Wavelets and their Applications*, 1992.

[65] J. C. Goswami and A. K. Chan, *Fundamentals of wavelets: theory, algorithms, and applications* vol. 233: Wiley. com, 2011.

[66] X. Hu, Z. Wang, and X. Ren, "Classification of surface EMG signal using relative wavelet packet energy," *Computer methods and programs in biomedicine,* vol. 79, no. 3, pp. 189-195, 2005.

[67] C. E. Shannon and W. Weaver, "A mathematical theory of communication," ed: American Telephone and Telegraph Company, 1948.

[68] H. Zhengyou, L. Zhigang, and Q. Qingquan, "Study on wavelet entropy theory and adaptability of its application in power system," *Power System Technology -Beijing,* vol. 28, no. 21, pp. 17-21, 2004.

[69] C. E. Shannon, "A mathematical theory of communication," *ACM SIGMOBILE Mobile Computing and Communications Review,* vol. 5, no. 1, pp. 3-55, 2001.

[70] J. C. Pesquet, H. Krim, and H. Carfantan, "Time-invariant orthonormal wavelet representations," *IEEE Transactions on Signal Processing,* vol. 44, no. 8, pp. 1964-1970, 1996.

[71] J-L Starck, J. Fadili, and F. Murtagh, "The undecimated wavelet decomposition and its reconstruction," *Image Processing, IEEE Transactions on,* vol. 16, no. 2, pp. 297-309, 2007.

[72] Andrew P. Bradley, "Shift-invariance in the Discrete Wavelet Transform," in *Proc. VIIth Digital Image Computing: Techniques and Applications*, Sydney, pp. 29-38, 2003.

[73] M. J. Shensa, "The discrete wavelet transform: wedding the a trous and Mallat algorithms," *IEEE Transactions on Signal Processing,* vol. 40, no. 10, pp. 2464-2482, 1992.

[74] D. L. Fugal, *Conceptual wavelets in digital signal processing: an in-depth, practical approach for the non-mathematician*: Space & Signals Technical Pub., 2009.

[75] Simon S Haykin, *Neural networks: a comprehensive foundation*: Prentice Hall Englewood Cliffs, NJ, 2007.

[76] D. E. Rumelhart and J. L. McClelland, *Parallel Distributed Processing: Explorations in the Microstructure of Cognition. Foundations* vol. 1: MIT press, 1987.

[77] T. M. Cover, "Geometrical and statistical properties of systems of linear inequalities with applications in pattern recognition," *IEEE Transactions on Electronic Computers,* vol. EC-14, no. 3, pp. 326-334, 1965.

[78] K. Hornik, M. Stinchcombe, and H. White, "Multilayer feedforward networks are universal approximators," *Neural networks,* vol. 2, no. 5, pp. 359-366, 1989.

[79] Yoh-Han Pao, *Adaptive pattern recognition and neural networks*: Addison-Wesley Longman Publishing Co., Inc., 1989.

[80] K. Hornik and P. Baldi, "Neural networks and principal component analysis: Learning from examples without local minima," *Neural networks,* vol. 2, no. 1, pp. 53-58, 1989.

[81] B. B. Misra and S. Dehuri, "Functional Link Artificial Neural Network for Classification Task in Data Mining," *Journal of Computer Science,* vol. 3, no. 12, pp. 948-955, 2007.

[82] L. Tsu-Tian and J. Jin-Tsong, "The Chebyshev-polynomials-based unified model neural networks for function approximation," *IEEE Transactions on Systems, Man, and Cybernetics, Part B: Cybernetics,* vol. 28, no. 6, pp. 925-935, 1998.

[83] J. C. Patra and C. Bornand, "Development of Chebyshev neural network-based smart sensors for noisy harsh environment," in *The 2010 International Joint Conference on Neural Networks (IJCNN)*, Barcelona, Spain, pp. 1-8, 2010.

[84] J. C. Mason and D. C. Handscomb, *Chebyshev polynomials*: Chappman & Hall/CRC, 2003.

[85] N. Cristianini and J. Shawe-Taylor, *An introduction to support vector machines and other kernel-based learning methods*. Cambridge, UK: Cambridge university press, 2000.

[86] M. M. Abduljabbar, "Shared Congestion Detection: A Comparative Study," *Journal of Engineering,* vol. 18, no. 9, 2012.

[87] W. G. Zanardelli, E. G. Strangas, and S. Aviyente, "Failure prognosis for permanent magnet ac drives based on wavelet analysis," in *IEEE International Conference on Electric Machines and Drives*, pp. 64-70, 2005.

[88] J. L. Blackburn and T. J. Domin, *Protective Relaying Principles and Applications*, Third Edition ed.: CRC Press, 2007.

[89] A. G. Phadke and J. S. Thorp, *Computer relaying for power systems*: Wiley, 2009.

[90] F. Ghassemi, J. Goodarzi, and A. T. Johns, "Method to improve digital distance relay impedance measurement when used in series compensated lines protected by a

metal oxide varistor," *IEE Proc-Generation Trunsmission Distribution,* vol. 145, no. 4, pp. 403-408, 1998.

[91] S. M. Brahma and A. A. Girgis, "Fault location on a transmission line using synchronized voltage measurements," *IEEE Transactions on Power Delivery,* vol. 19, no. 4, pp. 1619-1622, 2004.

[92] *User's Guide on the use of PSCAD*: Manitoba HVDC Research Centre, 2010.

[93] P. M. Anderson and A. A. Fouad, *Power system control and stability*: Wiley. com, 2008.

[94] F. H. Magnago and A. Abur, "Fault location using wavelets," *IEEE Transactions on Power Delivery,* vol. 13, no. 4, pp. 1475-1480, 1998.

[95] N. Yamashita and M. Fukushima, "On the rate of convergence of the Levenberg-Marquardt method," in *Topics in numerical analysis*ed: Springer, pp. 239-249, 2001.

[96] B. Das and J.V. Reddy, "Fuzzy-logic-based fault classification scheme for digital distance protection," *IEEE Transactions on Power Delivery,* vol. 20, no. 2, pp. 609-616, 2005.

[97] S. P. Valsan and K. S. Swarup, "Wavelet transform based digital protection for transmission lines," *International Journal of Electrical Power & Energy Systems,* vol. 31, no. 7–8, pp. 379-388, 2009.

[98] M. R. Azimi-Sadjadi and R. J. Liou, "Fast learning process of multilayer neural networks using recursive least squares method," *IEEE Transactions on Signal Processing,* vol. 40, no. 2, pp. 446-450, 1992.

[99] R. L. Schultz and M. T. Hagan, "Online least-squares training for the underdetermined case," in *International Joint Conference on Neural Networks (IJCNN'99)*, pp. 1870-1875, 1999.

[100] Q. Xu, K. Krishnamurthy, B. McMillin, and W. Lu, "A recursive least squares training algorithm for multilayer recurrent neural networks," in *American Control Conference, 1994*, pp. 1712-1716, 1994.

[101] S. Dehuri, "A novel learning scheme for Chebyshev functional link neural networks," *Advances in Artificial Neural Systems,* vol. 2011, no. 1, pp. 1-10, 2011.

[102] P. Kundur, *Power system stability and control*: Tata McGraw-Hill Education, 1994.

[103] Stefan Bergman, *The kernel function and conformal mapping* vol. 5: American Mathematical Soc., 1970.

[104] C. C. Chang and C. J. Lin, "LIBSVM: a library for support vector machines," *ACM Transactions on Intelligent Systems and Technology (TIST),* vol. 2, no. 3, pp. 1-27, 2011.

[105] DC Jiles and DL Atherton, "Theory of ferromagnetic hysteresis," *Journal of Magnetism and Magnetic Materials,* vol. 61, no. 1, pp. 48-60, 1986.

[106] U. D. Annakkage, P. G. McLaren, E. Dirks, R. P. Jayasinghe, and A. D. Parker, "A current transformer model based on the Jiles-Atherton theory of ferromagnetic hysteresis," *IEEE Transactions on Power Delivery,* vol. 15, no. 1, pp. 57-61, 2000.

[107] MW Conroy, BD Nelson, B Bozoki, JW Chadwick, PR Drum, LL Dovrak, IO Hasenwinkle, JD Huddleston III, WC Kotheimer, and JR Linders, "C37. 110 guide for the application of current transformers used for protective relaying purposes," *IEEE Transactions on Power Delivery,* vol. 14, no. 1, pp. 94-97, 1999.

[108] Current transformer relaying accuracies – IEEE compared to IEC [Online]. Available: www.usa.siemens.com/techtopics

[109] T. S. Sidhu and M. Khederzadeh, "Series compensated line protection enhancement by modified pilot relaying schemes," *IEEE Transactions on Power Delivery,* vol. 21, no. 3, pp. 1191-1198, 2006.

[110] S. M. Hashemi, M. T. Hagh, and H. Seyedi, "A Novel Backup Distance Protection Scheme for Series-Compensated Transmission Lines," *IEEE Transactions on Power Delivery,* vol. 29, no. 2, pp. 699-707, 2014.

[111] H. Eristi, "Fault diagnosis system for series compensated transmission line based on wavelet transform and adaptive neuro-fuzzy inference system," *Measurement,* vol. 46, no. 1, pp. 393-401, 2013.

[112] M. M. Tawfik and M. M. Morcos, "ANN-based techniques for estimating fault location on transmission lines using Prony method," *IEEE Transactions on Power Delivery,* vol. 16, no. 2, pp. 219-224, 2001.

[113] S. R. Samantaray, "Decision tree-based fault zone identification and fault classification in flexible AC transmissions-based transmission line," *IET Generation, Transmission & Distribution,* vol. 3, no. 5, pp. 425-436, 2009.

[114] A. I. Megahed, A. M. Moussa, and A. E. Bayoumy, "Usage of wavelet transform in the protection of series-compensated transmission lines," *IEEE Transactions on Power Delivery,* vol. 21, no. 3, pp. 1213-1221, 2006.

[115] G.P. Nason and B.W. Silverman, "The stationary wavelet transform and some statistical applications," *Lecture Notes in Statistics- New York - Springer Verlag,* no. pp. 281-281, 1995.

[116] X.Y. Wang, H.Y. Yang, and Z.K. Fu, "A new wavelet-based image denoising using undecimated discrete wavelet transform and least squares support vector machine," *Expert Systems with Applications,* vol. 37, no. 10, pp. 7040-7049, 2010.

[117] Y. Zhang, S. Wang, Y. Huo, L. Wu, and A. LIU, "Feature extraction of brain MRI by stationary wavelet transform and its applications," *Journal of Biological Systems,* vol. 18, no. spec01, pp. 115-132, 2010.

[118] M. M. Saha, J. Izykowski, E. Rosolowski, and B. Kasztenny, "A new accurate fault locating algorithm for series compensated lines," *IEEE Transactions on Power Delivery,* vol. 14, no. 3, pp. 789-797, 1999.

[119] R. N. Mahanty and P. B. D. Gupta, "Application of RBF neural network to fault classification and location in transmission lines," *Generation, Transmission and Distribution, IEE Proceedings-,* vol. 151, no. 2, pp. 201-212, 2004.

[120] M. Abe, N. Otsuzuki, T. Emura, and M. Takeuchi, "Development of a new fault location system for multi-terminal single transmission lines," *IEEE Transactions on Power Delivery,* vol. 10, no. 1, pp. 159-168, 1995.

[121] T. Funabashi, H. Otoguro, Y. Mizuma, L. Dube, and A. Ametani, "Digital fault location for parallel double-circuit multi-terminal transmission lines," *IEEE Transactions on Power Delivery,* vol. 15, no. 2, pp. 531-537, 2000.

[122] A. A. Yusuff, C. Fei, A. A. Jimoh, and J. L. Munda, "Fault location in a series compensated transmission line based on wavelet packet decomposition and support vector regression," *Electric Power Systems Research,* vol. 81, no. 7, pp. 1258-1265, 2011.

[123] V. Malathi, N. S. Marimuthu, and S. Baskar, "Intelligent approaches using support vector machine and extreme learning machine for transmission line protection," *Neurocomputing,* vol. 73, no. 10, pp. 2160-2167, 2010.

[124] S. Ekici, "Support Vector Machines for classification and locating faults on transmission lines," *Applied Soft Computing,* vol. 6, no. 12, pp. 1650-1658, 2012.

[125] R. K. Aggarwal, A. T. Johns, and D. S. Tripp, "The development and application of directional comparison protection for series compensated transmission systems," *IEEE Transactions on Power Delivery,* vol. 2, no. 4, pp. 1037-1045, 1987.

[126] A. Hosny and M. Safiuddin, "ANN-based protection system for Controllable Series-Compensated transmission lines," in *Power Systems Conference and Exposition, 2009. PSCE'09. IEEE/PES*, pp. 1-6, 2009.

[127] J. Sadeh, A. M. Ranjbar, N. Hadsaid, and R. Feuillet, "Accurate fault location algorithm for series compensated transmission lines," in *Power Engineering Society Winter Meeting, 2000. IEEE*, pp. 2527-2532, 2000.

[128] S. G. Jalali, R. H. Lasseter, and I. Dobson, "Dynamic response of a thyristor controlled switched capacitor," *IEEE Transactions on Power Delivery,* vol. 9, no. 3, pp. 1609-1615, 1994.

[129] B. J. Mann and I. F. Morrison, "Digital calculation of impedance for transmission line protection," *IEEE Transactions on Power Apparatus and Systems,* no. 1, pp. 270-279, 1971.

[130] B. Hadzi-Kostova, "Protection Concepts in Distribution Network with Decentralised Energy Resources," Otto-von-Guericke-Universität Magdeburg, Universitätsbibliothek, 2005.

[131] L. Wang, "Frequency responses of phasor-based microprocessor relaying algorithms," *IEEE Transactions on Power Delivery,* vol. 14, no. 1, pp. 98-109, 1999.

[132] J. J. Paserba, N. W. Miller, E. V. Larsen, and R. J. Piwko, "A thyristor controlled series compensation model for power system stability analysis," *IEEE Transactions on Power Delivery,* vol. 10, no. 3, pp. 1471-1478, 1995.

[133] C. R. Fuerte-Esquivel, E. Acha, and H. Ambriz-Perez, "A thyristor controlled series compensator model for the power flow solution of practical power networks," *IEEE Transactions on Power Systems,* vol. 15, no. 1, pp. 58-64, 2000.

[134] IEEE Std., "IEEE guide for determining fault location on AC transmission and distribution lines," vol. C37.144, ed, 2005.

[135] B. R. Bhalja and R. P. Maheshwari, "High-resistance faults on two terminal parallel transmission line: analysis, simulation studies, and an adaptive distance relaying scheme," *IEEE Transactions on Power Delivery,* vol. 22, no. 2, pp. 801-812, 2007.

[136] Y. Liao and S. Elangovan, "Digital distance relaying algorithm for first-zone protection for parallel transmission lines," *IEE Proceedings-Generation, Transmission and Distribution,* vol. 145, no. 5, pp. 531-536, 1998.

[137] A. L. Dalcastagnê, H. H. Zurn, and R. Seara, "An iterative two-terminal fault-location method based on unsynchronized phasors," *IEEE Transactions on Power Delivery,* vol. 23, no. 4, pp. 2318-2329, 2008.

[138] D. J. Lawrence, L. Z. Cabeza, and L. T. Hochberg, "Development of an advanced transmission line fault location system. II. Algorithm development and simulation," *IEEE Transactions on Power Delivery,* vol. 7, no. 4, pp. 1972-1983, 1992.

[139] J. Persson, L. Rouco, and L. Soder, "Linear analysis with two linear models of a thyristor-controlled series capacitor," in *Power Tech Conference Proceedings, 2003 IEEE Bologna*, Vol. 3, 2003.

[140] C. Gama and R. Tenorio, "Improvements for power systems performance: modeling, analysis and benefits of TCSCs," in *Power Engineering Society Winter Meeting, 2000. IEEE*, pp. 1462-1467, 2000.

[141] *Neural Network Toolbox™ User's Guide*: The MathWorks, Inc., 2009.

[142] M Joorabian, "Artificial intelligent based fault location technique for EHV series-compensated lines," in *Proceedings of EMPD'98. 1998 International Conference on Energy Management and Power Delivery, 1998.*, pp. 479-484, 1998.

[143] R. K. Aggarwal, Q. Y. Xuan, R. W. Dunn, A. T. Johns, and A. Bennett, "A novel fault classification technique for double-circuit lines based on a combined unsupervised/supervised neural network," *IEEE Transactions on Power Delivery,* vol. 14, no. 4, pp. 1250-1256, 1999.

[144] P. Pillay and A. Bhattacharjee, "Application of wavelets to model short-term power system disturbances," *IEEE Transactions on Power Systems,* vol. 11, no. 4, pp. 2031-2037, 1996.

[145] K. M. Silva, B. A. Souza, and N. S. D. Brito, "Fault detection and classification in transmission lines based on wavelet transform and ANN," *IEEE Transactions on Power Delivery,* vol. 21, no. 4, pp. 2058-2063, 2006.

[146] H. Wang and W. W. L. Keerthipala, "Fuzzy-neuro approach to fault classification for transmission line protection," *IEEE Transactions on Power Delivery,* vol. 13, no. 4, pp. 1093-1104, 1998.

[147] I. Daubechies, "The wavelet transform, time-frequency localization and signal analysis," *IEEE Transactions on Information Theory,* vol. 36, no. 5, pp. 961-1005, 1990.

[148] S. Dehuri and S. B. Cho, "A Comprehensive Survey on Functional Link Neural Networks and an Adaptive PSO–BP Learning for CFLNN," *Journal of Neural Computing & Applications,* vol. 19, no. 2, pp. 187-205, 2010.

[149] Z. Haiquan and Z. Jiashu, "Pipelined Chebyshev Functional Link Artificial Recurrent Neural Network for Nonlinear Adaptive Filter," *IEEE Transactions on Systems, Man, and Cybernetics, Part B: Cybernetics,* vol. 40, no. 1, pp. 162-172, 2010.

[150] P. Mattavelli, G. C. Verghese, and A. M. Stankovic, "Phasor dynamics of thyristor-controlled series capacitor systems," *IEEE Transactions on Power Systems,* vol. 12, no. 3, pp. 1259-1267, 1997.

[151] D. Jovcic and G. N. Pillai, "Analytical modeling of TCSC dynamics," *IEEE Transactions on Power Delivery,* vol. 20, no. 2, pp. 1097-1104, 2005.

[152] D. Jovcic, N. Pahalawaththa, M. Zavahir, and H. A. Hassan, "SVC dynamic analytical model," *IEEE Transactions on Power Delivery,* vol. 18, no. 4, pp. 1455-1461, 2003.

[153] "PSCAD/EMTDC Version 4.2.0 " Winnipag, MB, Canada: Manitoba HVDC Research Centre.

[154] Z. Moravej, M. Pazoki, and A. Abdoos, "A new approach for fault classification and section detection in compensated transmission line with TCSC," *European Transactions on Electrical Power,* vol. 21, no. 1, pp. 997-1014, 2011.

[155] P. K. Dash, A. K. Pradhan, and G. panda, "Application of Artificial Intelligence Techniques for Classification and Location of Faults on Thyristor-Controlled Series-Compensated Line," *Electric Power Components and Systems,* vol. 31, no. 241, pp. 241-260, 2003.

[156] Y. G. Paithankar and S. R. Bhide, *Fundamentals of Power System Protection*: PHI Learning Pvt. Ltd, 2004.

[157] C.C. Chang and C.J. Lin, "LIBSVM: a library for support vector machines," *ACM Transactions on Intelligent Systems and Technology (TIST),* vol. 2, no. 3, p. 27, 2011.

[158] W. Li, L. Weixing, and L. Ruiye, "Applications of Entropy Principles in Power Systems: A Survey," in *Transmission and Distribution Conference and Exhibition: Asia and Pacific, 2005 IEEE/PES*, pp. 1-4, 2005.

[159] *MATLAB, version 7.10.0*. Natick, Massachusetts: The MathWorks Inc., 2010.

[160] C. W. Hsu, C. C. Chang, and C. J. Lin, "A practical guide to support vector classification," ed, 2003.

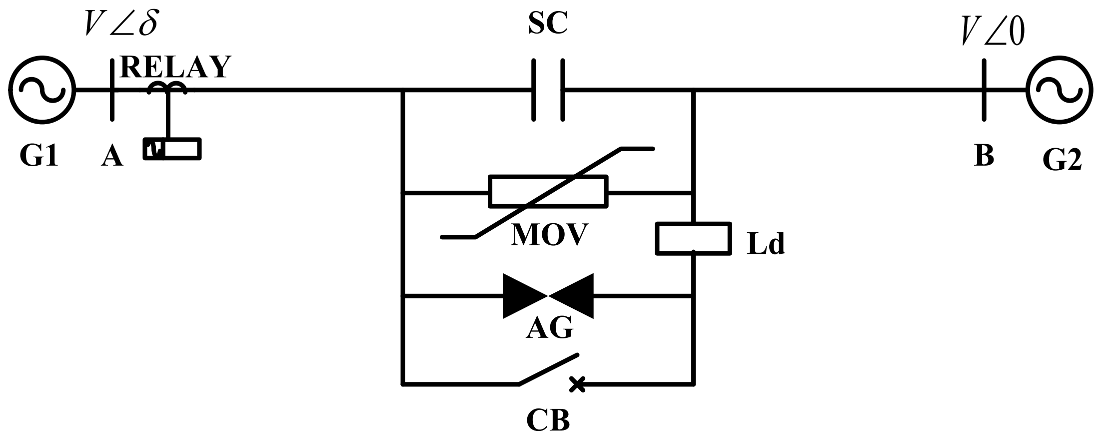

Figure A.1: Transmission line system model single line diagram with SC at mid of the line

Source Data at both Sending and Receiving Ends:

Positive sequence impedance	: 1.31 + j 15.0 Ω .
Zero sequence impedance	: 2.33 + j26.6 Ω
Frequency	: 50 Hz.

Transmission-Line Data:

Length	: 300 km.
Voltage	: 400 kV.
Positive-sequence impedance	: 8.25 + j94.5 Ω
Zero-sequence impedance	: 82.5 + j308 Ω
Positive-sequence capacitance	: 13 nF/ km.
Zero sequence capacitance	: 8.5 nF/ km.

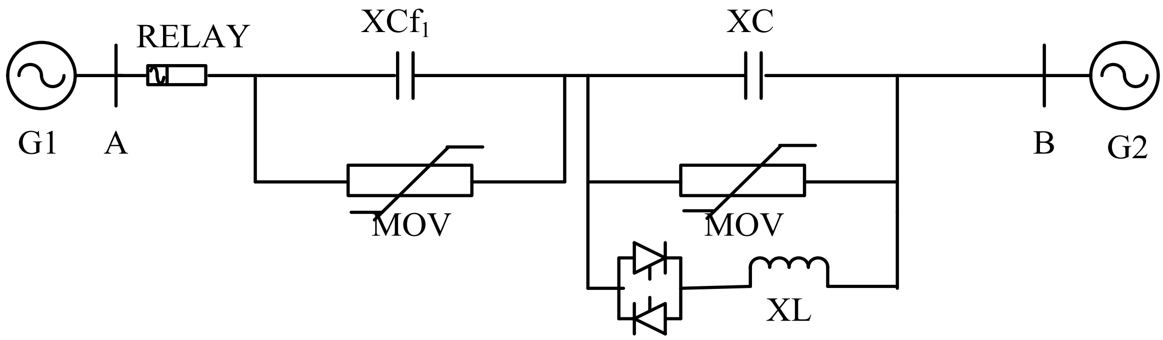

Figure B.1: Transmission line system model single line diagram with TCSC and fixed SC

XCf_1 = 112.27 μf = 30% compensation to the overall line inductance

X_{TCSC} = 0 % – 10 % compensation to the overall line inductance for firing angle of 180° to 153°

Source Data at both Sending and Receiving Ends:

Positive sequence Resistance	: 1.31 Ω
Positive sequence Reactance	: 15.0 Ω
Zero sequence Resistance	: 2.33 Ω
Zero sequence Reactance	: 26.6 Ω
Frequency	: 50 Hz.

Transmission-Line Data:

Length	: 300 km.
Voltage	: 400 kV.
Positive sequence Resistance	: 8.25 Ω
Positive sequence Reactance	: j94.5 Ω
Positive-sequence capacitance	: 13 nF/ km.
Zero-sequence Resistance	: 82.5 Ω
Zero-sequence Reactance	: j308
Zero sequence capacitance	: 8.5 nF/ km.

High Voltage Protection:

MOV current voltage relationship : $i = Kv^{\alpha}$

Where, *i* and *v* represent instantaneous compensator current and voltage respectively. The constant K is given by: $K = \frac{I_{\max}}{(V_{\max})^{\alpha}}$.